CHARACTERIZATION OF HOMOEPITAXIAL DIAMOND THIN FILMS GROWN BY HOT FILAMENT ASSISTED CHEMICAL VAPOR DEPOSITION

By

WILLIAM BROCK ALEXANDER

A DISSERTATION PRESENTED TO THE GRADUATE SCHOOL
OF THE UNIVERSITY OF FLORIDA IN PARTIAL FULFILLMENT
OF THE REQUIREMENTS FOR THE DEGREE OF
DOCTOR OF PHILOSOPHY

UNIVERSITY OF FLORIDA

1995

ACKNOWLEDGMENTS

I would like to express my sincere appreciation to my advisor, Dr. Paul H. Holloway, for his guidance, support, and encouragement. Thanks are also due to my doctoral committee members, Dr. Robert Park, Dr. Robert DeHoff, Dr. Rajiv Singh, and Dr. Tim Anderson, for their assistance and interest in my work.

This work would not have been possible without the samples and assistance provided by LMA, Inc. I am grateful to Dr. Robert Linares and Patrick Doering for their endless support of my work.

I would also like to thank Dr. Romulo Ochoa and Dr. Joseph Simmons for discussions of Raman scattering. Additional thanks go to Dr. Tim Anderson for providing continual use of his Raman spectrometer.

Thanks are due to Dr. Maggie Puga-Lambers and Dr. Balu Pathangey for providing SIMS analysis and Tom Joseph for collecting FTIR data. These data were instrumental for this work.

I am indebted to my friends and coworkers for their comradeship and encouragement through out my stay in Gainesville. I would like to thank Rob Thompson and Wishy Krishnamoorthy for entertaining conversations of x-ray diffraction. Special thanks go to my friend Chris Rouleau for numerous discussions and good times. I am also indebted to Michelle Somerday for her constant support and encouragement.

TABLE OF CONTENTS

ACKNOWLEDGMENTS. ii

ABSTRACT vi

CHAPTER 1 INTRODUCTION 1
Motivation and Objectives. 1
Scope of the Present Work. 3

CHAPTER 2 LITERATURE REVIEW ON HOMOEPITAXIAL DIAMOND FILM GROWTH AND CHARACTERIZATION 5
Introduction 5
Gas Phase Chemistry for Diamond Film Growth. . . 7
Homoepitaxial Diamond Film Growth 13
Raman Analysis of Stress in Thin Films 17
Raman Spectroscopy Background 19
X-Ray Diffraction 29
Rocking Curves. 29
Lattice Parameter and $\omega/2\theta$ Rocking Curves. . 30
Mosaic Structure and ω Rocking Curves . . . 32

CHAPTER 3 EXPERIMENTAL APPROACH 54
Introduction 54
Hot Filament Assisted Chemical Vapor Deposition . 54
Diamond Growth Chamber and Parameters. 56
Characterization Techniques 59
Raman Spectroscopy Experimental Procedure . . . 59
Stress Measurement Precision and Method 62
Controlling Raman Probing Depth. 65
Curve Fitting. 67
X-Ray Experimental Procedures 70
Analyzer Crystal 72
Scanning Electron Microscopy. 74
Fourier Transform Infrared Spectroscopy 74

Secondary Ion Mass Spectrometry. 75
Quantitative Analysis with SIMS 76

CHAPTER 4 RESULTS 96
Surface Morphology 96
Raman Spectroscopy of Graphite Versus Diamond Deposition. 100
Raman Analysis of Stress 104
SIMS Analysis. 109
FTIR Analysis. 111
X-Ray Analysis 115

CHAPTER 5 DISCUSSION 207
Surface Morphology 207
Raman Spectroscopy of Deposited Films. 209
Raman Analysis of Stress in (110) Films 212
Intrinsic Stress. 216
Classification of Natural Diamond and SIMS Analysis of Diamond Films. 217
FTIR Analysis. 225
X-Ray Diffraction 226
Cracking of Films 229

CHAPTER 6 SUMMARY AND CONCLUSIONS. 239

APPENDIX CARBON PHASES 243

REFERENCE LIST 247

BIOGRAPHICAL SKETCH 256

Abstract of Dissertation Presented to the Graduate School of the University of Florida in Partial Fulfillment of the Requirements for the Degree of Doctor of Philosophy

CHARACTERIZATION OF HOMOEPITAXIAL DIAMOND THIN FILMS GROWN BY HOT FILAMENT ASSISTED CHEMICAL VAPOR DEPOSITION

By

William Brock Alexander

May, 1995

Chairperson: Dr. Paul H. Holloway
Major Department: Materials Science and Engineering

Diamond films were grown on (100), (110), and (111) oriented natural diamond substrates by hot filament assisted chemical vapor deposition (HFCVD) to thicknesses of 7 to 100μm. The precursor gas was either 3 to 100% methanol balance hydrogen, or 0.5 to 3% acetone balance hydrogen.

The accuracy and precision of Raman spectroscopy to reflect stress and sp^3 versus sp^2 bonding in thin diamond films was improved significantly using an internal krypton calibration line (1320cm^{-1}) and a pinhole aperture. Tensile stresses of up to ~2GPa were measured for some of the (110) films. Films grown with ≤20% methanol exhibited diamond

(1332cm^{-1}) and no graphitic (1360, 1525, or 1585cm^{-1}) peaks.

The development of stress during HFCVD growth of diamond was attributed to the incorporation of impurities (Re, Mo, O_2, and H_2) and to the influence of film orientation on the ability of diamond to plastically deform. Impurity concentrations were greater at the interface than through the film thickness and up to ~11% H_2 and ~50ppm Re were measured in the films with secondary ion mass spectrometry (SIMS).

The Griffith model of crack propagation versus slip was used to predict cracking of the (110) films. Two of the {111} cleavage planes are perpendicular to the (110) surface which precludes slip and results in maximum tensile stresses in the plane of the film. It was speculated that microflaws in the film created stress intensity factors which under tensile stress caused cracks to propagate along cleavage planes.

Homoepitaxial diamond films were further characterized using a seven crystal high resolution x-ray diffraction system. This new characterization tool allowed the separation of the effects of mosaicity from those of variations in lattice parameter. Broadening of the x-ray rocking curves due to mosaicity ranged from 15 to 1000 arcsec, and 12 to 360 arcsec for lattice parameter variations.

CHAPTER 1
INTRODUCTION

Motivation and Objectives

Diamond possesses many attractive properties such as high hardness ($10^4 kg/mm^2$), high thermal conductivity (22W/cmK), optical transparency, low coefficient of friction, chemical inertness and a wide bandgap (5.45eV) [Ang91]. These properties are suitable for many applications such as heat sinks, high temperature semiconductors and wear resistant coatings for mechanical, chemical, or optical applications. More specifically, the unique combination of mechanical and physical properties makes diamond a desirable material for electronic devices and applications.

Diamond-based electronic devices would be the components of choice for high temperature and radiation environments such as those encountered in outer space. Silicon devices require cooling to approximately 125°C for proper operation, and the cooling systems required to maintain these temperatures can occupy nearly 60% of the volume in an

unmanned satellite. Since diamond devices can operate at higher temperatures (400-500°C), a significant reduction of cooling systems and overall volume could be achieved [Gil91]. High power and high speed diodes, transistors, switches and other devices of the future will take advantage of diamond's high thermal conductivity, electrical resistivity, high breakdown electric field strength, low dielectric constant, chemical inertness and superior charge-carrier transport properties such as high electron mobility and velocity [Rav93]. Optical device applications utilizing single crystal diamond include optical detectors and emitters of radiation in the UV range of the spectrum, for example, metal-semiconductor-metal (MSM) and metal-insulator-semiconductor (MIS) radiation detectors. The quantum efficiency, transient response, and performance of these devices should improve with higher quality material [Mar94].

In order to realize diamond-based electronic devices, growth processes are required for single crystal, electronic-grade films. The incorporation of impurities such as hydrogen, the development of secondary defects such as stacking faults and development of strain would affect the electron transport properties of the diamond film [Peh94].

Scope of the Present Work

A review of the literature (Chap.2) shows that a range of diamond film quality has been obtained on (100), (111), and (110) diamond substrates. Evidence of stress and stress relief via crack formation has been reported, but detailed studies of the origin of this stress has not been reported.

One objective of this study was to grow homoepitaxial diamond films with HFCVD. Natural (100), (110) and (111) diamond were used as substrates, and the precursor gases were acetone or methanol. The diamond growth conditions will be discussed in Chapter 3. The diamond films developed smooth or rough surface morphologies, penetration twins, pits, graphitic inclusions, renucleation sites, cracking, mosaic structure, and relatively high quality epilayers. The results were a strong function of the growth chemistry and orientation of the film and substrate.

Another objective of the study was to define the magnitude and origin of stress which would lead to crack formation in some of the films. To accomplish this objective, methodologies to obtain reliable stress measurements using Raman spectroscopy and x-ray diffraction were developed.

Raman spectroscopy was used extensively throughout this study, and close evaluation of the technique and its limitations for analysis of stress in transparent materials (diamond) was required. The features and improvements implemented for using Raman spectroscopy to analyze diamond will be discussed in Chapter 3. High resolution and triple-axis x-ray diffraction was also employed for mosaic structure characterization. Since the x-ray techniques used in this study are relatively new, the technique and appropriate literature is also reviewed in Chapter 2. The experimental methods used for collecting x-ray data are discussed in Chapter 3.

The results of characterization are given in Chapter 4 followed by a discussion of those results in Chapter 5. The conclusions of the study are given in Chapter 6 with suggestions for future work in Chapter 7.

CHAPTER 2
LITERATURE REVIEW ON HOMOEPITAXIAL DIAMOND FILM GROWTH AND CHARACTERIZATION

Introduction

The synthesis of diamond by low pressure chemical vapor deposition (CVD) has been the subject of extensive research in the last several years [Chu90, Ang88, Spi81, Kob88]. Diamond has been produced by several low pressure methods including hot filament assisted chemical vapor deposition (HFCVD) [Figure 2.1] [Cla89, Ale92, Kaw87, Mat82], plasma assisted chemical vapor deposition (PACVD) [Ito91], and acetylene torch [Hir89]. In each process, hydrocarbon and hydrogen gases are activated by plasmas or hot filaments, creating a mixture of gas species which include atomic hydrogen, methane, and acetylene. The HFCVD system was used in this study and will be discussed further in Chapter 3. Various vapor deposition diamond growth methods have been discussed by Zhu et al. [Zhu91].

The chemical and physical reactions occurring in CVD diamond processes are complex and not well understood. The critical role of atomic hydrogen for growth of diamond rather than graphite has been recognized [Spi81], but the growth species and growth mechanisms are still unclear. Theoretical predictions and quantum mechanical calculations have been completed which show that the most probable diamond growth species are CH_3 radicals, CH_4, and C_2H_2 acting through gas/solid reactions. Chemical reaction models have been proposed based on previous work [Goo90, Har89, Fre88] which support the importance of particular growth species and mechanisms. Steps necessary for diamond growth include adsorption of hydrogen atoms and hydrocarbons; dissociation of H_2 and recombination of H; hydrogenation and dehydrogenation of adsorbed complexes; formation and decomposition of diamond, diamond-like carbon and graphite nuclei; desorption of H_2 and C_iH_j molecules; and preferential etching of graphitic carbon phases by atomic hydrogen.

In this Chapter, literature pertaining to vapor deposition of diamond and, more particularly, homoepitaxial diamond film growth, will be reviewed. Strain analysis using Raman spectroscopy was a major part of this work, and relevant

literature which pertains to measurement of strain in homoepitaxial diamond films and other epitaxial layered systems will be discussed. The fundamental mechanism by which stress affects Raman scattering are discussed below.

Gas Phase Chemistry for Diamond Growth

Bachmann et al. [Bac91] summarized the diamond growth gas phase compositions from many studies. Bachmann introduced a C/H/O ternary phase diagram to relate a number of diamond growth studies which used several low vapor deposition techniques. It was shown that diamond deposition was only feasible in a well defined field of the phase diagram. This field was along the CO line. Bachmann's C/H/O ternary diagram is shown in Figures 2.2a and b where the atom fractions are represented by

$$X_{O/\Sigma}=O/(O+H) \qquad (2\text{-}1)$$

$$X_{H/\Sigma}=H/(H+C) \qquad (2\text{-}2)$$

$$X_{C/\Sigma}=C/(C+O) \qquad (2\text{-}3)$$

where O, H, and C are the atomic fractions of oxygen, hydrogen, and carbon, respectively, and each side of the

equilateral triangle represents the gas composition from a binary system. A C/H/O ternary phase diagram is shown again in Chapter 3 to illustrate the gas compositions used in this study. (In this dissertation, a mixture of 1%CH_4 and 99%H_2 will be referred to as 1% CH_4 for brevity. It will be assumed that the balance consists of hydrogen. Also, a mixture of 1%CH_3OH and 99%H_2 is referred to as 1%CH_3OH).

Researchers continue to investigate the gas species responsible for diamond growth. This information is important to understand growth mechanisms, increase growth rates, and improve film quality. Gas phase analysis and modeling of the diamond growth environment have revealed the most probable diamond growth species to be CH_3, CH_4, C_2H_2, and C_2H_4 [Har88, Cel91]. Calculated concentrations of gas phase species at thermal equilibrium for 0.5%CH_4 is shown in Figure 2.3 [Cel90]. The H_2 curve at a mole fraction of ~1 was not shown. A significant fraction of methane was converted to acetylene at higher temperatures (>1500K=1227°C).

The relative concentration of activated gas species are a function of both the precursor gas composition and the filament temperature. Increasing the filament temperature results in higher concentrations of acetylene and its cracking

products versus methane and its cracking products [Fig. 2.4] [Ale92, Som90, Som91, Wu90, Har88]. Since the filament temperature affects the concentrations of the various gas species, it was important to hold the filament temperature constant during growth in this study. This facilitated the mapping of growth chemistries versus the quality of diamond grown.

Gas composition greatly affects the quality of diamond films grown by vapor deposition as measured by Raman spectroscopy and scanning electron microscopy. It is important to understand the influence of gas composition on diamond growth since this also affects film quality [Kaw87, Kob88]. Raman spectroscopy of polycrystalline diamond films grown with 2%, 2.7%, and 3.9% CH_4 are shown in Figure 2.5 [Kaw87]. The diamond peak at 1332.5cm^{-1} was less pronounced and the graphite peak at ~1580cm^{-1} was more pronounced at higher methane concentrations. The peak (1340-1360cm^{-1}) which was overwhelming the diamond signal on the 3.9%CH_4 spectra was due to amorphous carbon. It should be noted that these samples were grown for 3 hours (0.5μm/hr) on silicon substrates which were pretreated with diamond powder. A majority of the diamond signal could be due to the diamond

powder and not the grown film which was relatively thin for Raman analysis.

The addition of oxygen to the precursor gas composition resulted in improved diamond deposition as measured by Raman spectroscopy [Figure 2.6] [Kaw87] for the same growth conditions. The amorphous carbon increased with increased methane in the oxygen/hydrogen (0.2:50) balance; however, the amorphous carbon and graphite signals are less pronounced than demonstrated in the previous figure.

Scanning electron microscopy (SEM) has been used to study the polycrystalline film texture and crystallite geometry [Ale92, Cla91, Cla89]. The development of texture is the result of competitive growth between randomly oriented crystals. Crystals with fast growth directions perpendicular to the substrate surface outgrow other crystals, resulting in a textured film with a columnar structure. The texture of polycrystalline films was important due to the dependence of mechanical and optical properties on the film orientation.

The diamond crystallite geometry was a result of the relative growth rates in the <100> and <111> directions which in turn was related to the surface morphology resulting from solid state growth. The growth rate ratio, designated by α,

was the ratio of that in the <100> to that in the <111> directions. This parameter was first used by Spitsyn et al. [Spi81], and has been used extensively by Clausing et al. [Cla91]. The ratio α is equal to the ratio of the distances from the center of the crystal to the center of the {100} and {111} facets. A growth rate ratio of $1/\sqrt{3}$, $\sqrt{3}/2$, and $\sqrt{3}$ results in a cube bounded by {100} planes, a cubo-octahedral, and a octahedral bounded by {111} planes, respectively. In other words, if α is greater than $\sqrt{3}/2=0.87$ the crystal grows faster in the <100> direction causing the {111} facets to increase in size. When α is less than $\sqrt{3}/2$ the crystal grows faster in the <111> direction causing the {100} facets to increase in size. The geometric features are used to correlate growth conditions with texture of polycrystalline films. Computer generated cubo-octahedrons with $0.6 \leq \alpha \geq 1.65$ are shown in Figure 2.7. Diamond crystallites grown with HFCVD are shown in Figures 2.8 and 2.9 which demonstrate an $\alpha=0.85$ and $\alpha=0.9$, respectively. Note the smoother {100} faces as compared to the {111} faces exhibited by the diamond crystallites [Figures. 2.8 and 2.9].

It has been shown that changes in growth parameters, e.g. gas composition [Kob88, Spi81], substrate temperature [Cla91, Cla89], or filament temperature [Ale92], affect the shape of crystallites and the texture of the polycrystalline films. The results are not always similar. For example, Kobashi et al. [Kob88] observed {111} faceting at lower methane concentrations and {100} faceting at higher methane concentrations, while Spitsyn et al. [Spi81] observed the opposite relationship. The reason for these discrepancies was that other growth parameters, in addition to gas chemistry, affect film texture. It is believed that gas chemistry and substrate temperature are the dominant growth parameters affecting film texture.

Wild, Koidl, and coworkers [Wil94, Koi94] have measured texture with x-ray diffraction in a four circle x-ray powder diffractometer on (100) oriented polycrystalline films. The {400} and {220} pole figures are shown in Figure 2.10. This diamond film is highly oriented for a polycrystalline diamond film. This was achieved by α-mapping the growth parameters in the microwave plasma CVD system used to grow the film. The conditions which favored preferential growth along the <100> ($\alpha \approx 1.62$) were used to grow the film. The results of their α-

mapping are shown in Figure 2.11. Using α~1.7 conditions, they grew a 120μm thick homoepitaxial film on a (100) diamond substrate which exhibited a "smooth" surface without any "major defects" [Wild94]. However, the SEM photograph of this film showed what we believe to be {111} growth steps and penetration twins.

Homoepitaxial Diamond Film Growth

Homoepitaxial diamond growth refers to a single crystal of diamond growing with the same orientation on a single crystal diamond substrate. This type of growth is generally conducted on (100), (111), and (110) oriented diamond substrates and will be discussed in this order.

Most groups report that diamond growth on (100) surfaces is of a higher quality than the diamond grown on (111) and (110) substrates [Bad93, Bad91, Sut92, Sna91, Chu91, Chu92, Fuj90] as measured by Raman spectroscopy and/or SEM. Evidently the only exception was a paper by Kamo et al. [Kam88] which reported that (100) oriented growth was more difficult than (111) and (110) oriented growth. Badzian et al. [Bad91] have reported that the thickest films they grew were approximately 250μm thick on (100) diamond substrates.

These films were reported to exhibit good, stress free Raman peaks at ~1332cm^{-1} with FWHM of <2.5cm^{-1}. However, a microscopic image under crossed polarizers of a 60μm thick film indicated that the film was stressed [Bad93]. The magnitude of the stress, nor why the results from the image and Raman did not agree, were not discussed. Films have been grown at substrate temperatures ranging from 850 to 1200°C, and it was proposed by Badzian et al. [Bad93] that substrate temperatures >1100°C would be beneficial for (100) homoepitaxial diamond film growth. As stated earlier, substrate temperature and gas chemistry are the paramount growth parameters, and in the paper by Badzian et al. [Bad93] only the substrate temperature was varied; the gas composition was 1% methane.

Growth on the (100) evidently proceeded by a step growth process along <110> crystallization fronts [Bad93]. There have been no reports of Raman peak shifts and therefore stress measurements via Raman for (100) oriented films.

A variety of growth results have been achieved on (111) oriented diamond substrates; from smooth single crystal surfaces to polycrystalline films resulting from renucleation. Some surfaces exhibited cracking and striations. Films grown

thicker than a few micrometers typically lost their epitaxial structure and became polycrystalline and smooth (111) surfaces have only been reported for films with thicknesses less than a few micrometers.

Graphitic inclusions have been reported in diamond and appear to be more common in films grown on (111) oriented substrates. Chu et al. [Chu91, Chu92] detected graphite or amorphous carbon in their films with Raman spectroscopy and also reported tensile peak shifts of approximately -5.1cm^{-1} from the ^{13}C diamond Raman mode. Their films were grown with isotopically labeled methane so the film peak could be distinguished from the substrate peak. The observed peak shifts are rather large, and though the FWHM of the peak was not given, it was well larger than 10cm^{-1} by visual inspection of the Raman spectra. After a few micrometers of growth the film cracked and relieved the stress and the Raman peak shifted toward the stress free value of the ^{13}C diamond Raman frequency (1280cm^{-1}).

Growth on the (111) surface appears to be sensitive to defect propagation [Bad93] and the increase in defect density as the film grows inhibits epitaxial growth. Rough (111) surfaces and smooth (100) surfaces are typical for

polycrystalline films grown on silicon and other non-diamond substrates. The diamond crystallites shown previously in Figures 2.8 and 2.9 exhibit smoother (100) surfaces compared to the (111) surfaces.

Diamond films grown on the (110) diamond surface have been reported to have rough surface morphologies [Kon93, Fuj90, Sut92] and to grow faster then (100) or (111) surfaces [Fuj90, Chu91, Chu92, Gei90]. The (110) homoepitaxial surface can exhibit a corrugated or microfaceted morphology revealing (111) and $(11\bar{1})$ surfaces [Bad93, Kon93]. This surface structure may be the result of three dimensional growth as suggested by RHEED patterns [Kon93]. Badzian et al. [Bad93] reported that after several micrometers, films can lose their epitaxial relationship and become polycrystalline at typical substrate temperatures. However, a (110) oriented film grown at a substrate temperature of 1200°C to a thicknesses of 1.2mm, remained homoepitaxial. This thick film also demonstrated good Raman characteristics with a FWHM of $3.5cm^{-1}$ and no apparent frequency shift, i.e. a peak position at $\sim 1332cm^{-1}$.

Raman frequency shifts of $-1.1cm^{-1}$ were observe from a $5\mu m$

thick ^{13}C homoepitaxial film [Chu91]. Films were grown from isotopically labeled methane in order to ease interpretation of the Raman spectra. Smaller diamond Raman frequency shifts [Fuj90] in addition to cracking of films at thicknesses of only a few micrometers [Kam88] have been reported.

Although the diamond Raman frequency shifts were reported to be due to tensile stress, the origin of stress was not investigated, nor were vales for Raman peak position versus stress. It has been postulated [Chu91] that the stresses could be caused by graphitic inclusions or defects.

Raman Analysis of Stress in Thin Films

Raman spectroscopy was used extensively in this work for the analysis of stress in homoepitaxial diamond, thus a brief discussion of the literature is warranted. Although diamond Raman mode peak shifts have been observed for homoepitaxial films, detailed investigations into the origin(s) of these frequency shifts have not been reported. Since diamond is transparent at the argon ion laser frequency of 514.5nm, the Raman effect was generated in the bulk as well as near the surface. This affect inhibited the ability to accurately measure the Raman signal of the film, since the substrate

signal may overwhelm the film signal. There are no published work addressing this problem for homoepitaxial diamond thin film characterization using Raman spectroscopy. Some groups have used isotopic labeling which allowed the film peak to be resolved from the substrate peak. Due to the insufficient literature pertaining to strain analysis via Raman spectroscopy of homoepitaxial diamond films, other material systems will be discussed which demonstrate the feasibility and non-destructive nature of this technique to probe strain.

Epitaxial layers of GaAs grown by MBE on (100) and (111) silicon exhibited tensile stress which was revealed by a decrease in the Raman frequency. The biaxial stress in the film resulted in a $2cm^{-1}$ shift in the longitudinal optical (LO) phonon mode for both the (100) and (111) GaAs layers [Figures 2.12 and 2.13] and the calculated stress was 350MPa and 490MPa respectively [Qua93]. A profile of the stress was completed by etching away layers of the film which revealed greater strain near the interface than at the film surface. The stress was from differences in the thermal coefficients of expansion (TCE) and not lattice mismatch, since the layers greatly exceeded the critical thickness.

Silicon-germanium alloys have been characterized with Raman spectroscopy [Mey91, Die93]. The Raman frequency of the Si-Ge alloy film is a function of the composition and the stress in the layer. Compressive stresses as large as 1.5GPa were measured from 20%Ge films (grown by MBE) after misfit dislocations had developed [Die93]. Raman stress results were compared with XRD and TEM results and were in relatively good agreement with respect to sign and magnitude. Silicon-germanium films prepared by ion-beam sputter deposition resulted in compressive stresses of 1.5GPa also, which were relieved by heating to 800°C for 110 minutes [Mey91]. Homoepitaxial silicon films prepared by ion-beam sputter deposition exhibited compressive stresses of 1.8GPa for low temperature growths.

Thus, Raman spectroscopy has been proven to be useful for stress analysis of epitaxial layers of semiconducting materials and is a desirable characterization tool due to the nondestructive nature of the technique.

Raman Spectroscopy Background

In this section, a description of Raman scattering and additional background information will be presented. This

will be followed by the reasons for using Raman in this study. The steps used for gathering Raman data are discussed in Chapter 3.

Absorption, emission, and scattering are phenomena which occur when electromagnetic radiation interacts with a molecule [Kit86]. Absorption occurs when the molecular excited state is separated from the ground state by the energy of a photon. Emission occurs when the excited molecule decays towards the ground state, and the emitted photon has an energy equal to the energy difference between the excited and ground states of the molecule. Scattering occurs when the photon energy is not equal to the energy difference between the excited and ground states.

Two types of scattering events can occur [Kit86]. Scattering without a change in the energy of the incident photon is termed Rayleigh scattering; scattering with a change in the incident photon energy is termed Raman scattering. Raman scattering can be explained quantum mechanically when momentum conservation is considered, and semiclassically when we consider the concept of polarizability. Both explanations are discussed below.

The incident photon will increase (anti-Stokes scattering) or decrease (Stokes scattering) its energy during Raman scattering [Kit86]. The two processes can be expressed by employing Planck's formula:

$$E=h\nu \tag{2-4}$$

where E is the photon energy, ν the photon frequency, and h is Planck's constant. The Raman scattered photon has an energy, E_s:

$$E_s=E_i\pm E_{phonon} \tag{2-5}$$

where E_i is the energy of the incident photon and E_{phonon} is the phonon energy. By definition, a phonon is a quantum of crystal vibrational energy [Sri90]. The corresponding frequency, ν_s, is then:

$$\nu_s=\nu_i\pm\nu_{phonon}\ . \tag{2-6}$$

Rewriting this equation considering momentum conservation results in:

$$h\mathbf{k}_s=h\mathbf{k}_i\pm h\mathbf{q} \tag{2-7}$$

where $\mathbf{q}$ is the wavevector of the phonon and $\mathbf{k}_i$ and $\mathbf{k}_s$ are the

wavevector of the incident and scattered photon, respectively. Stokes scattering (ν_i-ν_{phonon}) is generally measured in most Raman spectroscopy because the intensity is stronger then for anti-Stokes scattering (ν_i+ν_{phonon}).

For the semiclassical approach, we need to introduce the concept of polarizability. Polarizability is the extent to which an electron cloud and nuclei are distorted when interacting with an electric field, e.g. the electric field of the photon. The electrons are attracted to the positive end and the nuclei are attracted to the negative end of the electric field. The polarization (P) is the induced electric dipole moment and is related to the electric field (E) by:

$$P=\alpha E \qquad (2\text{-}8)$$

where α is the polarizability. Thus α is a measure of the ease by which the oscillator may be distorted. For an electric field given by:

$$E=E_0\cos(\nu_i t), \qquad (2\text{-}9)$$

where E_0 is the magnitude and ν_i the frequency of the electric field, the polarization may be expressed as:

$$P=\alpha E_0 \cos(\nu_i t) \qquad (2\text{-}10)$$

where the oscillator vibrates at the same frequency (ν_i) as the electric field and can act as a source of radiation (Rayleigh scattering). The inherent or natural frequency (ν_p) and polarizability of an oscillator is related to the polarizability:

$$\alpha=\alpha_0+\sum\alpha_P \cos(\nu_P t) \qquad (2\text{-}11)$$

where α_0 is the static polarizability of the dipole. Rewriting the polarization by:

$$P=E_0\alpha_0 \cos(\nu_i t)+1/2E_0\sum\alpha_P[\cos(\nu_i-\nu_P)t+\cos(\nu_i+\nu_P)t], \qquad (2\text{-}12)$$

it is easy to associate the first term with Rayleigh, the second term with Stokes ($\nu_i-\nu_p$), and the third term with anti-Stokes ($\nu_i+\nu_p$) scattering.

An illustration of a transverse optical (TO) phonon coupled to an electric field is shown in Figure 2.14. The positive and negative poles of the dipole vibrate against each other, with the center of mass unchanged. The dipole oscillation is perpendicular to the direction of propagation

of the electric field for a transverse wave. The dipole oscillation is in the direction of the electric field propagation for a longitudinal wave, e.g. a longitudinal optical (LO) phonon.

Our Raman analysis was performed with unpolarized radiation, so our discussion will not include consideration of polarization selection rules. However, it should be noted that it is possible to resolve the three optical phonons (one longitudinal and two transverse) when using polarized radiation [Pol91]. A good explanation of the application of polarization selection rules to Raman analysis of diamond-cubic materials is given by Pollack [Pol91].

Raman analysis can be performed with 180° (back scattering) or 90° scattering geometry [Figure 2.15], where the angle refers to the angle between the propagation direction of the incident ($\mathbf{k}_i$) and scattered light ($\mathbf{k}_s$) [Bar87]. The back scattering geometry was used in this study. The back scattering geometry results in an electric field which is parallel to the sample surface when the direction of propagation is perpendicular to the surface.

Raman spectroscopy can be used to measure stress in the lattice [Pol91]. The stress induces changes in the force

constant between the atoms and therefore the frequency of their vibration [Pol91]. Detailed discussions of the effects of stress on the atomic force constants and Raman frequency have been given by Cerdeira et al. [Cer72] and others [Par77, Gri78, Ana70, Gan70]. The approach used here to describe the dependence of the phonon frequency with stress is as follows. The displacement of atoms by elastic vibrations is related to the mass of the atoms (m) and the force constant (C) between two neighboring atoms [Kit86]. Considering only two neighboring atoms for brevity, the force acting on an atom at point u_s by an atom at u_{s+1} is:

$$F_s=C(u_{s+1}-u_s). \qquad (2\text{-}13)$$

The equation of motion of the atom u_s is:

$$m(d^2u_s/dt^2)=C(u_{s+1}-u_s). \qquad (2\text{-}14)$$

The dispersion relation for lattice vibration is [Kit86]:

$$\omega^2=(4C/m)\sin^2(1/2ka) \qquad (2\text{-}15)$$

where ω is the frequency, k is the wavevector magnitude, and a is the repeat distance. (Derivation of the dispersion relation has been outlined by Kittel [Kit86].) An applied

stress affects the force constant C, and thus the frequency of the lattice vibration.

Raman spectroscopy [Cah94, Pol91, Kit86] was used for two purposes in this study: 1) to detect both sp^2 (characterized by a peak at ~1585cm^{-1}) and sp^3 (characterized by a peak at ~1332cm^{-1}) bonded carbon, and 2) measure stress in the diamond films by measuring frequency shifts of the diamond Raman peak. A typical Raman spectra from a polycrystalline diamond film is shown in Figure 2.16. Both the sp^2 and sp^3 carbon peaks were detected at 1585 and 1334cm^{-1}, respectively. The diamond Raman mode peak position may be used to measure the stress as discussed below.

The stress-free Raman frequencies of diamond and several other semiconducting materials are shown in Table 2.1. Several groups have used Raman spectroscopy to measure the shift versus pressure for the diamond Raman mode [Bop85, Par77, Gri78, Tar90, Wha76, Sha85] or the Raman mode of other materials [Cer72, Ana70, Ven73, Ona77, Tek73]. The Raman frequency increases under compressive stress and decreases with tensile stress. The hydrostatic pressure dependence of the diamond Raman mode, κ which was used in this study, was an

average value 2.94cm^{-1}/GPa of those reported in the literature (Table 2.1). The average value of 2.94cm^{-1}/GPa was used to determine the stress in the homoepitaxial diamond films as described below.

Table 2.1 Optical phonon frequencies at **q**=0 for various semiconductors [Gan70, Cah94].

Semiconductor	Structure	LO phonon frequency (cm^{-1})	TO phonon frequency (cm^{-1})
diamond	diamond	1332.5	1332.5
silicon	diamond	520	520
germanium	diamond	300.9	300.9
AlAs	zincblende	404.1	360.9
GaP	zincblende	403	367.3
GaAs	zincblende	291.9	268.6
InP	zincblende	345.0	303.7
InAs	zincblende	238.6	217.3
ZnS	zincblende	348.3	276.9
ZnSe	zincblende	253.2	213.2
ZnTe	zincblende	206.8	176.8
CdTe	zincblende	169.5	140.1

Table 2.2 Values for the pressure dependence of the first-order Raman mode of diamond.

Reference	$(\partial\nu/\partial P)_T$ (cm^{-1}/GPa)	ΔP(GPa)
Bop85	2.87±0.10	0-27
Par77	3.6±0.3	0-2.4
Gri78	3.2±0.2	0-1
Tar90	2.64±0.10	0-15
Wha76	2.96±0.11	0-2.5
Sha85	2.37	0-25

X-Ray Diffraction

X-ray diffraction [Cul78] was used in this study to measure strain and misorientation, since it is sensitive to both the lattice constant and orientation of a crystalline material. Ideally, homoepitaxial systems should not exhibit strain or mosaicity (relative misorientation of mosaic blocks). However, Raman data showed that some diamond films were strained, and cracking in some films was apparent from optical microscopy. This study is the first to use the type of x-ray diffraction methods described below to study diamond

films. Background information and the experimental approach for obtaining lattice parameters (strain) and relative tilts of homoepitaxial films are therefore discussed.

Rocking Curves

A rocking curve is a plot of the diffracted x-ray intensity around the Bragg angle of a particular crystallographic reflection [Phi93]. For example, to record a rocking curve from the (220) reflection of a (110) diamond substrate, (Bragg angle = 37.6°) the detector and/or sample were "rocked" or moved angularly through 37.6° (e.g., 36.6° to 38.6°). A schematic is shown in Figure 2.17 of the x-ray configuration used to obtain rocking curves [Phi93]. As shown in Figure 2.17, omega (ω) is the angle between the crystal surface plane and the optical axis of the x-ray source. Two-theta (2θ) is the angular position of the detector relative to the same optical axis. Ideally, ω=Bragg angle(θ) for symmetric reflections. However, due to samples being miscut or misoriented, this is generally not the case.

Two types of rocking curves can be recorded; an omega/2theta (ω/2θ) or an ω rocking curve. The terminology

reflects the configuration geometry of the sample, detector, and the optical axis of the x-ray source. During recording of an $\omega/2\theta$ rocking curve (also known as an $\omega/2\theta$ scan), both the detector (2θ) and the sample are "rocked", with the detector moving at twice the angular velocity of the sample. During an ω scan, only the sample is "rocked".

Lattice Parameter Measurement and $\omega/2\theta$ Rocking Curves

The $\omega/2\theta$ rocking curve is sensitive to differences in lattice plane spacing [Few91a]. X-ray diffraction has been used to measure lattice-mismatch in heteroepitaxial systems [Slu93, Maz92, Pes91, Few91a, Few91b, Few87, Bra90, Rya87, Bar83]. Consider an epitaxial film with lattice parameter a_{film}, on a substrate with a smaller lattice parameter a_{sub} [Figure 2.18]. Through Bragg's law, $n\lambda=2d\sin\theta$, $\theta_{film}<\theta_{sub}$. To record the x-ray rocking curves from both the film and the substrate, the detector and sample are "rocked" through the Bragg angle of the film and substrate.

The angular separation of the film and substrate peaks, $\Delta\omega$, are used to calculate the lattice mismatch using the differential form of Bragg's law:

$$(\Delta a/a)_{\perp}=-\Delta\omega\cot\theta/\cos^2\phi \qquad (2\text{-}16)$$

where θ is the Bragg angle of the substrate, ϕ is the asymmetric angle, and $(\Delta a/a)_{\perp}=(a_{film}-a_{sub}/a_{sub})_{\perp}$ is the perpendicular lattice mismatch between the film and the substrate [Few87].

Bartels [Bar83] expressed the perpendicular and parallel mismatch for asymmetric reflections to be:

$$(\Delta a/a)_{\perp}=\Delta\phi\tan\phi-\Delta\theta\cot\theta \qquad (2\text{-}17)$$

$$(\Delta a/a)_{||}=-\Delta\phi\cot\phi-\Delta\theta\cot\theta \qquad (2\text{-}18)$$

where $\Delta\phi$ is the difference in lattice plane orientation. The x-ray beam makes an angle of $(\theta+\phi)$ or $(\theta-\phi)$ with the sample surface and the angular separation between the film and substrate peaks is either $(\Delta\theta+\Delta\phi)$ or $(\Delta\theta-\Delta\phi)$, respectively for asymmetric reflections. In terms of the x-ray diffractometer geometry:

$$\omega^{+}=\theta+\phi \qquad (2\text{-}19)$$

$$\omega^{-}=\theta-\phi \qquad (2\text{-}20)$$

where ω+ is referred to as the positive ω geometry and ω- the negative ω geometry. It should be noted that if the film is not misoriented from the substrate, $\Delta\phi=0$. This causes the left side of equations 2-17 and 2-18 to go to 0, and therefore they are not valid for layers which are not tilted off the substrates.

Mosaic Structure and ω Rocking Curves

A "ideal" single crystal has no defects, and the atoms are at their appropriate lattice positions. However, real single crystalline materials consists of many small blocks of varying size and orientation. Mosaic structure [Cul78] refers to the distribution, size, and orientation of these blocks, and can result from the segregation of defects which enclose regions of perfect crystal [Few91a].

The mosaic structure of a film will affect the x-ray rocking curve by increasing the integrated intensity (area under the curve) and the angular position of the diffracted beam [Cul78]. A mosaic block which is misoriented relative to θ by an angle +δ will satisfy Bragg's law at θ+δ. A collection of mosaic blocks will have a range of δ's (mosaic

spread), and this leads to increased broadening of the ω rocking curve.

The ω rocking curve is sensitive to lattice plane tilt or mosaicity. Fewster [Few93, Few92, Few91a, Few91b, Few89] and others [Hei94, Hol93a, Hol93b, Kop94, Slu93] have demonstrated that x-ray analysis can be used to characterize crystal mosaicity of heteroepitaxial layers.

Consider an "epitaxial" film which is misoriented or tilted at an angle δ with respect to the substrate, but has the same lattice parameter [Figure 2.19]. Since the Bragg angle for the film and substrate are the same, only the sample is "rocked" through the Bragg angle; the detector is stationary. The angular separation of the peaks (Δω):

$$\Delta\omega=\delta \qquad (2\text{-}20)$$

is therefore equal to the tilt angle. The experimental procedures used for collecting x-ray data are discussed in Chapter 3.

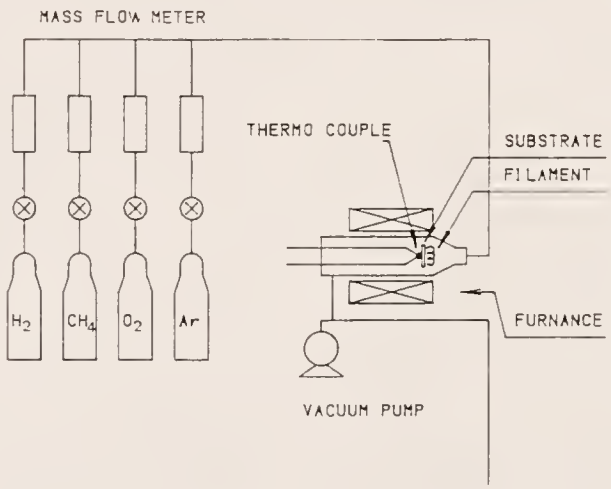

Figure 2.1 Schematic diagram of a typical hot filament chemical vapor deposition system [Kaw87].

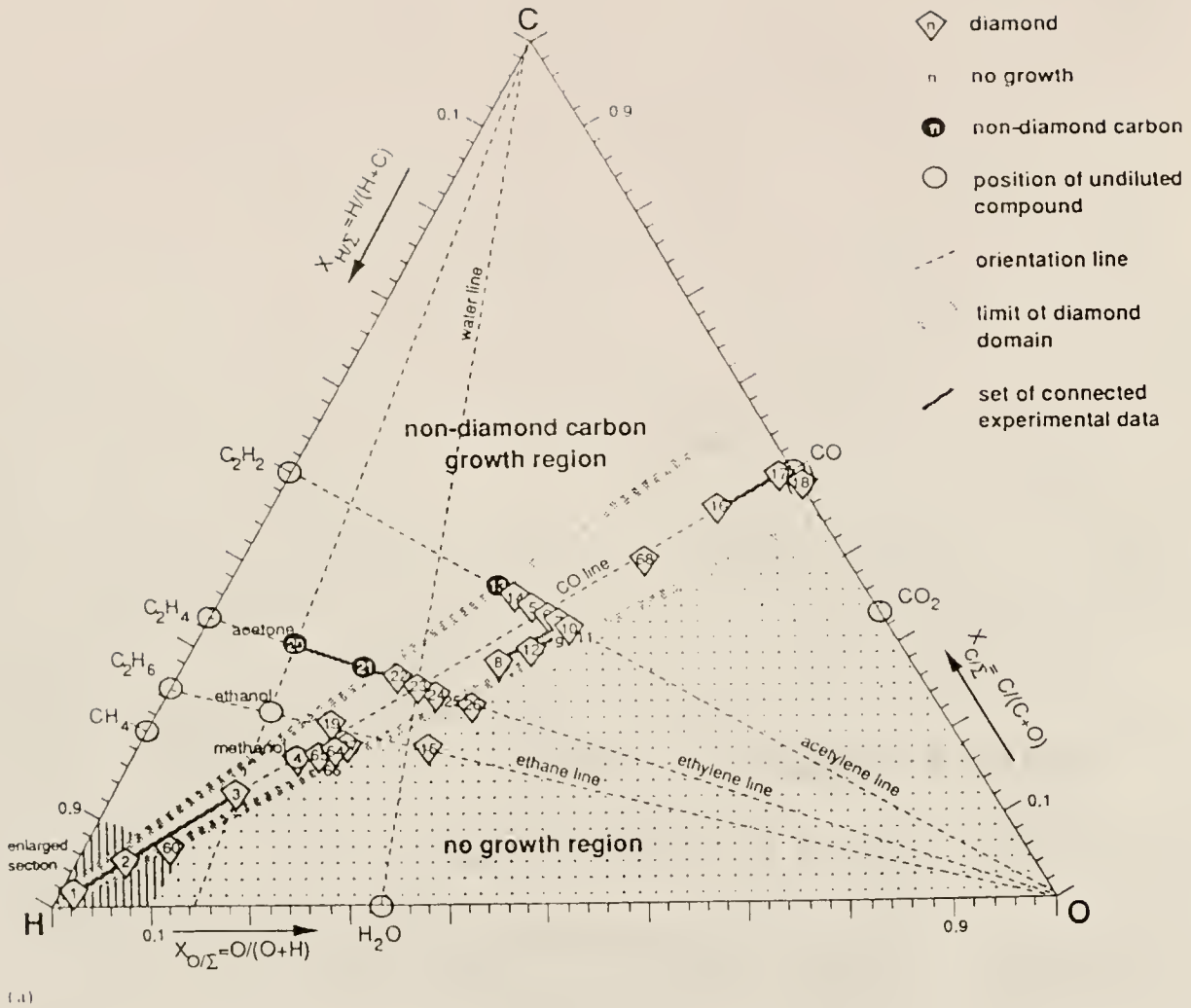

Figure 2.2a Atomic C-H-O diamond deposition phase diagram constructed from over 80 deposition experiments and 25 references [Bac91]. The numbers on the diagram indicated which experiment Bachmann was referencing and the symbols indicated whether diamond was deposited (number and ◊), non-diamond carbon was deposited (number and ●), or nothing was deposited (a number with no symbol).

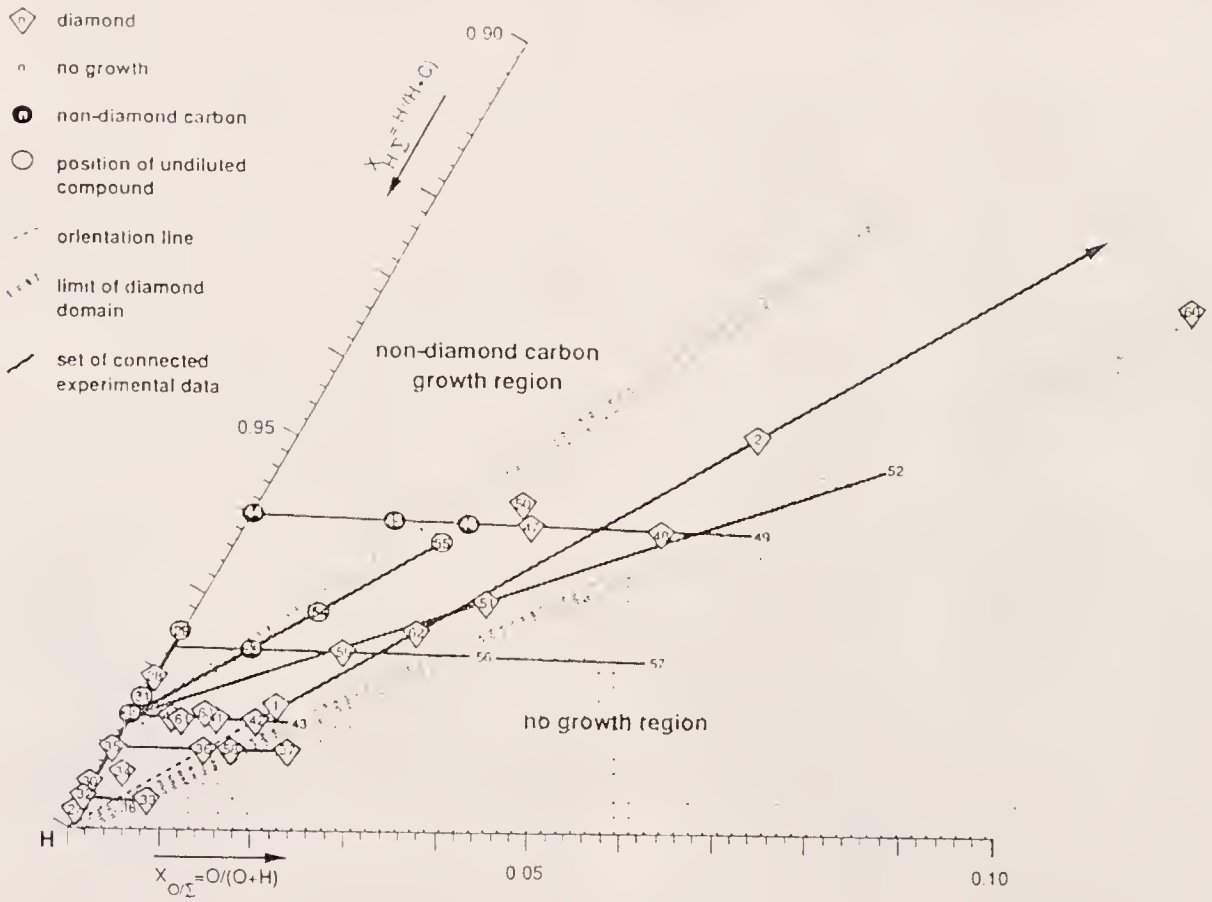

Figure 2.2b Enlarged hydrogen-rich section of the atomic C-H-O diagram showed in Figure 2.2a [Bac91].

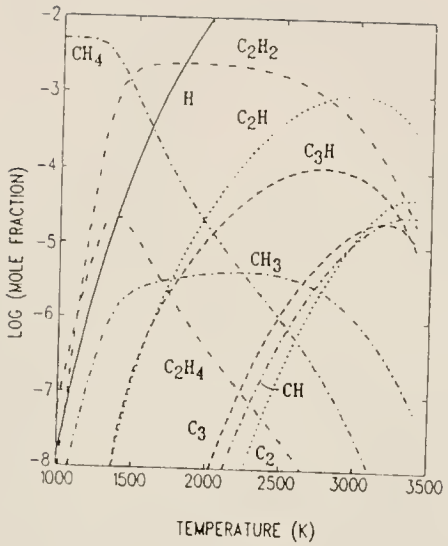

Figure 2.3 Calculated concentrations of the gas species at thermal equilibrium for 0.5% CH_4 in 99.5% hydrogen versus temperature [Cel90].

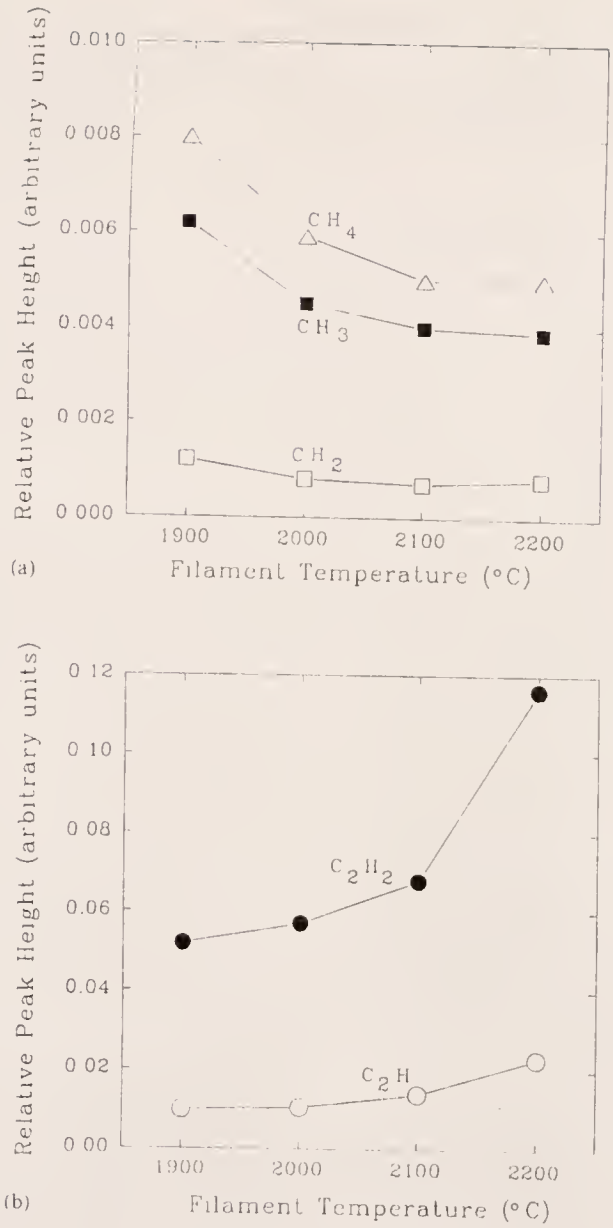

Figure 2.4 Relative partial pressures versus filament temperature of 1%CH_4/99%H_2: (a) methane and its cracking products from methane; (b) acetylene and cracking products from acetylene. The relative sensitivity factors are the same for (a) and (b) and the pressure was 40Torr [Ale92].

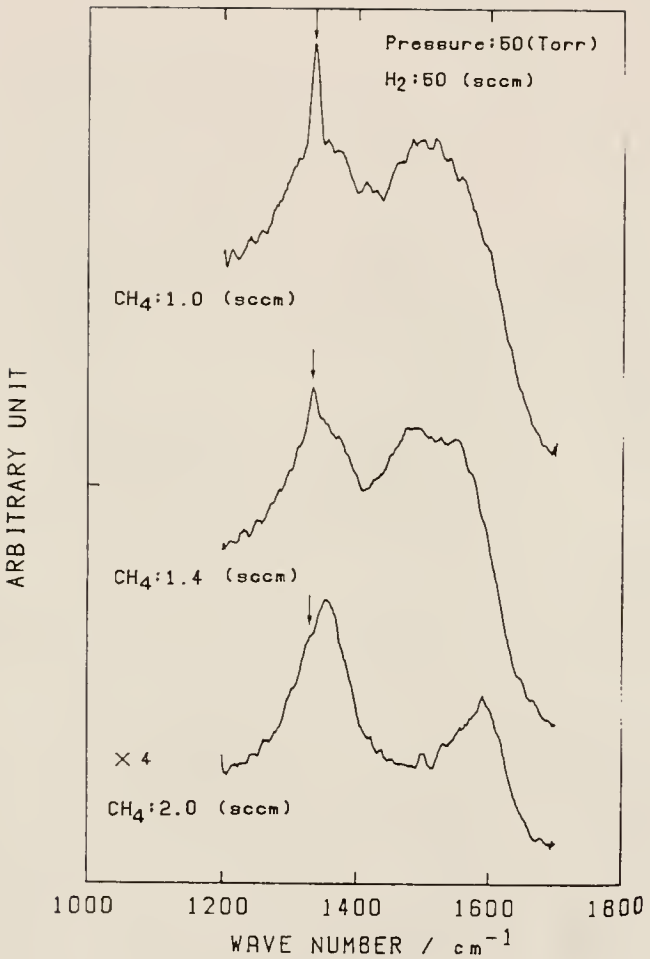

Figure 2.5 Raman spectrum from polycrystalline films grown with 2, 2.7, and 3.9% CH_4. Note the strong diamond signal at 1332cm^{-1} for 2%CH_4 versus 2.7 and 3.9%CH_4. Also the amorphous and graphitic carbon peaks at 1360 and 1585cm^{-1} are stronger for the 3.9%CH_4 film versus 2 and 2.7%CH_4 which exhibit an amorphous carbon peak at about 1525cm^{-1} [Kaw87].

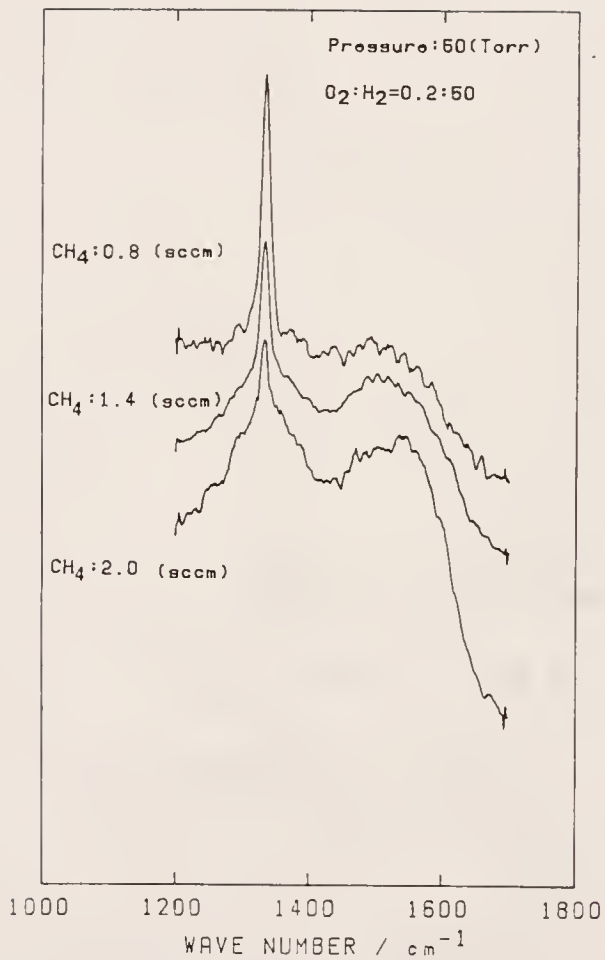

Figure 2.6 Raman spectrum from polycrystalline films grown under the same growth conditions as the films shown in Figure 5, except with the addition of 0.4%O_2 to the precursor gas for all three concentrations. The addition of O_2 resulted in diamond deposition at higher methane concentrations [Kaw87].

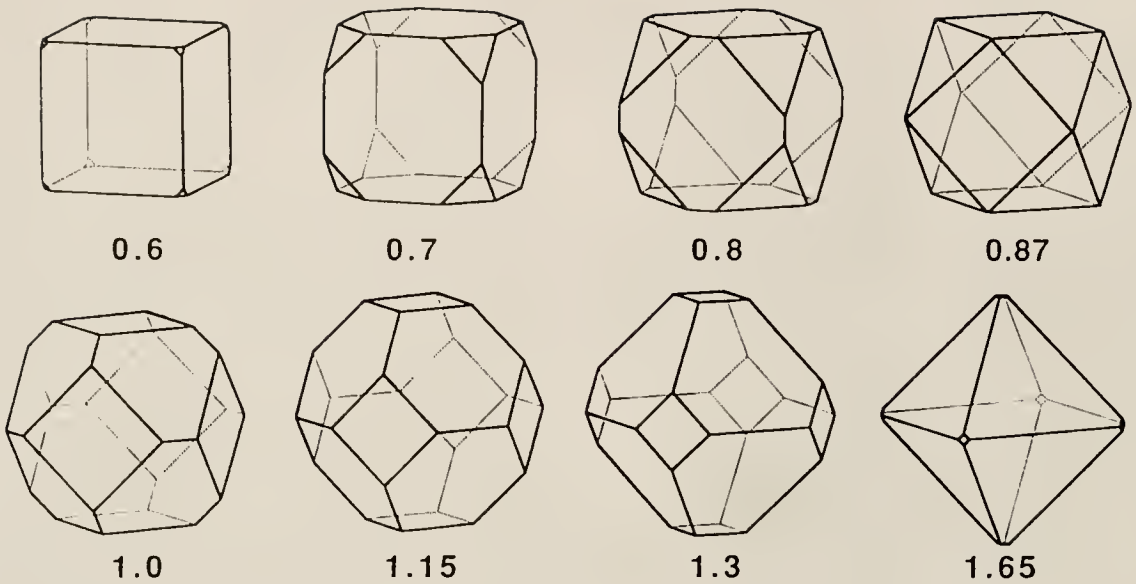

Figure 2.7 Computer generated cubo-octahedrons of diamond for $0.6 \leq \alpha \geq 1.65$, where α is defined to be the ratio of the distances from the center of the cubo-octahedron to the center of the {100} and {111} facets [Ale92].

Figure 2.8 Diamond crystallite shape for α=0.85 [Ale92].

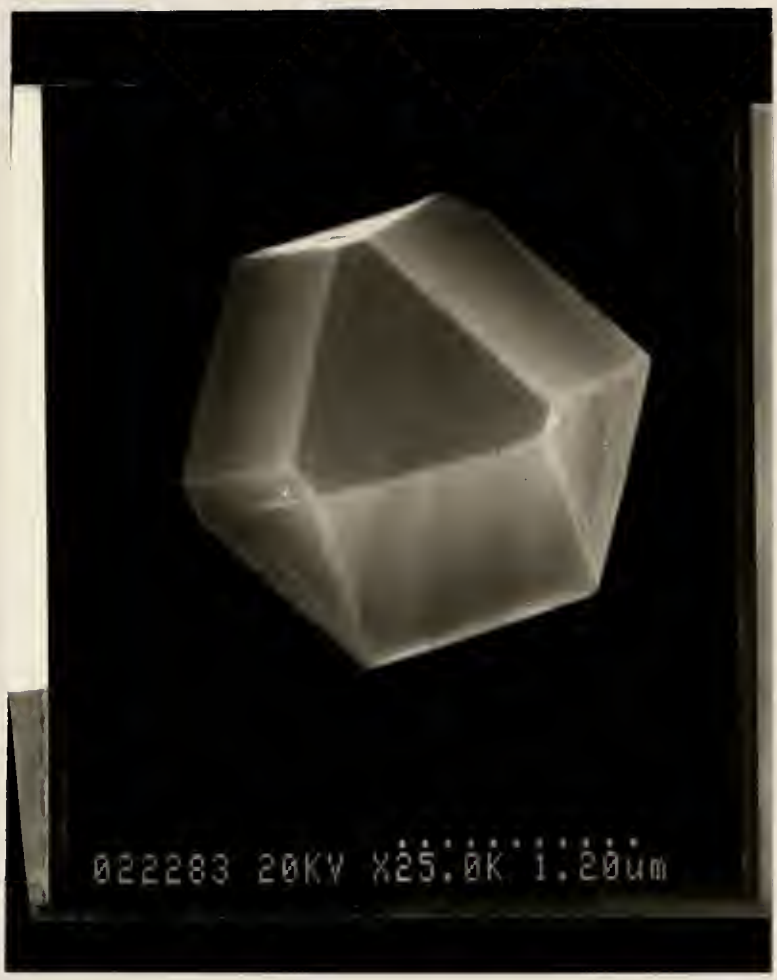

Figure 2.9 Diamond crystallite shape for α=0.9 [Ale92].

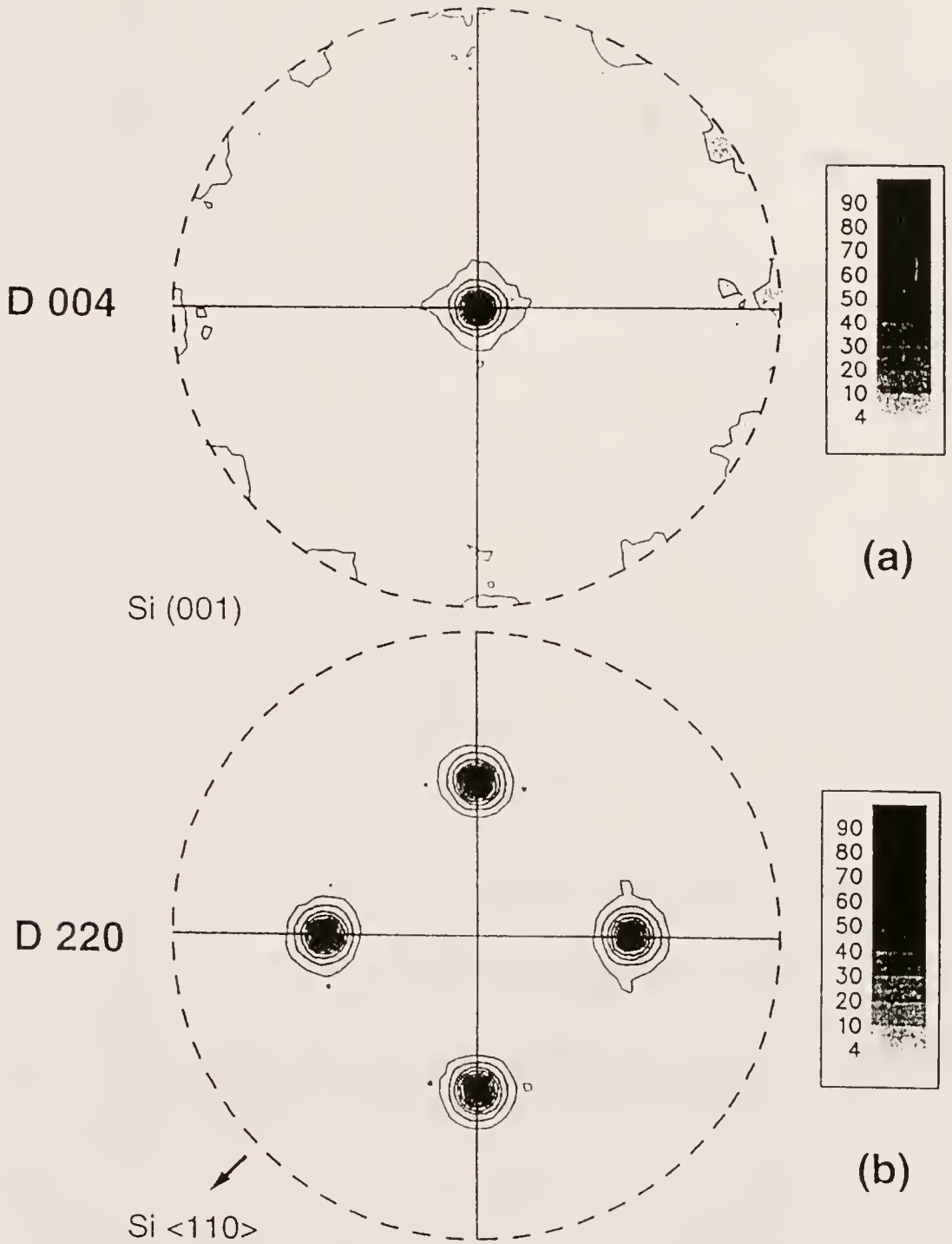

Figure 2.10 The {004} and {220} x-ray pole figures from a textured diamond film grown on a (100) silicon wafer. The film was grown under conditions favoring <100> growth, i.e. $\alpha \approx 1.6$ [Wil94].

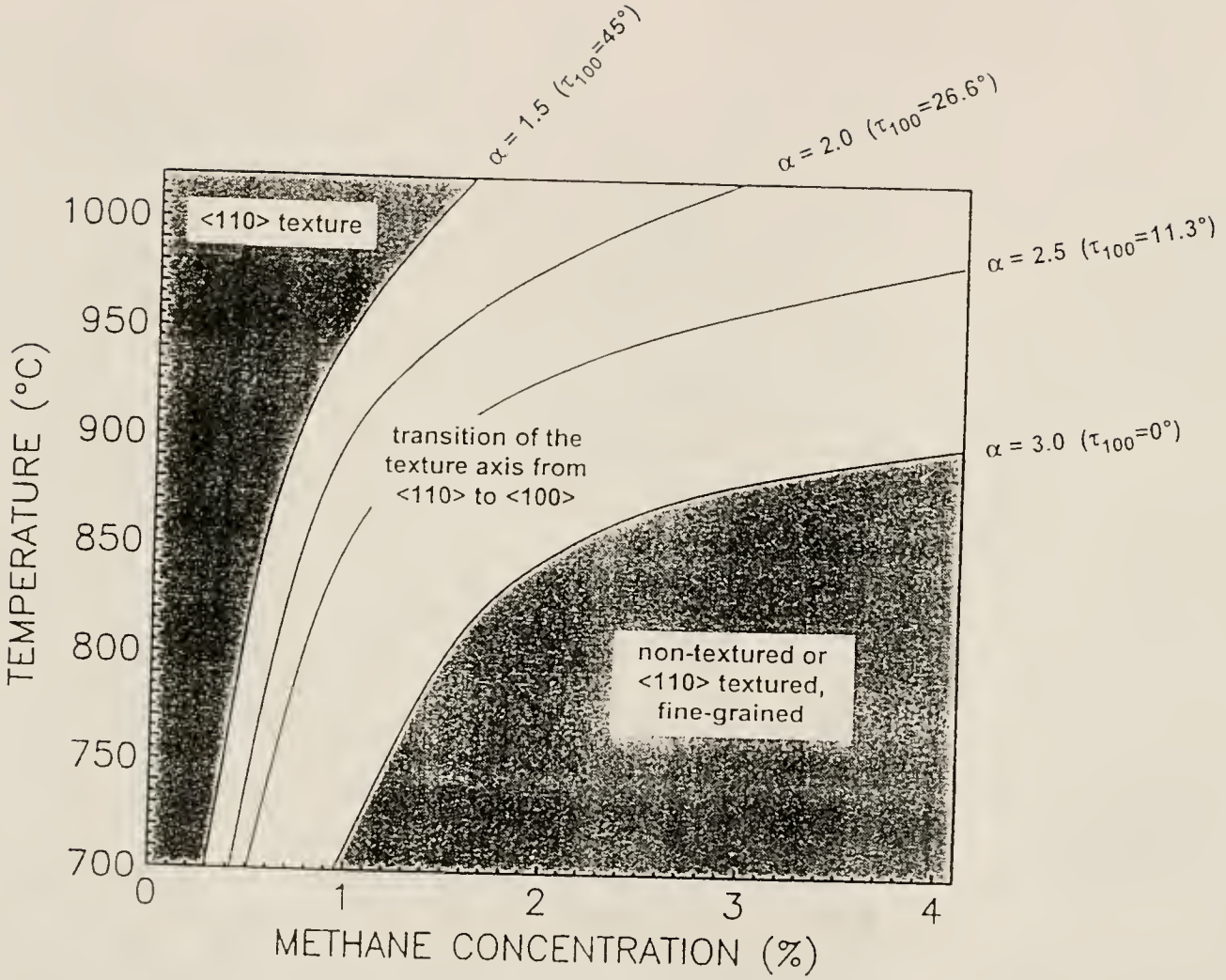

Figure 2.11 The dependence of film texture on methane concentrations from 0 to 4% and substrate temperatures from 700 to 1000°C [Wil94].

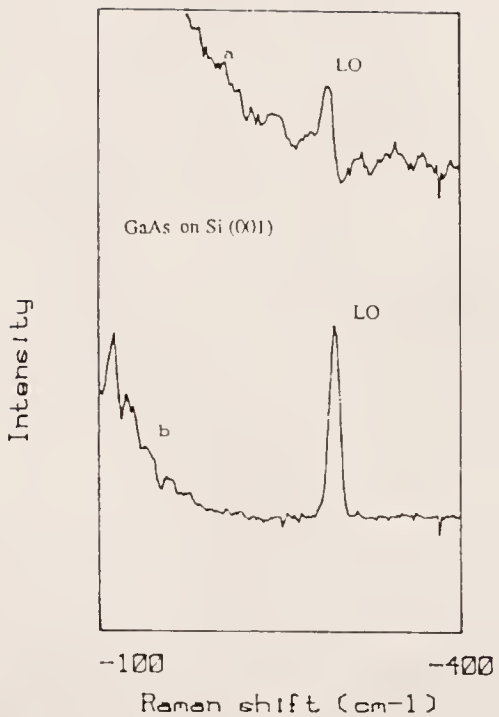

Figure 2.12 Raman spectrum showing the longitudinal optical (LO) phonon from: (a) 4.1μm GaAs film homoepitaxial to a (100) Si substrate (290cm^{-1}), (b) homoepitaxial GaAs on a (100) GaAs wafer (292cm^{-1}). The GaAs peak from (a) was shifted 2cm^{-1} from (b) and the tensile stress calculated from this shift was 3.5kbar [Qua93]. (The LO phonon oscillation is in the same direction as the propagation of the electric field versus a transverse optical (TO) phonon which oscillates perpendicular to the direction of propagation of the electric field).

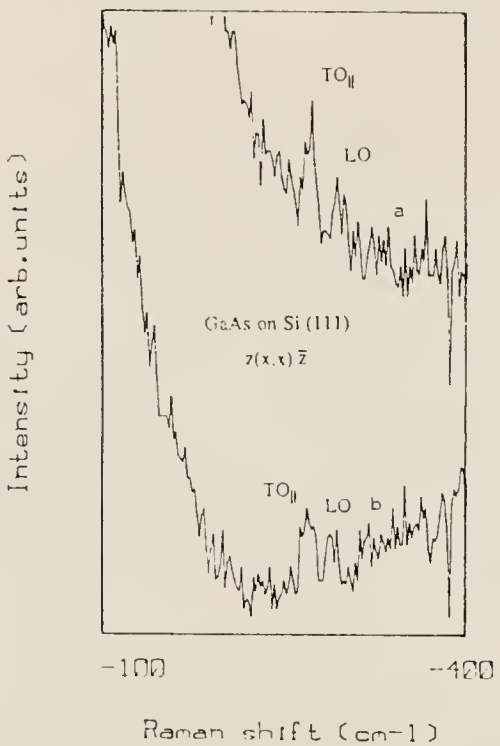

Figure 2.13 Raman spectrum showing both the TO and LO phonons from: (a) 4.1μm GaAs film homoepitaxial to a (111) Si substrate, (b) bulk (111) GaAs wafer [Qua93].

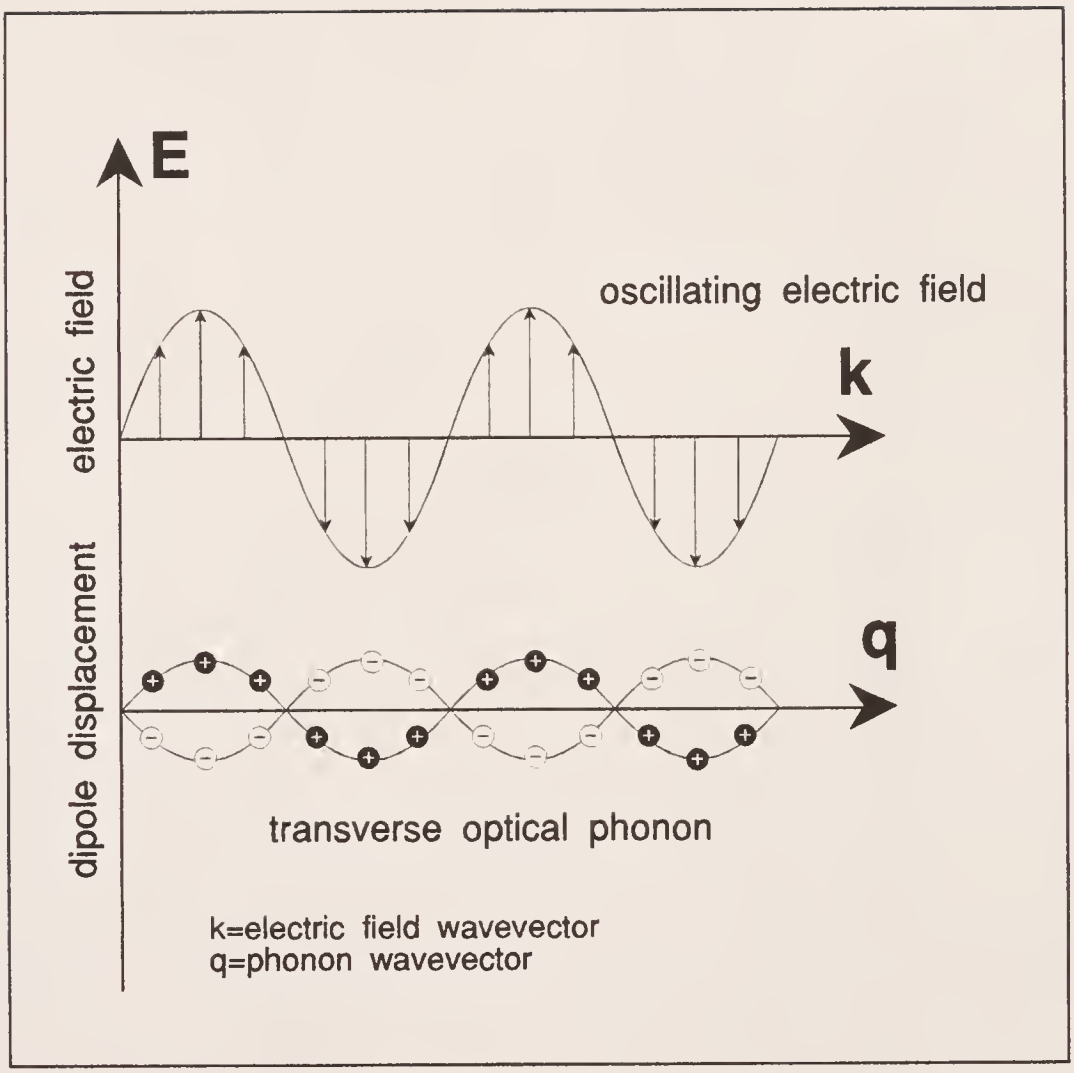

Figure 2.14 Illustration of the coupling of a transverse optical (TO) phonon to an electric field [Kit86]. The center of mass of the dipole is fixed and the opposite charges vibrate against each other.

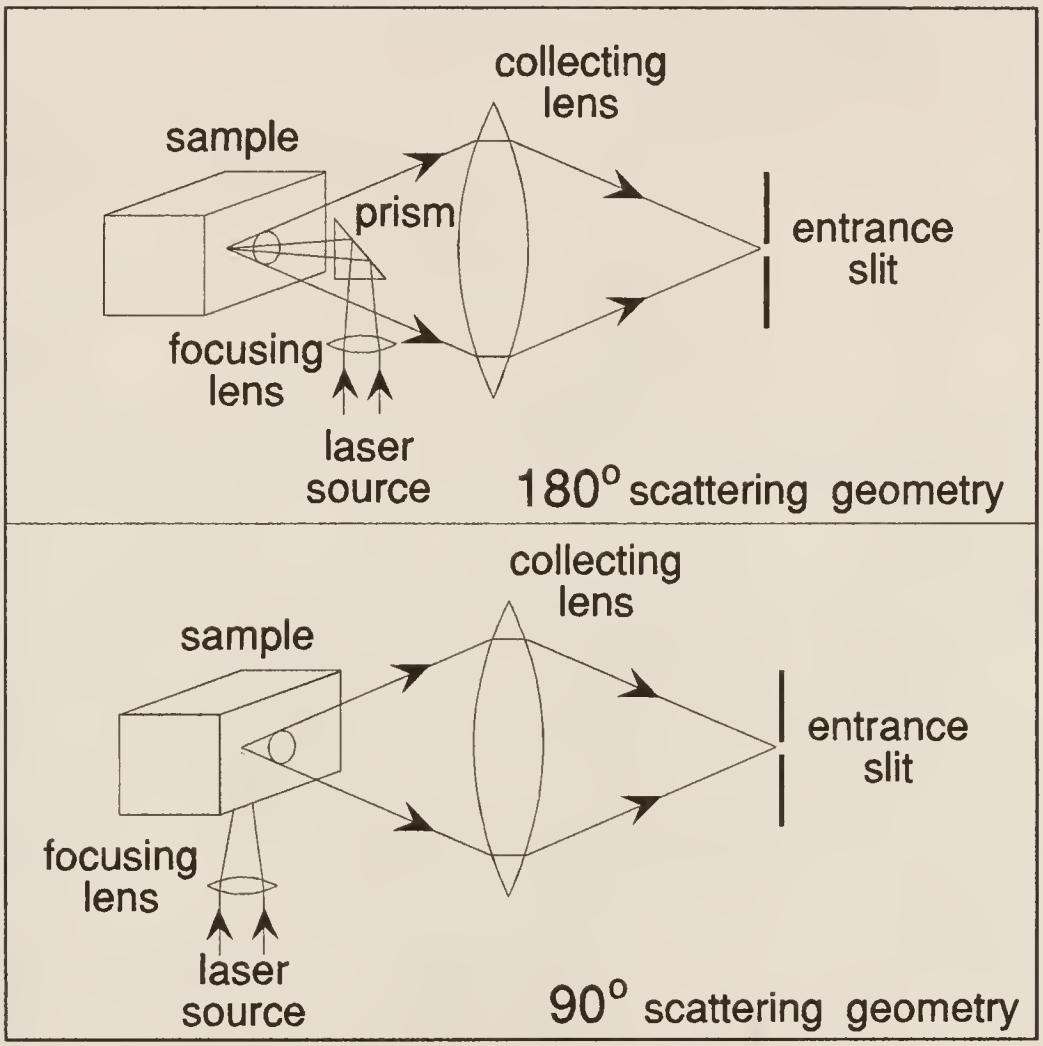

Figure 2.15 Schematic of the 180° (back scattering) and 90° scattering geometries used for Raman analysis [Bar87]. the sample in this figure is transparent to the laser, and the laser is focused below the surface of the sample, where the surface is represented by the circle in the outgoing trajectories.

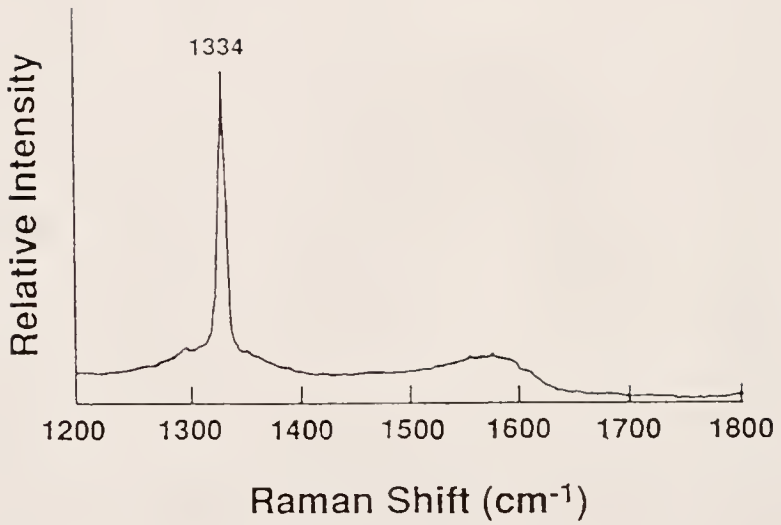

Figure 2.16 Raman spectrum from a polycrystalline diamond film exhibiting the sp^3 diamond peak ($1332cm^{-1}$) and the sp^2 graphite peak at $1585cm^{-1}$ [Yan93].

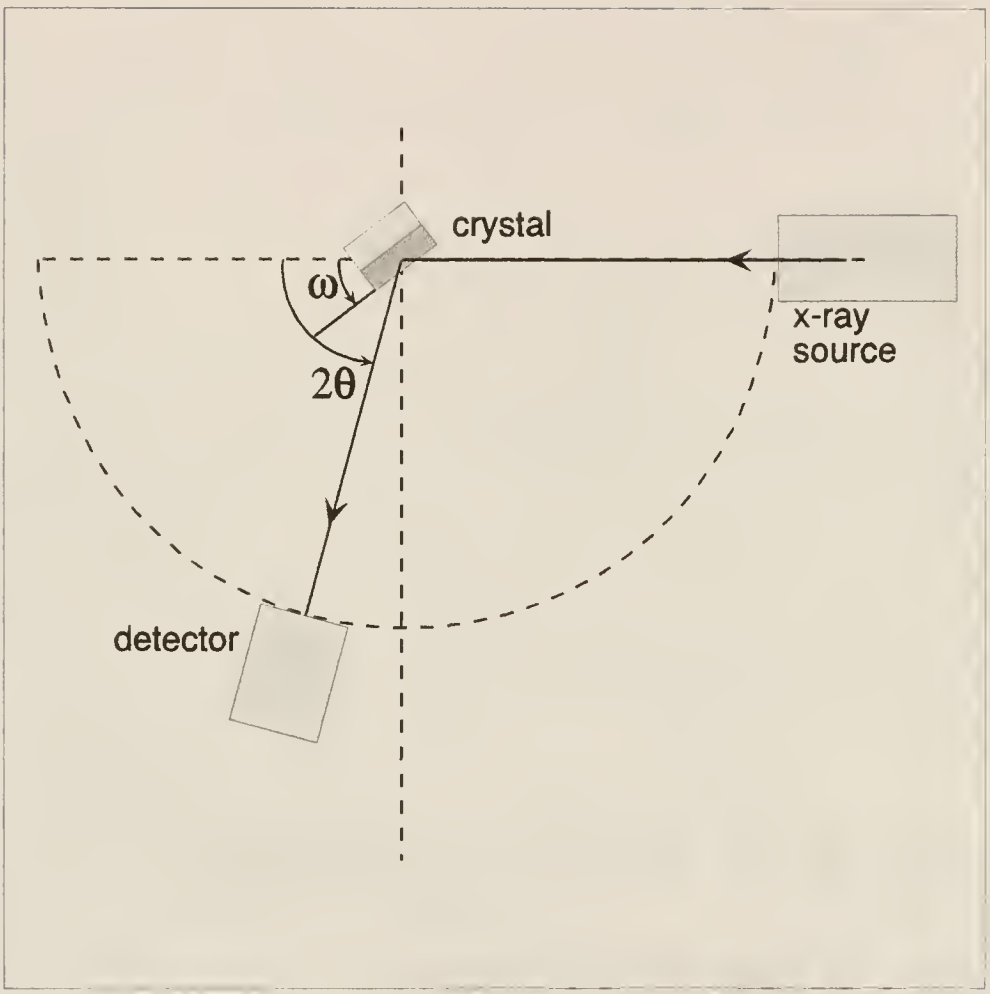

Figure 2.17 Schematic of the x-ray source, sample, and detector geometry for HRXRD. The angle 2θ is measured from the optical axis to the detector and the angle ω is measured from the optical axis to the sample surface.

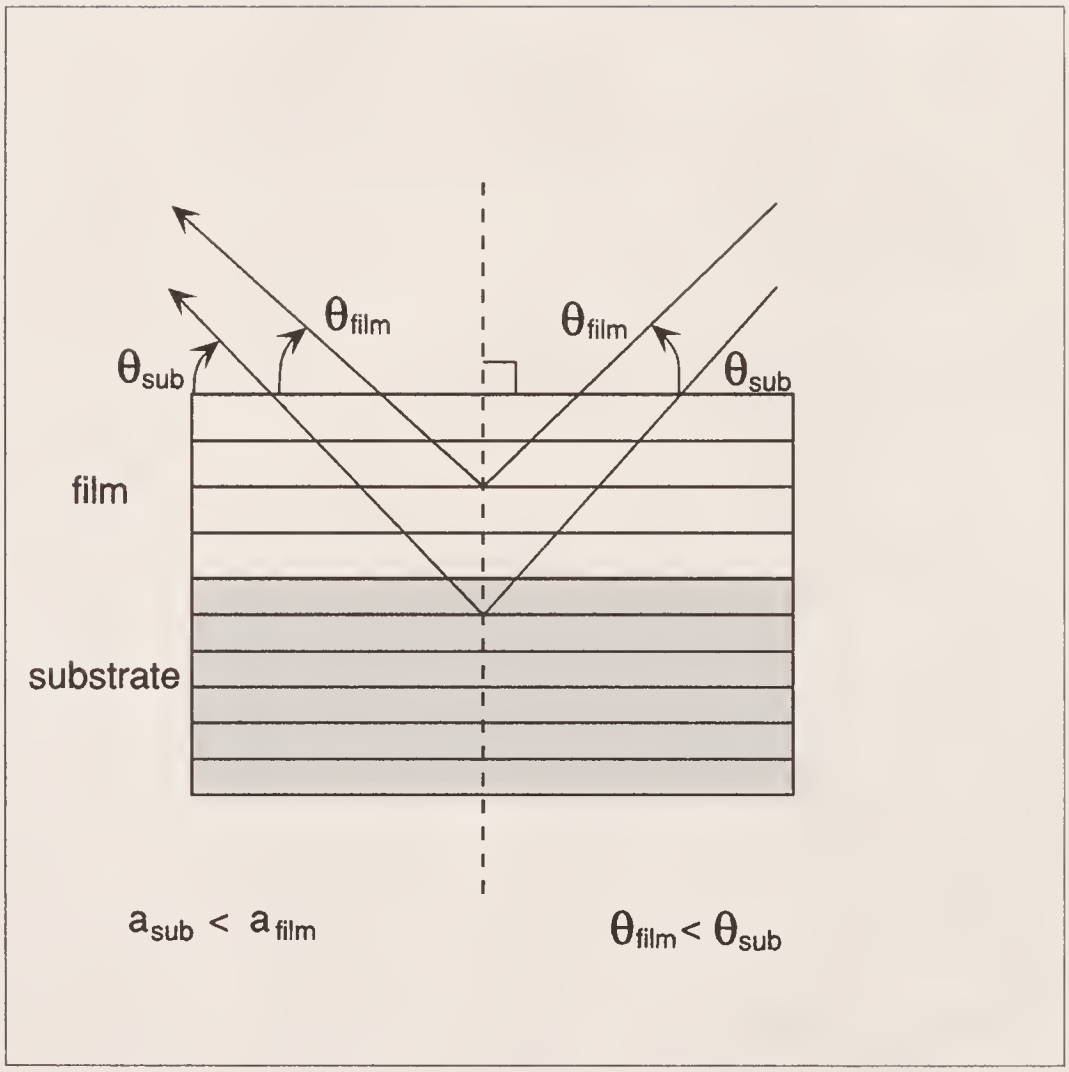

Figure 2.18 Illustration of the relationship between the lattice parameter and the Bragg angle for a film with a larger lattice parameter than a substrate. Both the sample and the detector must be moved to satisfy the Bragg condition for both the film and the substrate.

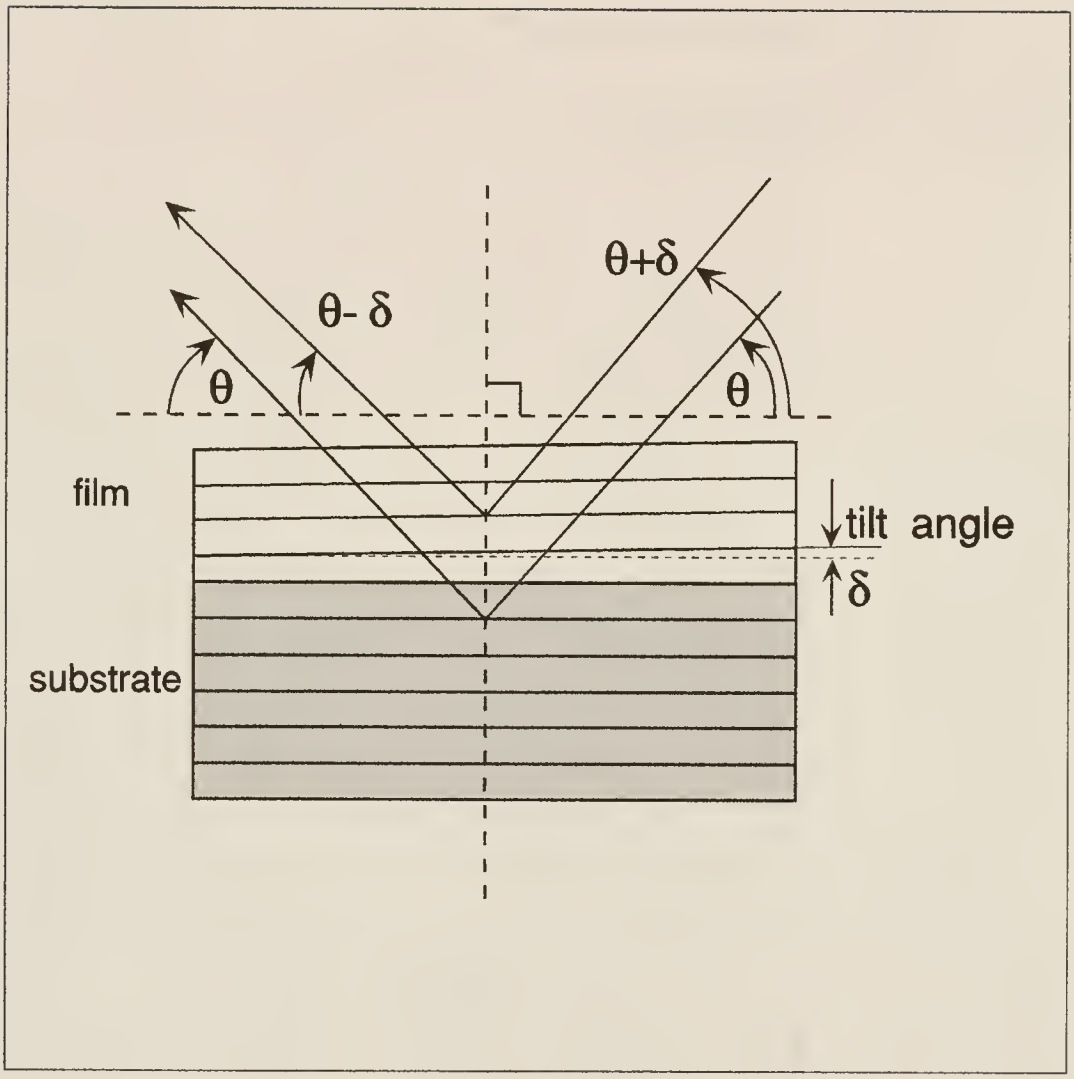

Figure 2.19 Illustration of the relationship between the orientation and the Bragg angle for a film which is tilted an angle δ with respect to the substrate. Only the sample must be moved to satisfy the Bragg condition for both the film and the substrate.

CHAPTER 3
EXPERIMENTAL APPROACH

Introduction

In this study, homoepitaxial diamond films were grown by hot-filament chemical vapor deposition (HFCVD). The films were characterized by various techniques including microRaman spectroscopy, high resolution X-ray diffraction (HRXRD), optical microscopy (OM), secondary electron microscopy (SEM), Fourier transform infrared spectroscopy (FTIR), and secondary ion mass spectrometry (SIMS). The HFCVD growth conditions and details of the characterization techniques are discussed in the following chapter.

Hot Filament Chemical Vapor Deposition

For hot filament chemical vapor deposition [Kaw87, Hir86, Mat82, Ang68], a wire filament (typically W, Ta, Mo, or Re) is heated to 1700-2500°C for the purpose of dissociating gas molecules to more reactive molecules or atoms. Typical diamond deposition parameters are shown in Table 3.1. The

precursor gas for diamond deposition is generally high in hydrogen (95-99%) and the hydrocarbon specie, typically methane or acetylene, is the balance. The dissociation

Table 3.1 Typical hot filament chemical vapor deposition parameters used to deposit diamond. (From Spear[Spe89])

Variable	Typical conditions	Best crystals
Substrate Temp. (°C)	700-1000	950-1050
Pressure (Torr)	10^{-4}-100	40-100
CH_4(in H_2) (mol%)	0.1-5.0	0.1-1.0
Flow Rate (cc/min)	20-200	50-100
Filament Temp. (°C)	1800-2500	2000-2500

products from methane or acetylene in hydrogen have been modeled [Cel90, Goo90] and measured [Har88] by several groups, and consists mainly of CH_4, CH_3, C_2H_2, C_2H_4, C_2H, and atomic hydrogen. Calculated concentrations of gas-phase products versus the dissociation temperature (i.e. filament temperature) for a 0.5%CH_4/H_2 mixture at thermal equilibrium were shown in Figure 2.3.

After dissociation, the gas species may impinge on the substrate which is heated to around 1000°C. Diamond is deposited through gas/solid reactions. Silicon substrates are most commonly used for diamond deposition, although others (W,

Mo, Ti, diamond, etc.) have been used [Lux91, Bad93]. Non-diamond substrates are generally pretreated with diamond seeds or scratched with diamond paste to facilitate the nucleation of diamond [Yar90].

Diamond Growth Chamber and Parameters

The HFCVD diamond growth system used in this study was custom built by LMA, Incorporated [Lin95]. The cylindrical chamber was made of quartz, with a diameter of 3 inches and a height of 12 inches [Fig. 3.1]. The substrate heater was a tungsten pancake heating coil encased in a molybdenum block. The temperature was monitored by a type S (Pt:Pt/10%Rh) thermocouple which was the input for an Omega CN2001 controller. The substrate thermocouple was calibrated by observing the melting point of silver (99.99%Ag), which is at 960°C. The calibration step was performed under run conditions with gas flowing in the chamber. The thermocouple was recalibrated if the filament position was changed or the substrate heater coil was replaced.

The substrates for homoepitaxial growth were type IIa [Fie92] (100), (111), and (110) diamond plates from Dubbeldee Harris. No polishing of the substrates was done, but they

were cleaned with acetone and methanol prior to growth. The cleaned diamond substrates were placed on the molybdenum block. The growth chamber was evacuated with a mechanical pump to a pressure of ~10^{-2}Torr. Hydrogen was introduced, raising the chamber pressure to 40Torr. The pressure was held constant using a capacitance manometer gauge (MKS baratron model 122A) to measure and provide a signal to an MKS type 250 pressure controller which automatically throttled the exhaust valve. After the chamber pressure was stabilized, the rhenium wire (dia.=0.02in, 99.99% Re) filament temperature was raised slowly to 2000°C; the filament temperature was monitored using an optical pyrometer with no correction for emissivity. The substrate temperature was also raised to 960°C as measured by the thermocouple. After the filament and substrate temperatures were stabilized, the precursor gas was introduced. Precursor gases were methanol or acetone (Aldrich, HPLC Grade) and hydrogen (Airco 99.999% H_2). In addition, a mixture of methane and oxygen with a balance of hydrogen was used for several growths. The precursor gas flow was controlled by an MKS type 1259 mass flow controller valve and 247 mass flow controller power supply. The total flow rate was 100 cc/min, and the flow rates of hydrogen

Table 3.2 Gas chemistry, substrate orientation, and growth times for diamond samples used in this study.

Gas chemistry	Substrate orientation	Growth time (hr)
3% methanol	(110) (111)	20,64 20,64
10% methanol	(100) (110) (111)	3.5,5,21,93 3.5,5,20,93 93
20% methanol	(100) (110)	3.5 3.5,20
30% methanol	(100) (110)	5 5
50% methanol	(100) (110) (111)	5,20 5,20 20
90% methanol	(100)	24
100% methanol	(110)	20
0.5% acetone	(100) (110)	19 19
1.0% acetone	(100) (110) (111)	16 16,20 16
3% acetone	(100 (110)	20 20

(0-99 cc/min) and acetone or methanol (1-100 cc/min) were varied to result in different precursor gas concentrations.

Films were grown for varying lengths of time, ranging from 2 to 100 hours. The growth run was terminated by first

shutting off the carbon precursor. After several minutes the filament temperature was reduced followed by the substrate temperature. Finally the hydrogen flow was shut off, the chamber evacuated (~10^{-2} Torr), and the chamber opened to air.

Characterization Techniques

A variety of techniques were used to characterize the diamond films. A description of the tool and important attributes of the technique are discussed below.

Raman Spectroscopy Experimental Procedure

In microRaman spectroscopy, a microscope is used to focus the laser to a small spot (1~100μm depending on the lens and excitation wavelength). The scattered light is collected by the microscope as shown in Figure 3.2. The small probe size allows data to be acquired from different regions of a sample. A schematic of the Raman spectrometer used in this study is shown in Figure 3.2. Raman data were collected using the 180° geometry and excitation by 514.5nm radiation from a Coherent Innova 90 5-watt Ar-ion laser. The laser was operated at a power of 100mW (at 514.5nm), which resulted in approximately

10mW at the sample. An Olympus BH2 microscope was used to focus the laser on the sample and the spot size was ~5μm, which resulted in a power density of ~510W/mm^2. The magnification of the objective lens was 100X, the numerical aperture was 0.95, and the depth of focus (DOF$\approx\lambda/4\cdot NA^2$) [Mel90] was calculated to be ~143nm. The four independent slits of the Ramanor U-1000 double monochromator were all either 100μm for the 1200-1700cm^{-1} scans, or 40μm for the 1320-1340cm^{-1} scans.

The procedure used for acquiring Raman data were as follows. Water flow to the laser power supply was turned on. A fault switch prevented the laser from operating when the water was not flowing. The power switch to the laser was turned on and the power to the laser was increased slowly until the meter on the laser control panel read 100mW. The laser power was unstable for approximately 10 minutes and the power was periodically adjusted. A SPEX 1450 Tunable Excitation Filter consisting of a compact grating monochromator, was adjusted with a micrometer for the selected wavelength, was used to filter plasma emissions. The band pass of the filter was 5Å and the power loss was 75%. Several

aluminized mirrors, with reflectivities of 92%, were used to guide the laser into the microscope and align the excitation beam perpendicular to the sample surface. A Type IIa, (110) oriented, natural diamond substrate was used to align the beam and to calibrate the monochromator. A video camera mounted on the microscope and connected to a monitor was used to image the laser spot on the sample surface. The laser beam was aligned perpendicular (±5°) to the sample surface by changing the alignment mirrors until the laser spot defocused symmetrically (versus asymmetrically for the under-focus and over-focus condition of the microscope). There was one mirror between the microscope and the monochromator which was used to visually align the laser beam on the center of the entrance slit. The spectrometer was interfaced with a computer through a SpectraLink IEEE interface. A Prism software package was used to control the spectrometer and collect the data. The step sizes between data points was varied from $0.02cm^{-1}$ to $1cm^{-1}$. The time per step was typically 3 seconds, although counting times of 10 seconds were used occasionally for better signal to noise ratios. The typical scan range was $1200cm^{-1}$ to $1700cm^{-1}$ when measuring both graphite and diamond signals, which resulted in a data accumulation time of 25 minutes. A

scan range of 1315cm^{-1} to 1345cm^{-1} was generally used when measuring the diamond signal only and the data acquisition times were 25 to 85 minutes, depending on the step size and dwell time.

Stress Measurement Precision and Method

For greater precision and accuracy in measuring the diamond Raman peaks, their position was generally referenced to the position of a 5520Å krypton line (1322cm^{-1}) [Ale94]. This refinement was required due to a mechanical lag of the stepping motor in the monochromator which caused small shifts in the peak position from run to run, making it difficult to measure small stresses. Shown in Figure 3.3 are the diamond peak positions recorded from a natural diamond substrate for ten consecutive runs, with no changes in instrumental parameters or sample position. Shifts to lower wavenumbers of 0.0 to 0.10cm^{-1}/scan with an average shift of 0.053cm^{-1}/scan was typical. While most shifts were to lower wavenumbers, sometimes the peak would be shifted to higher wavenumbers. Attempts to control these effects by unidirectional scanning were unsuccessful.

By using a krypton line as an internal reference, it was possible to dramatically improve the precision of the measured peak position to $\pm 0.03 cm^{-1}$. Figure 3.4 shows the peak position measured in 10 sequential runs on the same sample as Figure 3.3 while using the same spectrometer parameters and the krypton reference line. This precision was achieved in part because the krypton calibration line is only 11 cm^{-1} from the diamond Raman line, as shown in Figure 3.5. Both the Raman spectrum from a natural diamond and the krypton line which was used as the reference are shown in Figure 3.5. The krypton line was detected by placing a krypton lamp near the optical axis in front of the monochromator entrance slit [Figure 3.6]. One of the problems with using the krypton internal standard was that light (from the Kr lamp) entering the monochromator increased the background or dark counts. This decreased our ability to observe weak Raman signals. To reduce background, the krypton lamp position could be varied with respect to the optical axis to control the measured krypton intensity. However, movement of the lamp during the course of recording data was avoided since such movement relative to the optical axis affected the peak position of the krypton line. This effect results from the different incidence angles of the

light on the diffraction grating. A second method used to control the dark counts was to turn off the lamp after the monochromator had scanned through the krypton peak (1319 to1324cm-1), so the dark counts were minimized under the diamond peak (1325 to 1340cm^{-1}).

The procedure used to determine average shifts (due to stress) of the diamond Raman peak from a homoepitaxial film was as follows. The peak position (ν_p) from an unstressed, single crystal, diamond substrate without a film was measured along with the peak position of the krypton line. The difference in the peak positions of the diamond and the krypton resulted in:

$$\Delta\nu_{sk}=\nu_{sub.}-\nu_{krypton} \qquad (3\text{-}1)$$

where $\Delta\nu_{sk}$ was the wavenumber difference between the diamond Raman peak and the krypton line in cm^{-1}. Similarly, a homoepitaxial diamond film on a substrate was measured:

$$\Delta\nu_{fk}=\nu_{film}-\nu_{krypton} \qquad (3\text{-}2)$$

where $\Delta\nu_{fk}$ was the wavenumber difference between the diamond film signal and the krypton line. Finally,

$$\Delta\nu_{sf}=\Delta\nu_{sk}-\Delta\nu_{fk} \qquad (3\text{-}3)$$

where $\Delta\nu_{sf}$ was the difference between the measured diamond substrate position and the film position. The film stress was calculated by:

$$\sigma=\Delta\nu_{sf}/\kappa \qquad (3\text{-}4)$$

where κ = 2.94cm^{-1}/GPa, as reported above.

Controlling Raman Probing Depth

The Raman spectrum (solid line) from a 25μm thick diamond film on a 200μm thick diamond substrate is shown in Figure 3.7. Two Voight curves (shown as dashed lines), representing Raman scattering from the film and substrate, can be summed to generate the total Raman peak. Curve fitting of the Raman data is discussed below. The total diamond peak in Figure 3.7 (solid line) exhibited asymmetric broadening to lower wavenumbers. The peak doublet results from independent contributions from the homoepitaxial film and the diamond substrate. The homoepitaxial film versus substrate peaks could be better resolved using a pinhole aperture after the

microscope. A Raman spectrum from the same sample as in Figure 3.7 was recorded with a pinhole (~400μm) aperture and is shown in Figure 3.8. The lower wavenumber peak has increased in intensity relative to the peak at higher wavenumbers. If the asymmetric broadening of the Raman peak in Figure 3.7 was caused by microcrystalline structures [Pol91], using the pinhole aperture would not have changed the relative intensities of the peaks.

Diamond is transparent at 514.5nm, the wavelength used to excite Raman scattering, therefore the Raman signal is generated in the bulk of the transparent media. The depth of focus of our microscope objective was calculated to be ~143nm (see above), so Raman scattering from deep within the sample was being recorded. It was possible to limit the signal from the substrate with the pinhole, however the substrate signal was detected through the homoepitaxial films which were less than ~70μm thick.

Although natural diamond is typically colorless [Fie92] as were our substrates, the homoepitaxial films ranged from black to nearly colorless. The color of the homoepitaxial film was related to the carbon concentration in the precursor gas as shown below. Films were relatively colorless when

grown with <10%CH_3OH and black when grown with >90%CH_3OH. The color of the films affected the transparency to the probing laser and therefore the probed depth for the Raman peak. This fact, in addition to surface scattering, makes the comparison of Raman scattered intensities from various samples very difficult. Therefore Raman spectral intensities are reported below only in arbitrary units.

Curve Fitting

Peak positions and linewidths of the diamond Raman mode peaks were obtained by non-linear least squares curve fitting. Lorentzian, Gaussian, and Voight functions [Arm67] were used to curve fit the spectral lines obtained with Raman. The Lorentzian line shape has been reported to best represent the spectral line shape produced by a radiating oscillator [Arm67]. Gaussian (or Doppler) line broadening has been reported to result from a statistical distribution of radiation frequency [Kle86]. If the spectral line shape were influenced by both Lorentz and Doppler broadening, the profile is represented by a Voight function [Arm67], which is a convolution of a Lorentzian with a Gaussian.

The Lorentzian function used to test curve fitting in this study was:

$$I = \frac{A}{1+[(\nu-a)/b]^2} \qquad (3\text{-}5)$$

where I is the intensity, ν is the frequency, A is the amplitude, a is the peak center, and b is the linewidth. The Lorentzian function can be evaluated analytically. A Raman spectrum from a (110) diamond substrate, the Lorentzian fit using PeakFit software [Pea92], and the residuals from the curve fit are shown in Figure 3.9. The Lorentzian fit resulted in a peak position of 1332.55cm^{-1}, a linewidth of 2.13cm^{-1}, and a standard deviation of 19.1 cts/sec. The residuals plotted in Figure 3.9 demonstrate systematic effects, i.e., regions of mostly positive or mostly negative residuals over a range of wavenumbers. Systematic effects indicate that a Lorentzian peak was not the most appropriate function to model the Raman peak.

The Gaussian function used for curve fitting was:

$$I=A\exp(-.5[(\nu-a)/b]^2) \qquad (3\text{-}6)$$

where the variables are the same as for the Lorentzian. Fitting the same Raman spectra with a Gaussian function [Figure 3.13] using PeakFit resulted in a peak position of 1332.55cm^{-1}, a linewidth of 2.43cm^{-1} and a standard deviation of 43.2 cts/sec. The residuals plotted in Figure 3.10 demonstrate increased systematic variations when compared to the Lorentzian [Figure 3.9]. The Gaussian is therefore even a worse function to model the Raman peak.

The Voight function, cannot be evaluated analytically [Pea92]. However it can be approximated using an approach developed by Puerta and Martin [Pue81] which consists of four generalized Lorentzians. The Voight function used for curve fitting was:

$$I=\frac{\int\{A\exp(\zeta^2)/\{\{z^2+\{[(\nu-a)/b1-\zeta\}^2\}d\zeta}{\int\{\exp(-\zeta^2)/(z2+\zeta^2)\}d\zeta} \qquad (3\text{-}7)$$

where b is proportional to the Doppler width and z is the ratio of the collision width to the Doppler width.

The same Raman spectrum which was fit with a Lorentzian [Figure 3.9] and Gaussian [Figure 3.10] was also fitted with a Voight function and is shown in Figure 3.11 along with the residuals from the fit. The resulting peak position from the

Voight fit was equal to the value (1332.55cm^{-1}) obtained by the Lorentzian and Gaussian fit. The linewidth achieved from a Voight function fit (2.21cm^{-1}) was slightly higher (+0.06cm^{-1}) then the Lorentzian fit and -0.22cm^{-1} narrower then the Guassian fit. Fitting with a Voight function resulted in a standard deviation of 15.6 cts/sec which was an improvement over both the Lorentzian and Gaussian fits. The residuals from the Voight fit do not show the systematic effects versus wavenumbers which were observed from the Lorentzian and more noticeably from the Gaussian fit residuals. Although the peak positions were the same and the linewidths were similar for both Voight and Lorentzian fits, curve fitting with a Voight function was chosen due to the better standard deviation and lack of systematic patterns in the residuals.

X-Ray Experimental Procedures

A Philips HR1 x-ray diffractometer was used to perform x-ray analysis on the homoepitaxial diamond films. The x-ray tube generator was operated at 40kV and 40 mA and produced Cukα radiation at a wavelength (λ) of 1.54056Å. The radiation was conditioned by a Bartels [Bar83] 4-crystal monochromator [Fig. 3.12] to produce radiation with $\Delta\theta$=12arcsec divergence

and a $\Delta\lambda/\lambda=2.3x10^{-5}$ wavelength spread. X-ray analysis preformed with the 4-crystal monochromator is generally referred to as high-resolution x-ray diffraction (HRXRD) [Bar83, He93, Hei94, Seg89, Pet94].

To record rocking curve peaks which were representative of the film quality, optimization procedures were followed. This procedure was more difficult for the present study of diamond because of the small sizes (≈1mm x 2mm x 0.2mm) and irregular shapes of the diamond samples. The x-ray beam diameter in the HRXRD is approximately 5mm, i.e. larger than some of the samples. In addition, the crystallographic directions of the sample were completely unknown.

The goniometer and diffractometer arrangement are shown in Figure 3.13. The samples were mounted on glass slides with double sided tape. Care was taken to minimize any stresses on the sample. The glass slide and sample were mounted on the goniometer with tape holding the glass slide on the mounting plate. The sample surface was aligned to the center of the optical axis by using a dial gauge which was inserted at the base of the goniometer. The sample was moved along the z-axis with a micrometer until the sample came in contact with the dial gauge stylus, and the gauge read zero. To optimize the

rotation (R) and the tilt (Φ) angles, a series of ω rocking curves were recorded and R and Φ were adjusted until the maximum diffracted intensity and smallest linewidth was achieved. The sample was re-aligned in the x and y directions by maximizing the diffracted x-ray intensity while changing x and y slightly (≈0.2mm) via the computer.

Analyzer Crystal

Towards the end of this study, an analyzer crystal was added to the HRXRD system. The geometry of the crystal with respect to the monochomator, sample, and detector is shown in Figure 3.14. The analyzer crystal is a U-shaped (Bonse-Hart) [Bon65] crystal which was mounted directly in front of the detector to increase the resolution. The improved resolution is a direct result of limiting the acceptance angle to ~14arcsec, which allows the separation of lattice parameter and misorientation contributions to diffraction peak broadening.

To record the rocking curves using the analyzer crystal, an important first step was performed prior to the above optimization procedures. The alignment of the analyzer

crystal with respect to the beam optics was extremely critical. The crystal may have become misaligned from equipment operators touching the detector arm while exchanging receiving slits. The detector was rocked (2θ-scan) through the incident beam (without diffraction from a sample) to ensure that the FWHM of the intensity profile was ≤0.0040°. (If the FWHM was >0.0040°, the analyzer crystal required re-alignment).

To illustrate the effect of limiting the acceptance angle, the detector was rocked through the x-ray beam under three conditions: open-ended, receiving slit (slit width = 0.5mm), and analyzer crystal [Figure 3.15]. The term "open-ended" refers to the diffracted x-ray beam entering the detector without conditioning (no slits in front of the detector). The acceptance angle of the open-ended detector was ~7500arcsec. In the receiving slit mode, a slit was placed in front of the detector which limited the acceptance angle to ~920arcsec with a 0.5mm slit. When the analyzer crystal was used, the two Bragg reflections from the analyzer crystal limited the acceptance angle to ~14arcsec.

Scanning Electron Microscopy

Scanning Electron Microscopy (SEM) [Bru92] was used to characterize the surface morphology of the diamond films. A JEOL JSM 35C operating at 10-15kV and a working distance of 15-20mm was used to record SEM micrographs. Occasionally, the sample was tilted 30° to accentuate imaging of surface defects. The surface morphology of the diamond films were strongly dependent on substrate orientation and gas chemistry.

Fourier Transform Infrared Spectroscopy

Fourier Transform Infrared Spectroscopy (FTIR) [Bru92] was used to characterize hydrogen and oxygen impurities in the diamond films. The Nicolet Magna-IR system used for FTIR analysis of the homoepitaxial diamond films includes an FT-IR 750 spectrometer, Nic-Plan IR Microscope, and a Spectra-Tech Motorized Micropositioning Stage. The Nicolet system was operated via a 486/66 computer using OMNIC software. The microscope was used to focus the IR beam to ~250μm and collect the light. More precisely, the Nicolet system was equipped with an He-Ne laser which was aligned with the IR optics, and the He-Ne laser was focused with the microscope. (The He-Ne

laser was required for focusing because IR light can not be seen with the naked eye.) The scan range was from 600 to 4000 cm^{-1} with a resolution of $8cm^{-1}$ and a total data acquisition time of approximately 15 minutes. Spectra were recorded measuring the percent reflectance. The surface roughness and absorbance varied from one film to the next, therefore the spectra were normalized for intercomparison between different samples.

Secondary Ion Mass Spectrometry

Secondary Ion Mass Spectrometry (SIMS) [Bru92] was performed with a Perkin-Elmer 6600 system. The Cs^+ and O_2^+ primary ion beams operated at a voltage of 7keV and a beam current of 1.09 to 1.12μA. The rastered area was 150μm x 150μm and the analyzed area was 37.5μm x 37.5μm.

Impurity analysis was performed using both the mass scan and depth profiling modes. In the mass scan mode all impurities (hydrogen to uranium) in the film are surveyed. The depth profile mode was used to scan for preselected impurities as a function of time.

Quantitative Analysis with SIMS

Standards for quantifying SIMS data were not available for this study. The concentration of impurities in the diamond films were obtained by the procedure outlined by Wilson et al. [Wil89]. The Relative Sensitivity Factor (RSF) is defined as:

$$\rho_i = RSF(I_i/I_m) \qquad (3\text{-}8)$$

where ρ_i is the impurity atom density, I_i (cts/sec) is the impurity isotope secondary ion intensity, I_m (cts/sec) is the matrix isotope secondary ion intensity, and RSF has units of atoms/cm^3.

The RSF values for impurities in a diamond matrix are given in Table 3.3. These values are used to quantify an impurity element in diamond with results accurate to within a factor of 3 to 5. Figures 3.16 and 3.17 shows the RSF values from Table 3.3 plotted versus the ionization potential for an O_2^+ primary beam, and electron affinity for a Cs^+ primary beam, respectively. The RSF values for elements not listed in Table 3.3 were obtained through the ionization potential (O_2^+) or electron affinity (Cs^+) of the element of interest. A line

was drawn perpendicular to the x-axis in Figure 3.16 at the ionization potential value or at the electron affinity value in Figure 3.17 till it intersects the best-fit line. The RSF value for the element was then calculated.

Table 3.3 SIMS Relative Sensitivity Factors (RSF) for impurity atoms in a diamond matrix (from[Wil89]).

Element	RSF (atoms/cm^3) 8 keV O^{2+} primary beam	RSF (atoms/cm^3) 14.5 keV Cs^+ primary beam
H	6e23	4e23
Li	1.4e19	
Be	4e20	
B	3e21	2e24
C (matrix atom density)	1.8e23	1.8e23
O		2.3e23
F	3.4e22	4.8e22
Na	7e18	
Al	3.6e19	
Si	2e21	
P	3.6e22	2.2e23
Ca	2.2e19	
Ti	6e19	9e25
As	5e22	3e23

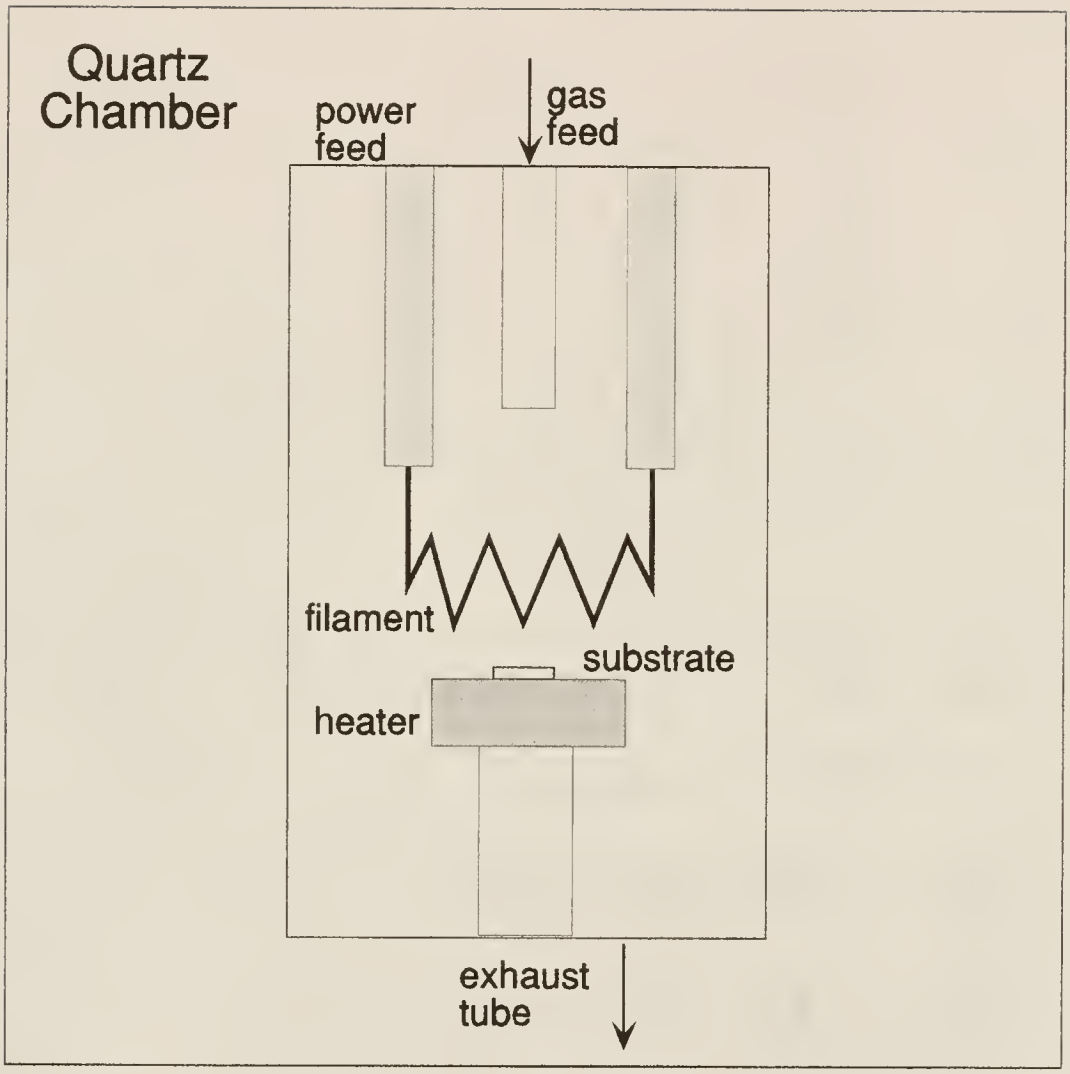

Figure 3.1 Schematic of the hot filament chemical vapor deposition (HFCVD) chamber used to deposit diamond films at LMA, Inc.

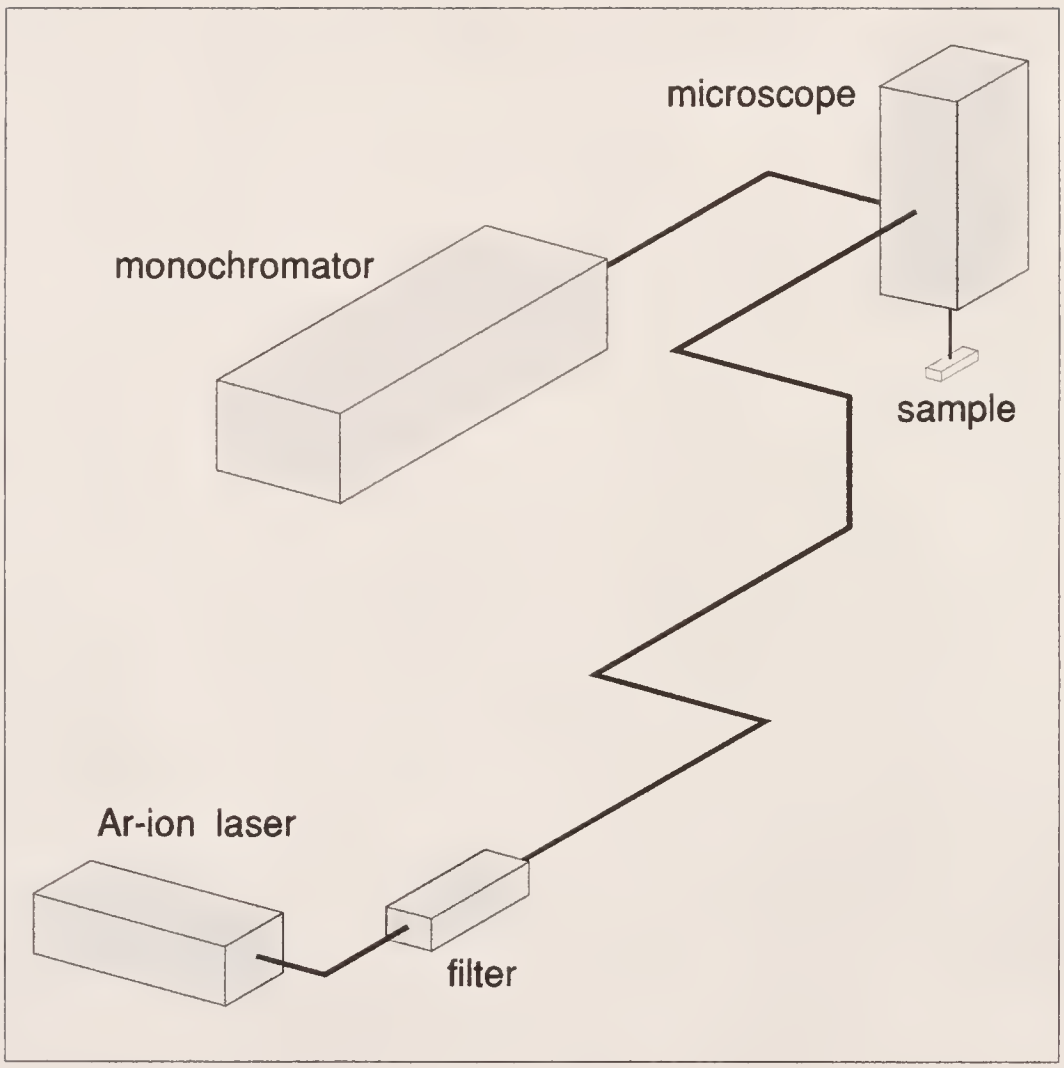

Figure 3.2 Schematic of the microRaman spectrometer used in this study.

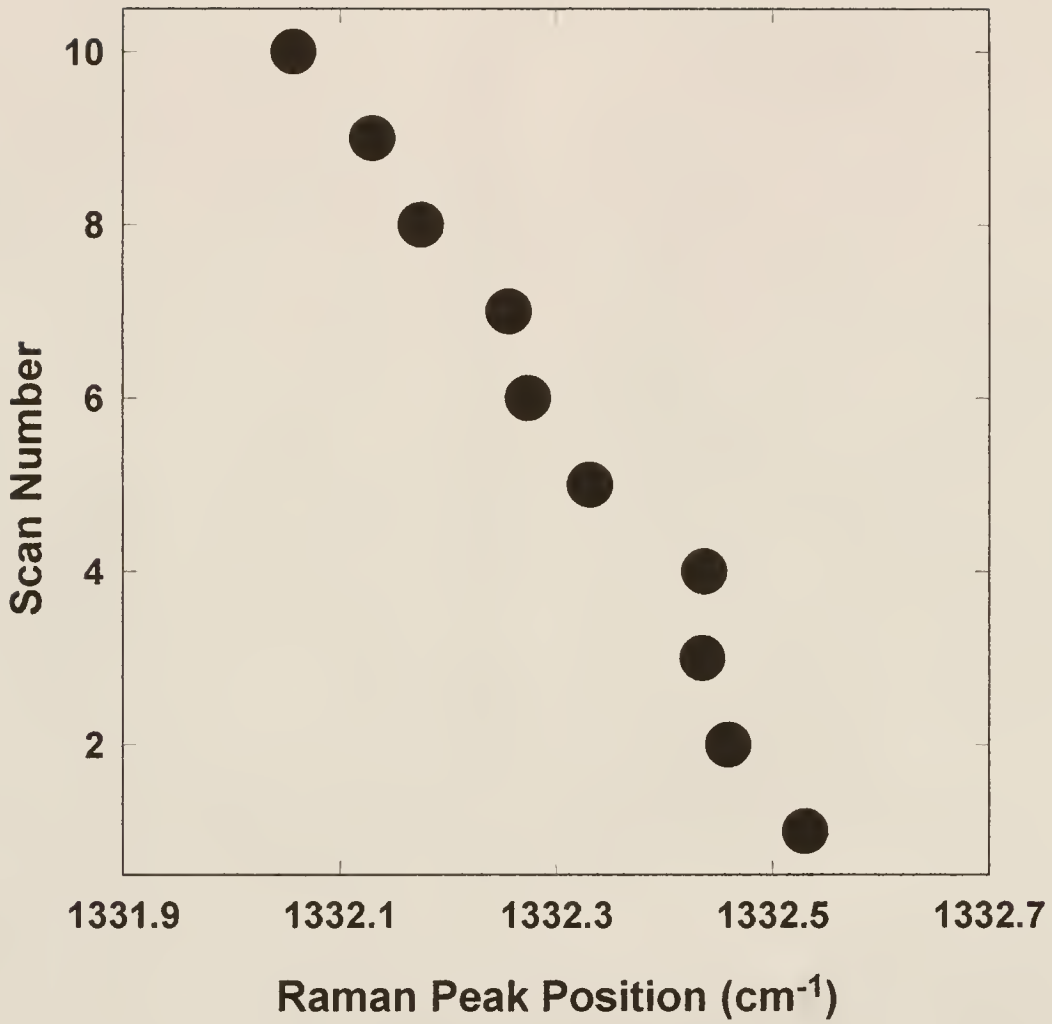

Figure 3.3 Raman peak position recorded from a diamond standard for ten sequential runs with no changes in sample position or spectrometer.

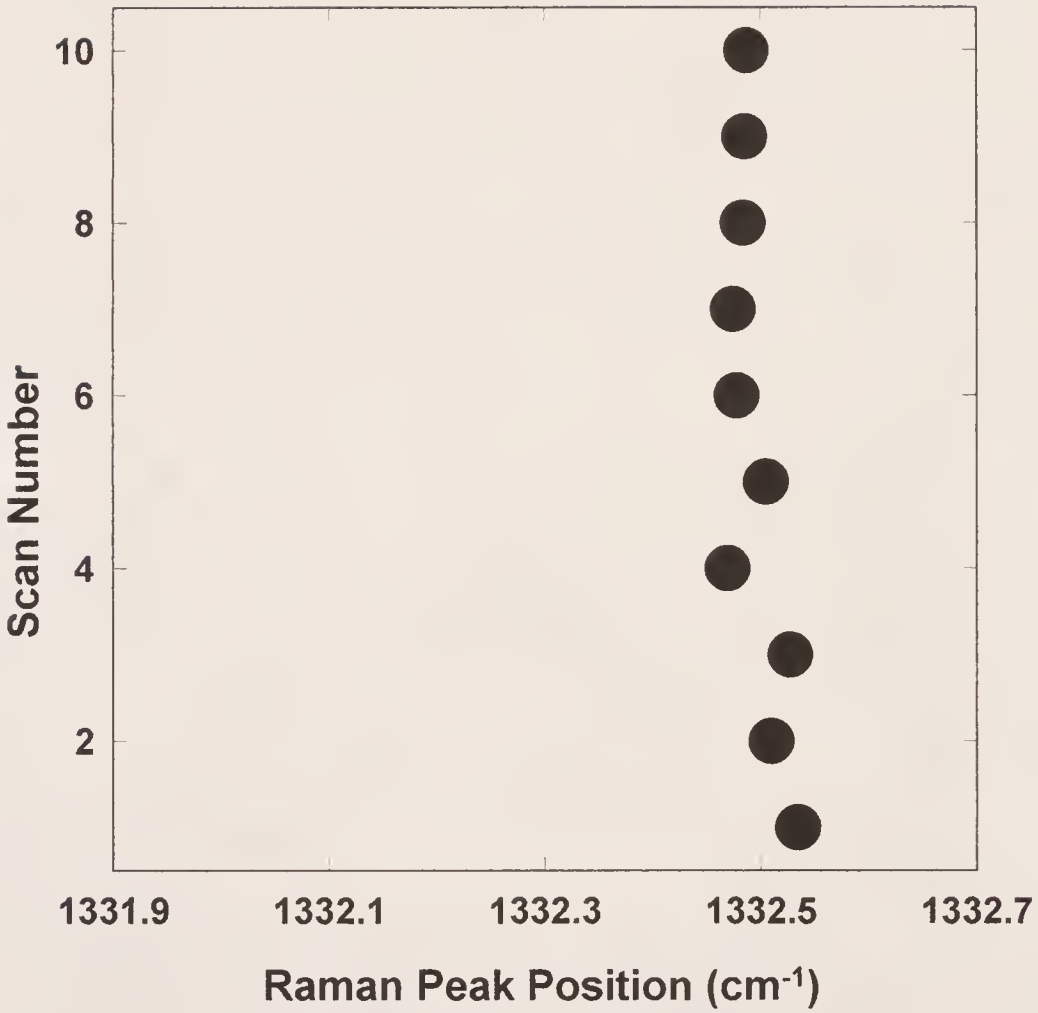

Figure 3.4 Raman peak position recorded from a diamond standard for ten sequential runs using the krypton lamp as a reference (see text).

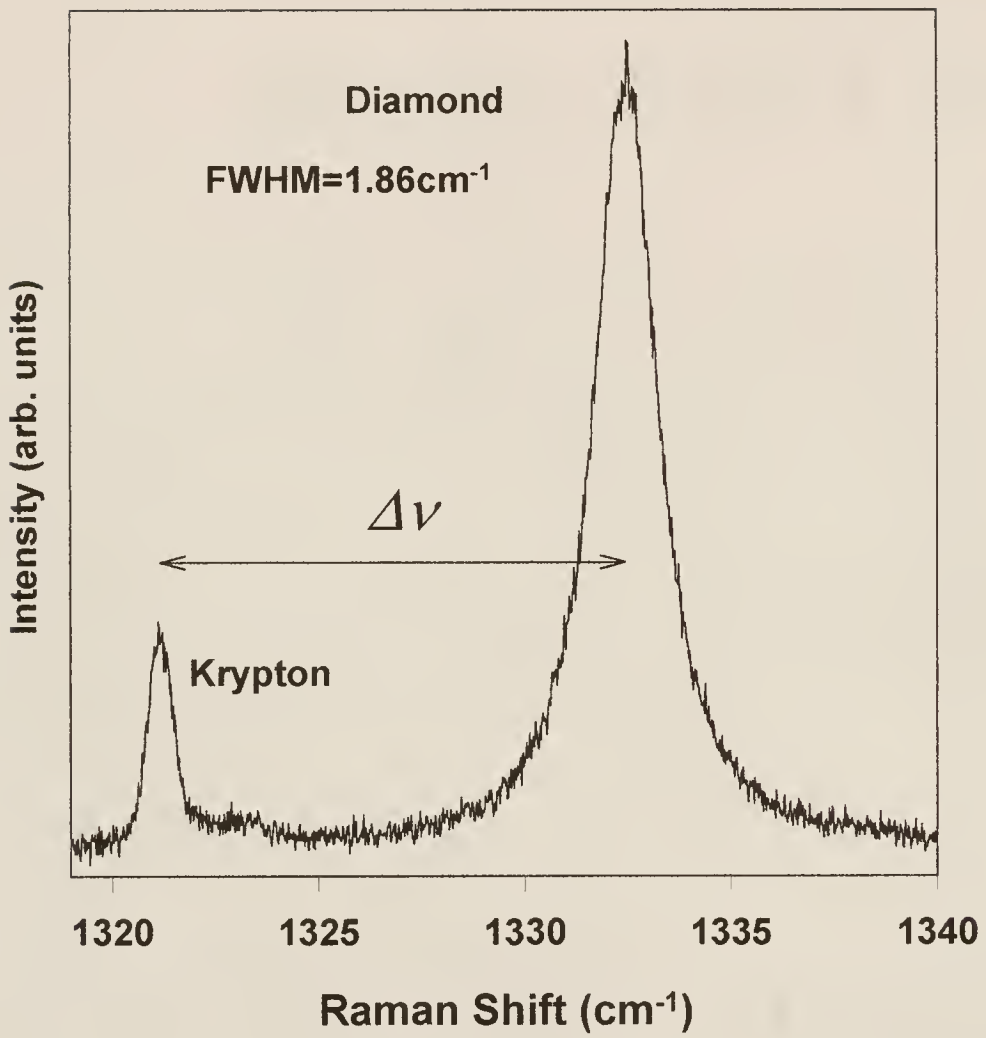

Figure 3.5 Raman spectrum showing the 1322cm^{-1} krypton peak and the 1332.5cm^{-1} diamond peak from a (110) bulk standard.

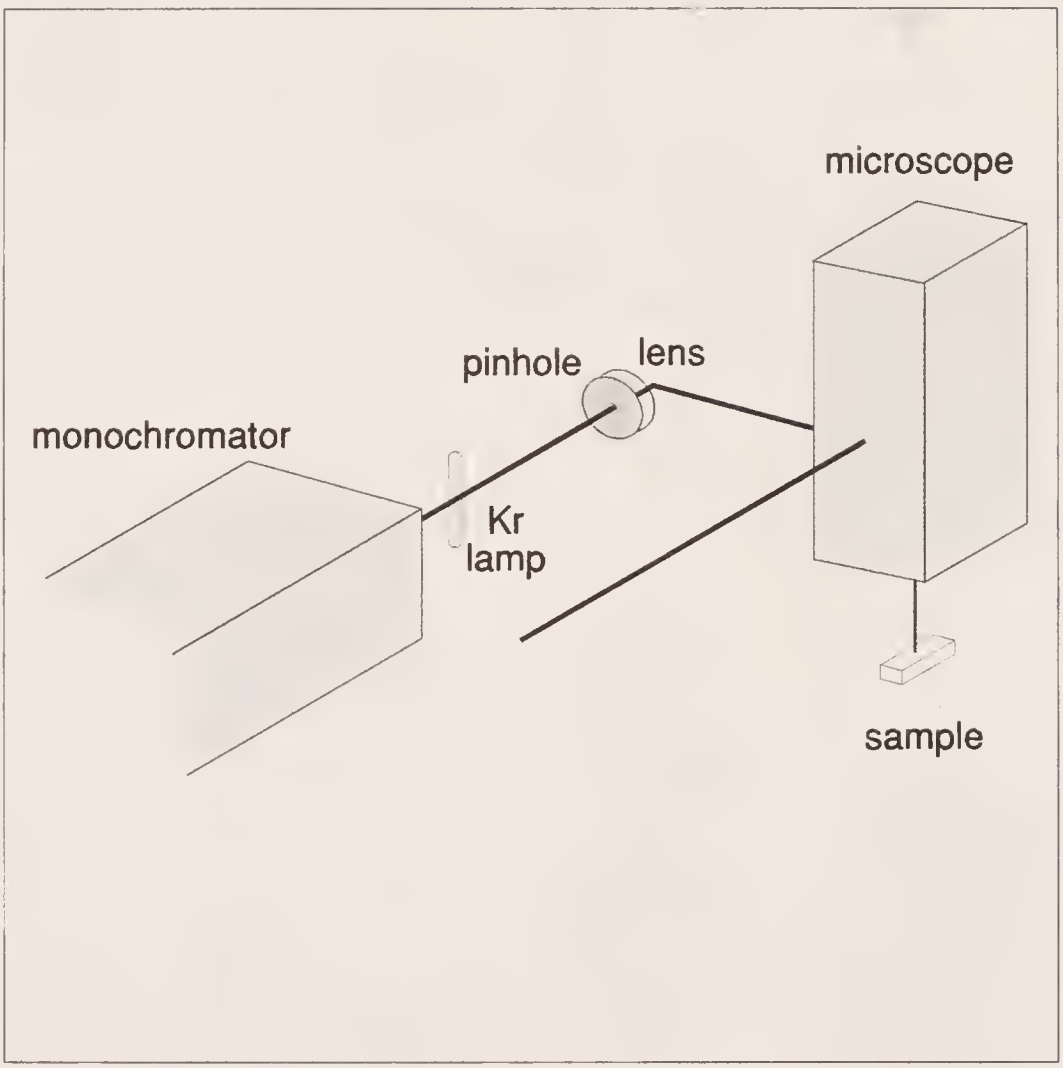

Figure 3.6 Schematic of the Raman spectrometer showing the position of the krypton lamp relative to the monochromator, pinhole, and microscope.

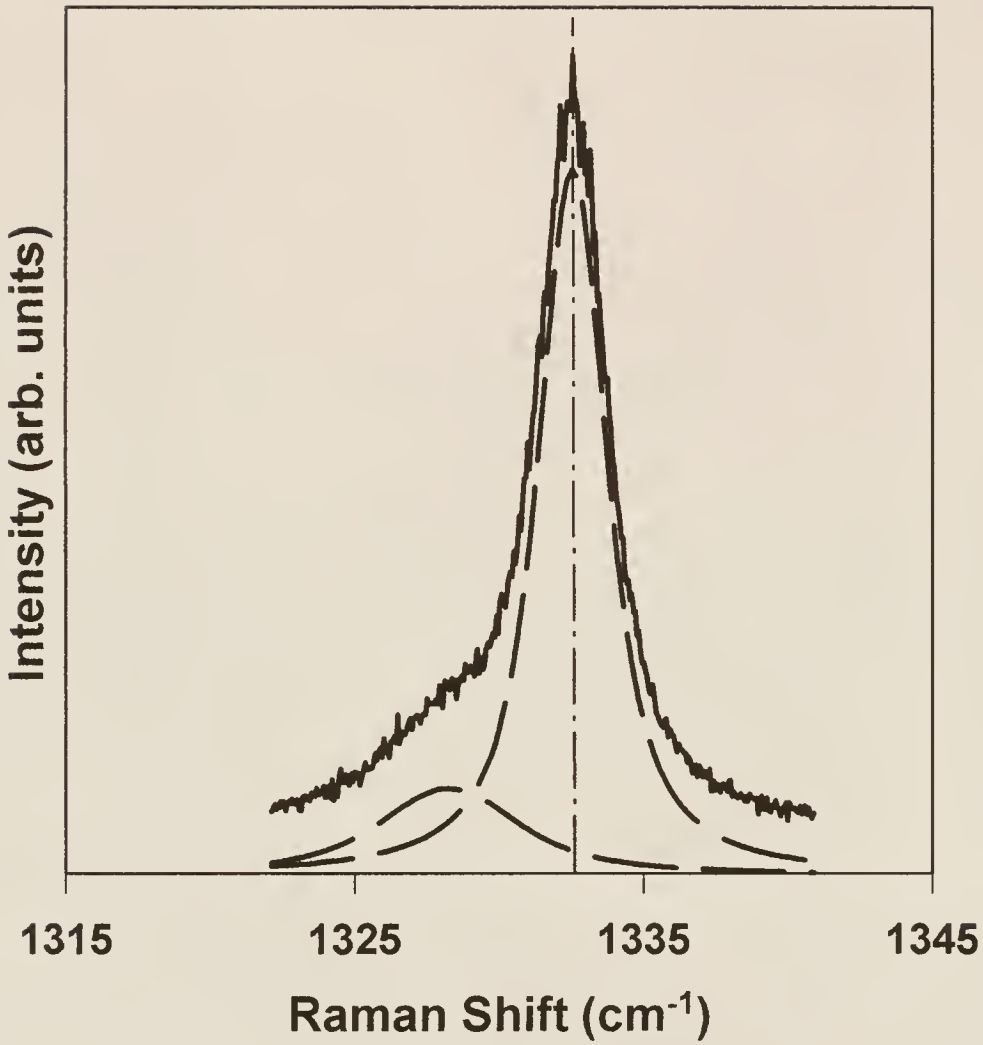

Figure 3.7 Raman spectrum from a 25μm thick, (110) homoepitaxial diamond film grown with 10% methanol. The solid line is the actual data and the dashed lines are the two Voight fits at 1328.4cm^{-1} and 1332.7cm^{-1}, representing the film and substrate, respectively.

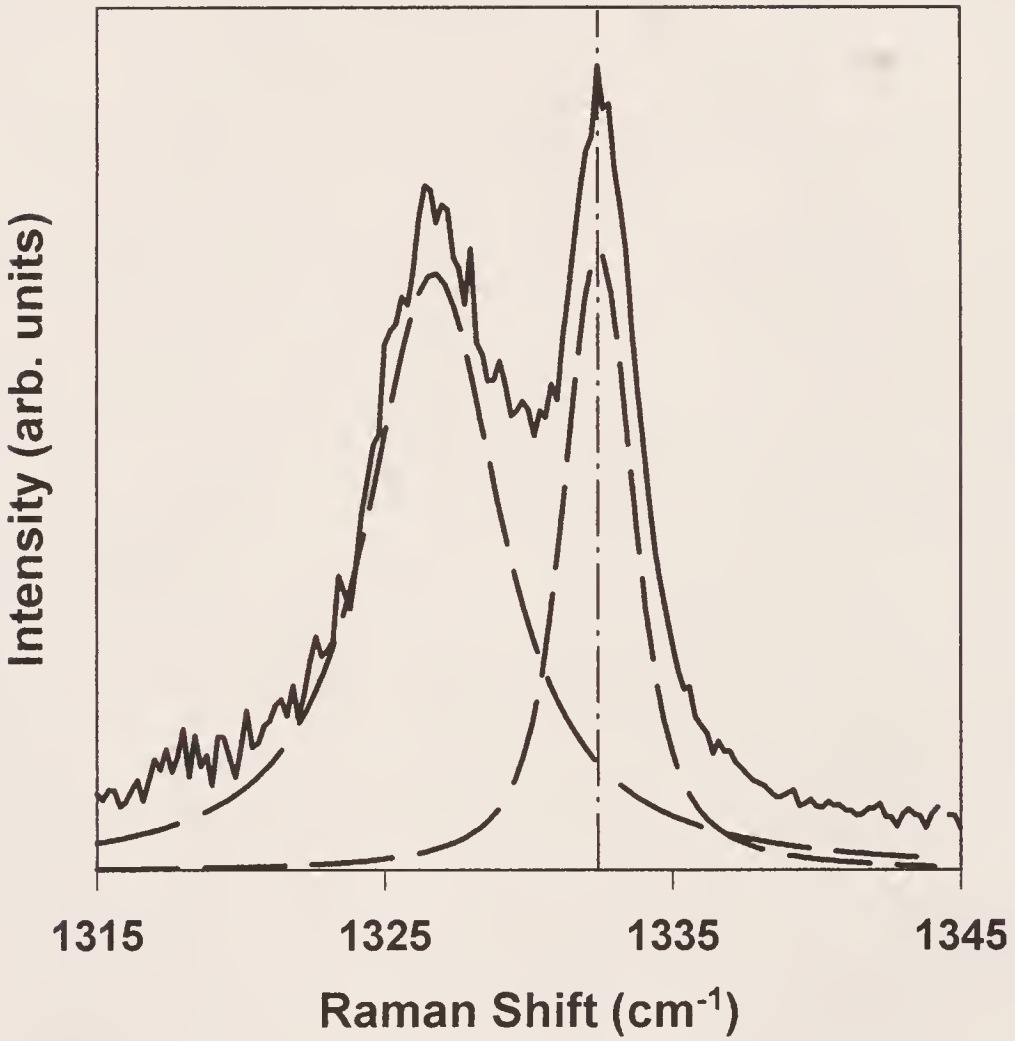

Figure 3.8 Raman spectrum from the same sample as shown in Figure 3.7, using a 400μm pinhole aperture.

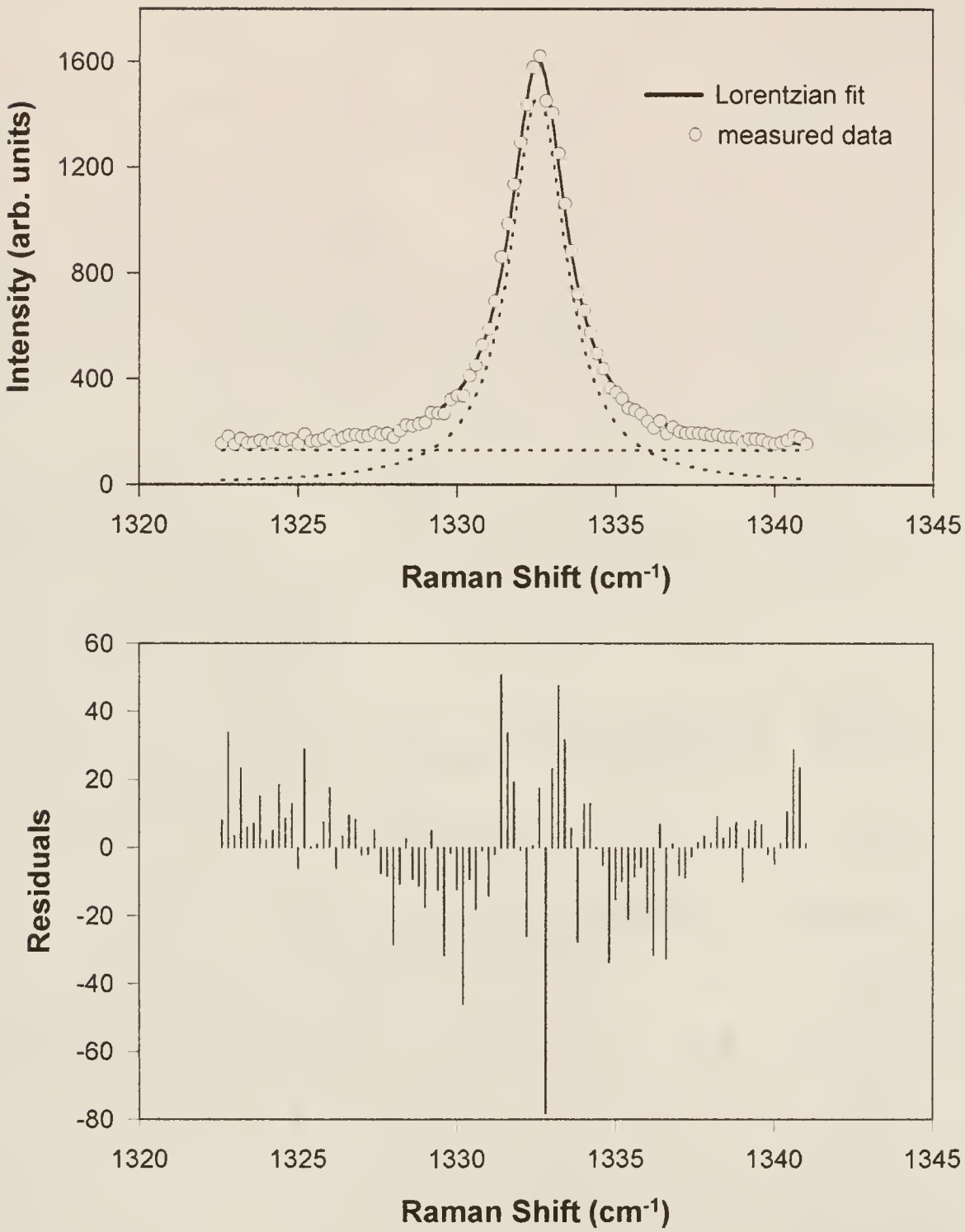

Figure 3.9 Lorentzian curve fit and residuals of a Raman peak from a (110) diamond standard. Note the systematic variations in the residuals with wavenumber indicating that a more appropriate function should be used for curve fitting.

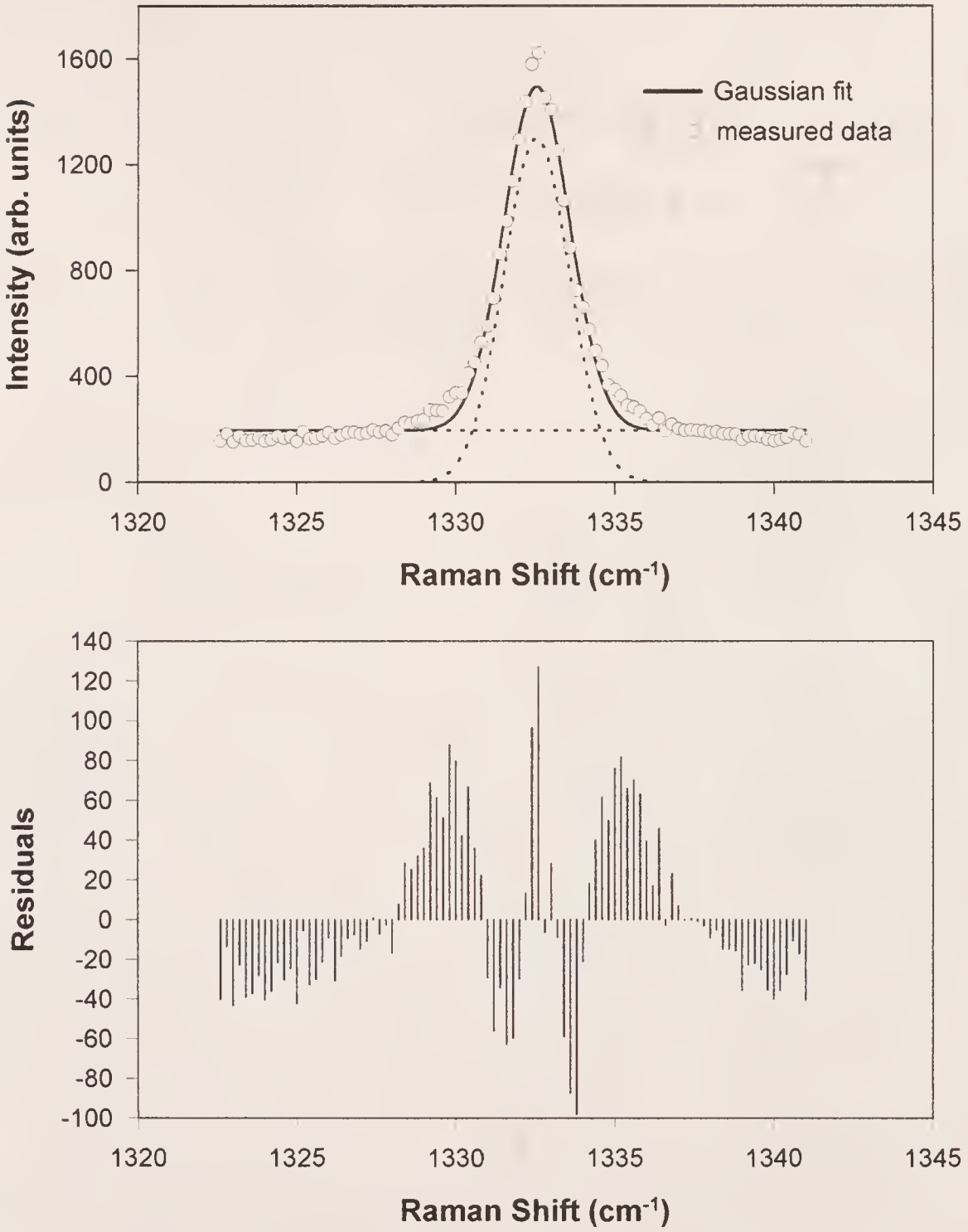

Figure 3.10 Gaussian curve fit and residuals of the Raman peak curve fit with a Lorentzian in Figure 3.9. The variations with wavenumber are more significant here than in Figure 3.9, indicating a poor fit.

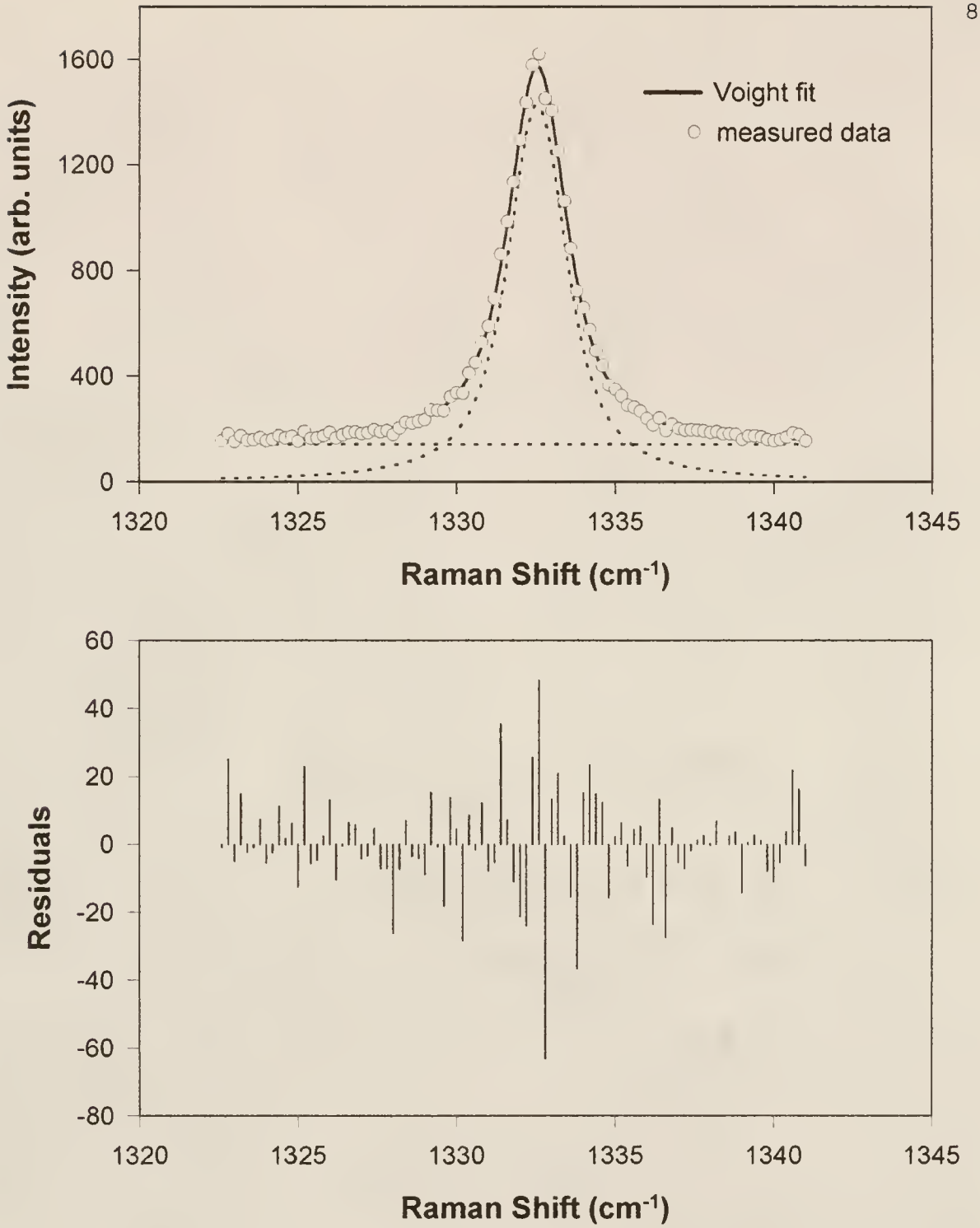

Figure 3.11 Voight curve fit and residuals of the Raman peak fit in Figures 3.9 and 3.10. Note that the systematic variations with wavenumber are not exhibited by the residuals. This was an appropriate function to fit the curve.

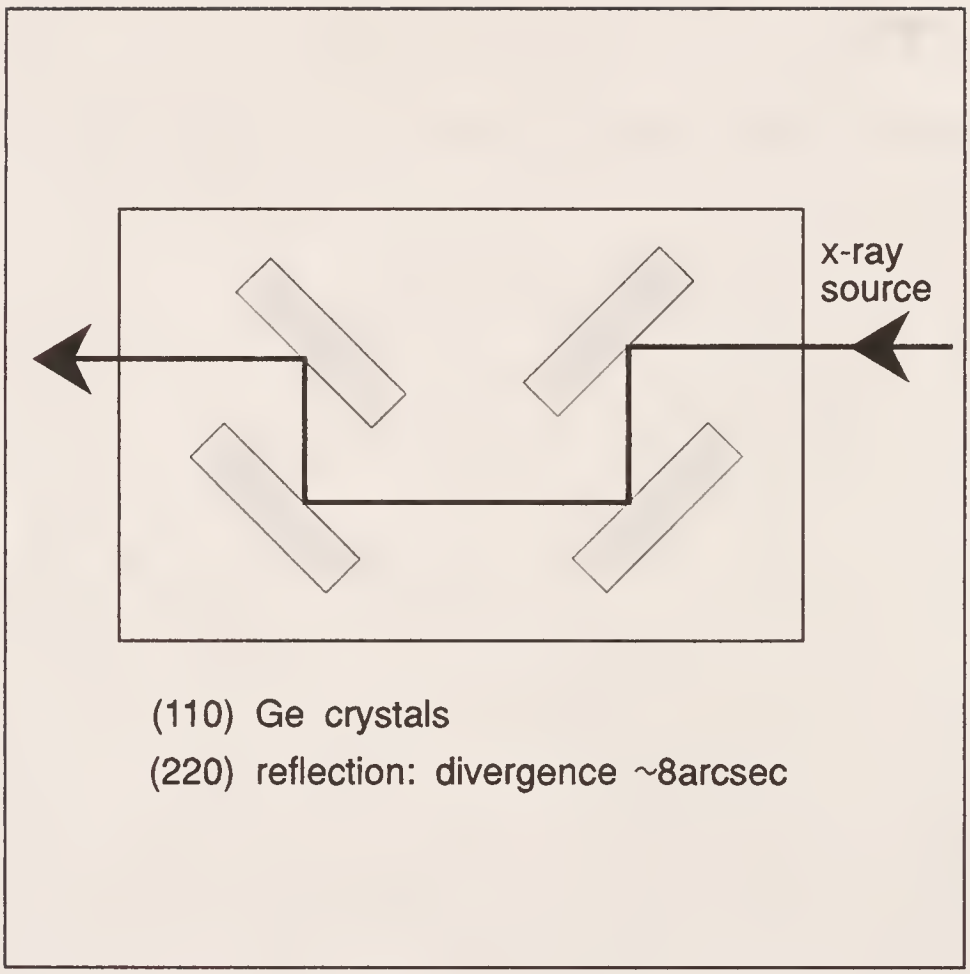

Figure 3.12 Schematic of the Bartels four-crystal monochromator used for high resolution x-ray diffraction [Bar83].

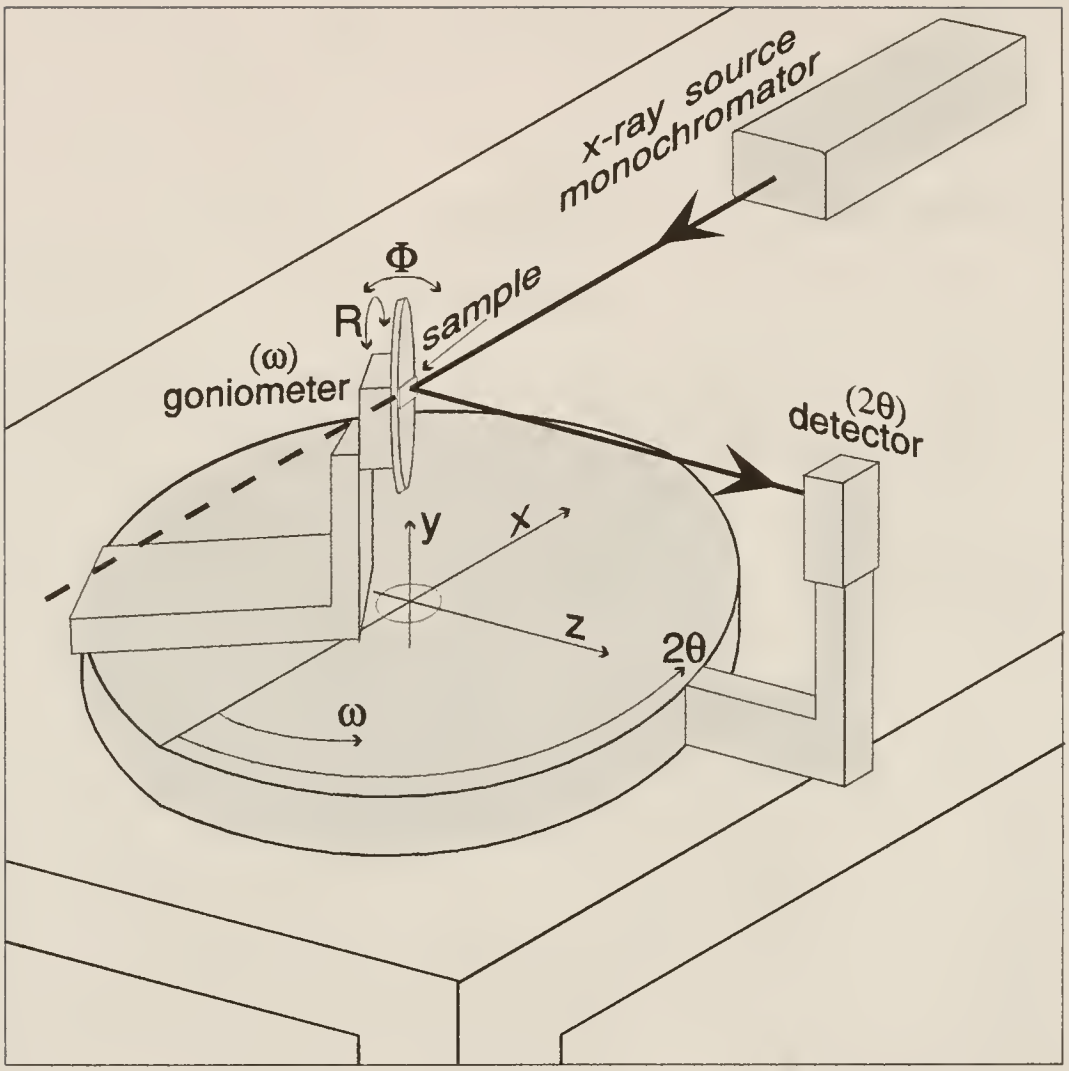

Figure 3.13 Schematic of the high resolution x-ray diffractometer used in this study.

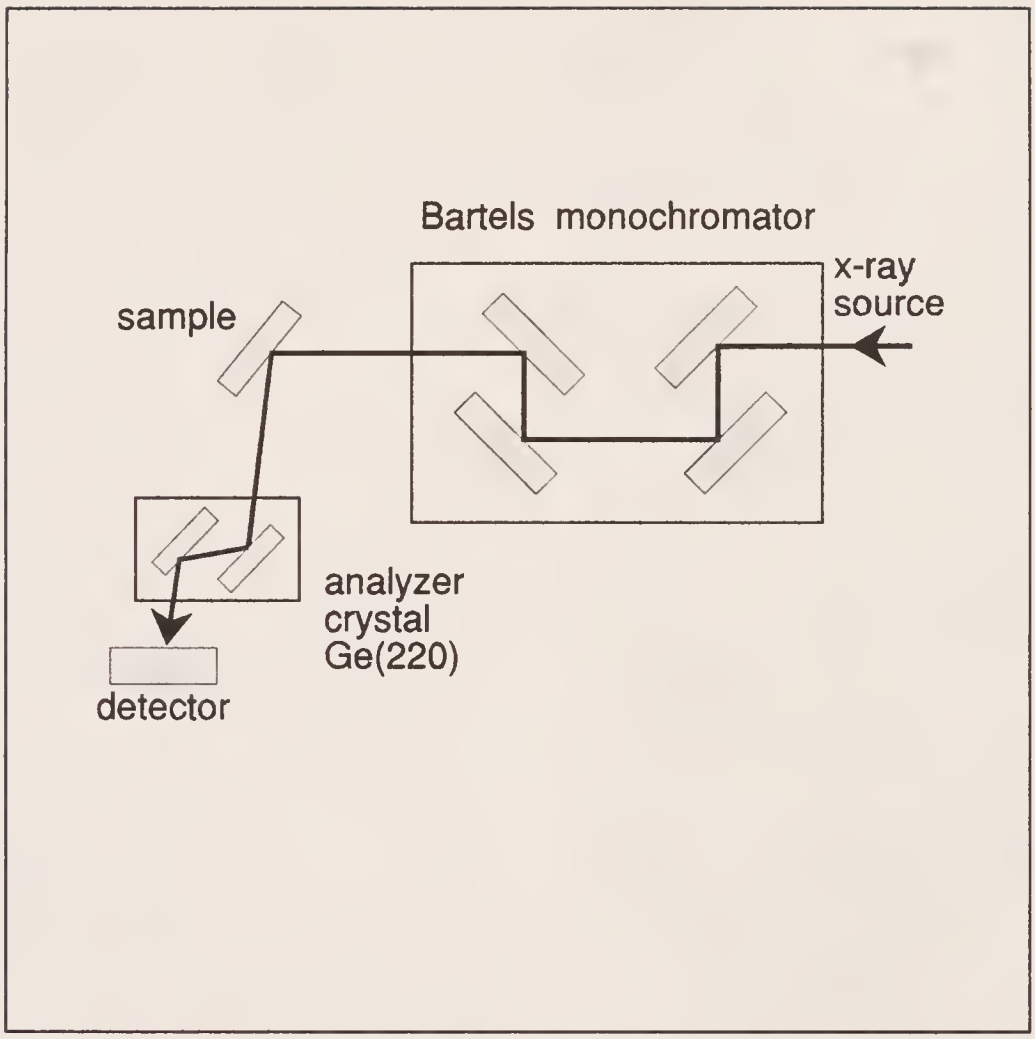

Figure 3.14 Schematic of the analyzer crystal and its position relative to the detector, sample, and monochromator. The x-ray beam path is shown.

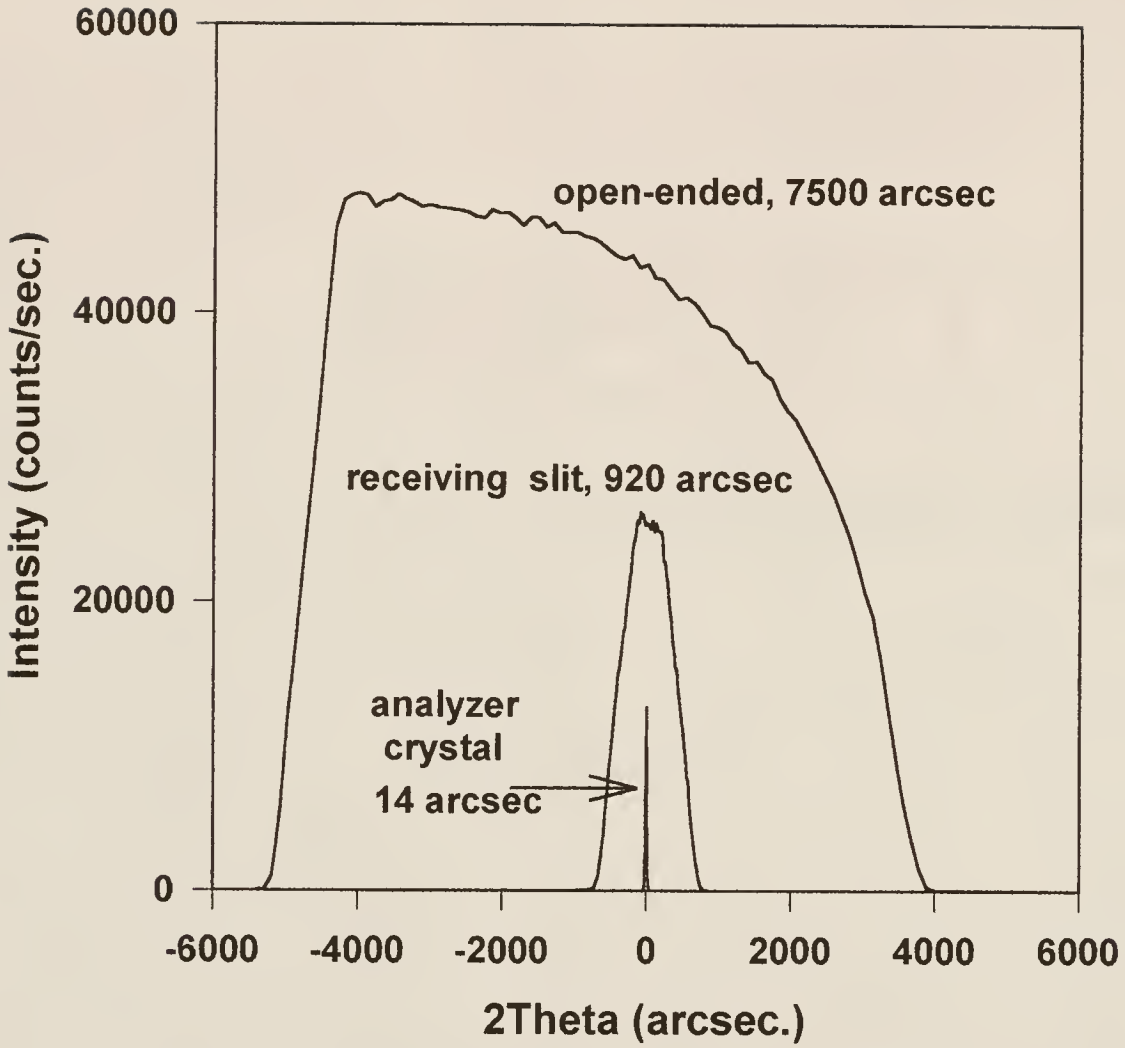

Figure 3.15 Rocking curves obtained from passing the detector through the x-ray beam under three conditions; open-ended (no slits in front of the detector), receiving slit, and analyzer crystal mode. The acceptance angle of the detector is dramatically reduced when using the analyzer crystal.

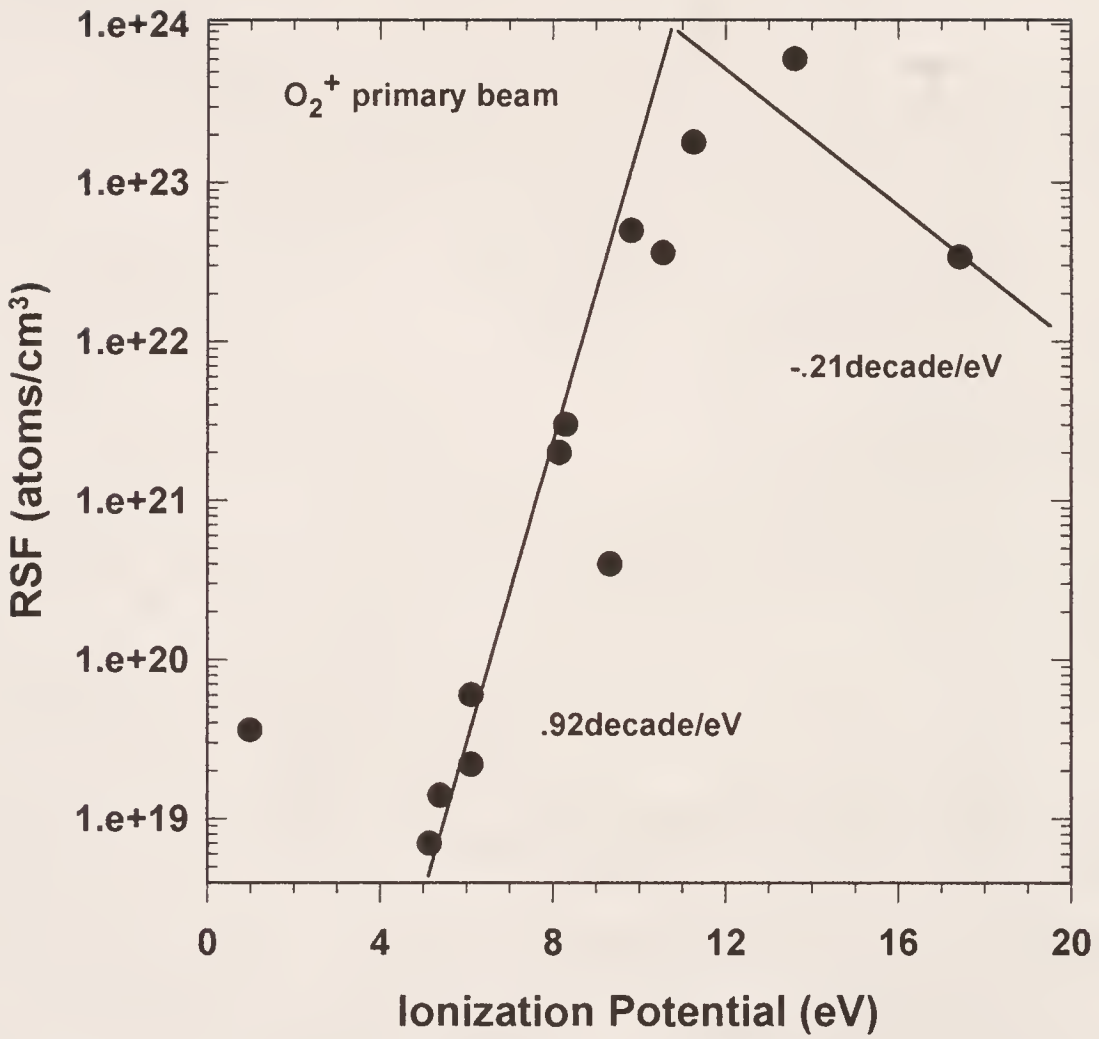

Figure 3.16 Relative Sensitivity Factor (RSF) versus ionization potential for impurity elements in a diamond matrix. This figure is used when sputtering with O_2^+.

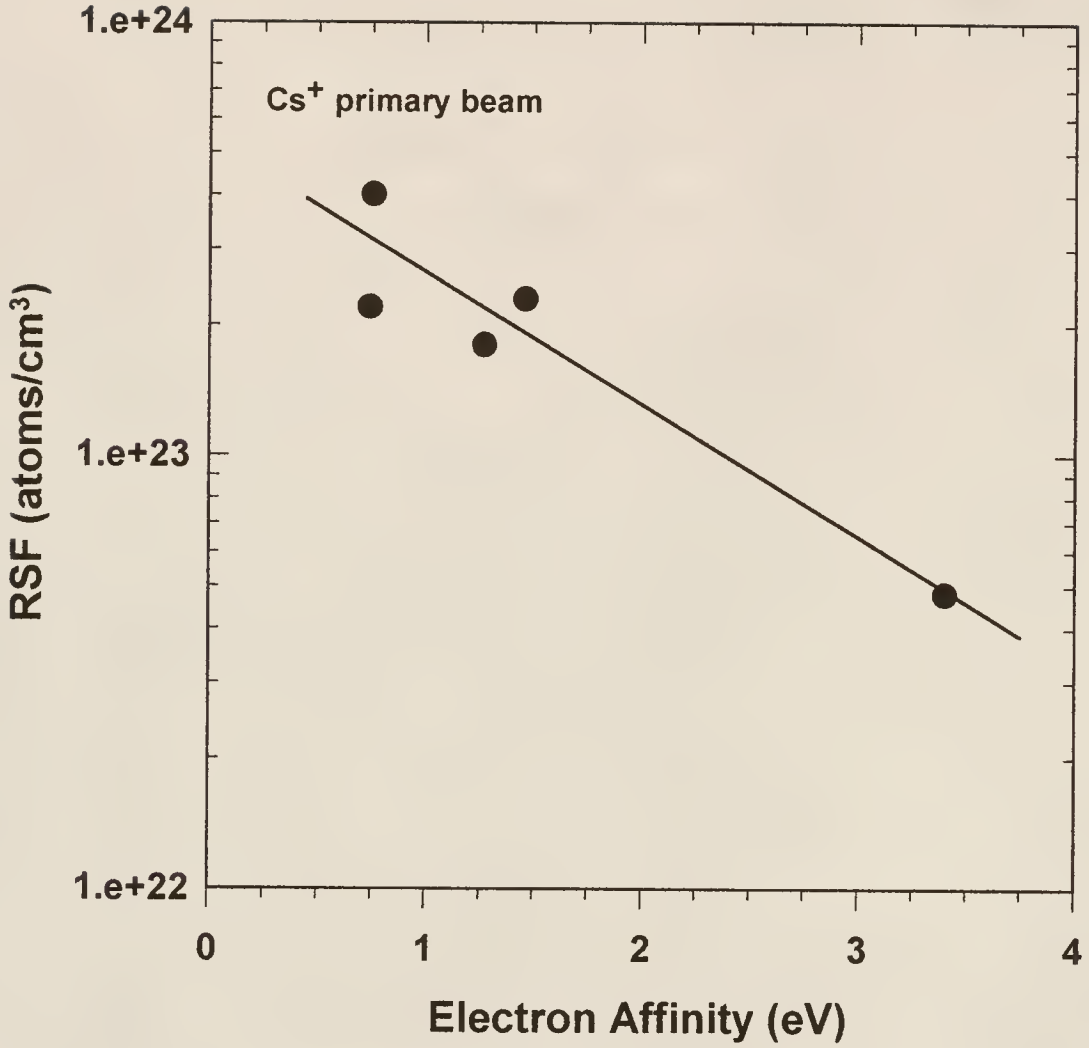

Figure 3.17 Relative Sensitivity Factor (RSF) verses electron affinity potential for impurity elements in a diamond matrix. This figure is used when sputtering with Cs^+.

CHAPTER 4
RESULTS

Surface Morphology

Scanning electron microscopy was used to examine the surface of the diamond films. In some cases it was easily discernable from the SEM micrographs that single crystal films were not achieved. Figure 4.1 is an SEM micrograph of a film grown on a (111) oriented substrate. The rough and polycrystalline structure of the surface was typical for growth on (111) faces. We were not able to achieve single crystal films on (111) oriented substrates with our current growth chemistries and growth parameters (as defined in Table 3.1).

Several different film morphologies were observed on the films grown on (100) substrates. Some films developed triangular defects [Fig. 4.2], dependent on the growth conditions, which are (111) penetration twins, based on reports by [Koi94, Eve94, Tam94]. A schematic representation

of the penetration twin shown in Figure 4.2 is shown in Figure 4.3. This film was grown with 1.5%methane(CH_4)/0.25%oxygen(O_2) and a balance of hydrogen (H_2). The film surface was smooth, including the areas near the defects. A (100) film grown with 30% methanol exhibited a rough morphology with pits as shown in Figure 4.4. The sides of the pits are defined by (111) faces. It was possible to minimize the development of penetration twins and pits on (100) surfaces by decreasing the concentration of carbon in the precursor gas (e.g. $\lesssim$10% methanol).

Diamond films grown on the (110) orientated substrates resulted in both smooth [Fig.4.5] and rough [Fig.4.6] films without the polycrystalline structure observed on (111) substrates. The smooth film was grown with 3%methanol and the rough film was grown with 30% methanol. Some localized surface defects were observed on some of the smooth (110) films, as shown in Figure 4.7. The defects were not uniformly present over the entire surface, but their density was ~$1.8 \times 10^5/cm^2$ in the region shown in Figure 4.7. The defects shown were ~50μm in length and ~15μm in width and were aligned along the same direction. The origin of these defects is unclear, however they may be associated with a

crystallographic direction.

Some of the films grown on (110) substrates developed stresses which were large enough to result in cracking of the films [Fig. 4.8]. The only film observed to crack were those on the (110) substrates. The cracks propagate on the (111) planes, which have lowest cleavage energy ($10.6 J/m^2$) [Fie86]. The angle between the cracks were ~70° which corresponded to the angle between (111) planes intersecting a (110) surface. As the film grew thicker, presumably tensile stress built up in the film with a corresponding compressive stress in the substrate. Upon propagation of the crack, the substrate relaxed by expanding and the film relaxed by contracting with both effects resulting in opening of the crack [Fig. 4.9]. If the cracks had been caused by compressive stresses in the film, they would have closed rather than opened. A 100μm thick film which cracked after growth (during handling with tweezers) is shown in Figure 4.10, and again demonstrates that residual tensile stress was present in the film. Another area of this same 100μm thick film is shown in Figure 4.11. This film cracked after some growth to a thickness less than 100μm, then growth occurred in the cracks. The cracks in some films were observed during growth through the optical pyrometer.

Additional cracking may have also occurred during cool down.

The observed surface characteristics for diamond films grown on (111), (100), and (110) diamond substrates are summarized in Table 4.1. Homoepitaxial growth was not achieved on (111) substrates. Penetration twins and pits were observed in films grown on (100) substrates, but could be minimized by decreasing the concentration of the carbon containing species in the growth chemistry to ≤30% methanol. Films grown on (110) substrates with high carbon concentrations (≥50%methanol) resulted in cracking with thicknesses ≥7μm. Films grown with 3%methanol to thicknesses of 70μm did not develop cracks.

Table 4.1 Typical surface morphologies and features observed for diamond films grown on (111), (100), and (110) diamond substrates with methanol chemistry.

Diamond substrates	(111)	(100)	(110)
Surface morphology	rough {all chemistries}	smooth {<30%CH_3OH}	smooth {≤10%CH_3OH} rough {≥30%CH_3OH}
Features	(111) facets, polycrystalline	penetration twins, pits defined by(111), growth steps	cracks {function of thickness and growth chemistry}

Raman Spectroscopy of Graphite Versus Diamond Deposition

Raman spectroscopy has been extensively used to characterize diamond and diamond-like films since the technique is sensitive to the different structures of carbon. This was discussed in Chapters 2 and 3, as was fitting the Raman data using Voight functions. In the following figures the experimental data, best fit curve and background intensities are shifted vertically, and the calculated peaks shown below for clarity. The best fit curve intensity was the summation of the background and calculated peak intensities. The peak positions and FWHM's which were determined from the calculated peaks are shown on the figures. The Raman peaks observed from films on (110) substrates for various growth chemistries are summarized in Table 4.2.

A Raman spectrum from a natural (110) diamond substrate (standard) is shown in Figure 4.12. The diamond Raman mode, indicating sp^3 bonding, is located at $1332cm^{-1}$ and has a FWHM=$3.0cm^{-1}$; no other Raman modes exists from 1200-$1700cm^{-1}$ for natural diamond. A Raman spectrum of a carbon film deposited on a silicon substrate from 3% acetone is shown in Figure 4.13. The peaks at $1358cm^{-1}$ (FWHM=$42cm^{-1}$) and $1580cm^{-1}$

(FWHM=22cm^{-1}) indicate the presence of sp^2 bonded carbon [Kni89].

The Raman spectra from films grown with 1% acetone on (100) and (110) diamond substrates are shown in Figures 4.14 and 4.15. Both films demonstrate Raman peaks from non-diamond carbon as indicated by the broad peaks at 1519cm^{-1} (FWHM = 180cm^{-1}) and 1525cm^{-1} (FWHM=163cm^{-1}) for the (100) and (110) films respectively. The diamond peak near 1332.5cm^{-1} for the (100) and (110) films have broader linewidths than a diamond substrate, thus we know the film is contributing to the diamond Raman peak. In addition, the broad peaks at 1329cm^{-1} (FWHM=113cm^{-1}) for the (100) film and 1338cm^{-1} (FWHM=116cm^{-1}) for the (110) film, indicate the presence of amorphous carbon. The graphitic peaks from (100) and (110) films were indistinguishable, therefore only the (110) films will generally be shown since this orientation is discussed later in more depth.

A film grown with 3% acetone on a (110) substrate demonstrated sp^2 peaks at 1595cm^{-1} (FWHM=86cm^{-1}) and 1360cm^{-1} (FWHM=93cm^{-1}) [Fig.4.16]. The sp^2 peak at 1595cm^{-1} is similar to that exhibited by amorphous or glassy carbon versus graphitic carbon [Kni89]. The sp^3 diamond Raman mode peak was

also observed at 1332cm^{-1}, however the signal was most likely coming from the diamond substrate. Decreasing the amount of acetone in the precursor gas to 0.5% resulted in less graphitic carbon in the diamond film as measured by Raman spectroscopy [Fig.4.17]. In fact the intensity of the graphitic carbon signal was only ~1% of the diamond intensity. The FWHM of the diamond peak was 6.5cm^{-1}, which is broader than

Table 4.2 Wavenumber, FWHM (shown in brackets), and origin of Raman peaks from diamond films (~20μm thick) deposited on (110) diamond substrates. (* Raman peak was not detected.)

Gas Chemistry	Diamond (cm^{-1})	Graphite/ Amorphous Carbon (cm^{-1})	Diamond-Like Carbon (cm^{-1})	Amorphous Carbon (cm^{-1})
3% acetone	*	1360 [93]	*	1595 [86]
1% acetone	1331 [13]	1338 [116]	1525 [163]	*
0.5% acetone	1331 [6.5]	*	1509 [118]	*
90% methanol	1332 [4.2]	1360 [43]	*	1591 [43]
50% methanol	1332 [4.7]	*	1525 [165]	*
18% methanol	1332 [3.1]	*	*	*

from a diamond substrate peak (~3.0cm^{-1}), indicating that diamond was deposited and contributed to the diamond Raman peak.

In addition to acetone precursors, diamond films were grown with a wide range (1.5%-100%) of methanol concentrations. Raman spectra from a film grown with 90% methanol on a (110) substrate are shown in Figure 4.18 and expanded along the y-axis in Figure 4.19. The 1360cm^{-1} (FWHM=43cm^{-1}) and 1591cm^{-1} (FWHM=43cm^{-1}) sp^2 peaks were detected in this film but they were weak (<1%) relative to the diamond peak. The sp^3 diamond peak at 1332cm^{-1} had a FWHM of 4.2cm^{-1}. A film grown with 50% methanol did not exhibit sp^2 Raman peaks, but an amorphous carbon peak was recorded at 1525cm^{-1} (FWHM=165cm^{-1}) as shown in Figure 4.20. The diamond peak was at 1332cm^{-1} with a FWHM=4.7cm^{-1}. While both 50 and 90% methanol samples showed graphitic carbon Raman peaks, their intensities relative to the diamond peak, was much less for growth in methanol versus acetone. For growth from 50% methanol, the sp^2 was ~2% of the intensity of the sp^3 peak, while the sp^2 peak from a (110) film grown with 1% acetone was ~70% of the sp^3 peak. Contrast to the 3% acetone film deposited on silicon (Fig. 4.13) which exhibited no diamond

signal, a 90% methanol film on silicon (Fig. 4.21) exhibited a strong sp^3 peak, further emphasizing the growth of diamond with high methanol concentrations versus high or low acetone concentrations.

No graphitic Raman carbon signals were detected for films grown with 18%, 10%, 3%, and 1.5% methanol on a (110) diamond substrates, indicating that the volume fraction of graphite was <0.02%. Raman spectra of a film grown with 18% methanol is shown in Figure 4.22; only the diamond peak at 1332cm^{-1} with a FWHM=3.1cm^{-1} was recorded.

Shown in Figure 4.23 is Raman spectrum which exhibits peaks at 3116, 3458, and 3971cm^{-1}. This spectrum is shown only as an example to illustrate that the bond-centered hydrogen defect (3116cm^{-1}) is Raman active. As will be discussed further in Chapter 5, H is located at different sites in the lattice, and this defect is not infrared active.

Raman Analysis of Stress

Close examination of the diamond Raman mode peak position revealed that it varied from 1332.5cm^{-1} to ~1327.5cm^{-1}. These peak position changes were only observed for films grown on (110) substrates. Shifts were not observed from films on

(100) substrates. The frequency shift of the diamond Raman mode from the normal position is due to strain, as discussed in Chapter 3. A shift to lower frequencies indicates tensile stress while a shift to higher wavenumbers indicates compressive stress [Cer72, Bop85].

Raman spectra from (100) and (110) films grown with 10% methanol to a thickness of 100μm are shown in Figure 4.24. The (100) films demonstrates little broadening (FWHM=3.2cm^{-1}) of the diamond Raman mode and no frequency shift. However the Raman peak from the (110) film, which also shows little broadening (FWHM=3.2cm^{-1}), is shifted 1.3cm^{-1} lower, indicating tensile strain.

Raman spectra from a film grown to a thickness of 70μm with 3% methanol are shown in Figures 4.25-4.30. This film was near colorless and the substrate signal was observed in the Raman spectrum. As a result the film peak was separated from the substrate by fitting with Voight functions. The spectrum in Figure 4.25 show peaks located at 1328.8cm^{-1} (film) and 1332.7cm^{-1} (substrate) with linewidths of 3.6cm^{-1} and 3.1cm^{-1}, respectively. As discussed in Chapter 3, a pinhole aperture before the spectrometer increased the film/substrate intensity ratio of the diamond Raman peak.

However, it was also necessary to determine if both peaks were produced from scattering in the film or if one of the peaks was coming from the diamond substrate. Figures 4.26-4.29 were all recorded using an aperture at different points across the film surface. The higher frequency peak near 1332cm^{-1} was attributed to the substrate since its intensity was dramatically reduced when a pinhole aperture was used. The lower frequency peak will be referred to as the film peak. It varied from 1328.3 to 1328.8cm^{-1}, and the linewidth varied from 3.3-3.8cm^{-1} for the different points on the film surface. The higher frequency peak position varied from 1331.3-1331.8cm^{-1} (Figs. 4.26-4.29) with linewidths from 3.8-4.6cm^{-1}. Raman spectra recorded from the back of the substrate of this sample contained a single diamond peak at 1332.5cm^{-1} with a FWHM=2.3cm^{-1} [Fig.4.30]. The results from Raman analysis at different locations across the film surface are summarized in Table 4.3.

Raman spectra from films grown with 10, 30 and 50% methanol to thicknesses of 7μm are shown in Figures 4.31-4.33. The positions and FWHM's for the diamond peaks from the films are plotted versus methanol concentration in Figure 4.34. The peak position decreased from 1331.6cm^{-1} to 1329.7cm^{-1} as the

methanol concentration increased from 10% to 30%. In contrast to the 10 and 30% methanol films the sp^3 peak position from the film grown with 50% methanol was shifted higher than for 30% methanol to 1330.2cm^{-1}. This frequency shift is counter

Table 4.3 Diamond Raman peak positions and FWHM for several locations across a 70μm thick film from 3% methanol.

Probe	Film ν_p (cm^{-1})	FWHM (cm^{-1})	Sub. ν_p (cm^{-1})	FWHM (cm^{-1})
Spot 1 (no aperture)	1328.8	3.6	1332.7	3.1
Spot 2	1328.8	3.3	1331.8	4.2
Spot 3	1328.5	3.7	1331.8	4.6
Spot 4	1328.8	3.8	1331.3	3.8
Spot 5	1328.3	3.8	1331.4	3.9
Back of substrate	-	-	1332.5	2.3

to the trend towards lower frequencies with higher methanol concentrations, but this shift can be explained by cracks in the 50% methanol film [Figures 4.8 and 4.9]. Cracking apparently resulted in partial stress relief, and therefore a shift of the Raman frequency back toward the higher (less stressed) frequency. The linewidths, 3.6, 4.9, and 12.5cm^{-1}, increased with increasing methanol concentration for the 10, 30, and 50% films, respectively.

The diamond Raman peak was not only a function of the methanol concentration, but also of the thickness of the film. The relationship between film thickness and the Raman peak position and/or linewidth for films grown with 10% methanol are shown in Figure 4.35. Raman spectra from a 25μm thick film grown with 10% methanol exhibited a peak position at 1326.8cm^{-1} and a linewidth of 4.9cm^{-1} [Fig. 4.36] versus 1331.6cm^{-1} and 3.6cm^{-1} for a 7μm thick film [Fig. 4.31]. Raman spectra from a 100μm thick film from 10% methanol, shown in Figure 4.37, has a peak position of 1331.0cm^{-1} and FWHM of 2.9cm^{-1}. Peaks from the substrate could not be detected due to the thickness of the film. This 100μm film was cracked, which resulted in partial strain relief and a corresponding shift of the Raman peak position to a higher wavenumber.

In summary, the frequency and linewidth of the diamond Raman mode was influenced by the growth chemistry, film thickness, and orientation. Films grown at lower concentrations methanol exhibited weak or undetectable peaks from sp^2 bonded carbon. Diamond films grown on (110) substrates developed stresses which were, in some cases, sufficiently large to crack some of the films. Films grown on (100) substrates did not exhibit shifts in the Raman peaks or

cracking in the films. The Raman data will be discussed further in Chapter 5.

SIMS Analysis

Mass surveys from SIMS of diamond grown with methanol revealed rhenium (Re), molybdenum (Mo), oxygen (O), hydrogen (H), and nitrogen (N) impurities were incorporated during growth. According to the literature as discussed in Chapter 2, metal from the filament and substrate holders are commonly incorporated into the diamond films. Thus, the sources of Re and Mo in this study almost certainly were the Re wire filament and Mo substrate heater block. A SIMS depth profile from a (110) 50% methanol film [Figure 4.38] using a primary beam of O_2^+ clearly shows the higher concentration of Re, Mo, and H impurities in the film relative to the substrate. The concentrations on the ordinate were quantitated as discussed in Chapter 5. The carbon intensity profile (not shown) was completely flat between the film and substrate, suggesting that the high Re and Mo signal at the interface was not an artifact, but rather reflects a true increase in the impurity concentration.

The H concentration in the film was also higher than in the substrate and decreased after sputtering through the substrate/film interface at ~15 min., indicating a higher concentration in the film. The Re, Mo, and H concentrations had the same characteristics in films grown with 30, 20, and 10% methanol on (110) substrates [see Figures 4.39-4.41]. As mentioned earlier the substrates were type IIa and contained N impurities [Fie92, Tre91]; the SIMS data show the higher N concentration in the substrate.

Films grown with 50 and 30% methanol on (100) substrates exhibited Re and Mo impurity distributions similar to that observed in the (110) films [Figures 4.42 and 4.43]. The H_2 count rate decreased slightly at the interface for (100) films grown with 50% methanol, but not for 30% methanol. In addition, the H_2 concentrations were generally lower in (100) versus (110) films as shown by the H/C ratios versus sputter time in Figure 4.44. Clearly, a decrease in the H/C ratio at the film/substrate interface was observed for (110) films, but the change for (100) films was smaller.

Intensity profiles using a Cs^+ primary beam for 20% and 10% methanol films on (110) substrates are shown in Figures 4.45 and 4.46, respectively. The H_2 and O_2 signals from both

the films are higher than for the substrates. Similar to the results for O_2^+ primary ions, the nitrogen signal from a molecular ion (CN^-) increased at the film/substrate interface.

FTIR Analysis

Infrared absorption spectra from a (110) oriented bulk diamond substrate (used as a standard) and a (110) diamond film grown with 50% methanol homoepitaxial on to a substrate, are shown in Figure 4.47. The inherent two-phonon absorption (1900 to 2300cm^{-1}) for diamond [Dav93] and C-N absorption (1100 to 1300cm^{-1}) [Dav93] was observed for both the natural diamond and the 50% methanol film. Absorption bands for C-H (~1450cm^{-1} and ~2800-3000cm^{-1}) and C=O (~1735cm^{-1}) were observed when the film was present, but not from the diamond standard. The C-H and C=O absorption regions, for 10%, 30%, and 50%methanol films are shown in Figures 4.48 and 4.49, respectively. The predicted and measured absorption frequencies from the methanol films are summarized in Table 4.4. The broad absorption band around 2900cm^{-1} consists of 5 vibrational frequencies, and this band was fit with 5 Voight functions to determine the area and position of the individual absorption bands, as shown in Figure 4.50. The positions and areas of

the individual peaks from the 50% methanol film as well as the 30% and 10% methanol films are listed in Table 4.5.

Table 4.4 List of the predicted and observed C-H vibration frequencies from films grown with 50%, 30%, and 10% methanol. The symmetric (s), asymmetric (a), or bending (b) configurations are designated in parenthesis. The predicted wavenumbers are from Liu et al. [Liu93].

C-H vibration	Predicted wavenumber (cm^{-1})	50% methanol (cm^{-1})	30% methanol (cm^{-1})	10% methanol (cm^{-1})
sp^1CH	3200-3305	-	-	-
sp^2CH sp^2CH_2	3000-3100	-	-	-
sp^3CH_3(a)	2960	2960	2959	2962
sp^3CH_2(a)	2925	2928	2928	2928
sp^3CH	2890	2903	2901	2905
sp^3CH_3(s)	2870	2872	2870	2870
sp^3CH_2(s)	2850	2848	2851	2847
sp^3CH_3(b) sp^3CH_2(b)	1450-1480	1458	1454	1430

Table 4.5 Area under the curves of the C-H (~1450cm^{-1}, 2800-3000cm^{-1}) absorption bands from 50, 30, and 10% methanol films. The area ratios are the C-H peak areas normalized to that from the 50% methanol film.

	50% methanol (cm^{-2})	30% methanol (cm^{-2})	10% methanol (cm^{-2})
C-H (~1450cm^{-1}, 2800-3000cm^{-1}) total area	35.2	20.1	1.3
x%area/50%area	1	0.571	0.037

The contributions of the various C-H configurations to the C-H absorption bands are summarized in Table 4.6. Symmetric and asymmetric stretching, and bending of sp^3CH_3 accounts for the majority of the C-H absorption. The results from curve fitting of the C=O absorption band are listed in Table 4.7. Similar to the results for hydrogen, the film grown with the higher methanol concentrations had higher C=O absorption. The FTIR results will be quantified and discussed in Chapter 5.

Table 4.6 Percent of the C-H (~1450cm^{-1}, 2800-3000cm^{-1}) absorption bands assigned to the listed configurations for the 50%, 30%, and 10% methanol films.

C-H vibration	50% methanol % of total area	30% methanol % of total area	10% methanol % of total area
sp^3CH_3(a)	35.2	26.3	34.5
sp^3CH_2(a)	21.6	19.7	30.2
sp^3CH	11.3	11.8	10.6
sp^3CH_3(s)	17.3	14.2	12.5
sp^3CH_2(s)	3.5	2.7	8.2
sp^3CH_3(b) sp^3CH_2(b)	11.1	25.3	4

Table 4.7 Area under the curves of the C=O (~1720cm^{-1}) absorption band from 50, 30, and 10% methanol films. The area ratios are the C=O peak areas normalized to that from the 50% methanol film.

	50% methanol	30% methanol	10% methanol
C=O (~1735cm^{-1}) total area	16.8(cm^{-2})	11.8(cm^{-2})	0.04(cm^{-2})
x%area/50%area	1	0.702	0.002

X-ray Analysis

X-ray rocking curves were recorded using both the five- and seven-crystal (analyzer crystal) configurations discussed earlier. Although a lot of data were collected with the five-crystal x-ray diffractometer (open-ended detector) prior to the availability of the analyzer crystal, only some of these rocking curves will be shown. As explained in Chapter 3, the analyzer crystal dramatically improves the resolution of the x-ray diffractometer, therefore rocking curves and reciprocal space maps from this experimental configuration will primarily be used.

Using the five-crystal configuration, the x-ray rocking curve from (220) symmetric reflections from a diamond standard and from a 7μm thick, homoepitaxial diamond films grown on (110) substrates with 10%, 30%, and 50% methanol are shown in Figures 4.51-4.54. The FWHM of the rocking curves were 25, 40, 190, and 265 arcsec from the diamond standard and substrates with 7μm thick (110) films grown with 10%, 30%, and 50% methanol, respectively.

Asymmetric reflections were collected using diffraction from the (313) diffracting planes, which make an angle of 49.5° with the (110) surface plane. Information about the in-plane (parallel) properties of the film can be obtained using asymmetric reflections as discussed in Chapter 2. The (313) rocking curves from the diamond films exhibited FWHM's of 80, 375, and 450 arcsec for the 10%, 30%, and 50% methanol films [Figs 4.55-4.57], respectively. These x-ray data are summarized in Table 4.8.

Table 4.8 The FWHM of ω x-ray rocking curves obtained from the 5-crystal configuration of the HRXRD configuration.

Sample	(220) FWHM (arcsec)	(313) FWHM (arcsec)
Diamond Substrate	25	25
10% methanol	40	80
30% methanol	190	375
50% methanol	265	450

The broadening of the (220) rocking curve is due to strain, defects, and/or mosaicity in a direction perpendicular to the surface of the substrate. The (313) rocking curve is

affected by distortions in directions both perpendicular to the surface. The (313) rocking curves are broader than the (220) rocking curves, indicating lattice distortions in both the parallel and perpendicular direction.

With the seven-crystal x-ray diffraction configuration, the data can be used to separate lattice plane spacing versus mosaic contributions to peak broadening. For example, two $\omega/2\theta$ rocking curves from the same diamond film (50% methanol, 7μm thick) are shown in Figure 4.58. The broader peak (210 arcsec) was recorded using only receiving slit in front of the detector, while the narrower peak (18 arcsec) was recorded using the analyzer crystal. Two ω rocking curves with FWHM's of 205 arcsec and 202 arcsec are shown in Figure 4.59 for the receiving slit mode and analyzer crystal mode, respectively. Recalling that $\omega/2\theta$ rocking curves show strain while ω rocking curves reveal mosaicity, these data show that the broadening of the rocking curve observed in the receiving slit mode was mostly due to mosaicity and not strain. The $\omega/2\theta$ and ω rocking curves from the film are shown together in Figure 4.60.

For the balance of the HRXRD, only data using the analyzer crystal mode will be reported. The symmetric ω rocking curve from a 7μm thick diamond film grown with 10% methanol is shown in Figure 4.61, and the ω/2θ rocking curve is shown in Figure 4.62. The FWHM of the ω rocking curve was 15 arcsec and the FWHM of the ω/2θ rocking curve was 12 arcsec. Rocking curves from the 10% methanol film do not exhibit any significant broadening compared to the 7μm films grown with 30 and 50% methanol [Figures 4.63-4.66]. The 30 and 50% methanol films exhibit little broadening of the ω/2θ rocking curves [Figures 4.63 and 4.64], with FWHM's of 14 and 15 arcsec, respectively. However there was significant broadening of the ω rocking curves with FWHM's of 180 and 200 arcsec, respectively [Figures 4.65 and 4.66]. The broadening due to mosaic effects increased with increased methanol in the precursor gas chemistry.

The ω/2θ and ω rocking curves from the 10, 30, and 50% methanol films using the (313) asymmetric reflection are shown in Figures 4.67 to 4.72. The FWHM of the symmetric and asymmetric ω/2θ and ω rocking curves versus methanol concentration are shown in Figures 4.73 and 4.74. The ω/2θ

rocking curves had FWHM's of 45, 75, and 55 arcsec, for the 10%, 30%, and 50% methanol films, respectively [Figure 4.73]. This broadening was due to lattice parameter changes, i.e. strain. The strain increased with increased methanol from 10% to 30%, and decreased for the 50% methanol film (which cracked and partially relieved the strain). The 10%, 30%, and 50% methanol films had FWHM's of 32, 375, and 290 arcsec for the asymmetric ω rocking curves, respectively. The ω rocking curve broadening at higher percent methanol is indicative of mosaic structure. The 50% methanol film exhibited interference fringes which were not observed on the other two 7μm films.

The asymmetric ω/2θ rocking curve from the 10% methanol film was modeled with Philips PC-HRS software. A calculated intensity profile was constructed for a 7.5μm thick diamond layer on a diamond substrate, where the strain increased exponentially from zero at the interface to +196ppm (+=tensile strain) at the surface. A stress of 224MPa was calculated from this strain value and assuming E=1143GPa. The simulated profile matches the experimental data well [Figure 4.75] and the stress value was similar to that measured with Raman

(~300MPa). Other rocking curves were more difficult to model. The Philips program uses a trial and error method of picking strain distributions to model the rocking curves. This program appears to be better suited for modeling heterostructures of known compositions and layer thicknesses, versus homoepitaxial layers of unknown composition and thickness. The Philips program could not simulate the ω rocking curves.

The (220) ω/2θ-ω maps from the 10% methanol film at rotations of 0° and 180° exhibited ω (mosaic) spreading [Figures 4.76 and 4.77]. The mosaic spreading was more apparent in ω/2θ-ω maps than from the rocking curves [Figures 4.61 and 4.62]. The (313) ω/2θ-ω map exhibited ω/2θ spreading toward lower angles, indicating tensile strain [Figure 4.78] in addition to mosaic broadening.

Thicker films (70μm) resulted in individual peaks on the (313) ω rocking curves, and broader (313) ω/2θ rocking curves [Figures 4.79 and 4.80, respectively]. A 70μm thick film grown with 3% methanol exhibited a FWHM of 80 arcsec for the ω/2θ rocking curve [Figure 4.80]. The ω rocking curve exhibited individual peaks, and a width of 300 arcsec [Figure

4.79]. The individual peaks in the ω rocking curve may be due to layers within the film being misoriented relative to the substrate and each other. A 100μm thick film grown with 10% methanol exhibited a FWHM of 360 arcsec for the (313) ω/2θ rocking curve [Figure 4.81]. This was the broadest ω/2θ rocking curve observed of all the films analyzed. The ω rocking curve for this thick film again exhibited individual peaks, similarly to the 3% methanol film [Figure 4.79]. The width of this rocking curve was over 1000 arcsec.

The (313) reciprocal lattice space map from the 3% methanol film is shown in Figure 4.83. This map was converted from a (313) ω/2θ-ω map. Shown in Figure 4.84 are the reciprocal lattice points for diamond and the ω/2θ and ω scan directions. The tilting of the film was perpendicular to the [313] direction. There was also spreading towards the origin indicating tensile strain, for both the prominent peaks.

The FWHM of the ω/2θ and ω rocking curves generally increased with increasing methanol concentration indicating increased mosaicity of the films and increased strain. In addition, broadening of the rocking curves increased significantly for thick films and individual peaks were

resolved with the ω rocking curves. Mosaic spreading was more apparent with the asymmetric reflection versus the symmetric reflections indicating a greater parallel versus perpendicular mosaic spreading contribution.

Figure 4.1 SEM micrograph showing the typical rough, polycrystalline surface morphology of films deposited on (111) substrates.

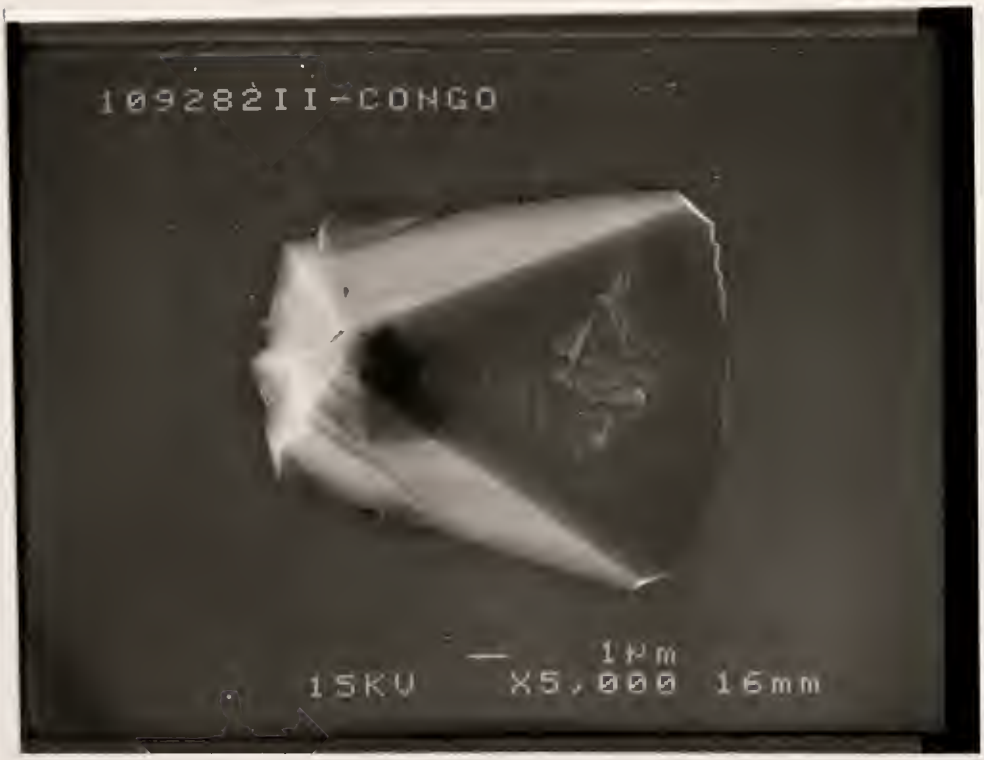

Figure 4.2 SEM micrograph of a penetration twin defect typically observed for films grown on (100) substrates.

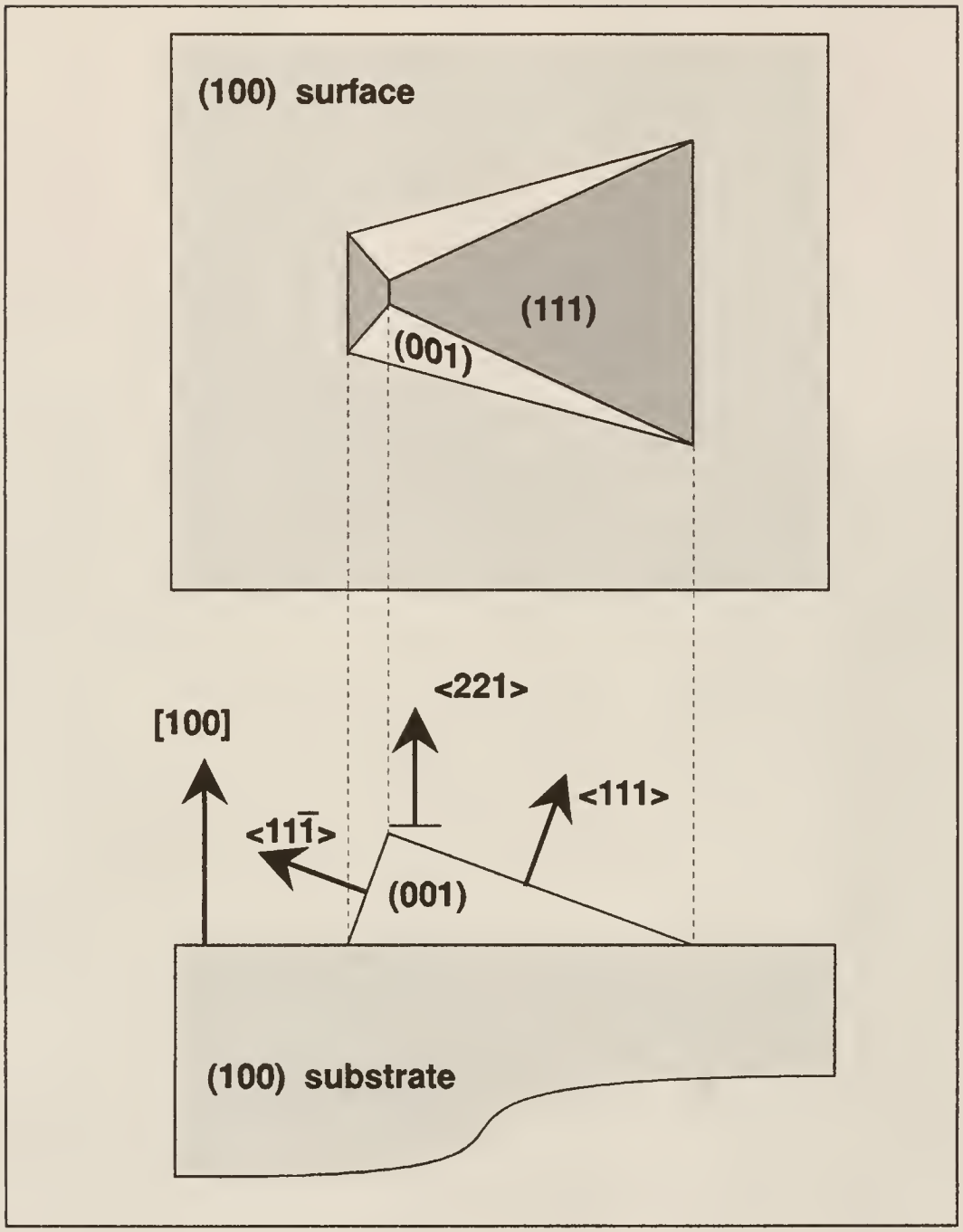

Figure 4.3 Schematic representation of the penetration shown in Figure 4.2.

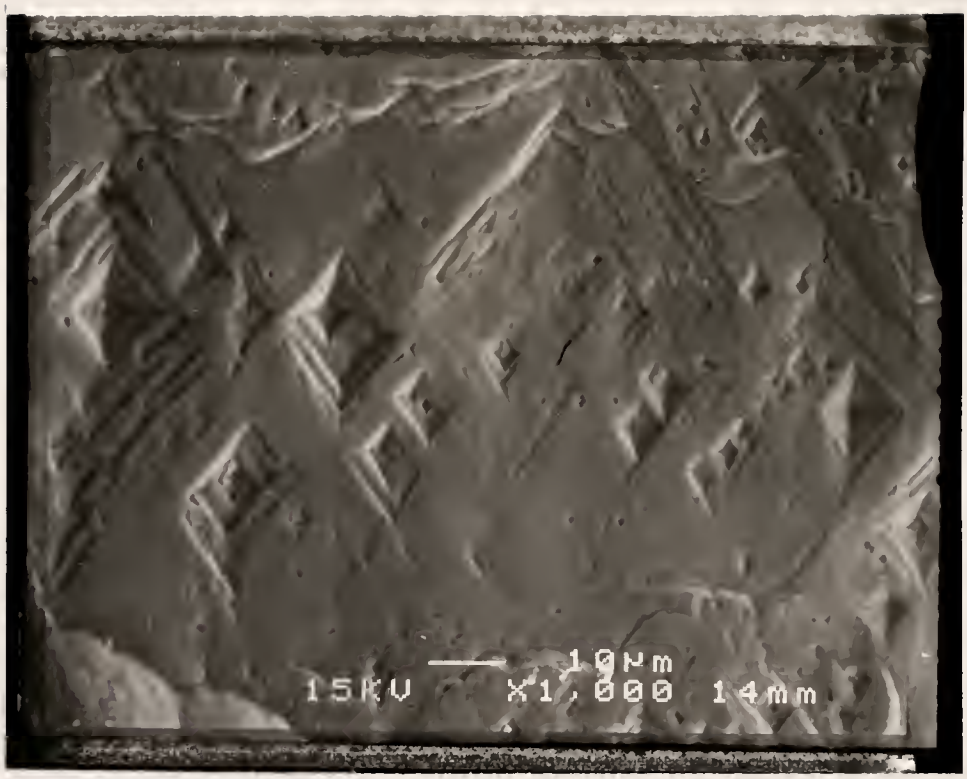

Figure 4.4 SEM micrograph of typical pits observed on (100) films. The pits are defined by {111} facets.

Figure 4.5 SEM micrograph of a typical smooth (110) film. This film was grown with 3% methanol.

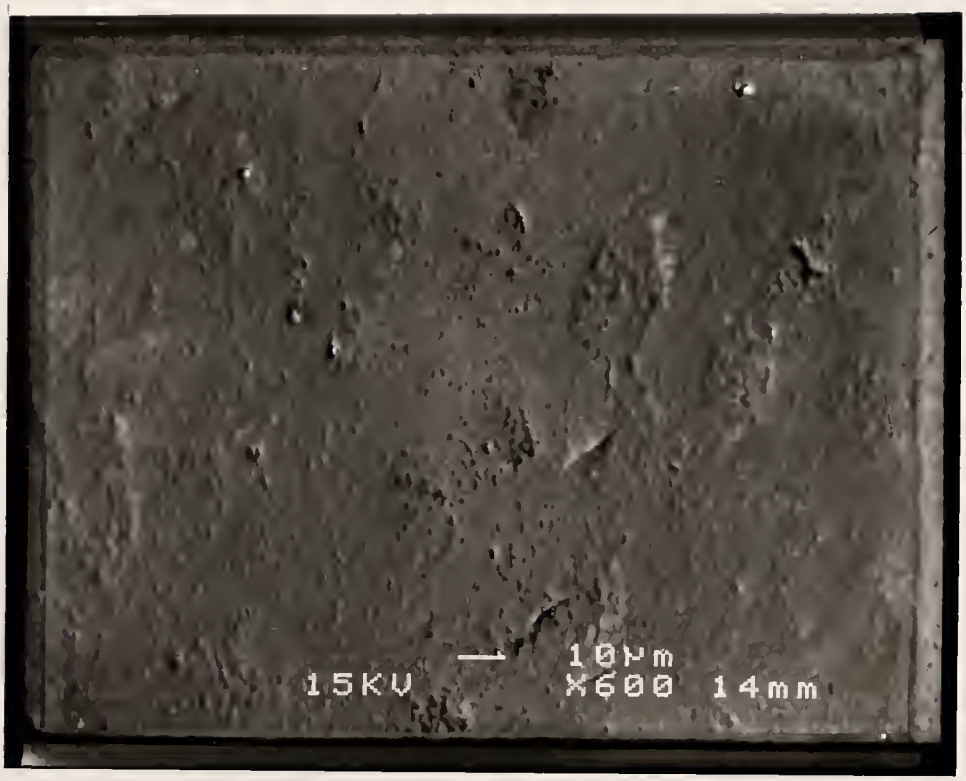

Figure 4.6 SEM micrograph of a typical rough (110) film. This film was grown with 30% methanol.

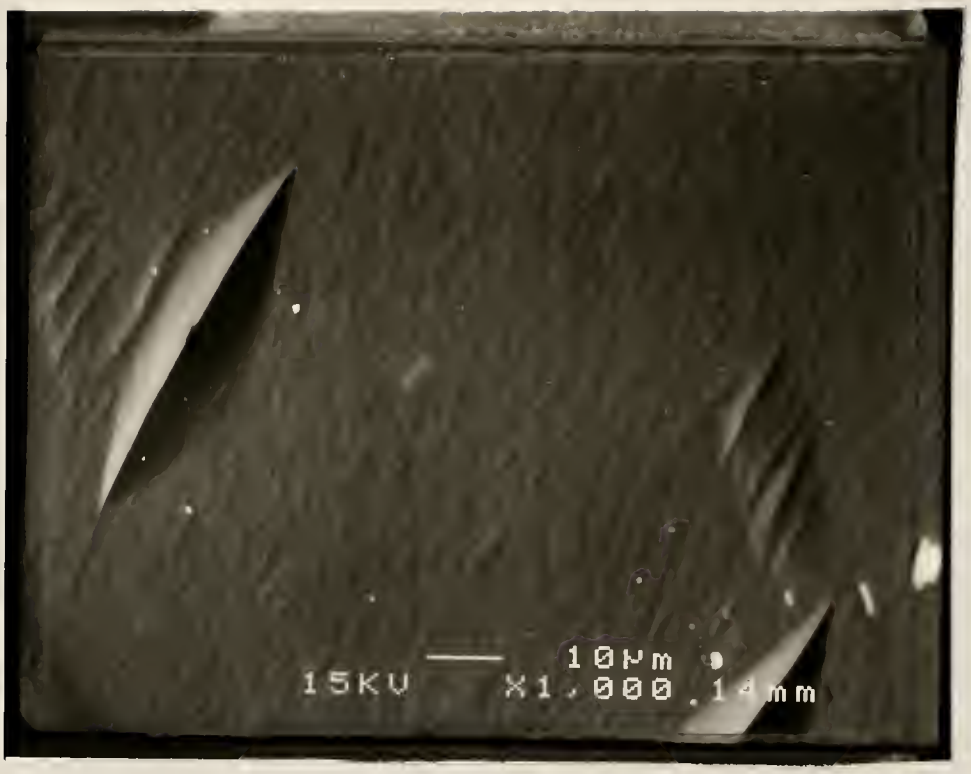

Figure 4.7 SEM micrograph of unidentified defects which were observed on some (110) films.

Figure 4.8 SEM micrograph of cracks in a (110) film grown with 50% methanol. The cracks propagated on {111} cleavage planes.

Figure 4.9 Higher mag SEM micrograph of the cracked film shown in Figure 4.8. Relaxation of stress caused the crack to open.

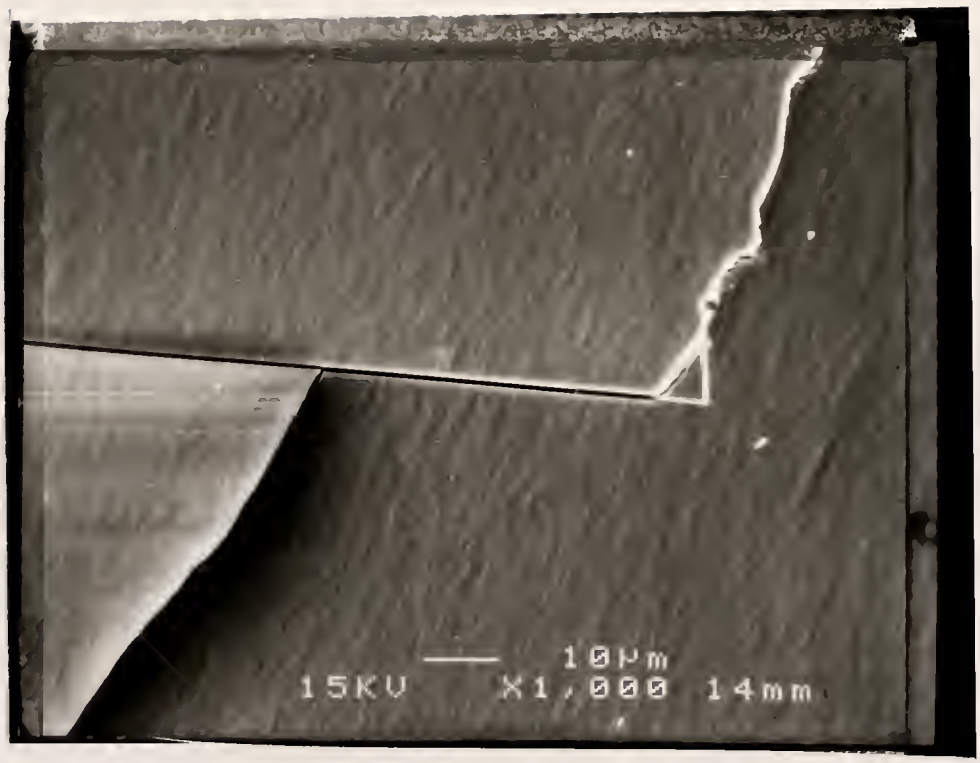

Figure 4.10 SEM micrograph of a 100μm thick (110) film grown with 10% methanol. This film cracked after handling with tweezers indicating high residual stress was present in the film.

Figure 4.11 SEM micrograph of secondary growth in a crack which developed early in a growth run for the 100μm thick film shown in Figure 4.10.

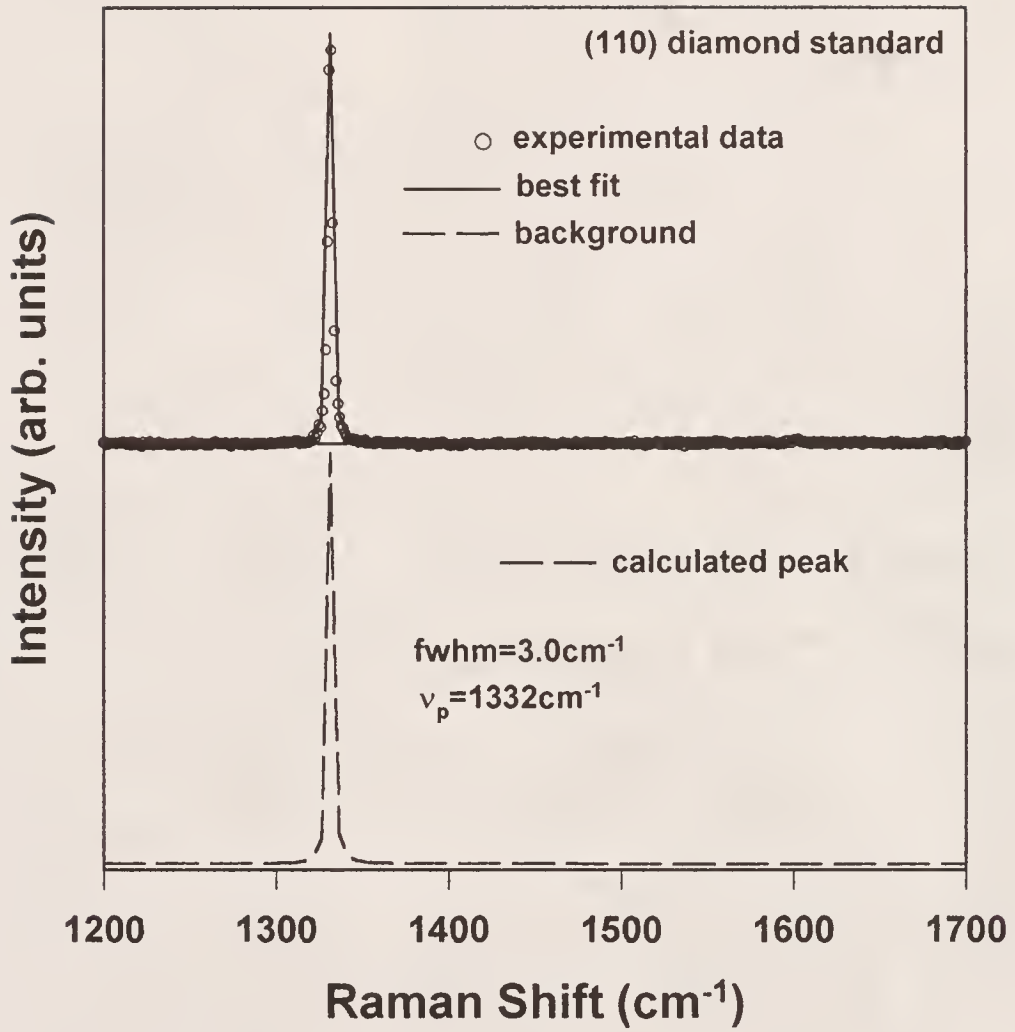

Figure 4.12 Raman spectrum from a (110) diamond substrate which was used as a standard. The experimental data, best fit curve, and background are shifted vertically from the calculated peak. The peak position ($1332cm^{-1}$) and FWHM ($3.0cm^{-1}$) of the diamond Raman peak was calculated by curve fitting with a Voight function.

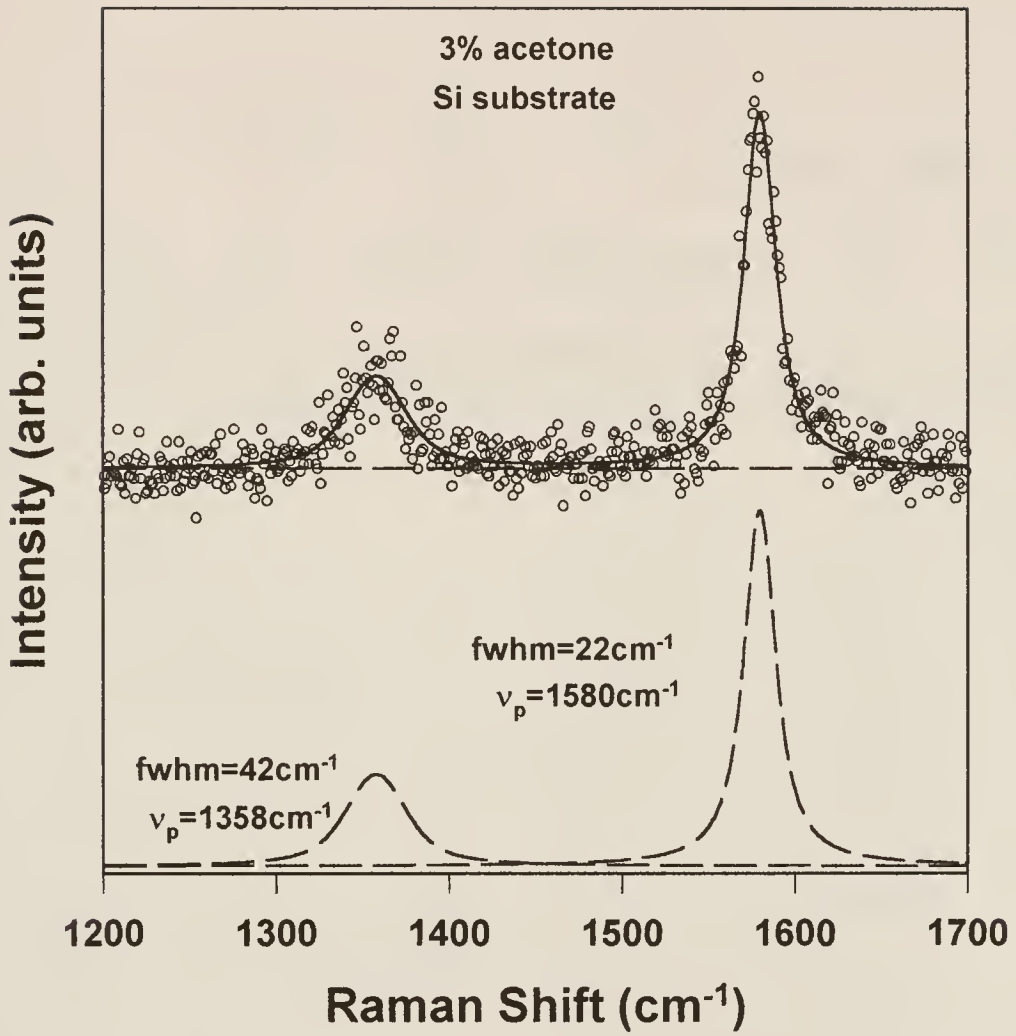

Figure 4.13 Raman spectrum from a film grown with 3% acetone on a silicon substrate. Graphitic carbon peaks at 1358cm^{-1} and 1580cm^{-1} were detected; no diamond peak (1332cm^{-1}) was detected.

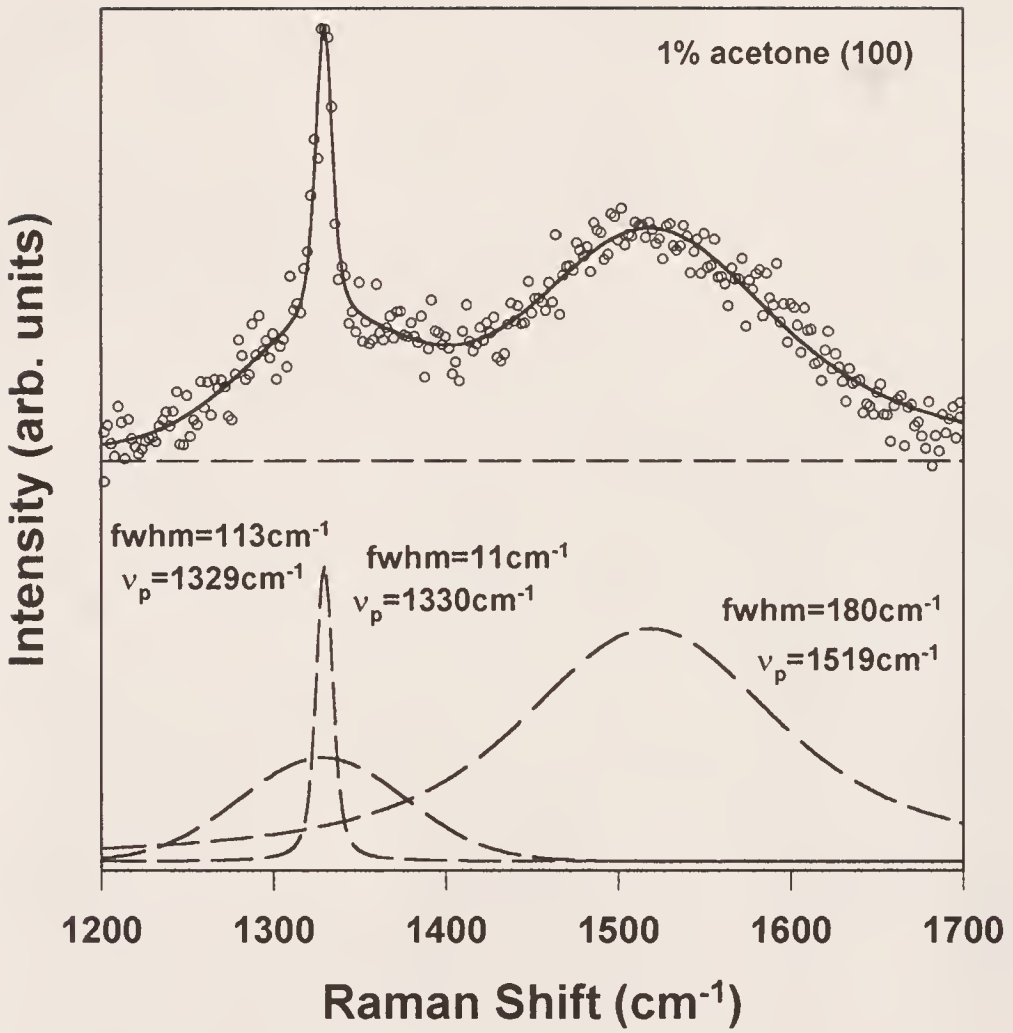

Figure 4.14 Raman spectrum from a film grown with 1% acetone on a (100) diamond substrate. Amorphous carbon peaks at 1329cm^{-1} and 1519cm^{-1} were detected and a broad (11cm^{-1}) diamond peak (1330cm^{-1}) was detected.

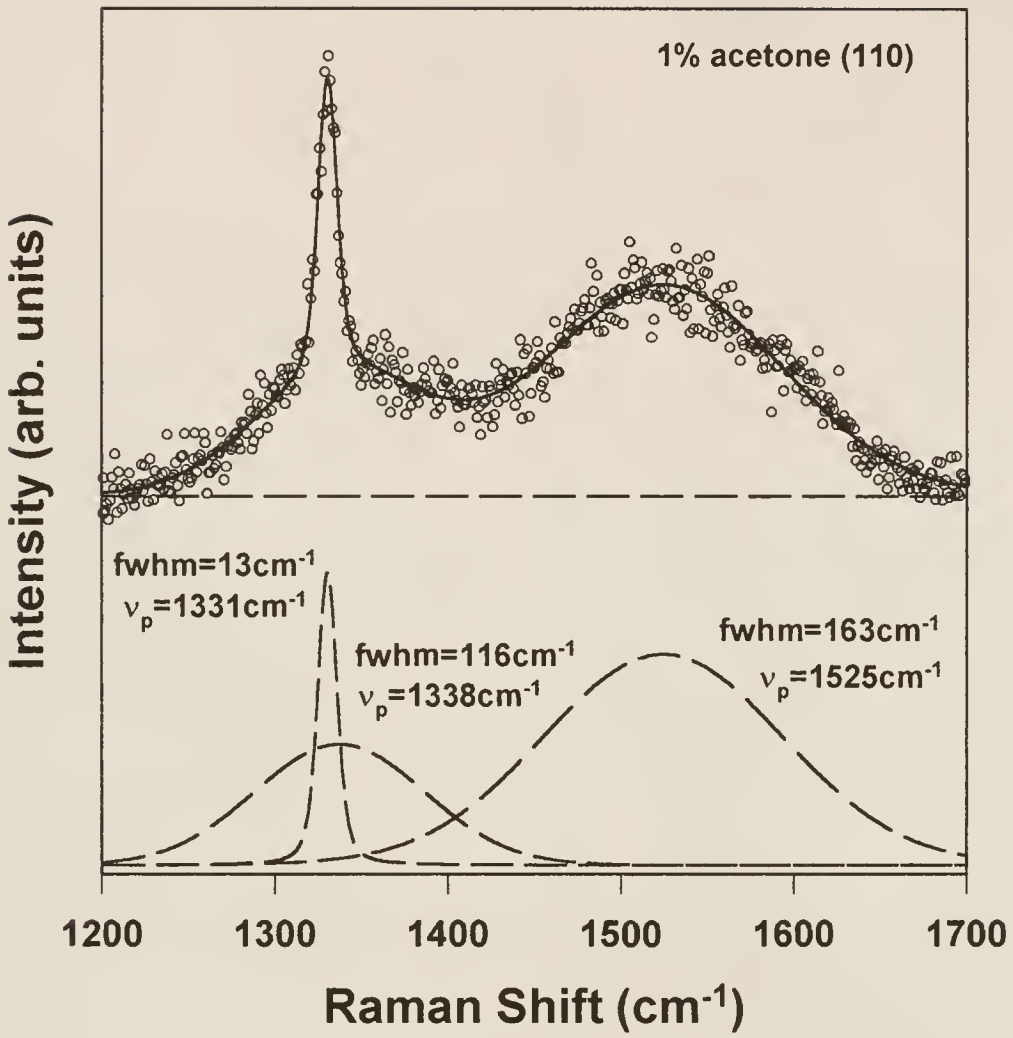

Figure 4.15 Raman spectrum from a film grown with 1% acetone on a (110) diamond substrate. Amorphous carbon peaks at 1338cm^{-1} and 1525cm^{-1} were detected and a broad (13cm^{-1}) diamond peak (1331cm^{-1}) was detected.

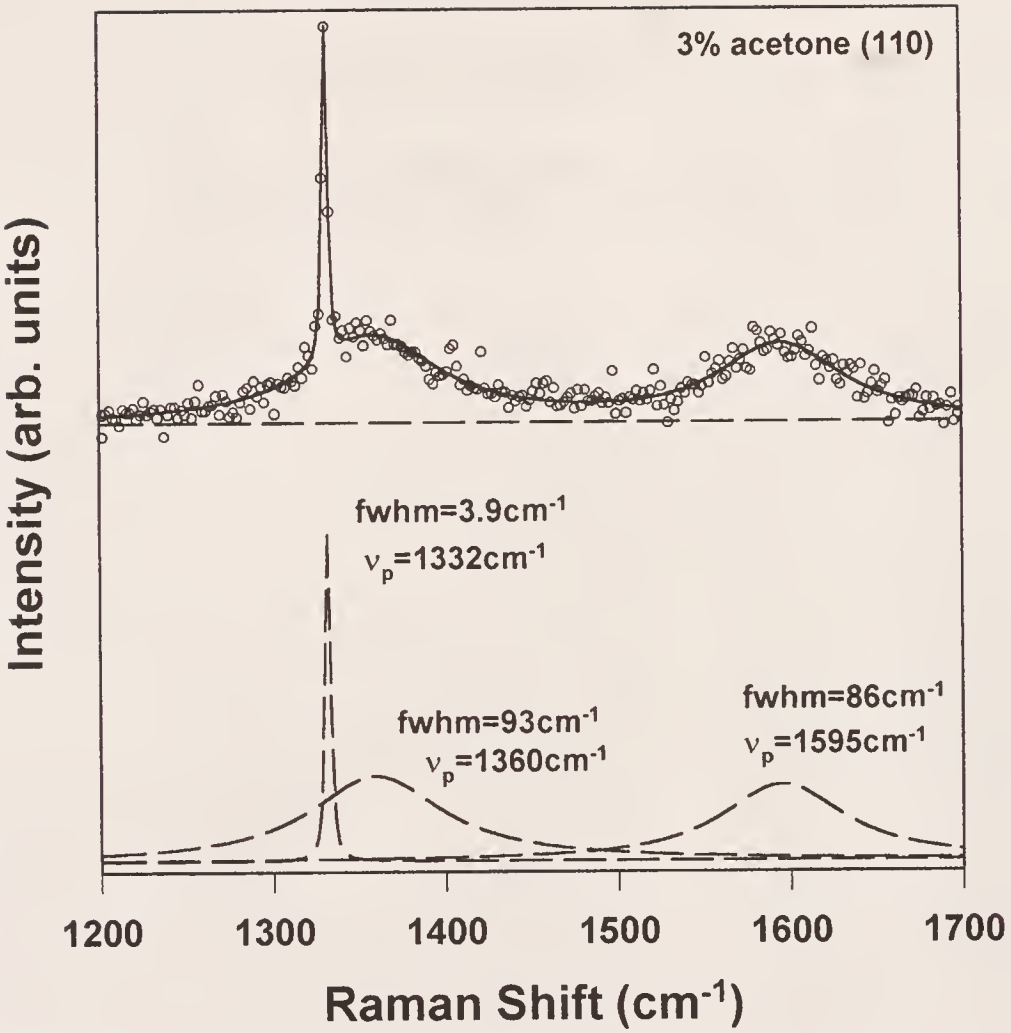

Figure 4.16 Raman spectrum from a film grown with 3% acetone on a (110) diamond substrate. Graphitic/amorphous carbon peaks at 1360cm^{-1} and 1595cm^{-1} were detected. The diamond peak (1332cm^{-1}) was primarily from the substrate and not the film.

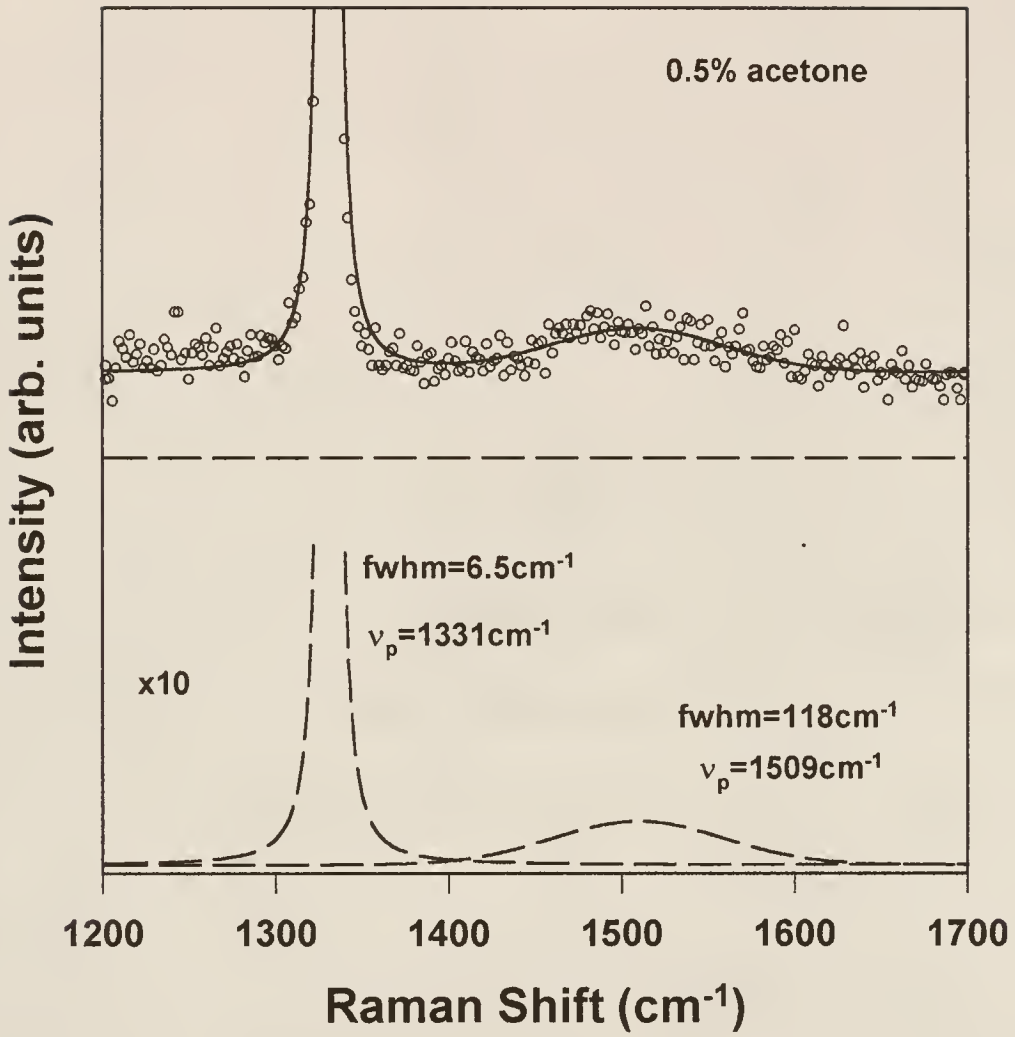

Figure 4.17 Raman spectrum from a film grown with 0.5% acetone on a (110) diamond substrate. A diamond ($1332cm^{-1}$) and weak amorphous carbon ($1509cm^{-1}$) peak were detected.

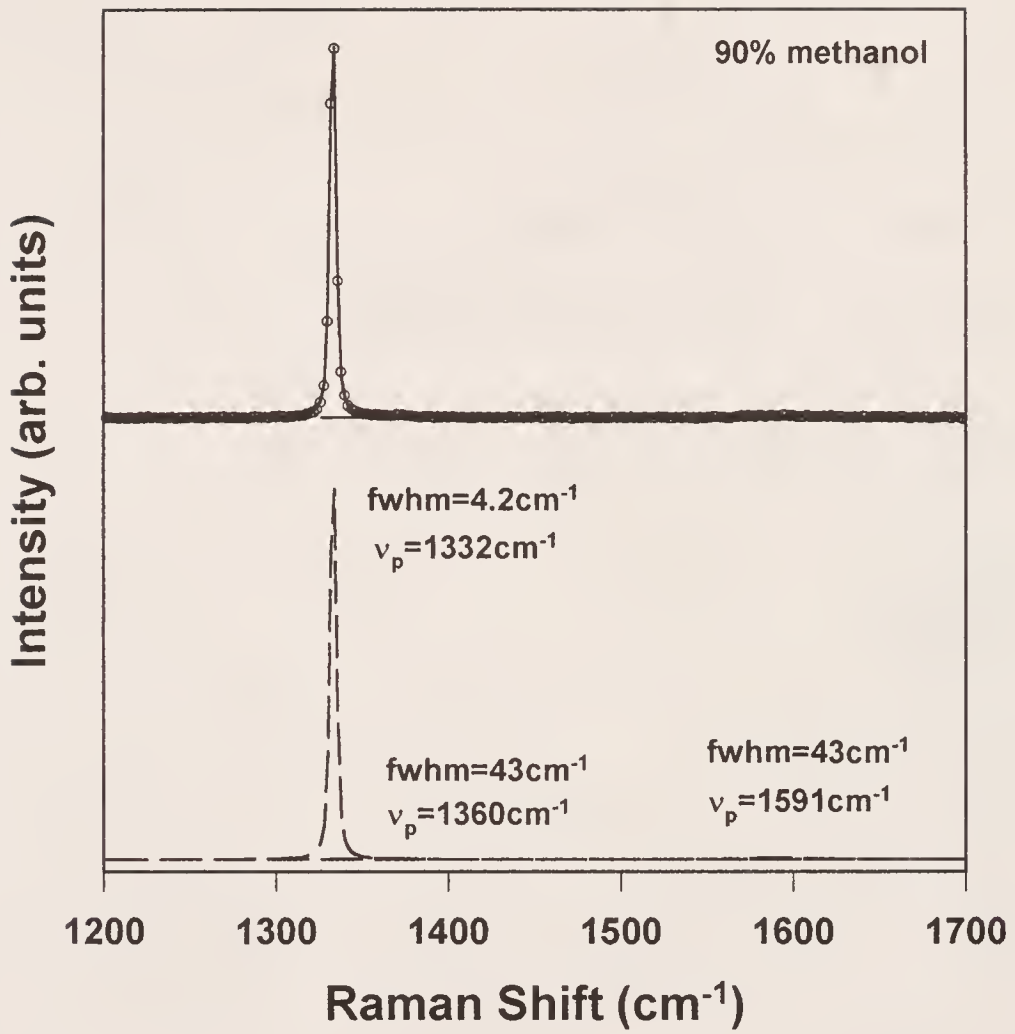

Figure 4.18 Raman spectrum from a film grown with 90% methanol on a (110) diamond substrate. A diamond (1332cm^{-1}) and weak amorphous/graphitic carbon (1360 and 1591cm^{-1}) peaks were detected.

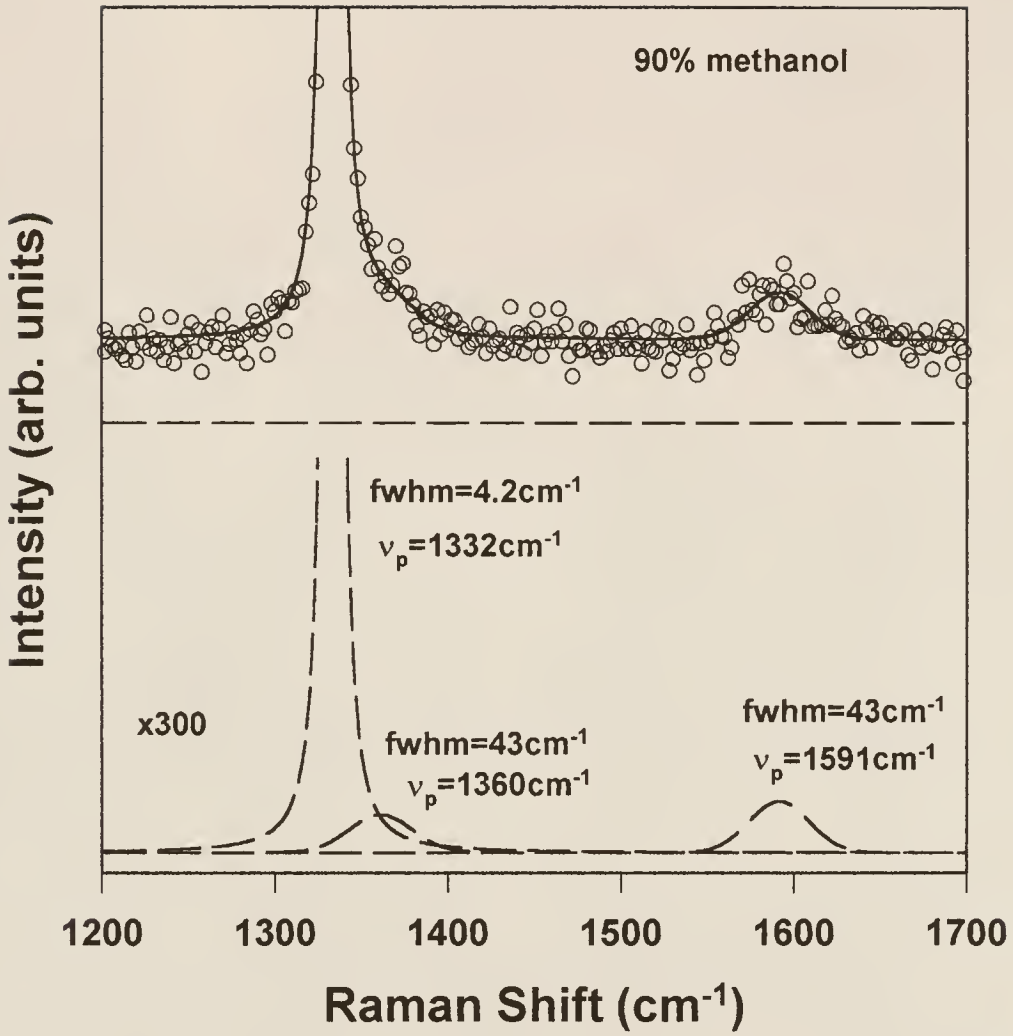

Figure 4.19 Expanded view of the Raman spectrum shown in Fig. 4.18.

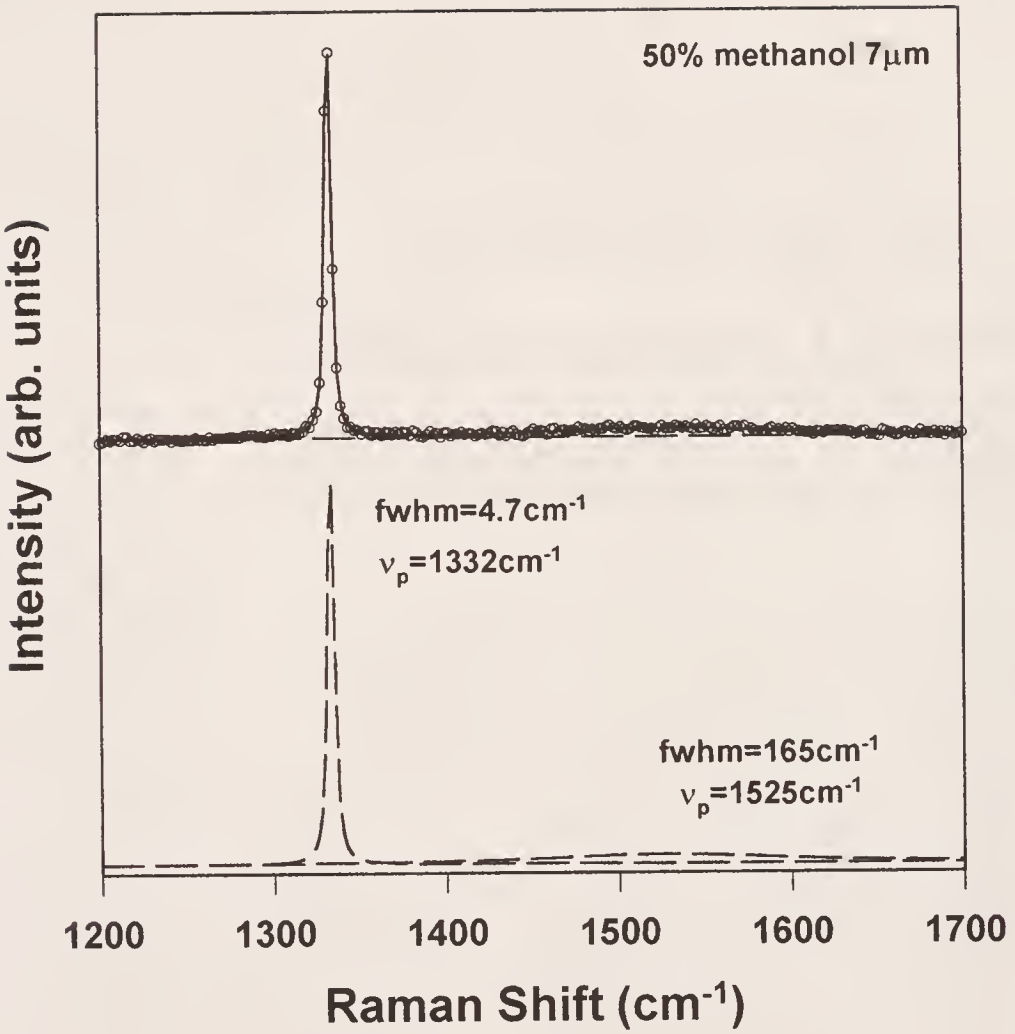

Figure 4.20 Raman spectrum from a film grown with 50% methanol on a (110) diamond substrate. A diamond ($1332cm^{-1}$) and a weak amorphous carbon ($1525cm^{-1}$) peak were detected.

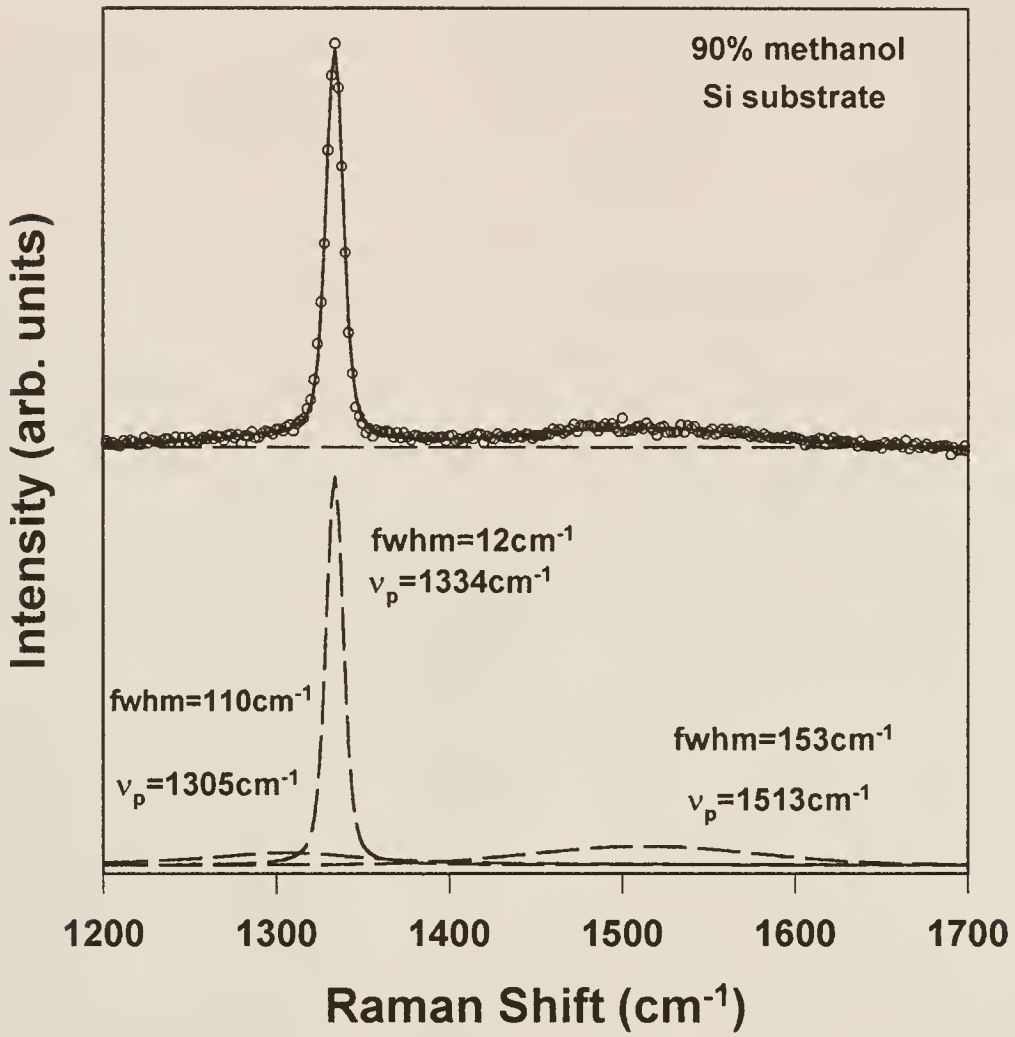

Figure 4.21 Raman spectrum from a film grown with 90% methanol on a silicon substrate. A diamond (1334cm^{-1}) and weak amorphous carbon (1305 and 1513m^{-1}) peaks were detected.

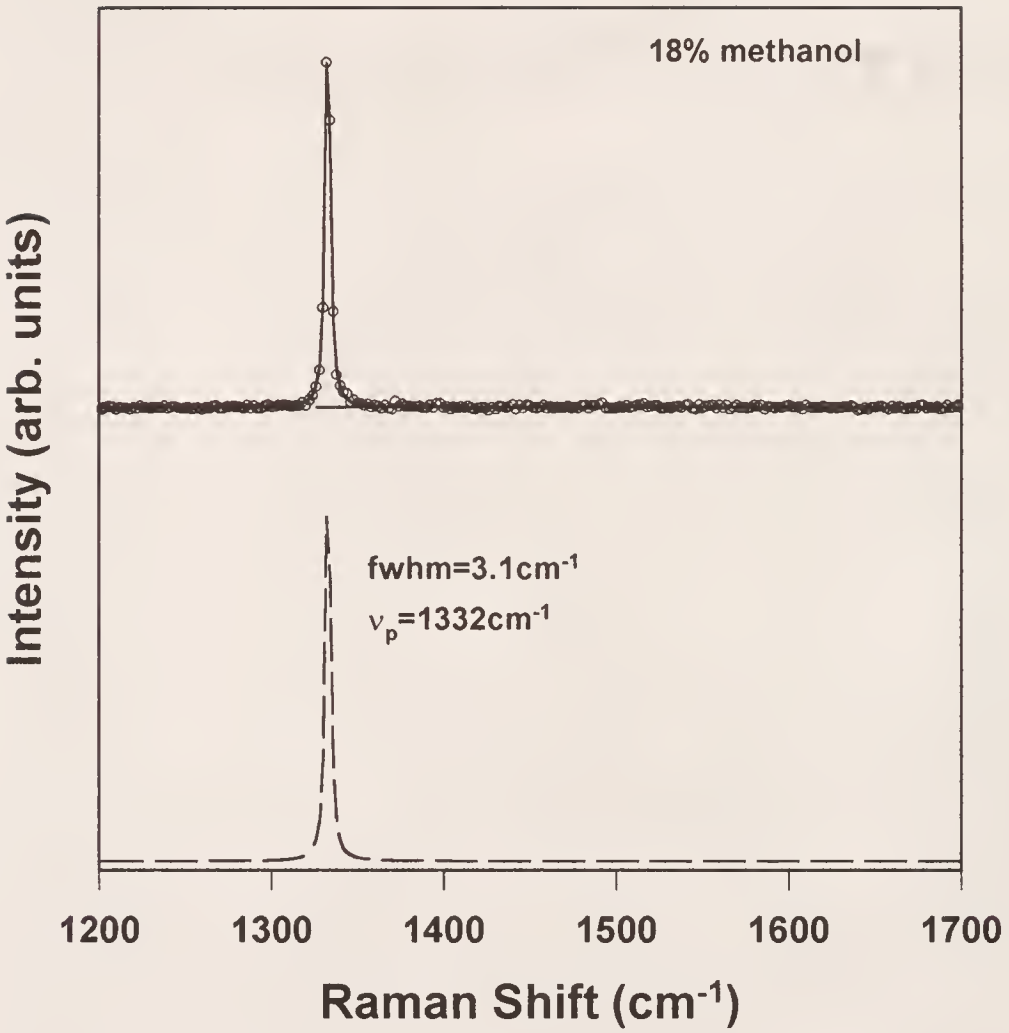

Figure 4.22 Raman spectrum from a film grown with 18% methanol on a (110) diamond substrate. Only a diamond ($1332cm^{-1}$) peak was detected.

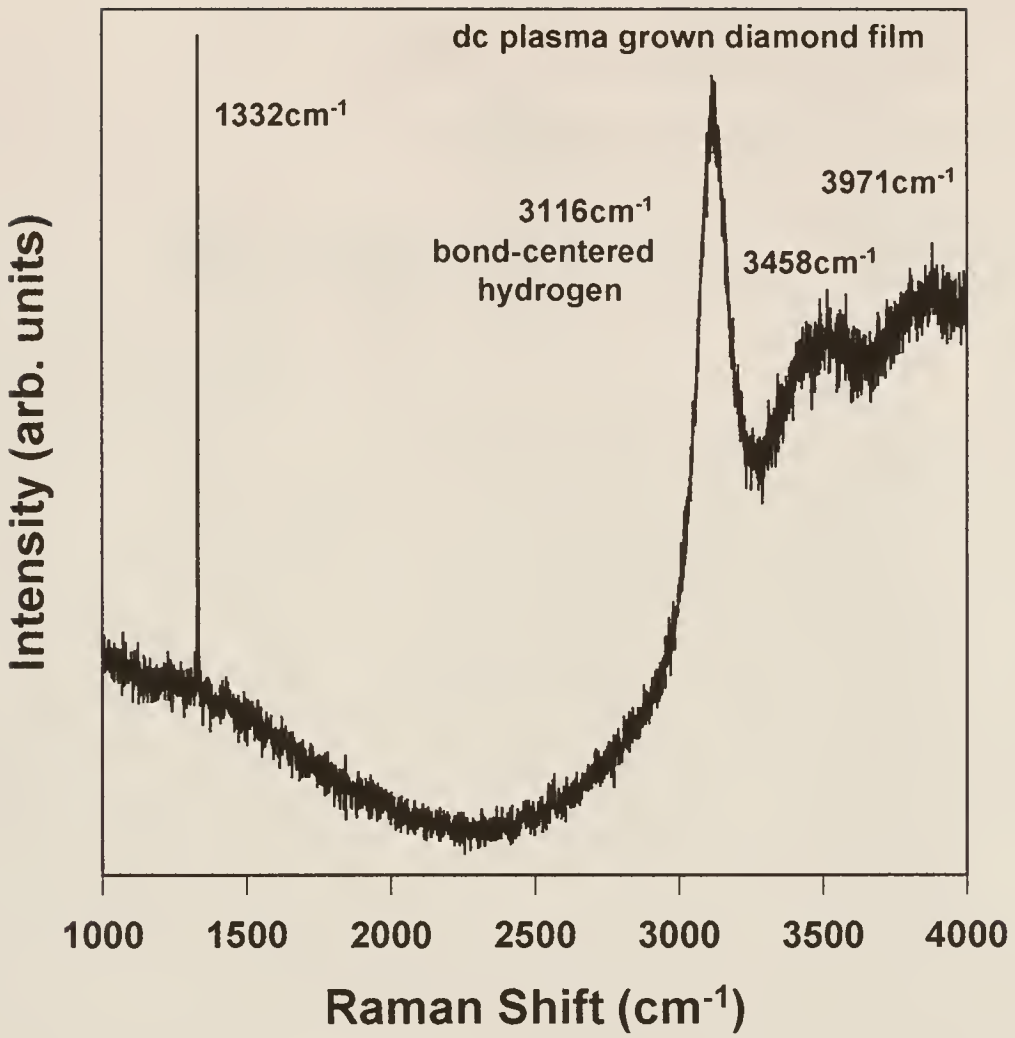

Figure 4.23 Raman spectrum exhibiting a peak from the bond-centered hydrogen defect ($3116cm^{-1}$). A diamond peak is also shown ($1332cm^{-1}$).

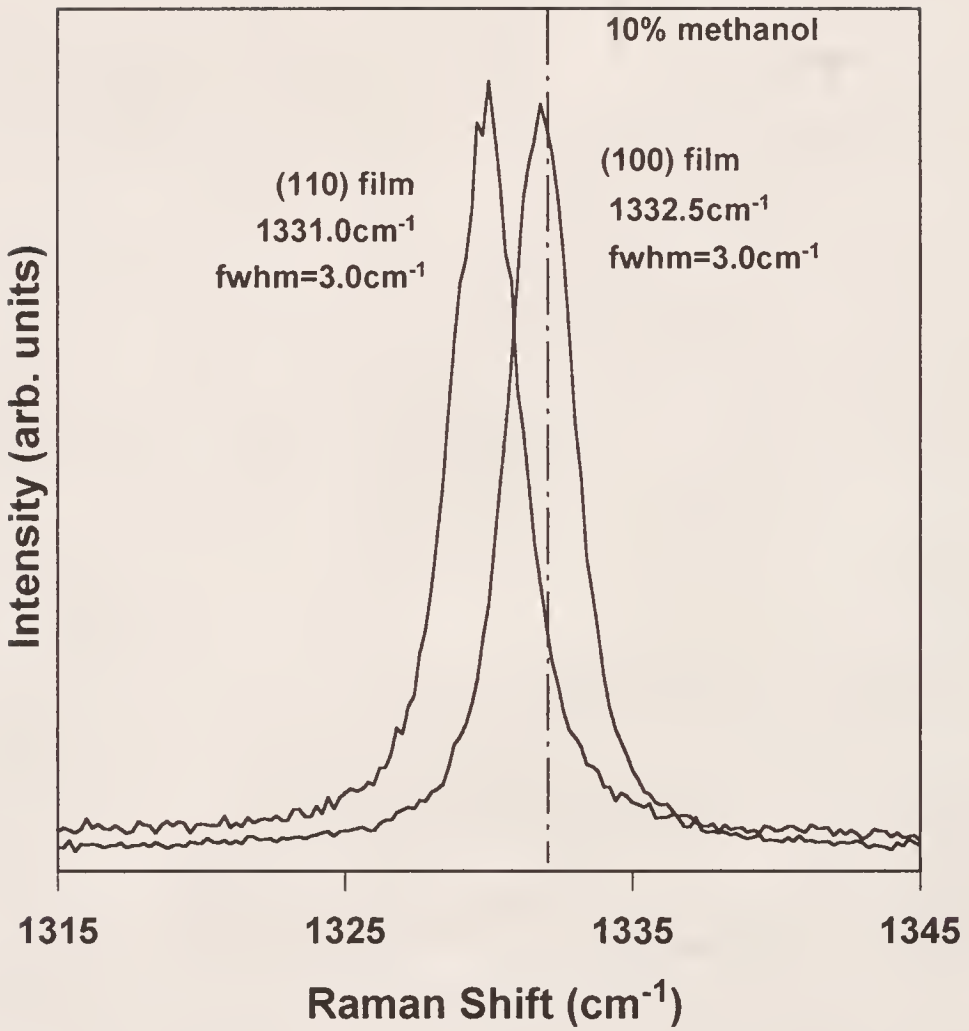

Figure 4.24 Raman spectrum from films grown with 10% methanol on (100) and (110) diamond substrates. The (110) film peak is shifted to lower wavenumbers (1331.0cm^{-1} versus 1332.5cm^{-1}) indicating tensile stress.

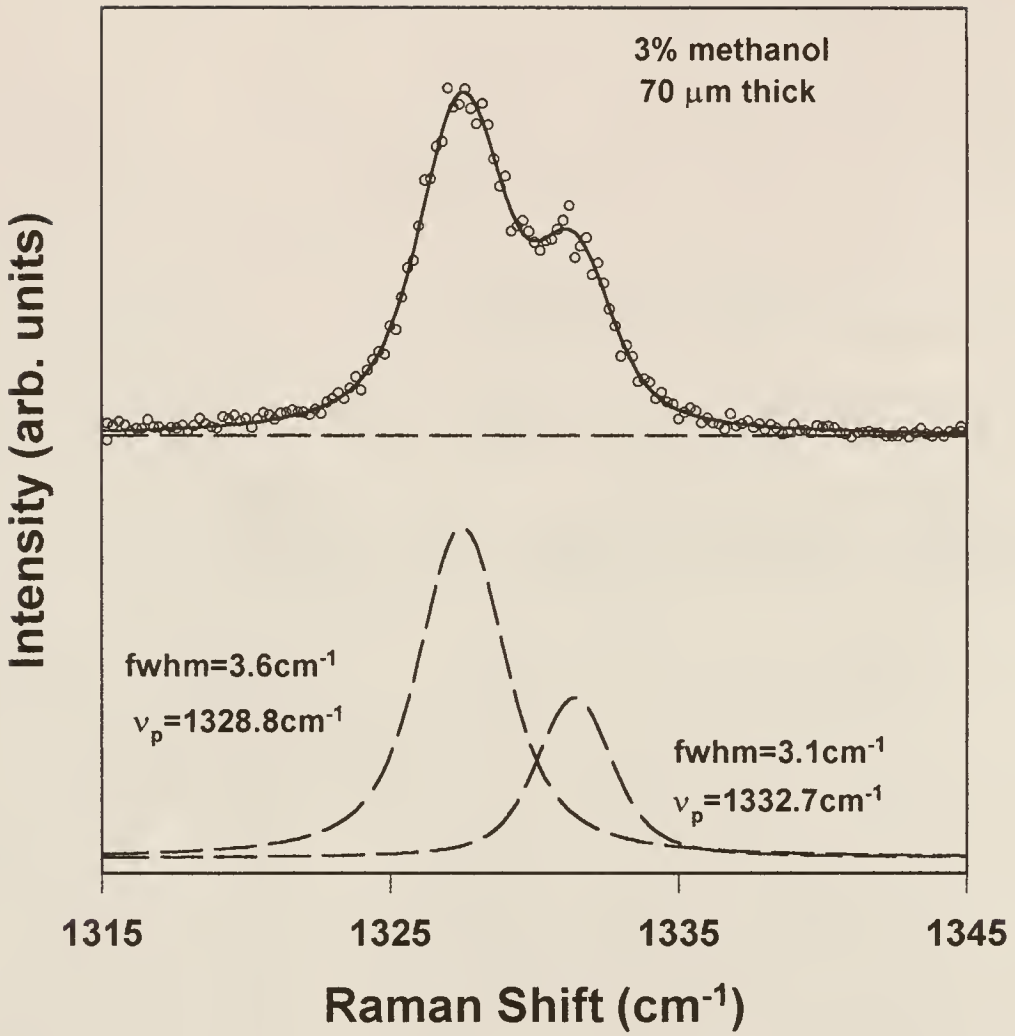

Figure 4.25 Raman spectrum from a 70μm thick film grown with 3% methanol on a (110) diamond substrate. The peak at lower wavenumbers (1328.8cm^{-1}) was from the film and the 1332.7cm^{-1} peak was from the substrate (spot 1).

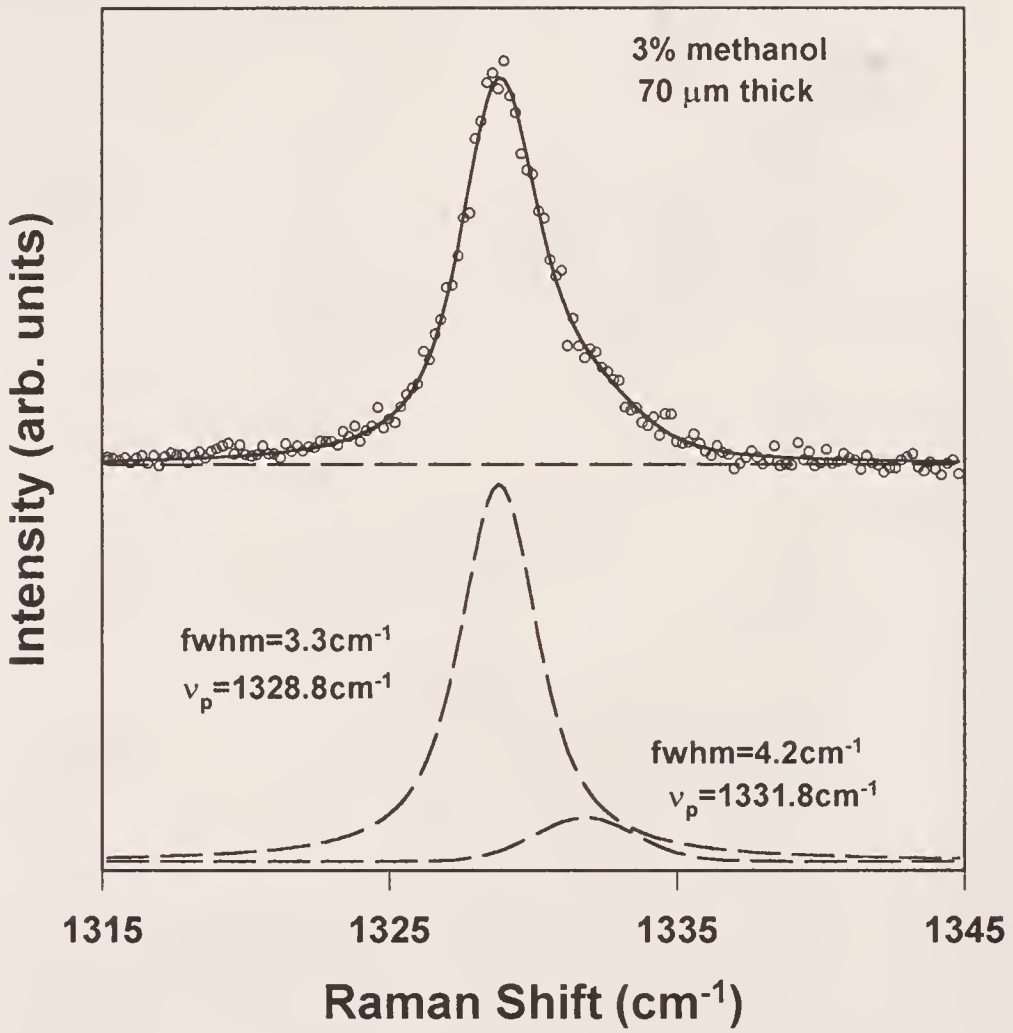

Figure 4.26 Raman spectrum from the same film and location (spot 1) as shown in Fig. 4.25. The increased film to substrate intensity ratio was obtained by using a pinhole aperture as discussed in Chapter 3.

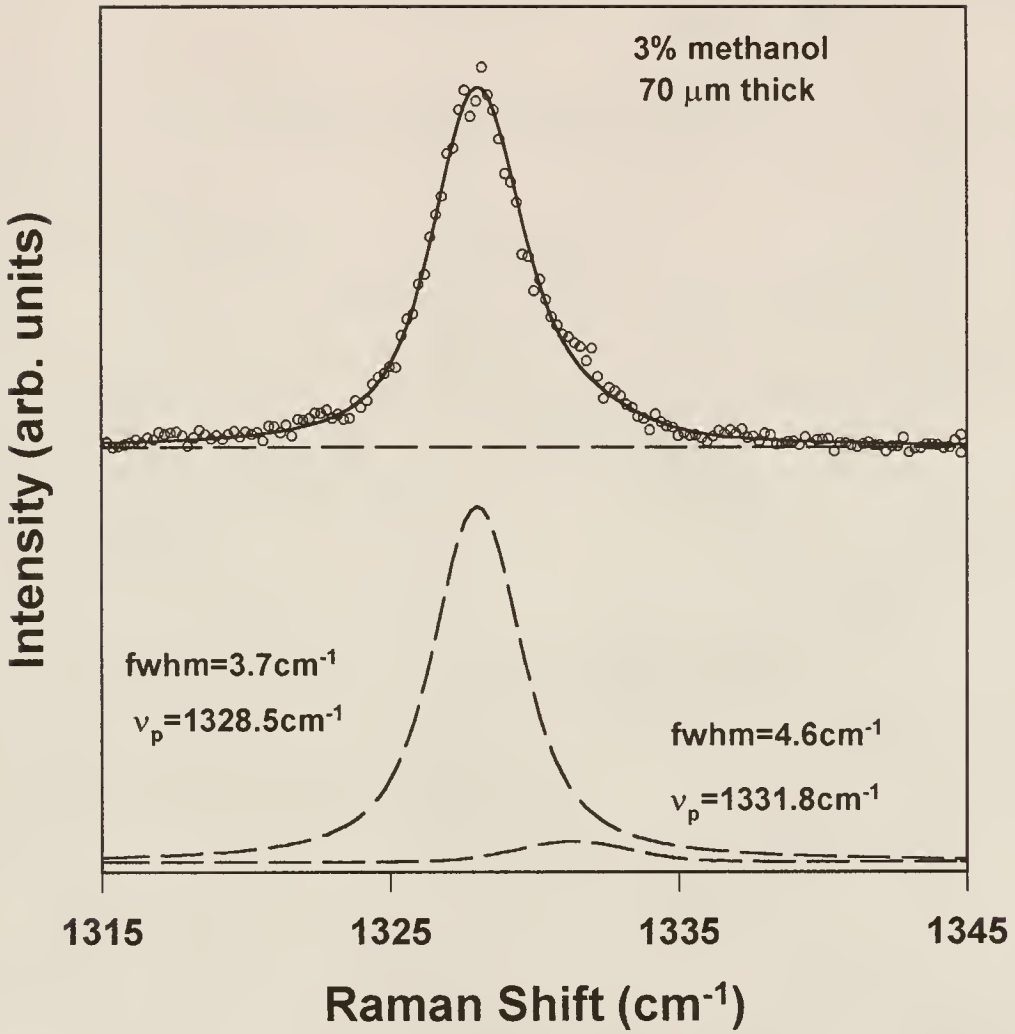

Figure 4.27 Raman spectrum from the same film as shown in Fig. 4.26, but from a second spot (spot 2).

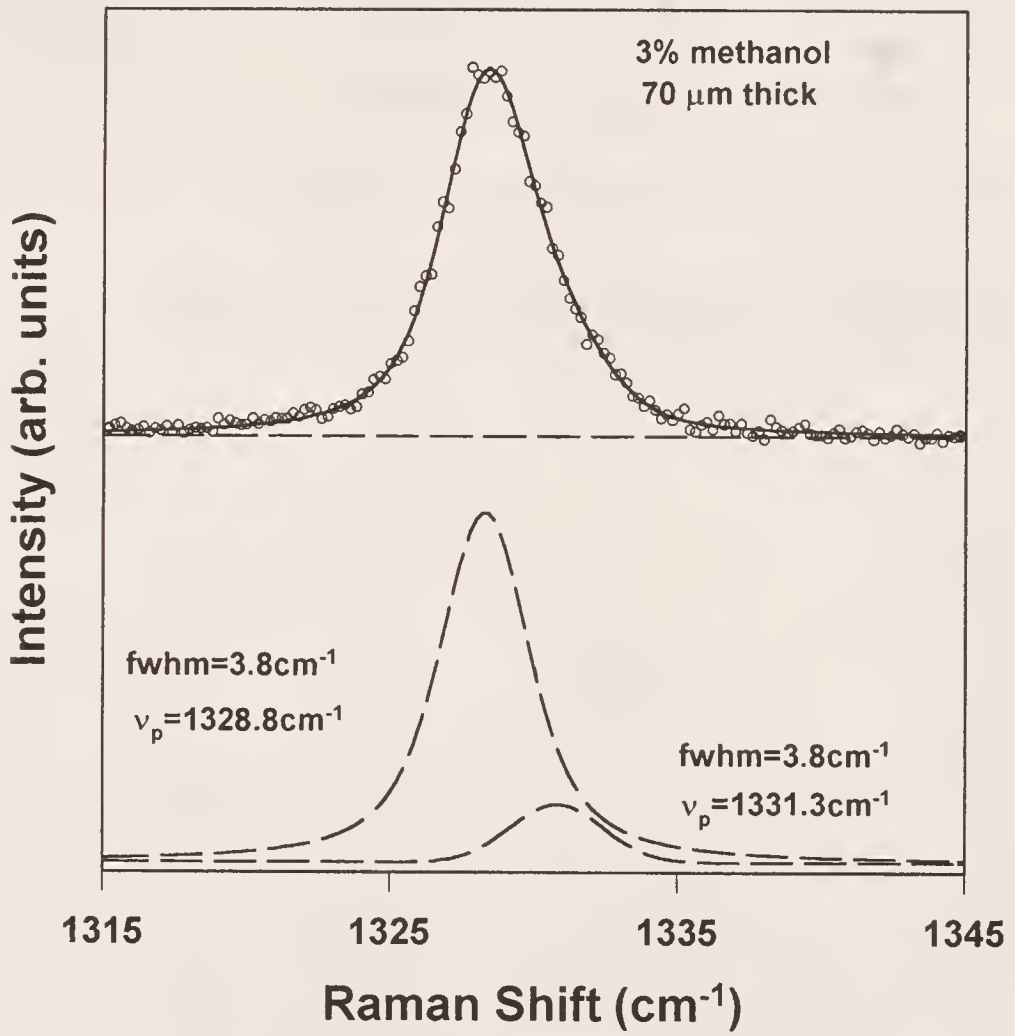

Figure 4.28 Raman spectrum from the same film as shown in Fig. 4.26, but from a third spot (spot 3).

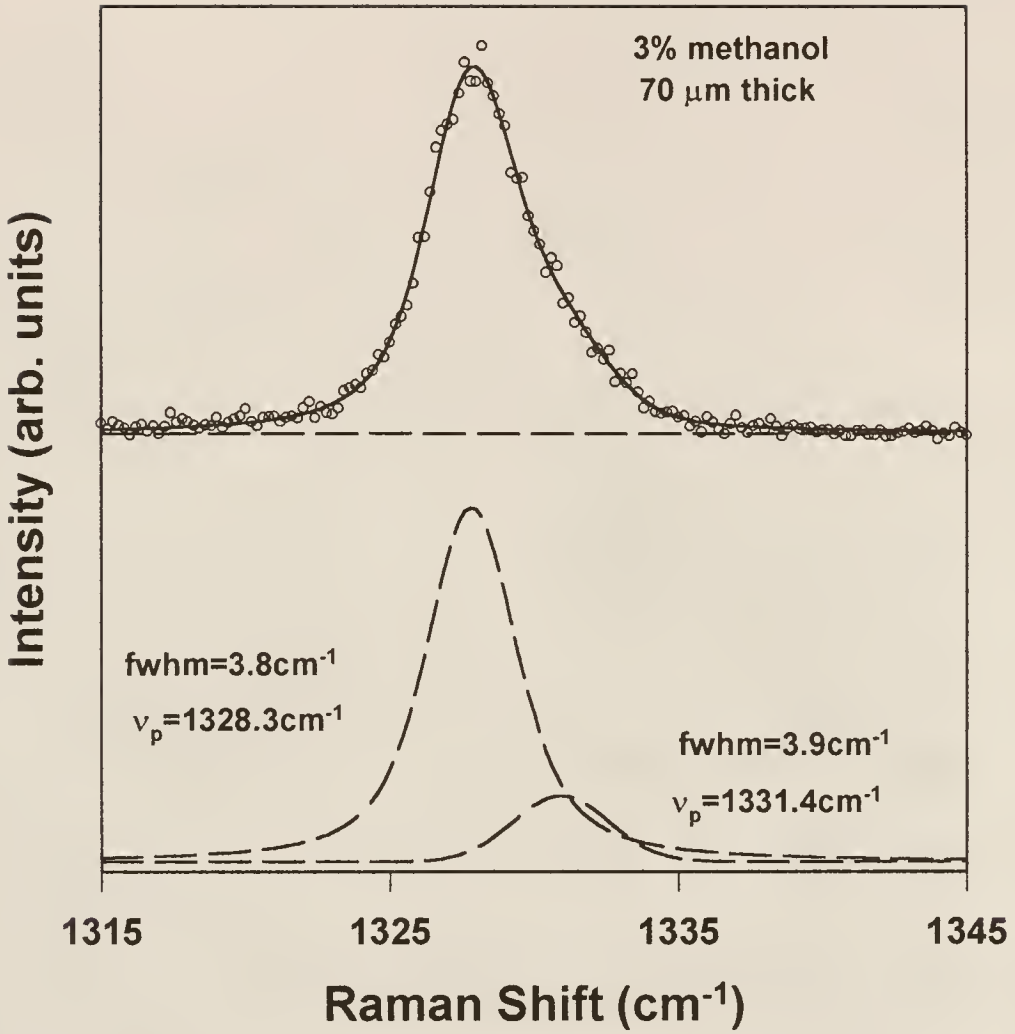

Figure 4.29 Raman spectrum from the same film as shown in Fig. 4.26, but from a forth spot (spot 4).

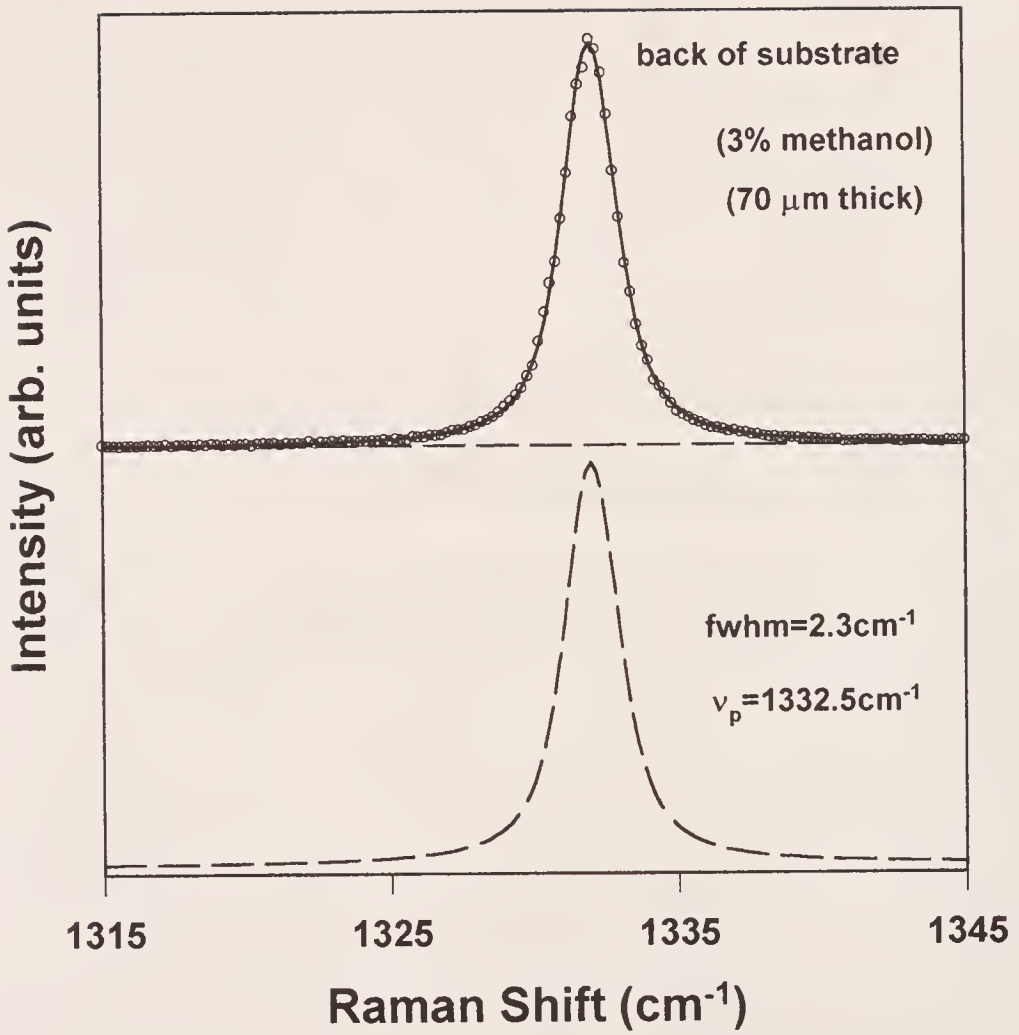

Figure 4.30 Raman spectrum from the back of the diamond substrate upon which with the film shown in Figs. 4.25-4.29.

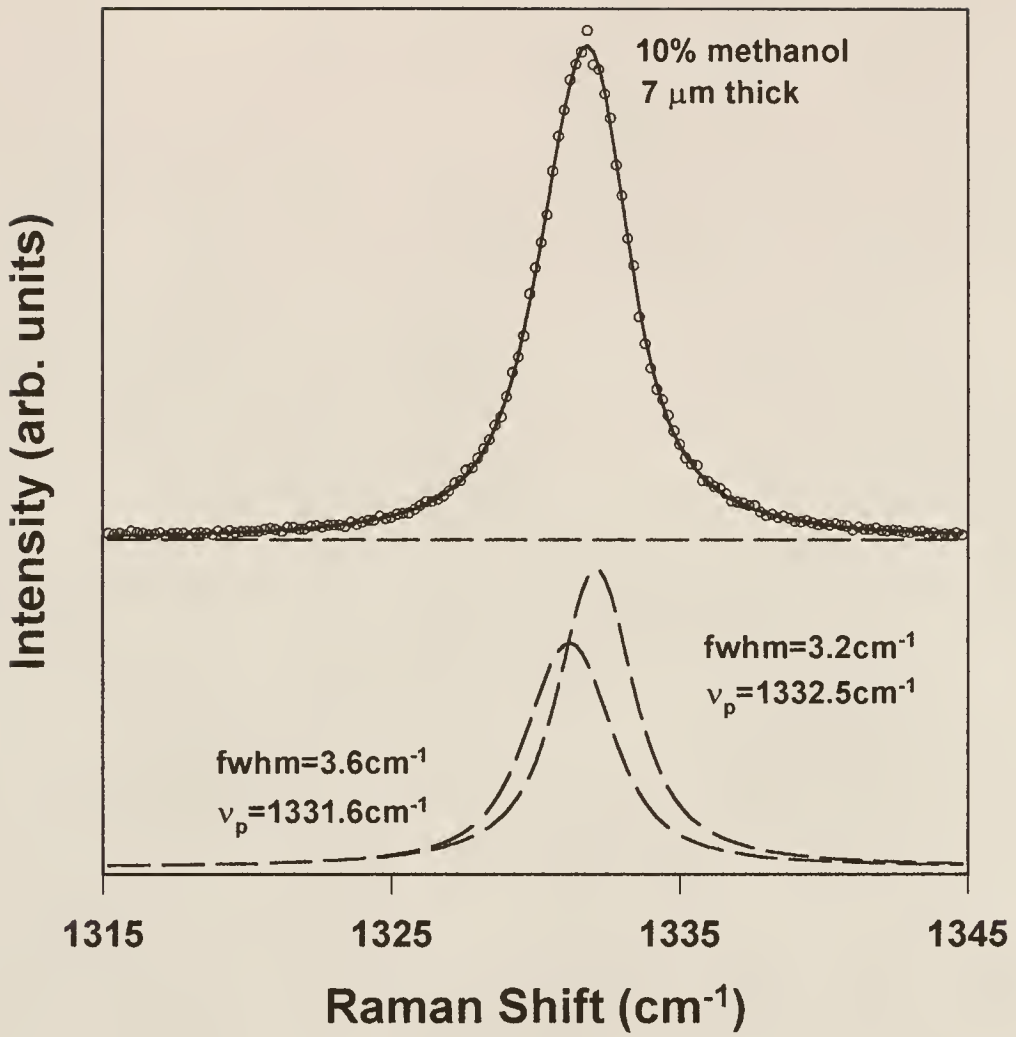

Figure 4.31 Raman spectrum from a 7μm thick film grown with 10% methanol on a (110) diamond substrate. The peak at lower wavenumbers (1331.6cm^{-1}) was from the film and the 1332.5cm^{-1} peak was from the substrate.

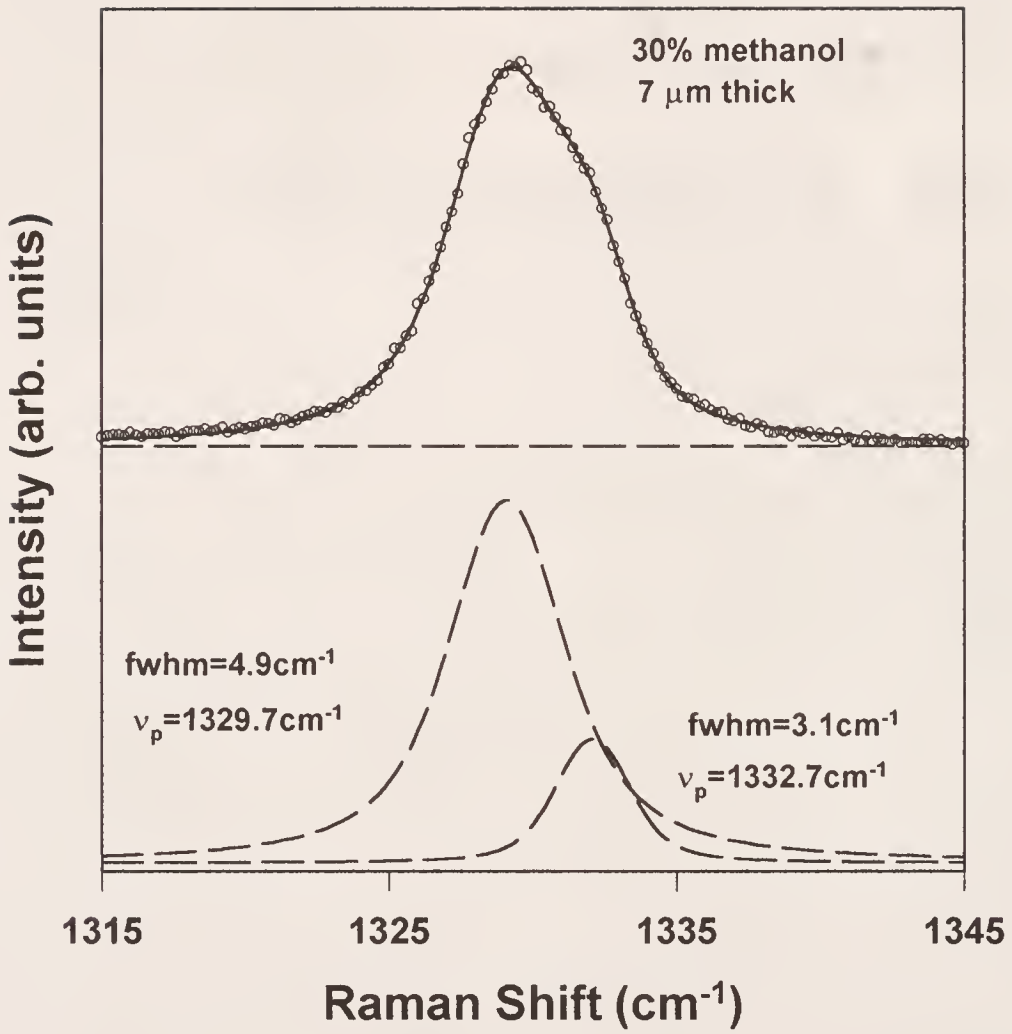

Figure 4.32 Raman spectrum from a 7μm thick film grown with 30% methanol on a (110) diamond substrate. The peak at lower wavenumbers (1329.7cm^{-1}) was from the film and the 1332.7cm^{-1} peak was from the substrate.

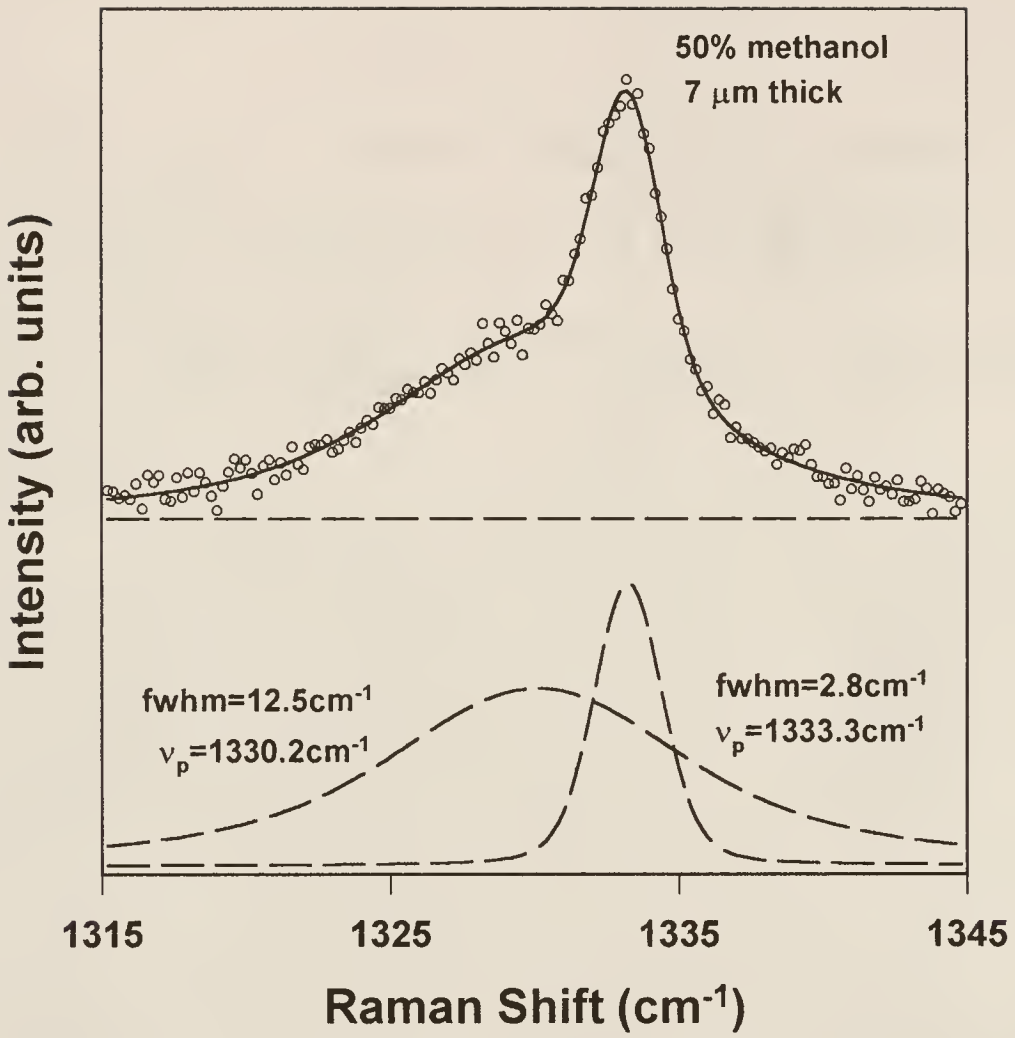

Figure 4.33 Raman spectrum from a 7μm thick film grown with 50% methanol on a (110) diamond substrate. The broad (12.5cm^{-1}) peak at lower wavenumbers (1330.2cm^{-1}) was from the film and the 1333.3cm^{-1} peak was from the substrate.

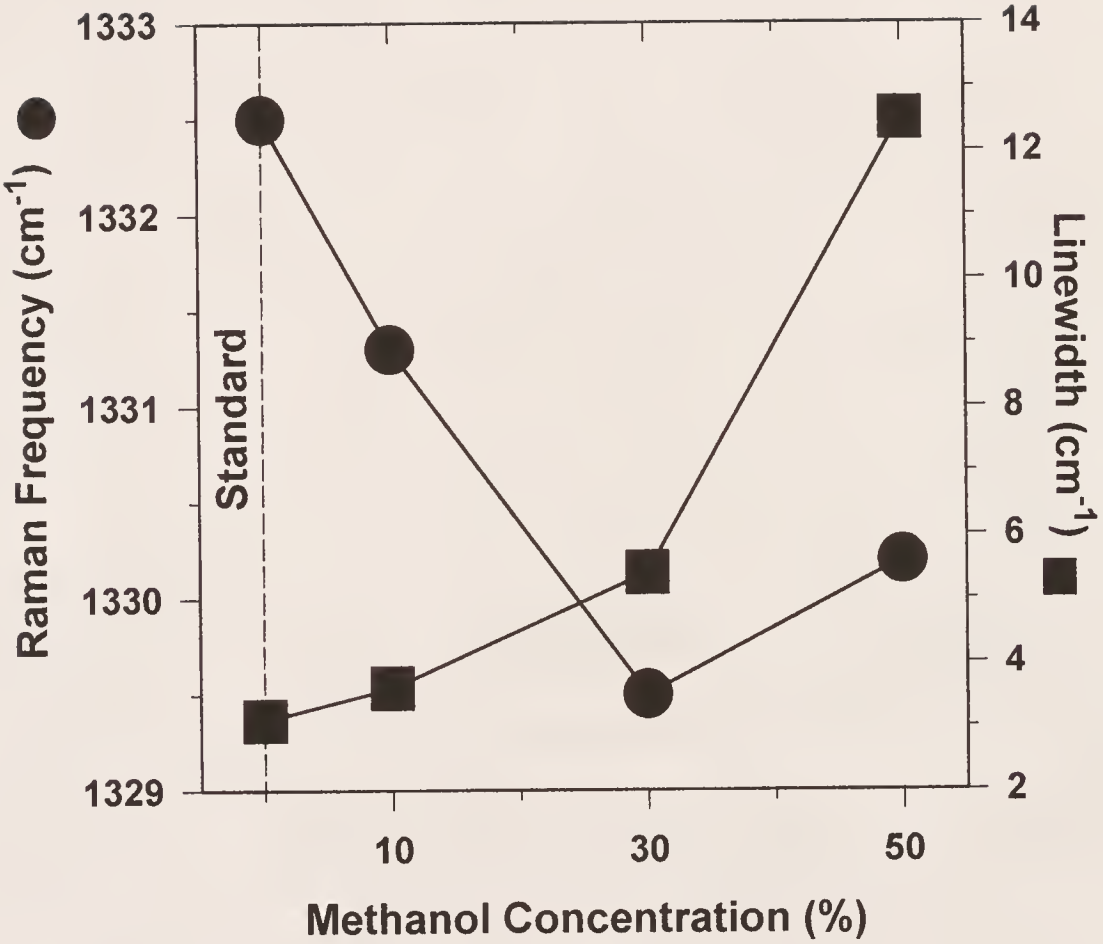

Figure 4.34 Position and FWHM of the diamond film Raman peaks versus methanol concentration for 7μm thick films on (110) substrates. The peak position decreased with increased methanol concentration indicating tensile stress. The 50% methanol film was cracked and demonstrated partial stress relief. The FWHM of the diamond peak increased with increased methanol concentration indicating a variation in stress in the sampling area.

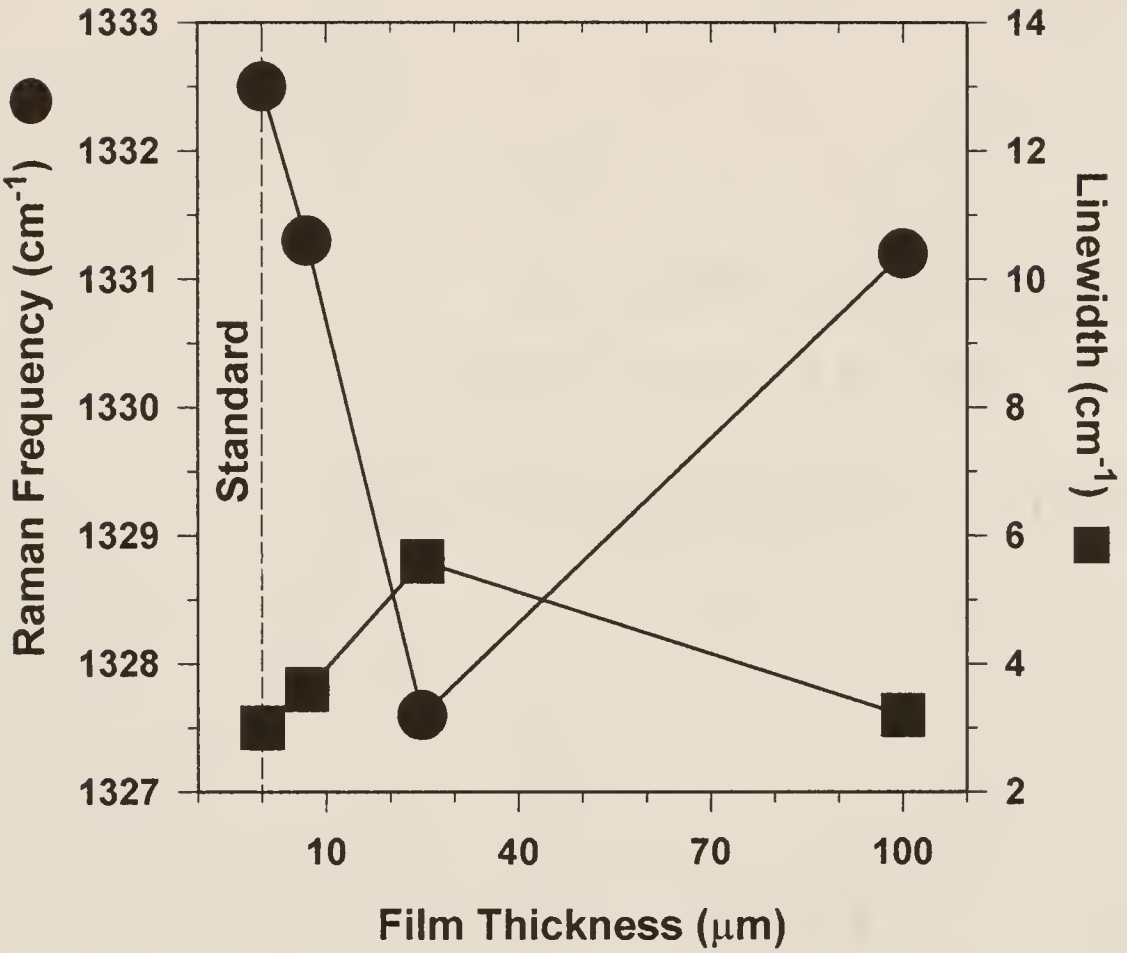

Figure 4.35 Position and FWHM of the diamond film Raman peaks versus film thickness for films grown with 10% methanol. The peak position decreased with increased film thickness indicating tensile stress. The 100μm thick film was cracked and demonstrated partial stress relief. The FWHM of the diamond peak increased with increased film thickness indicating a distribution of stress in the sampling area, except for the 100μm thick film which exhibits a FWHM similar to the 7μm thick film.

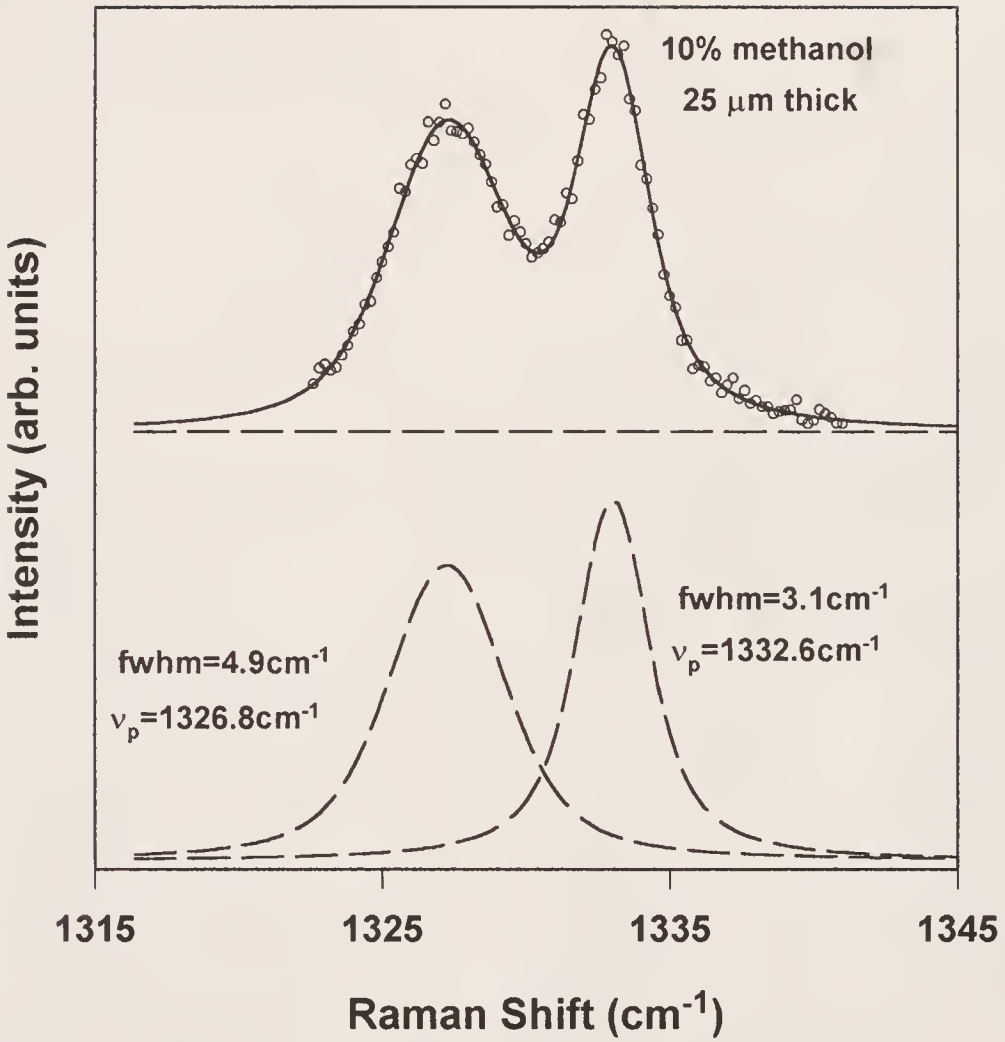

Figure 4.36 Raman spectrum from a 25μm thick film grown with 10% methanol on a (110) diamond substrate. The peak at lower wavenumbers (1326.8cm^{-1}) was from the film and the 1332.6cm^{-1} peak was from the substrate. This film exhibited the largest peak shift.

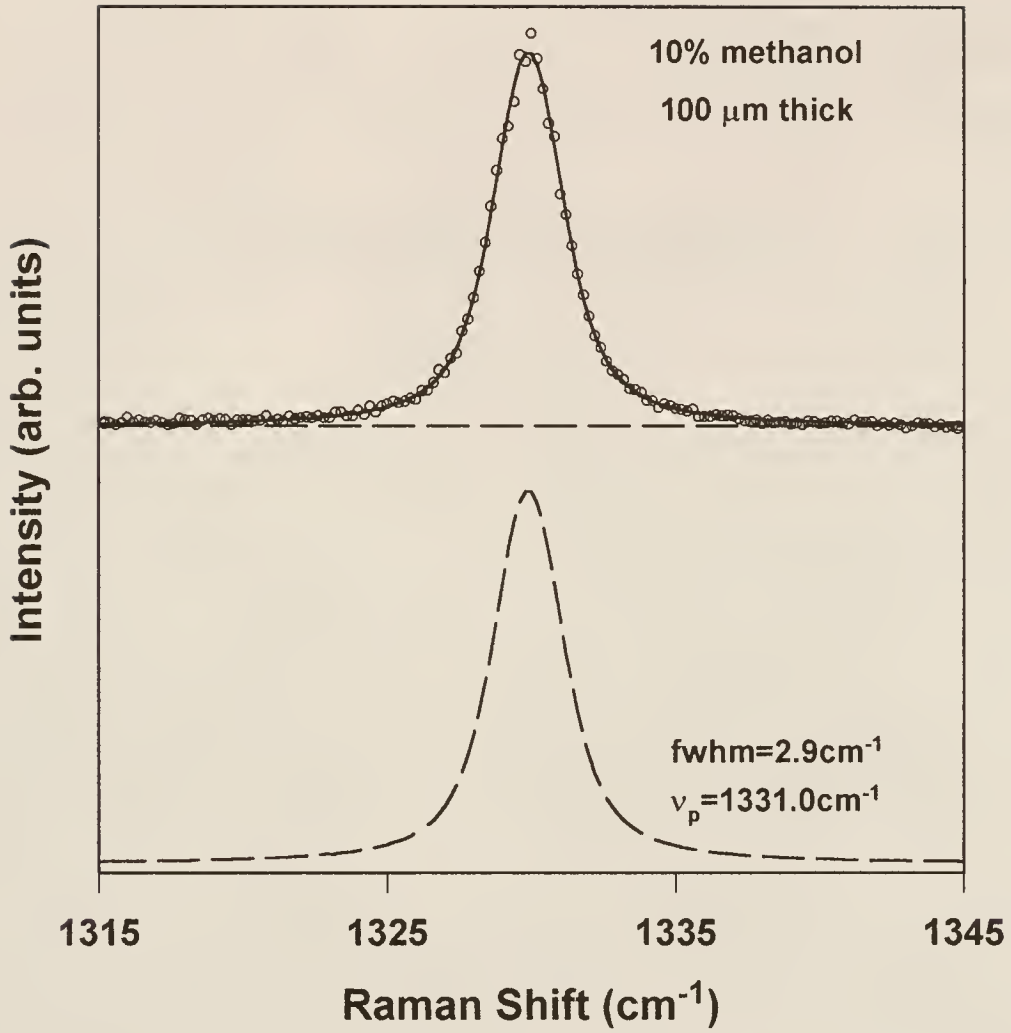

Figure 4.37 Raman spectrum from a 100μm thick film grown with 10% methanol on a (110) diamond substrate. Only the film (1331.0cm^{-1}) peak was detected due to the thickness of the film.

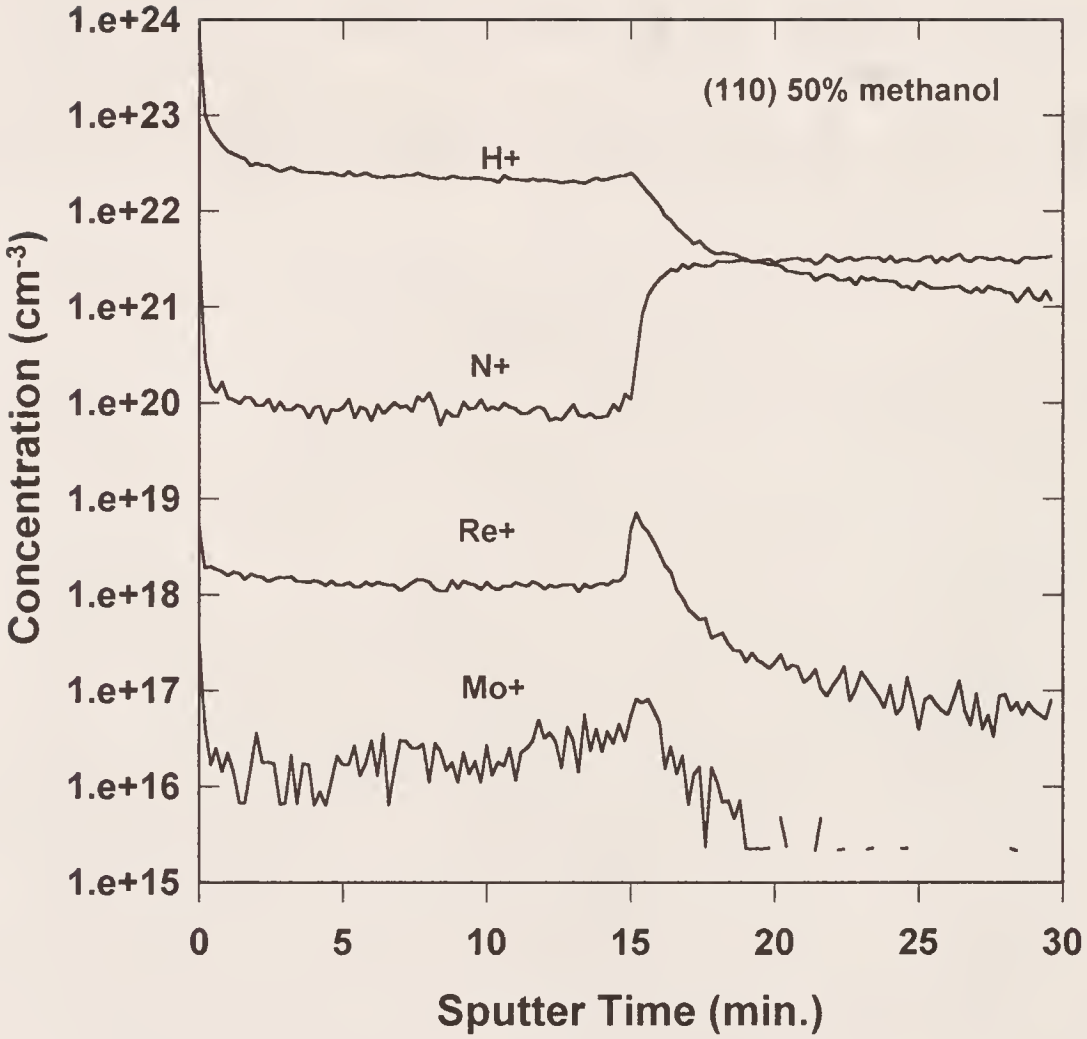

Figure 4.38 SIMS depth profile from O_2+ sputtering of a (110) 50% methanol film.

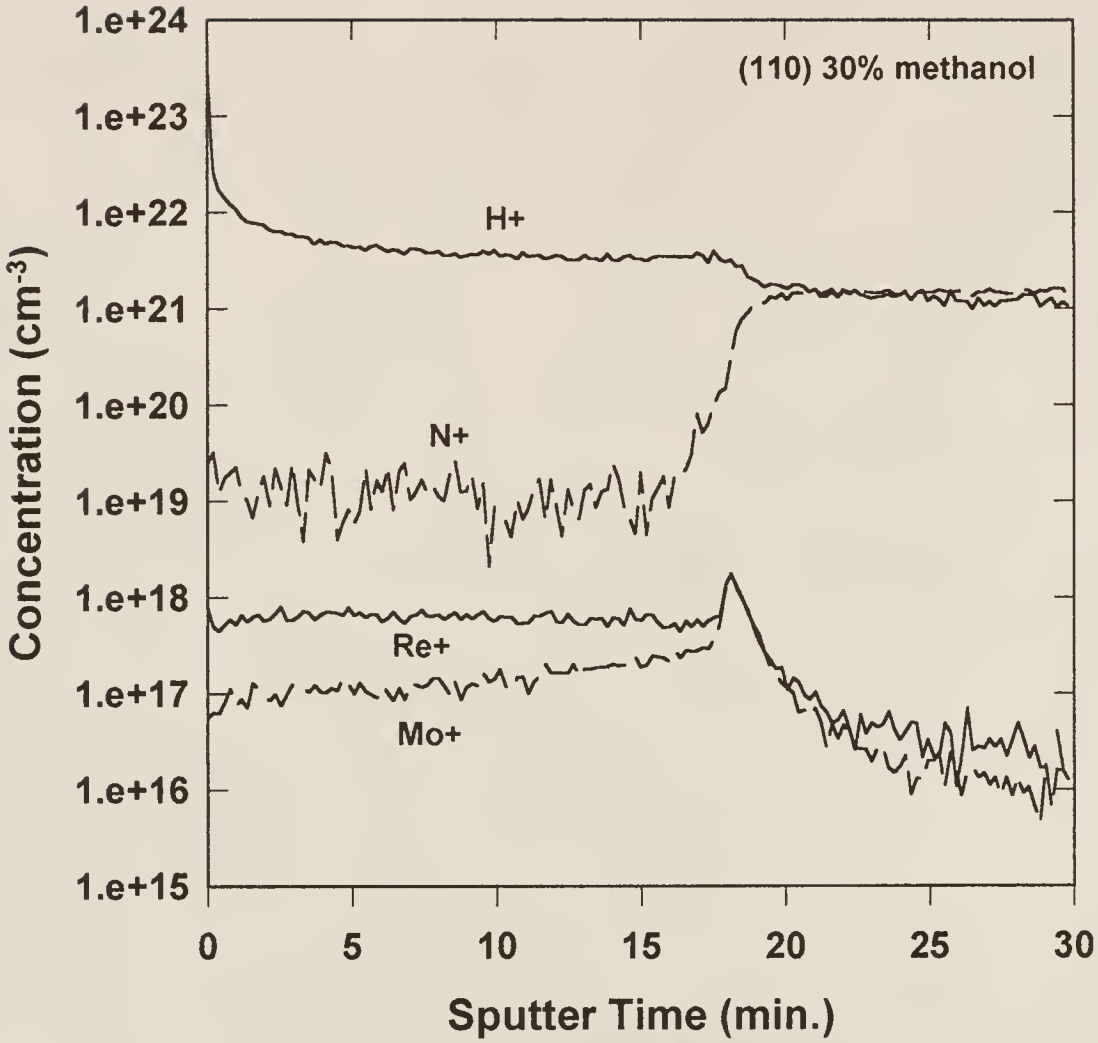

Figure 4.39 SIMS depth profile from O_2+ sputtering of a (110) 30% methanol film.

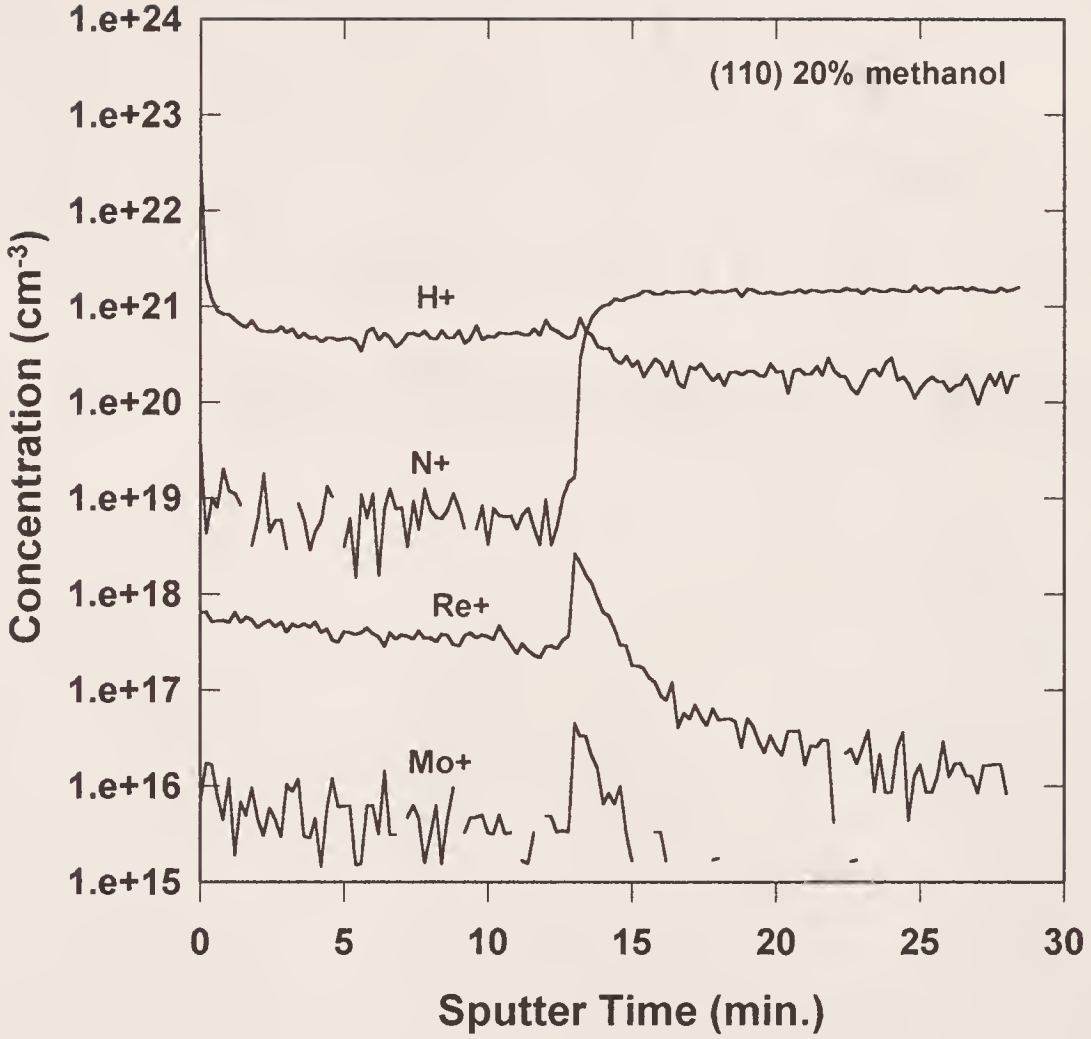

Figure 4.40 SIMS depth profile from O_2+ sputtering of a (110) 20% methanol film.

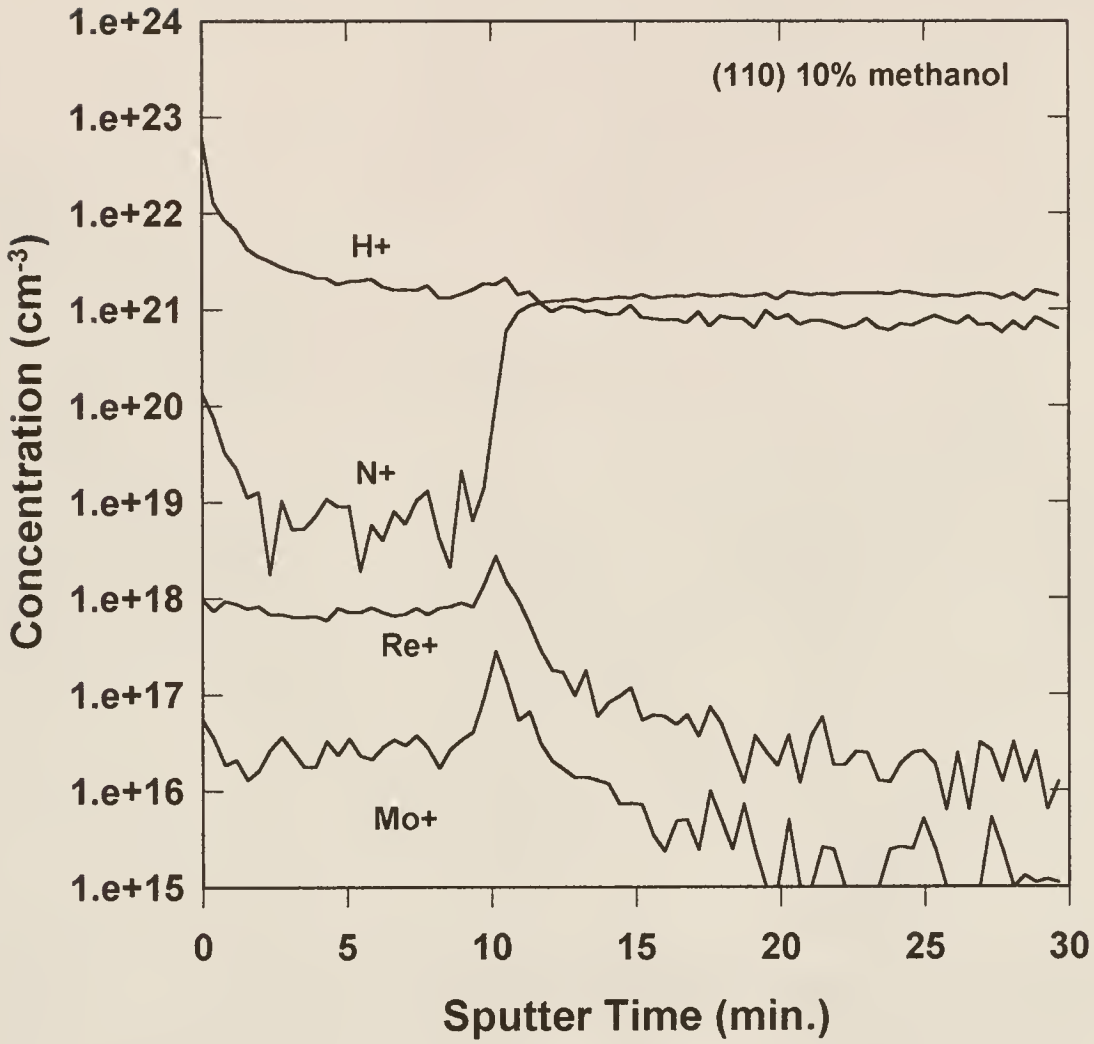

Figure 4.41 SIMS depth profile from O_2+ sputtering of a (110) 10% methanol film.

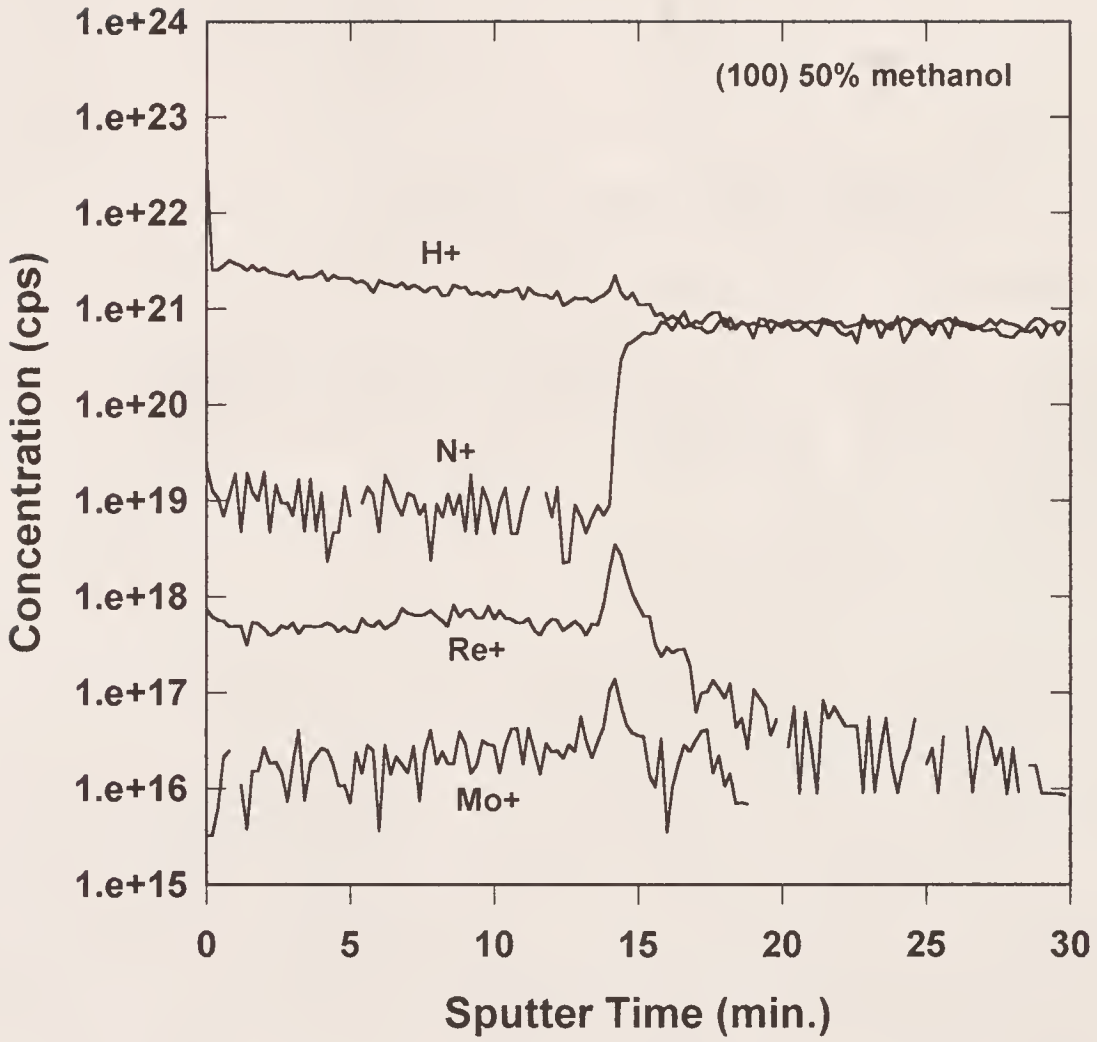

Figure 4.42 SIMS depth profile from O_2+ sputtering of a (100) 50% methanol film.

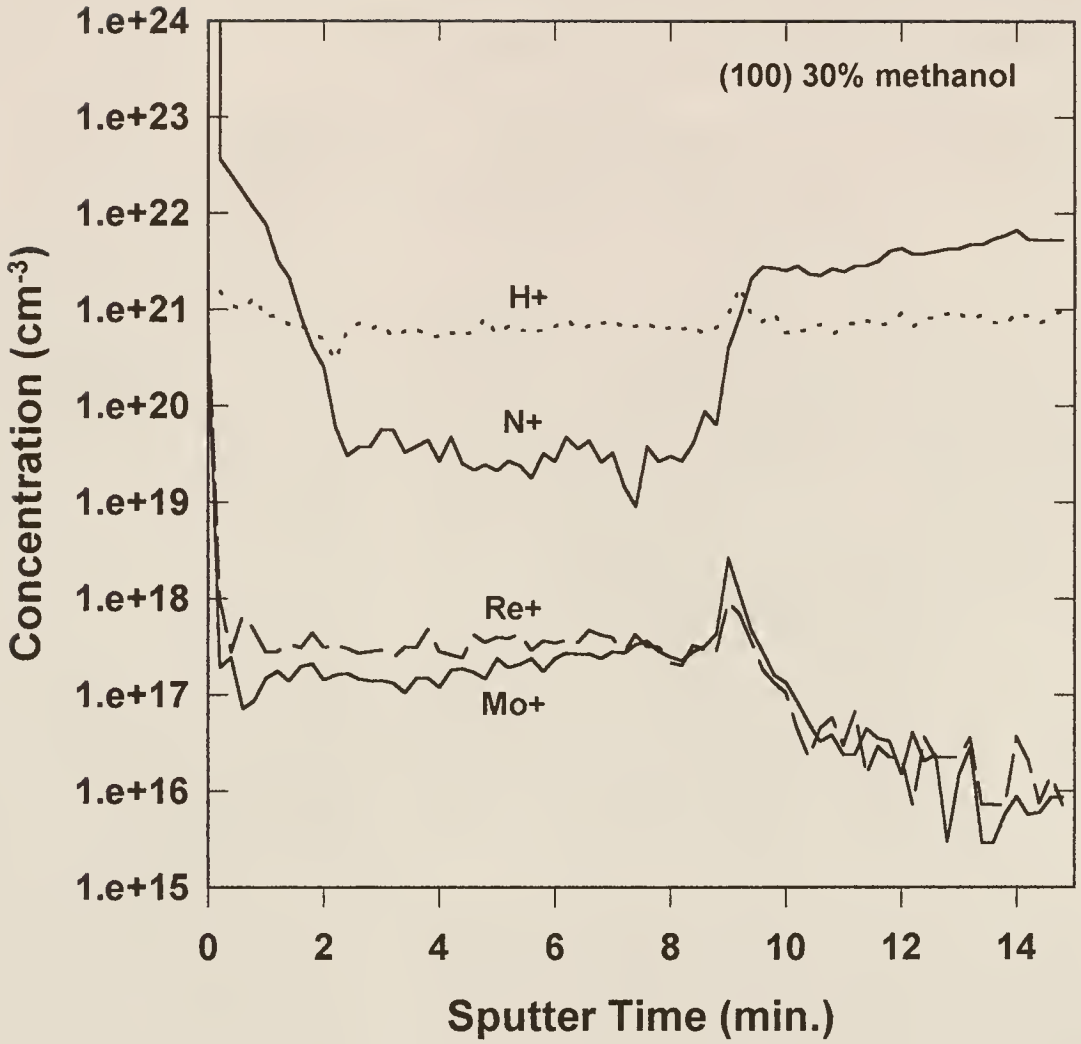

Figure 4.43 SIMS depth profile from O_2+ sputtering of a (100) 30% methanol film.

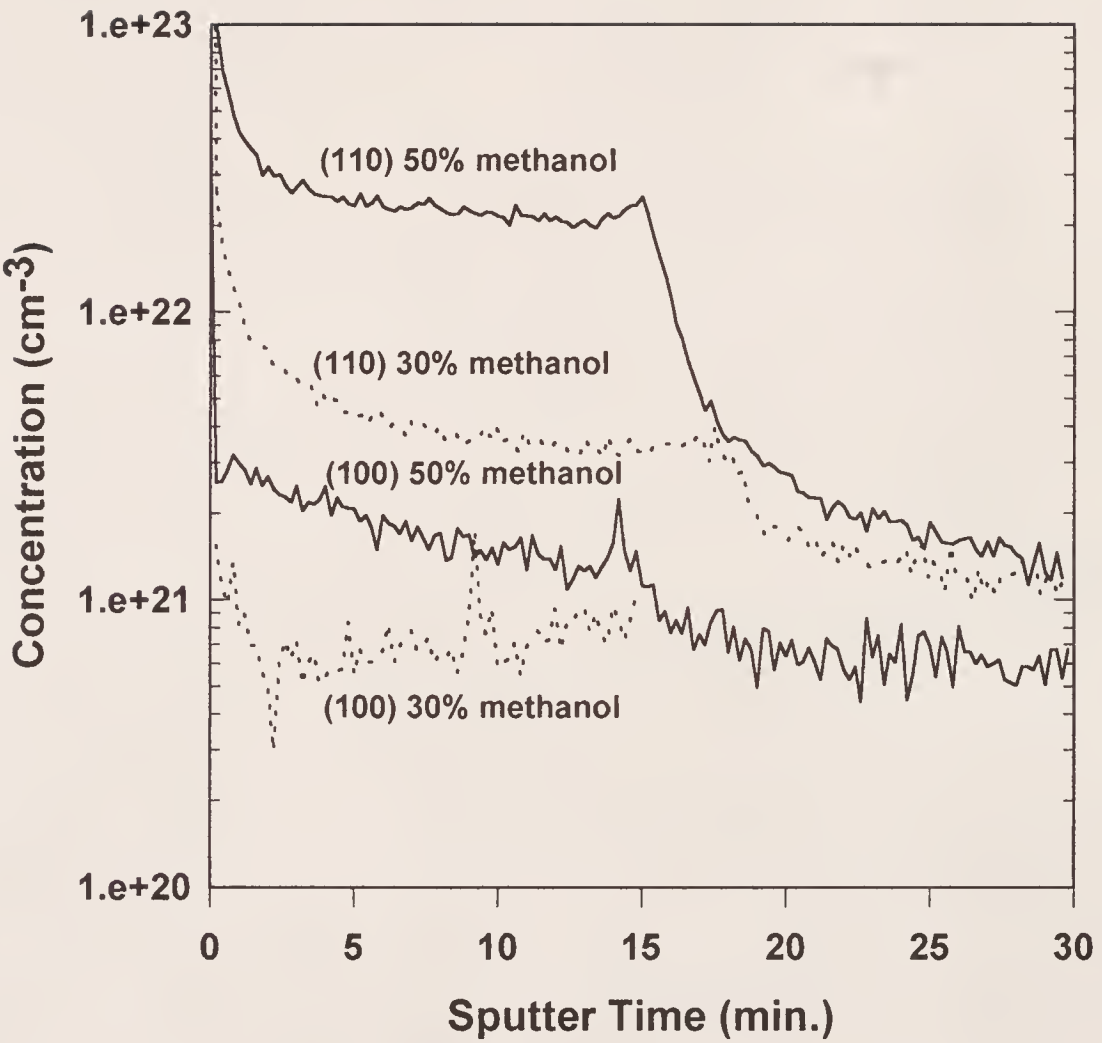

Figure 4.44 Hydrogen concentrations from (100) and (110) films grown with 30 and 50% methanol.

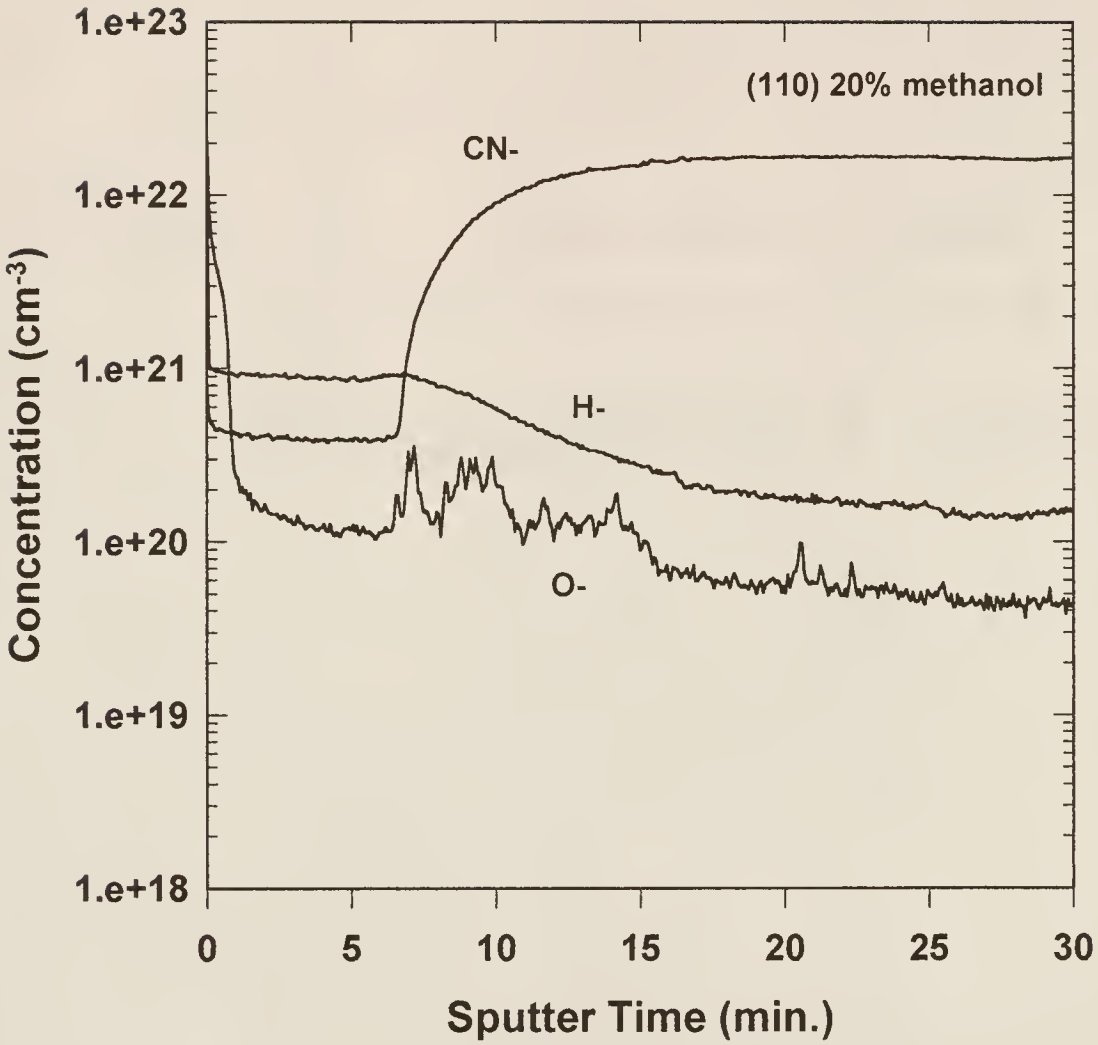

Figure 4.45 SIMS depth profile from Cs+ sputtering of a (110) 20% methanol film.

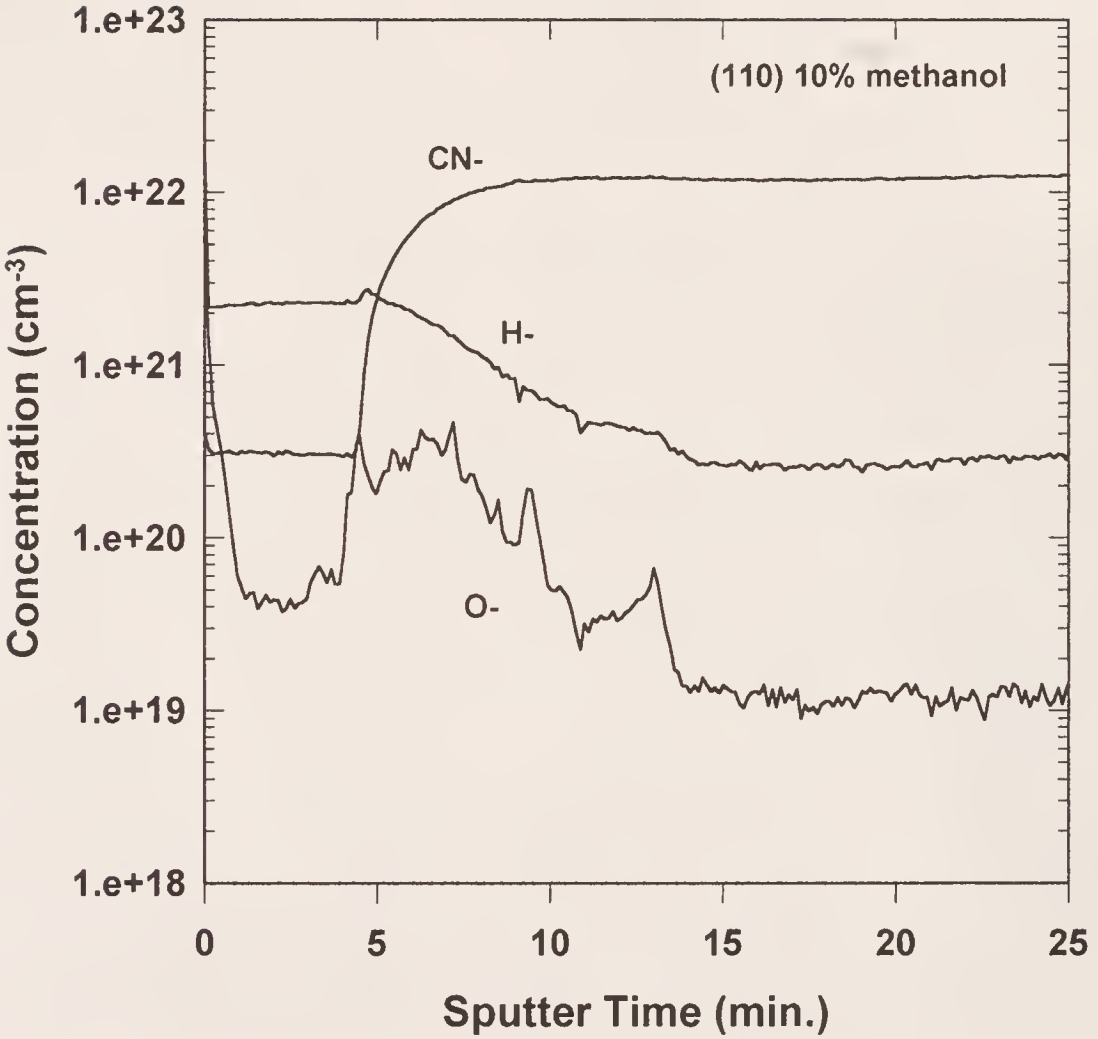

Figure 4.46 SIMS depth profile from Cs+ sputtering of a (110) 10% methanol film.

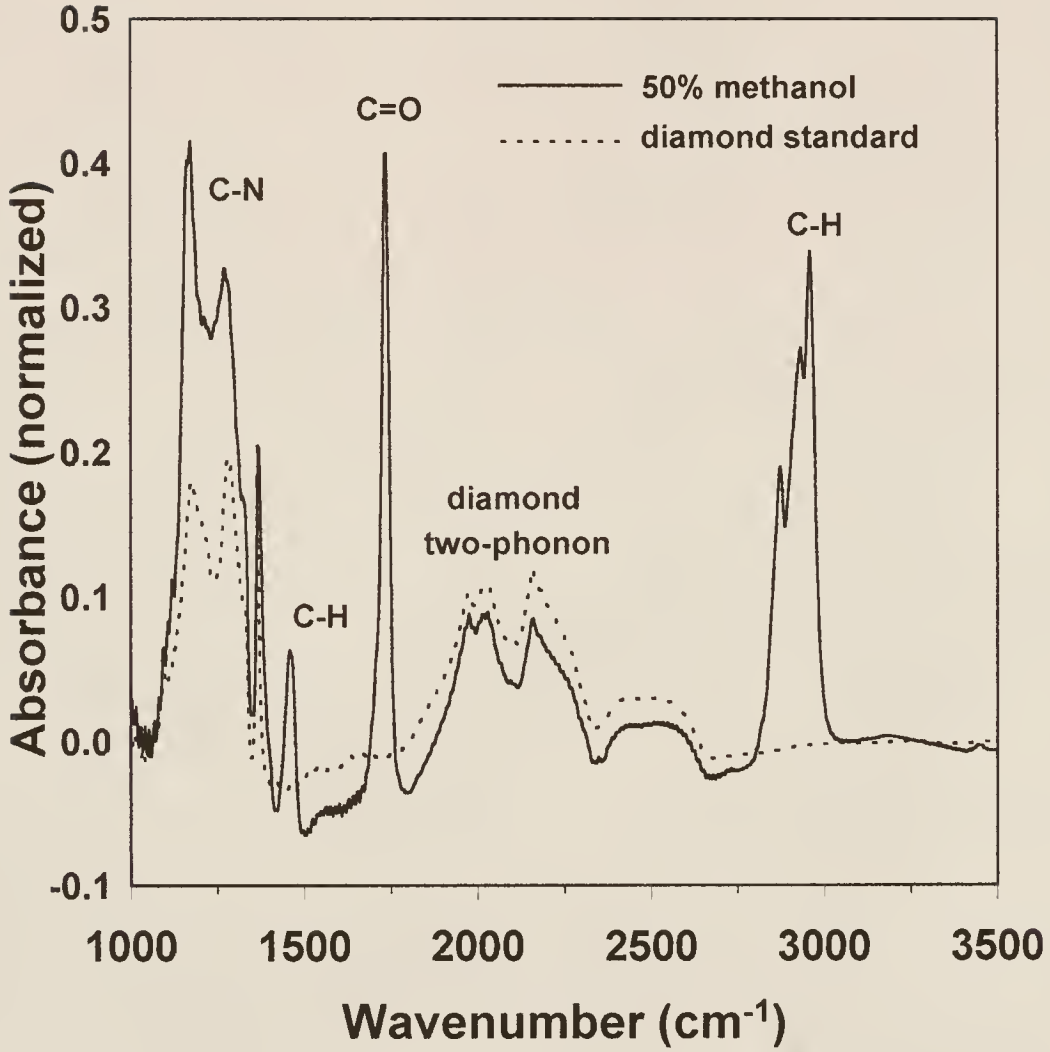

Figure 4.47 FTIR absorption spectra of a natural diamond substrate and a 50% methanol (110) film.

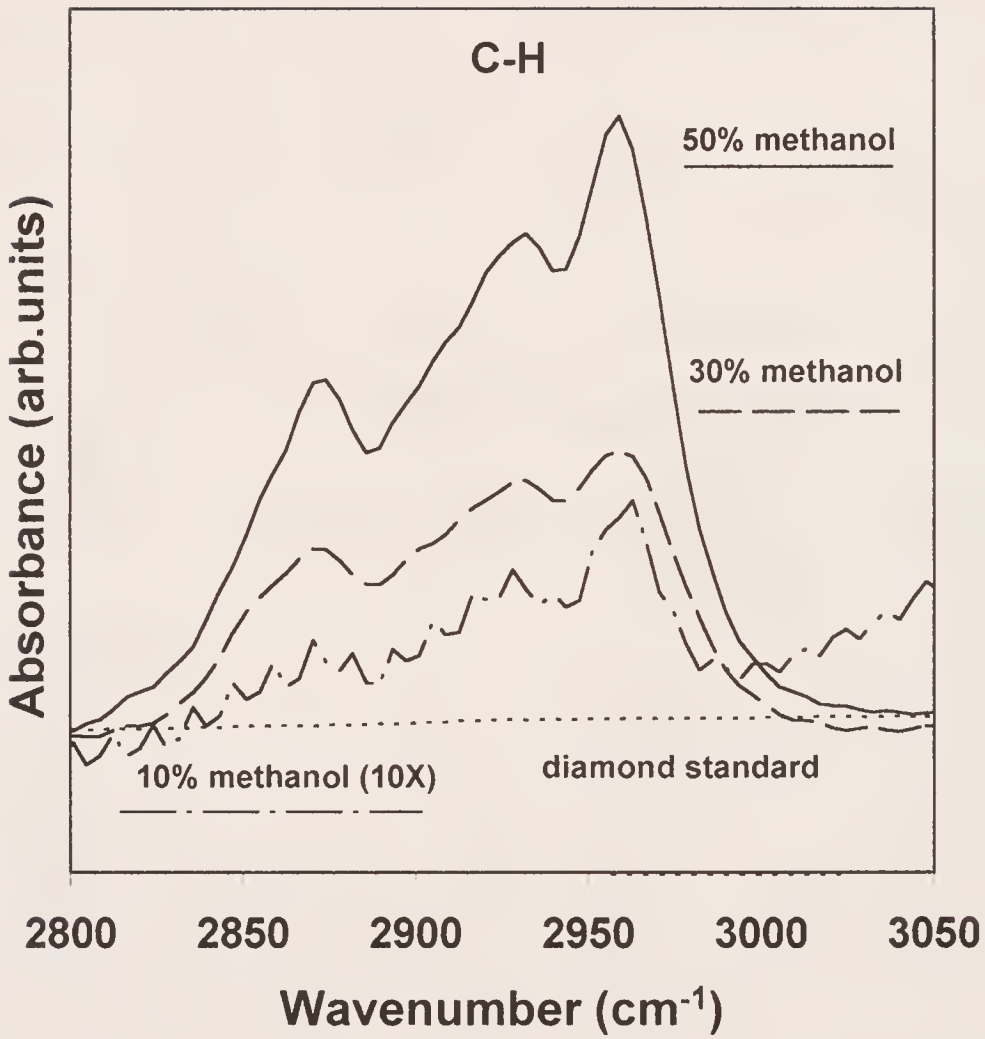

Figure 4.48 FTIR absorption spectra of a natural diamond substrate and 10, 30, and 50% methanol (110) films. The broad absorption band is due to C-H vibration.

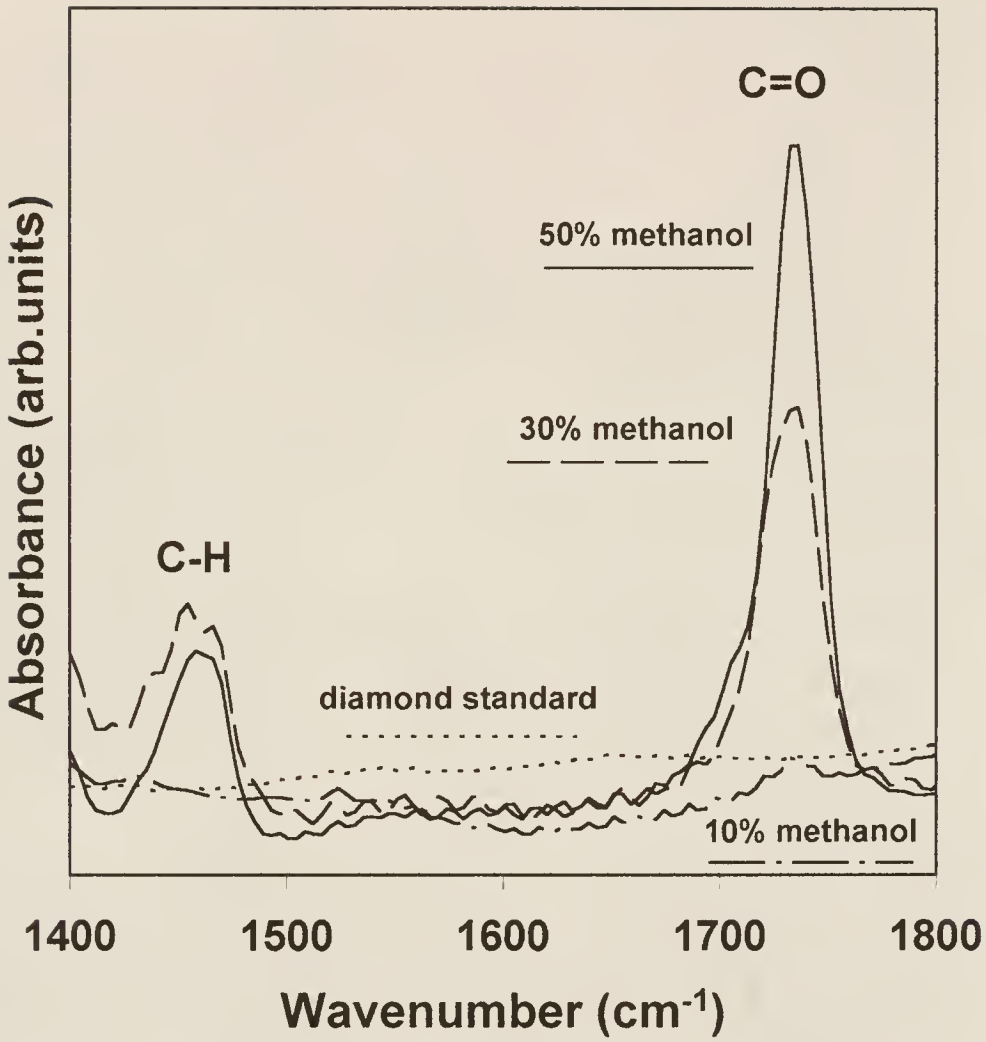

Figure 4.49 FTIR absorption spectra of a natural diamond substrate and 10, 30, and 50% methanol (110) films. The absorption bands at ~1460cm^{-1} and ~1735cm^{-1} are from the C-H and C=O vibration, respectively.

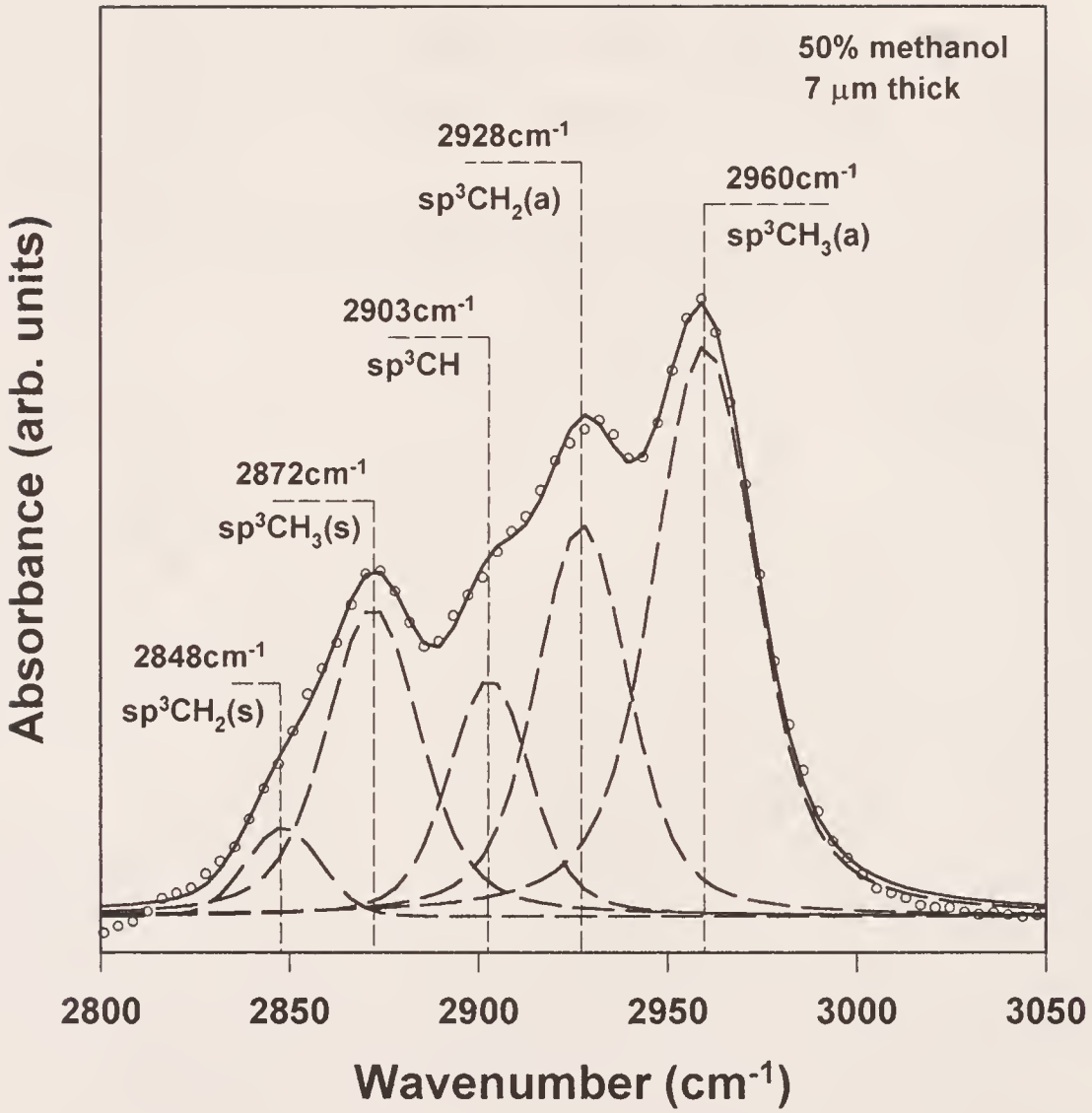

Figure 4.50 Voight curve fit of the C-H absorption band from the 50% methanol film shown in Fig. 4.48. The C-H absorption band was fit with 5 peaks.

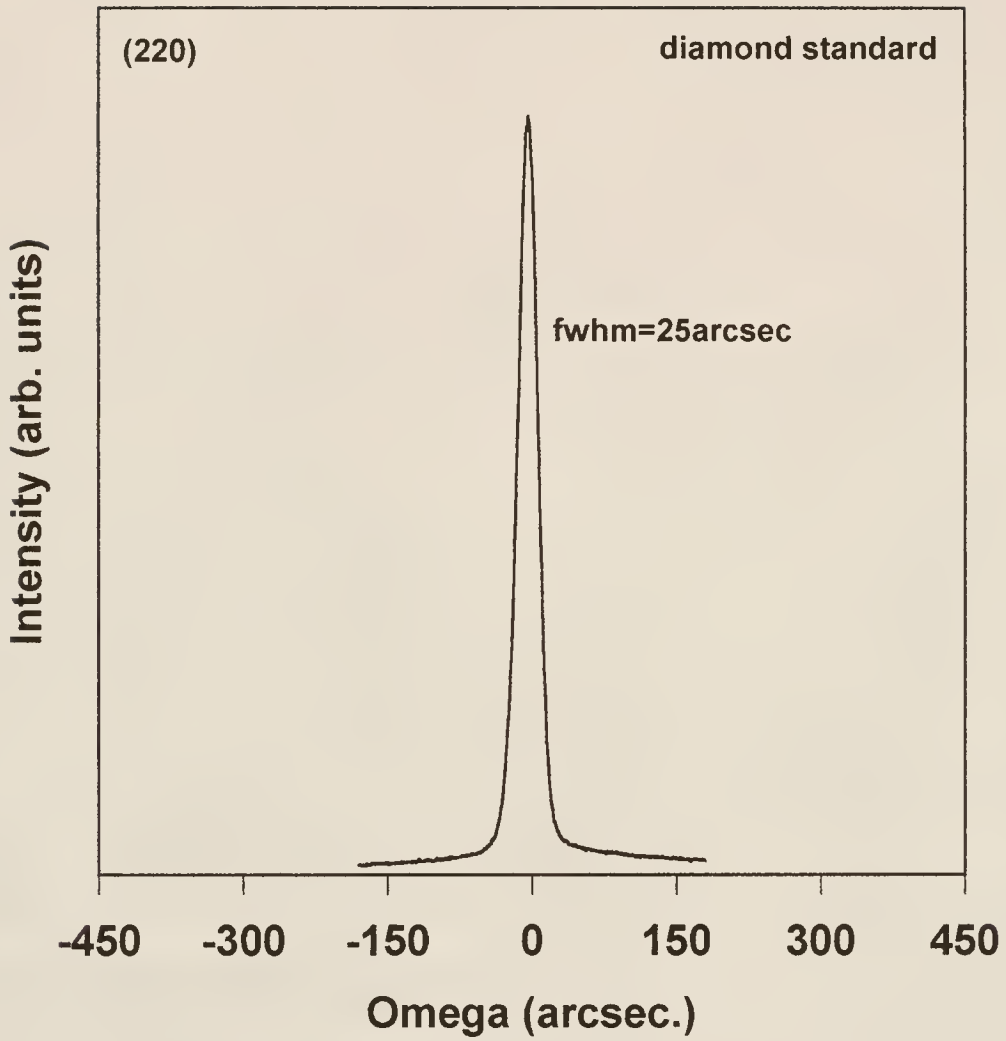

Figure 4.51 The (220) x-ray rocking curve from a (110) diamond substrate.

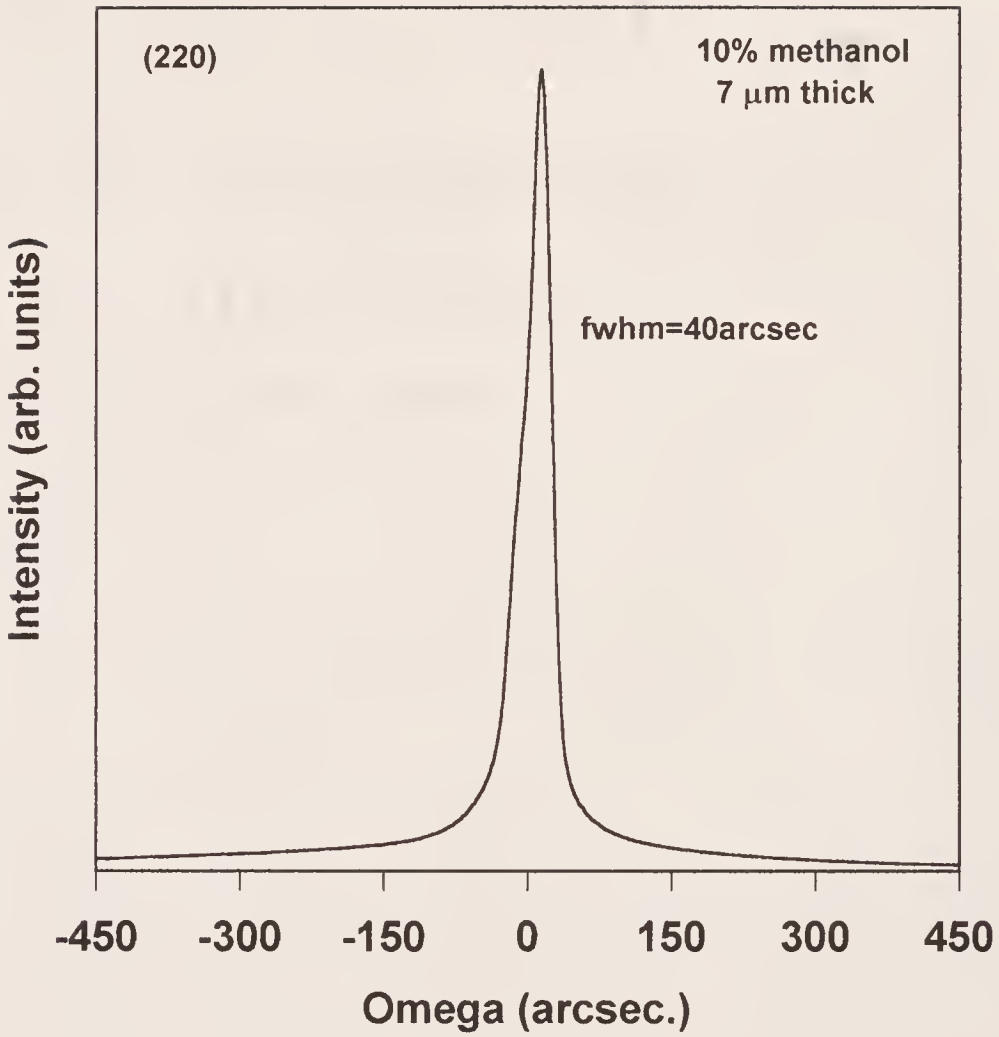

Figure 4.52 The (220) x-ray rocking curve from a 7μm thick 10% methanol film on a (110) diamond substrate.

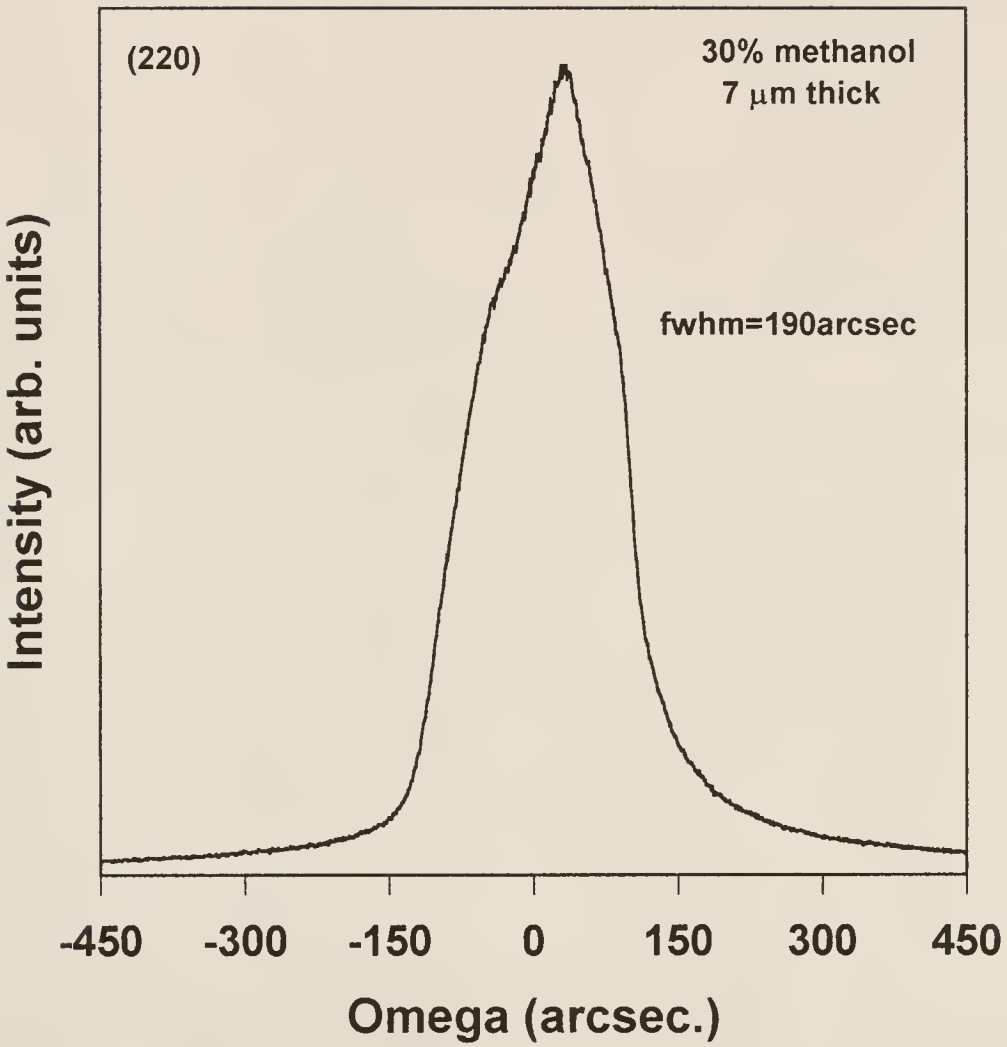

Figure 4.53 The (220) x-ray rocking curve from a 7μm thick 30% methanol film on a (110) diamond substrate.

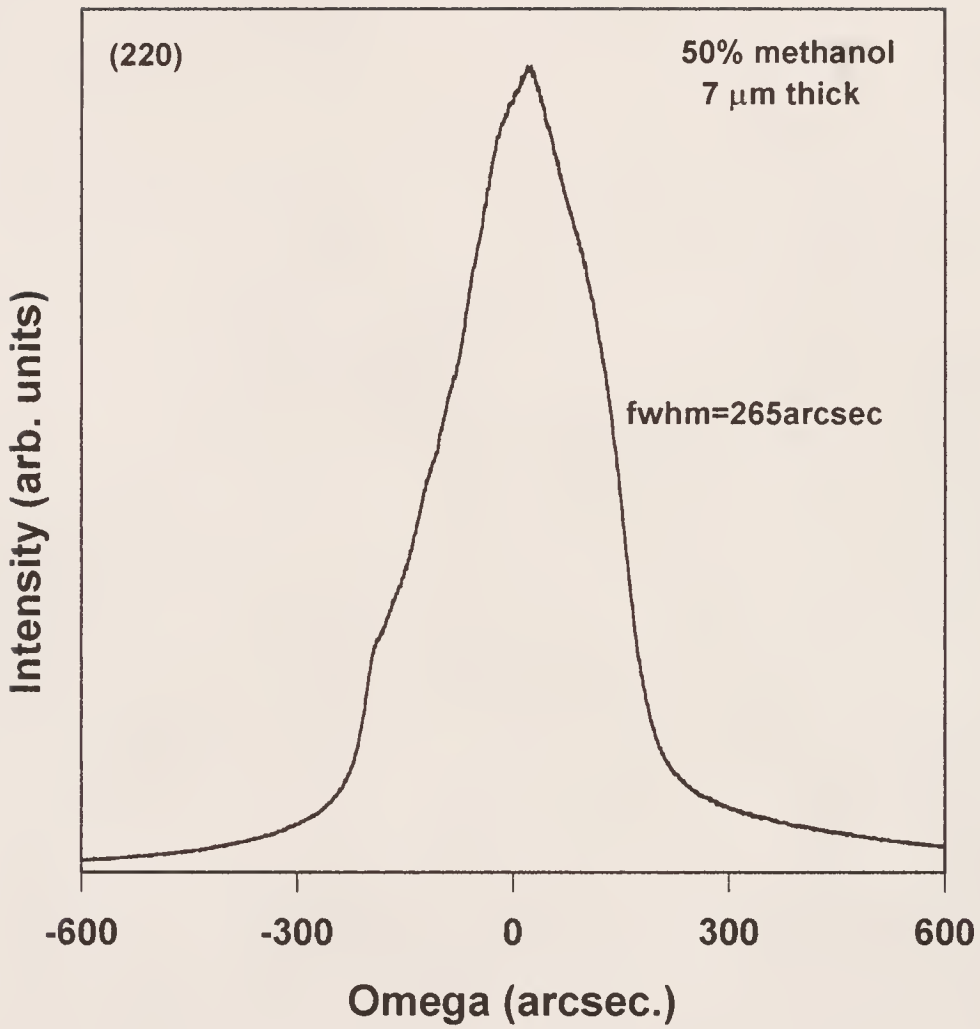

Figure 4.54 The (220) x-ray rocking curve from a 7μm thick 50% methanol film on a (110) diamond substrate.

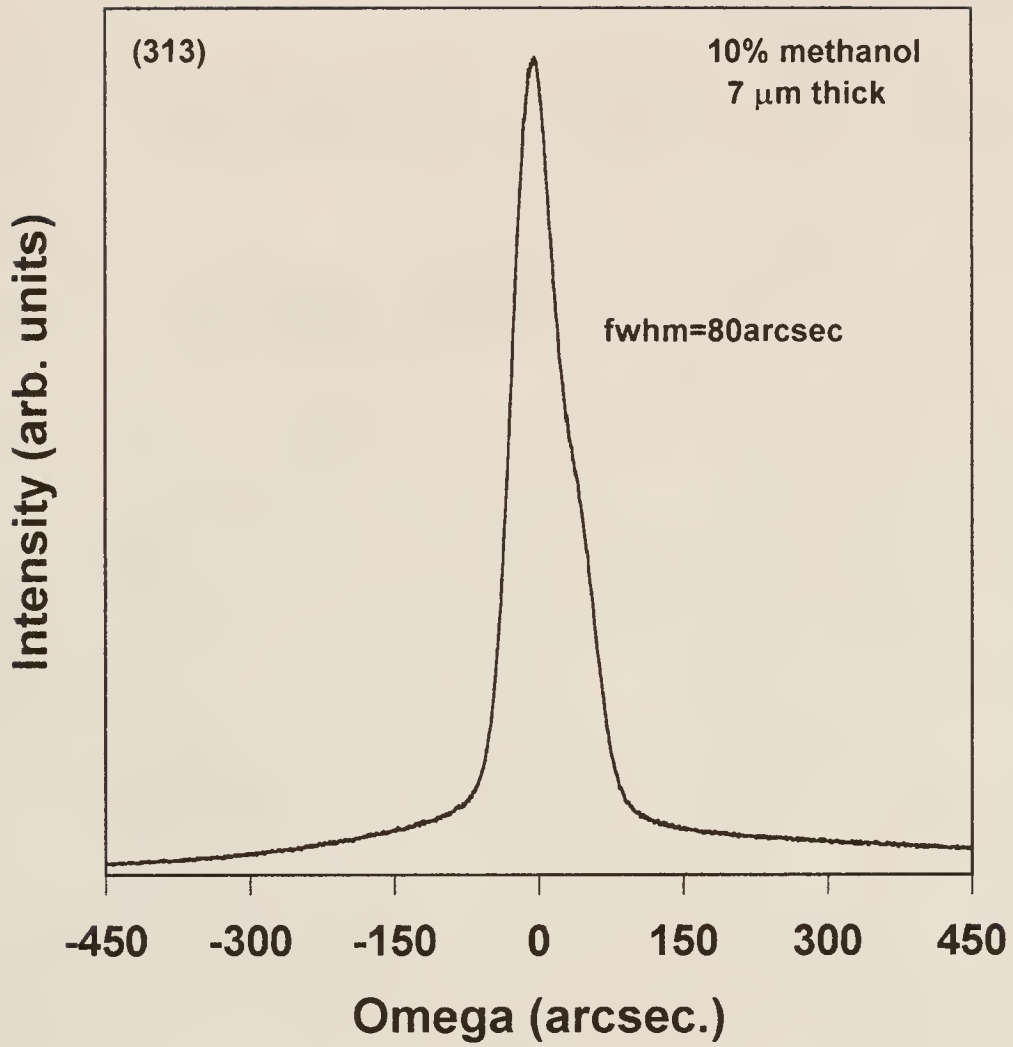

Figure 4.55 The (313) x-ray rocking curve from a 7μm thick 10% methanol film on a (110) diamond substrate.

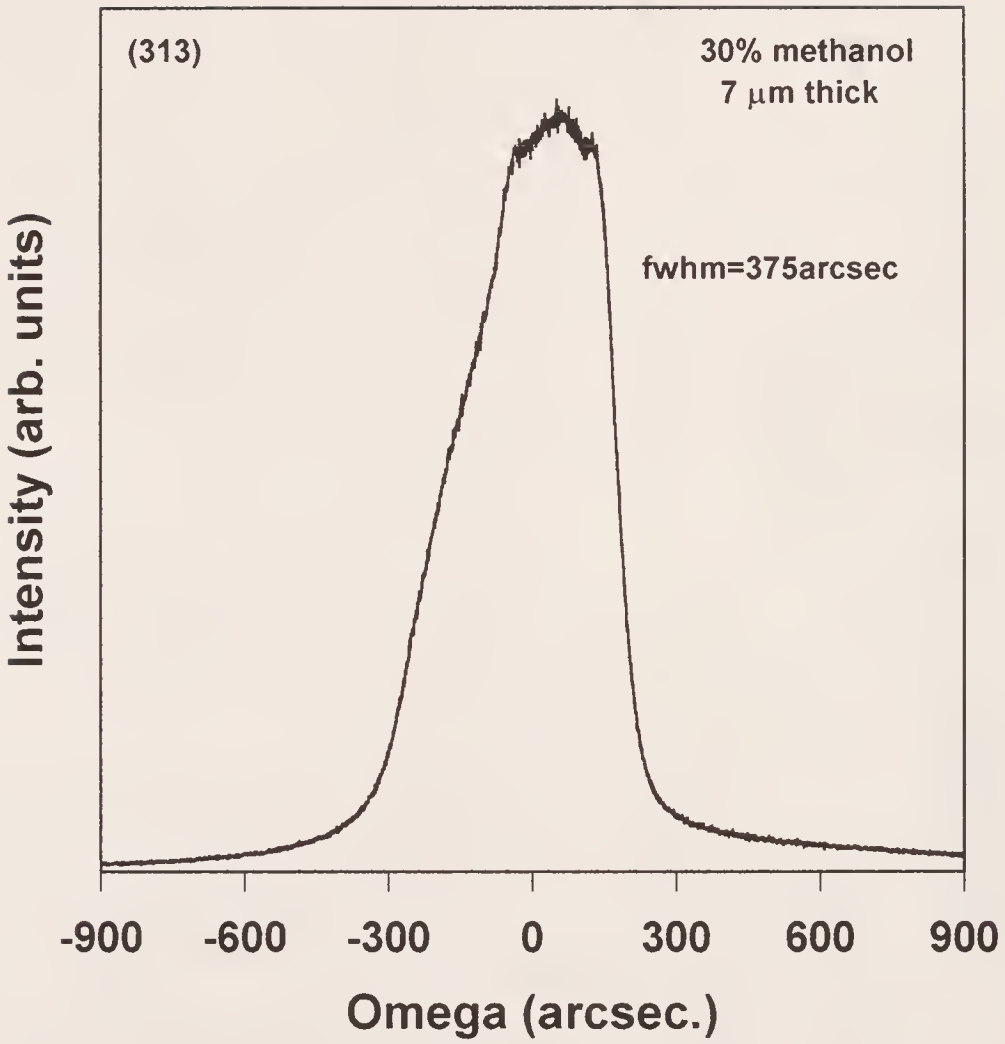

Figure 4.56 The (313) x-ray rocking curve from a 7μm thick 30% methanol film on a (110) diamond substrate.

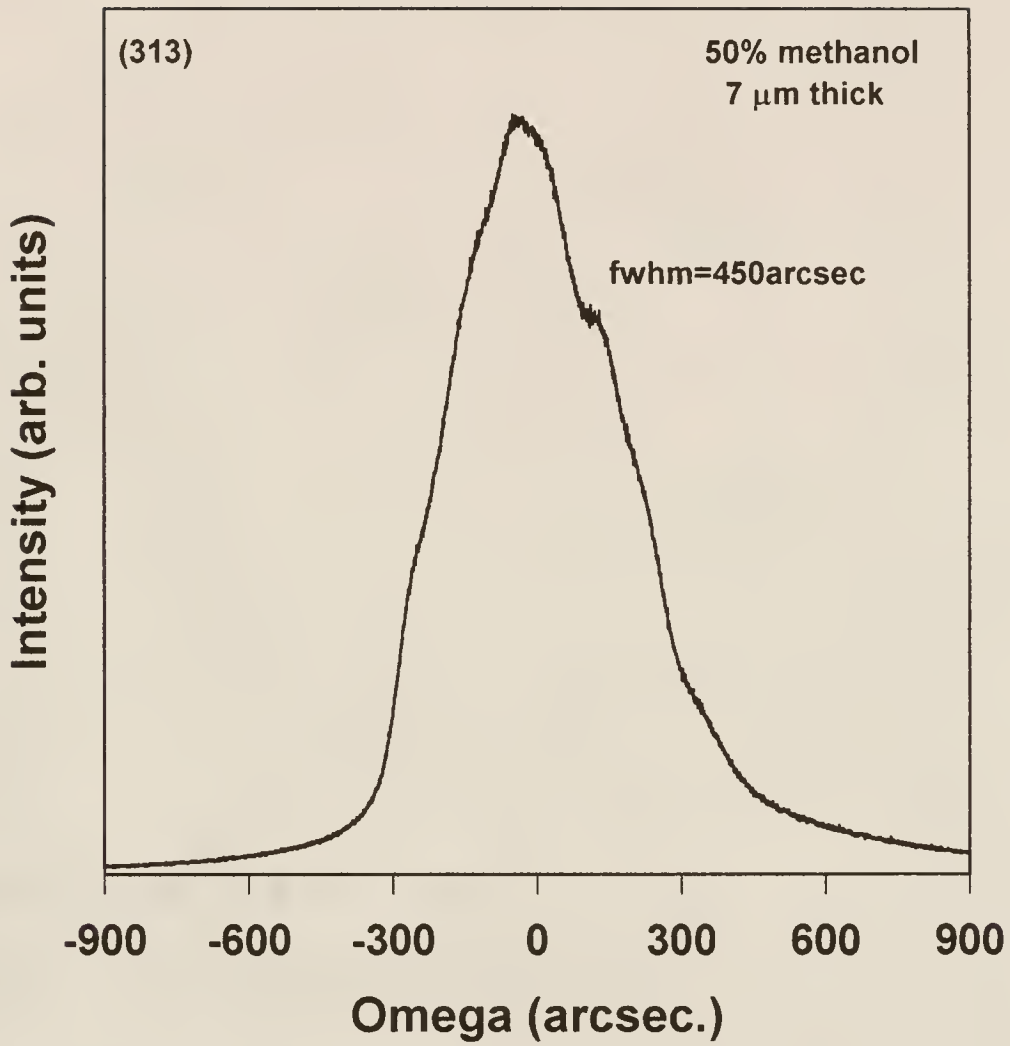

Figure 4.57 The (313) x-ray rocking curve from a 7μm thick 50% methanol film on a (110) diamond substrate.

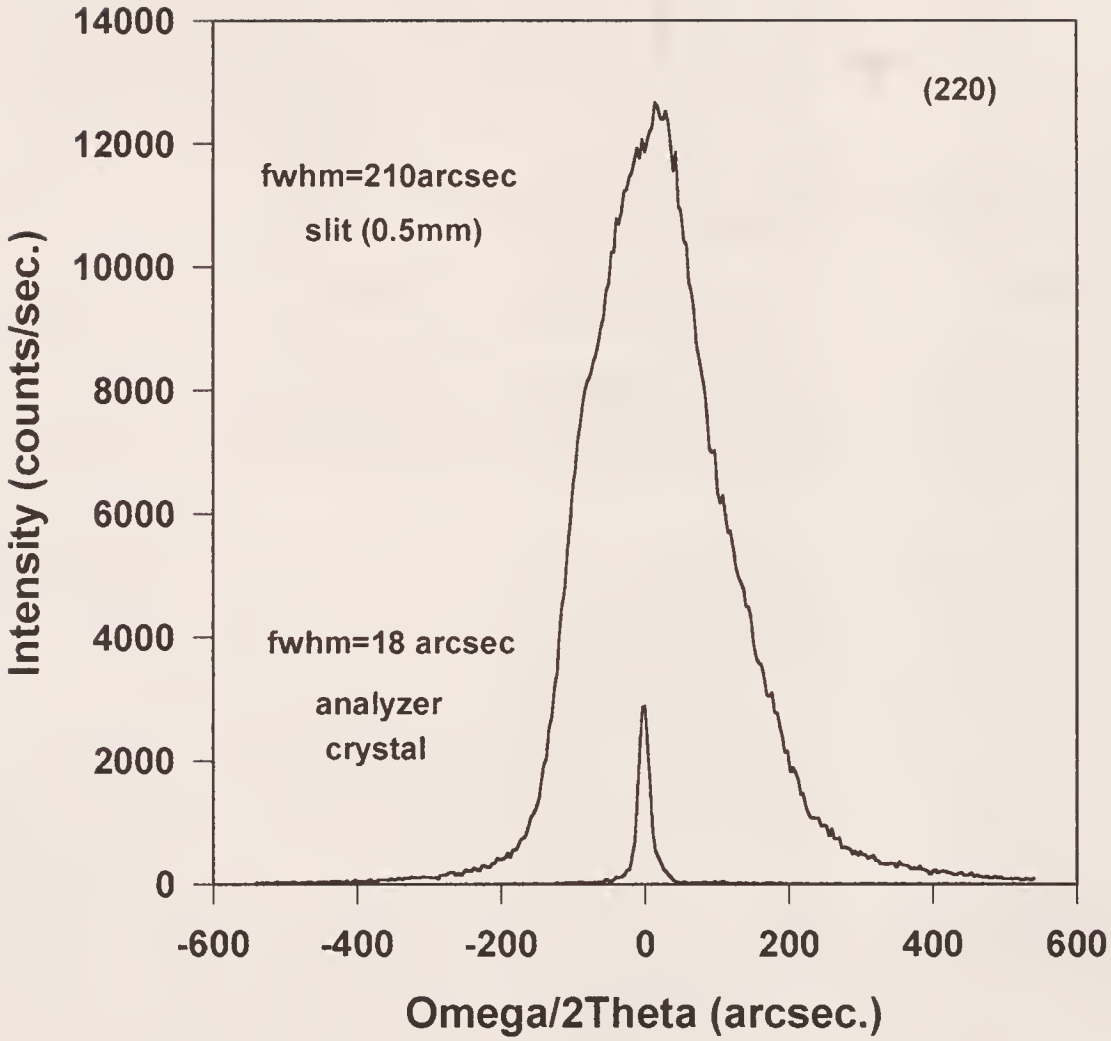

Figure 4.58 Two ω/2θ rocking curves from the same film but recorded in the receiving slit (FWHM=210 arcsec) and analyzer crystal (18 arcsec) modes. The drop in intensity is due to the two additional refections in the analyzer crystal.

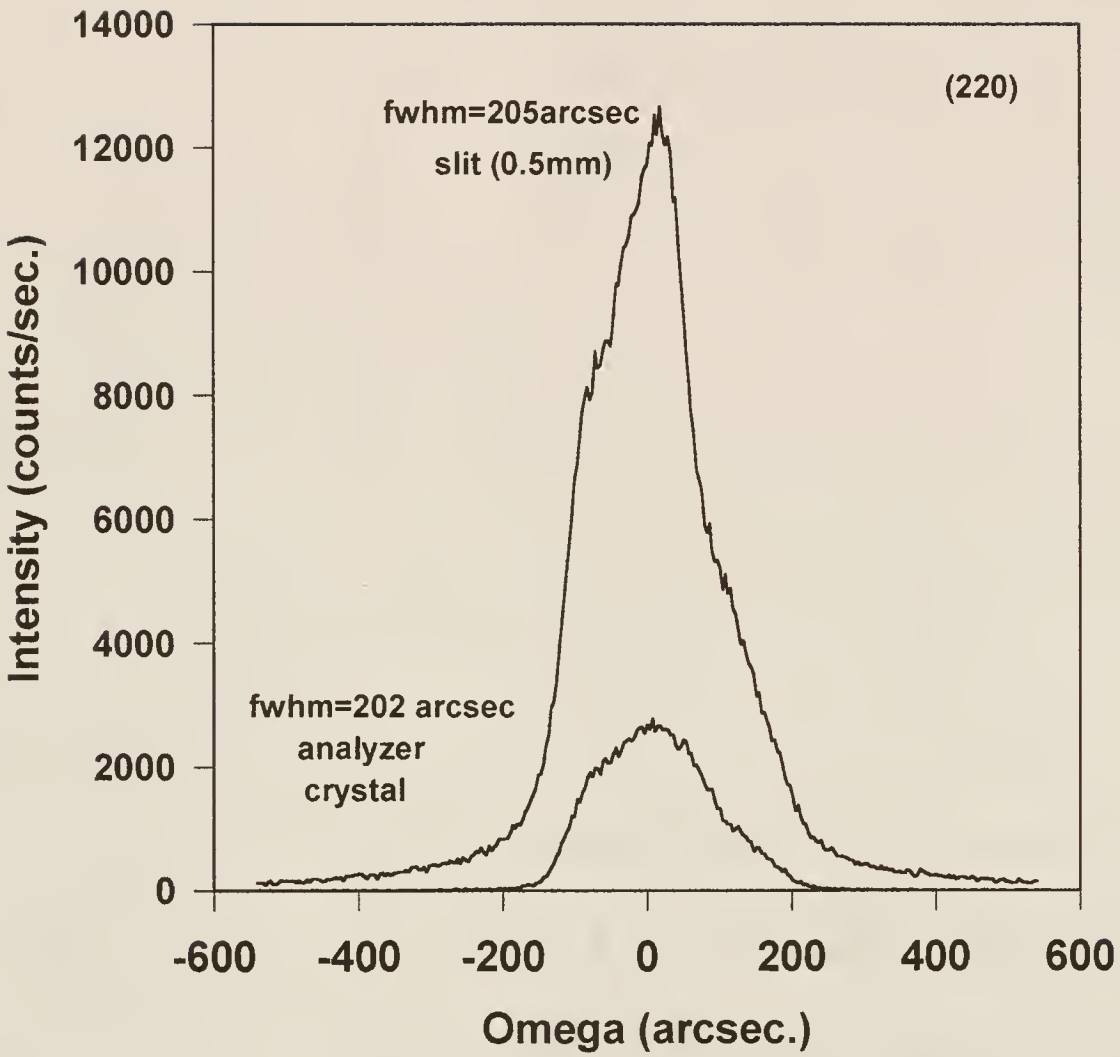

Figure 4.59 Two ω rocking curves from the same film but recorded in the receiving slit (FWHM=205 arcsec) and analyzer crystal (202 arcsec) modes.

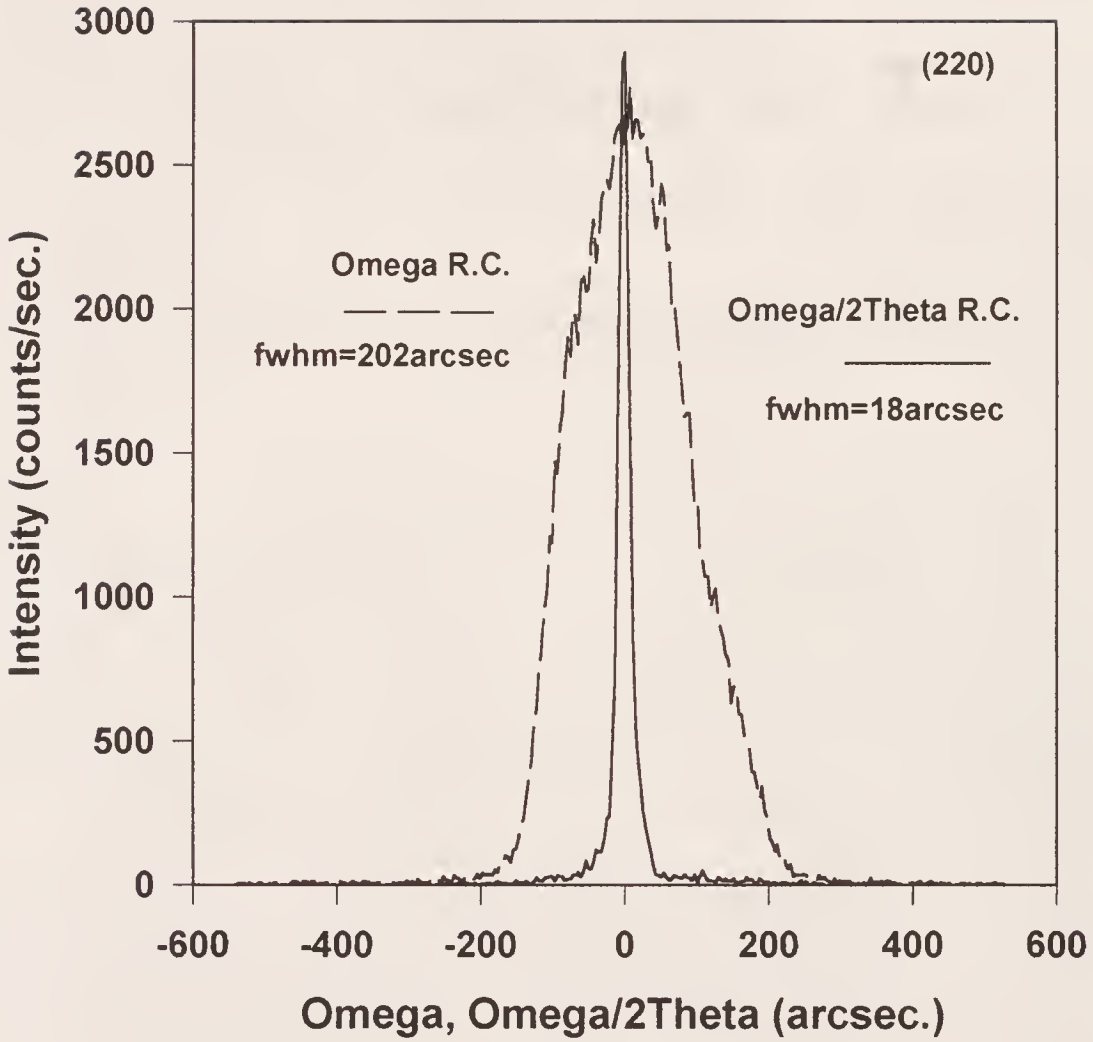

Figure 4.60 The ω/2θ and ω rocking curves from Figs. 4.58 and 4.59 recorded using the analyzer crystal. The analyzer crystal allowed separation of the mosaic and lattice parameter components of broadening. The rocking curve broadening was dominated by mosaic spreading.

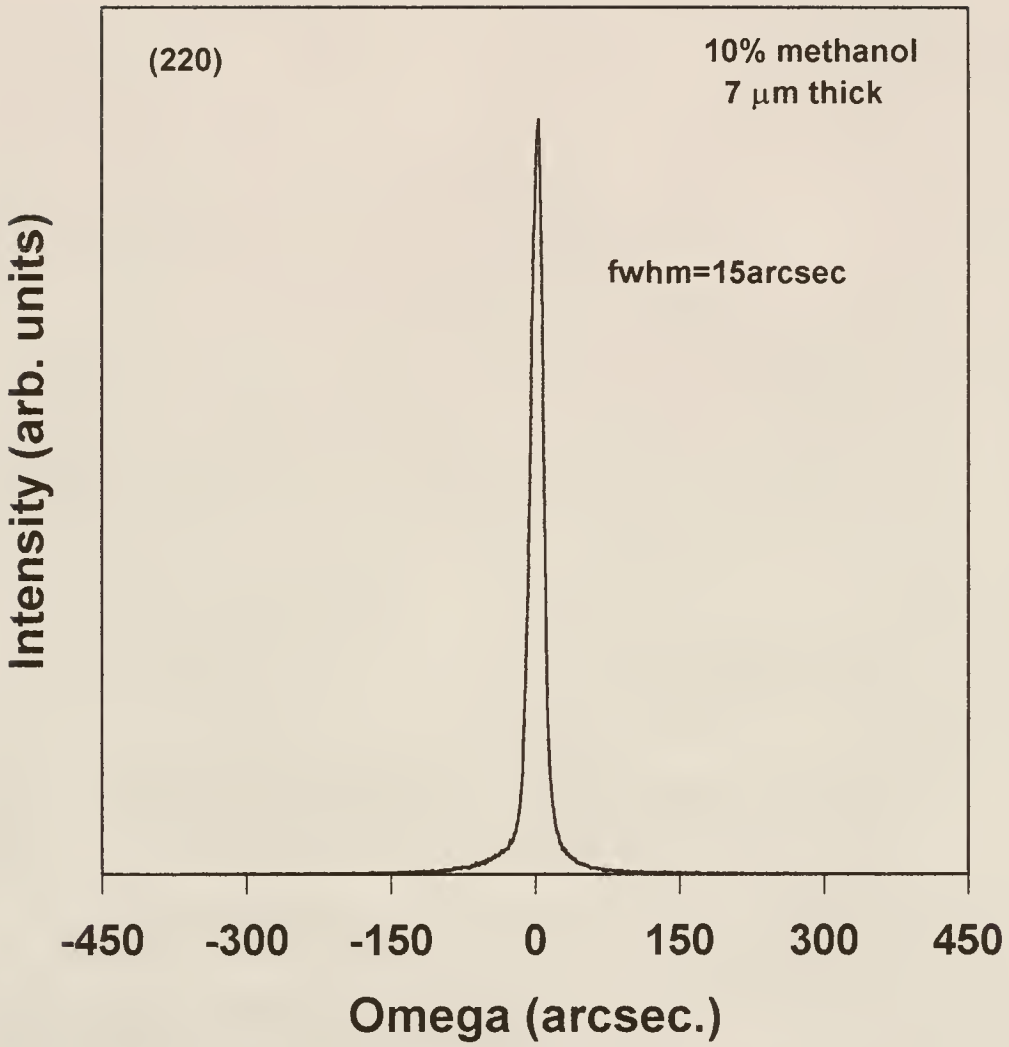

Figure 4.61 The (220) ω rocking curve from a 7μm thick 10% methanol film on a (110) diamond substrate.

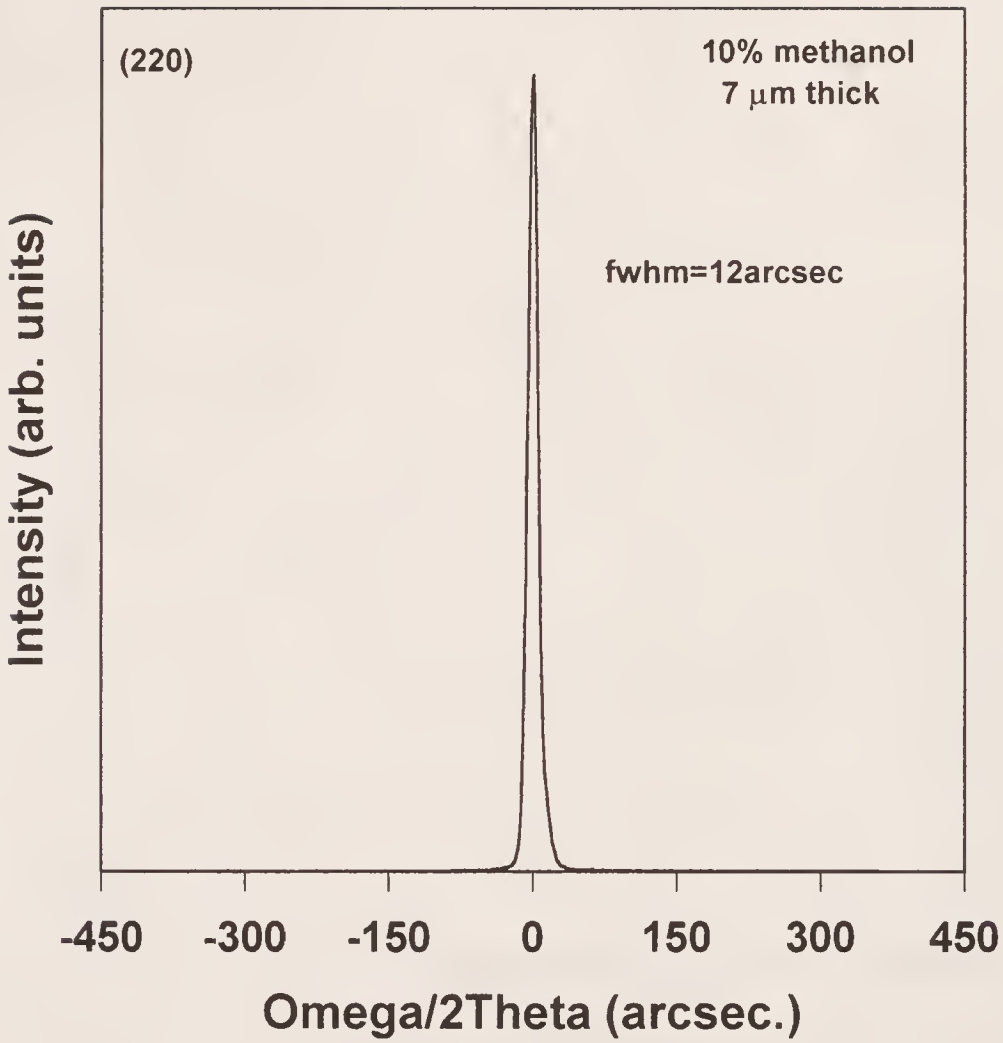

Figure 4.62 The (220) $\omega/2\theta$ rocking curve from a 7μm thick 10% methanol film on a (110) diamond substrate.

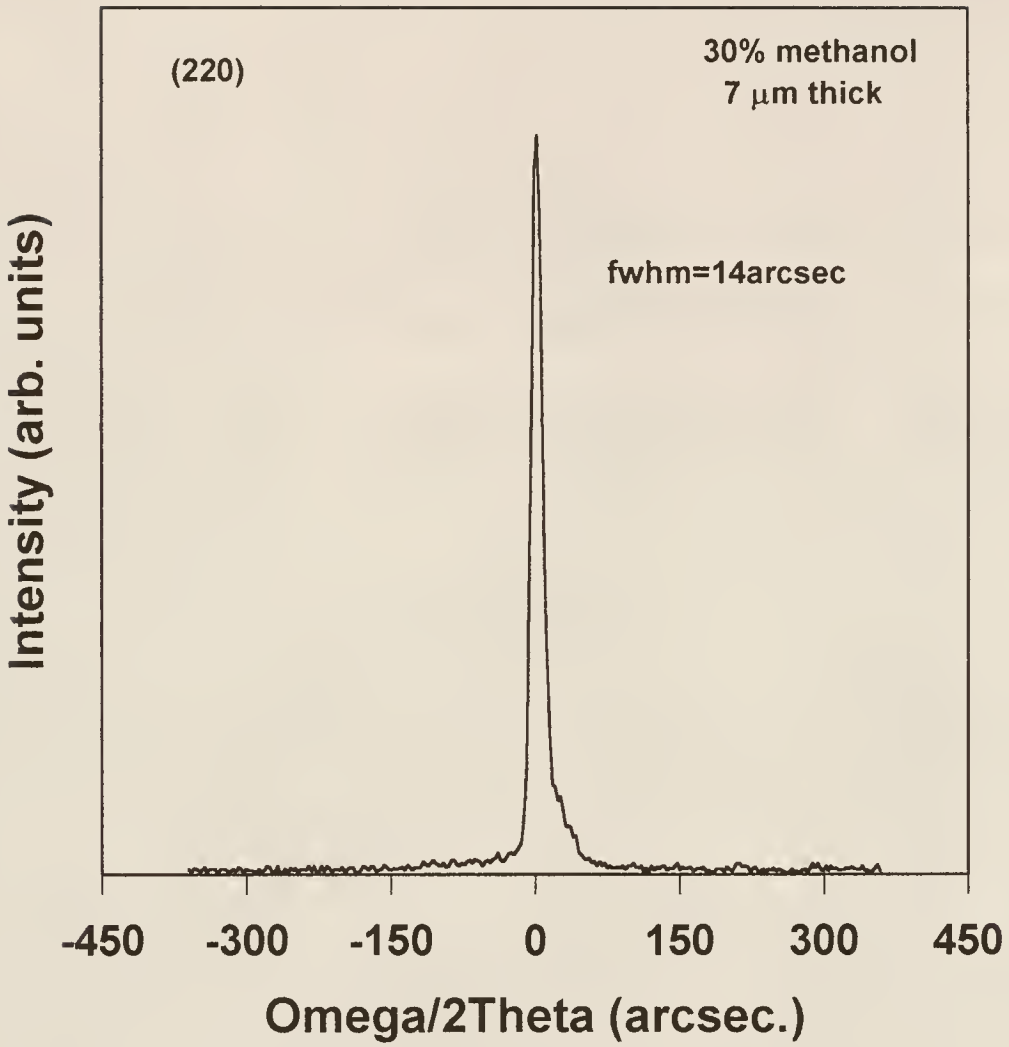

Figure 4.63 The (220) ω/2θ rocking curve from a 7μm thick 30% methanol film on a (110) diamond substrate.

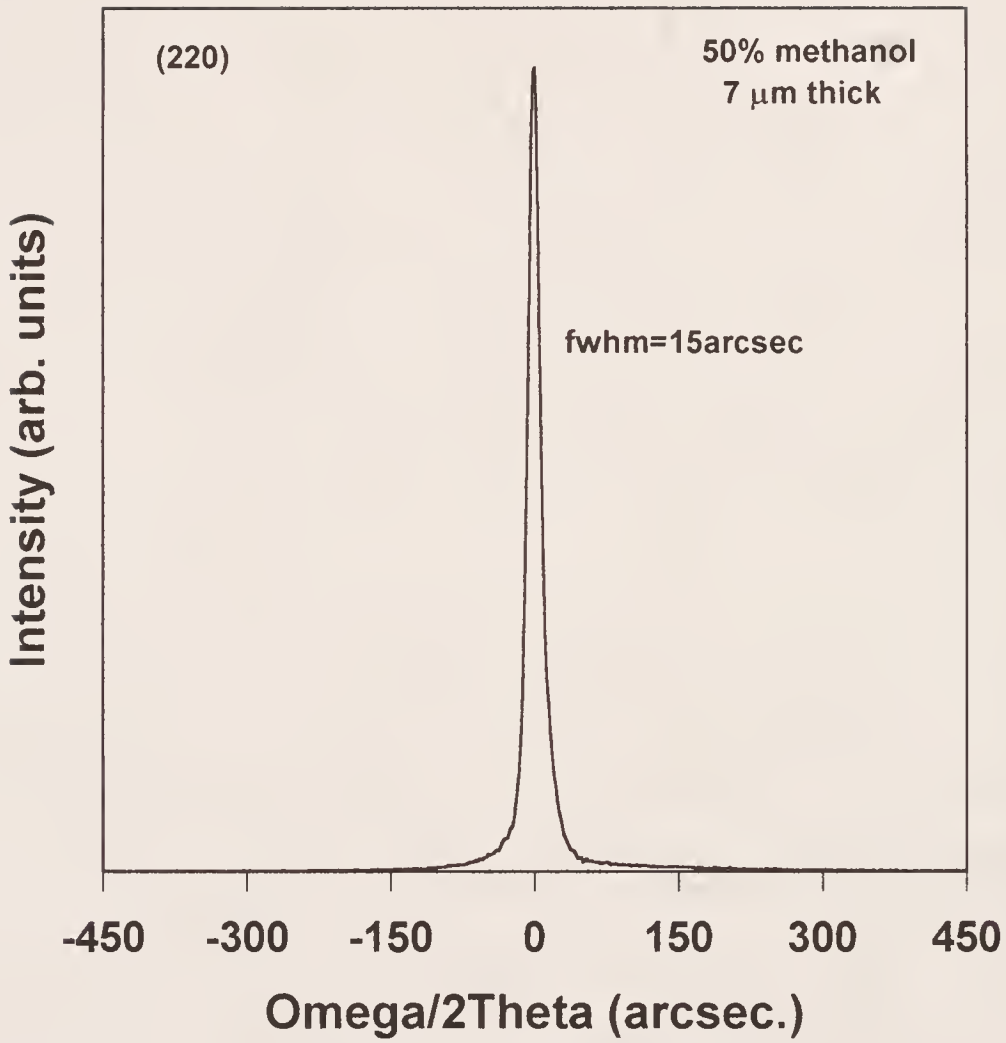

Figure 4.64 The (220) ω/2θ rocking curve from a 7μm thick 50% methanol film on a (110) diamond substrate.

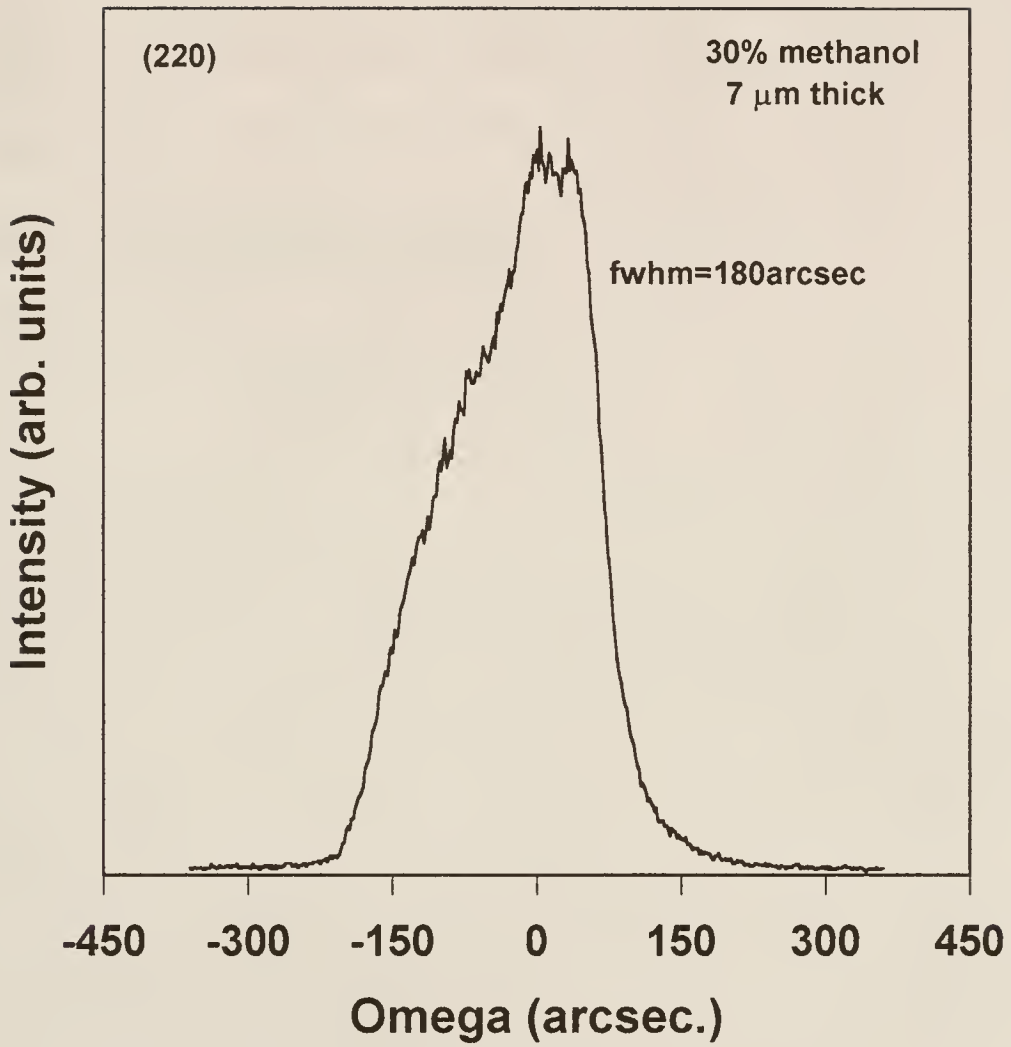

Figure 4.65 The (220) ω rocking curve from a 7μm thick 30% methanol film on a (110) diamond substrate.

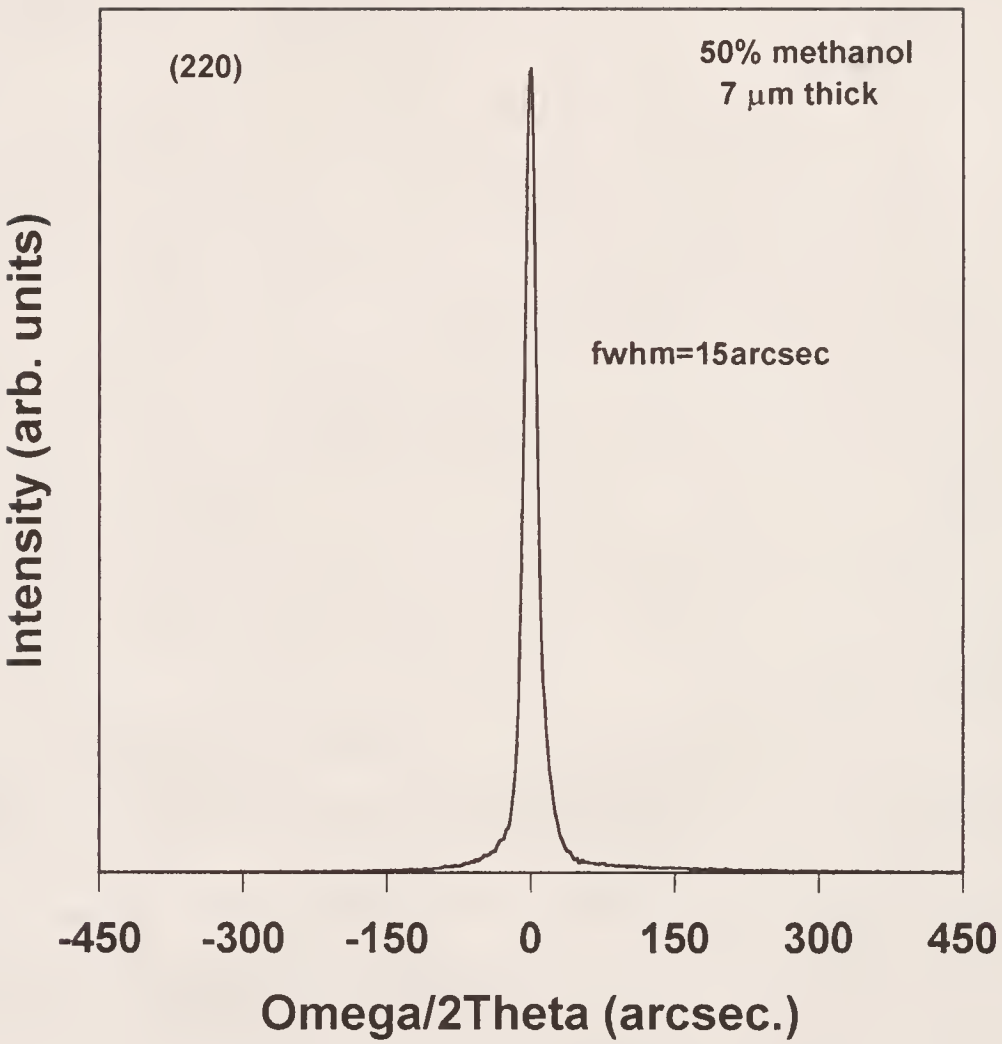

Figure 4.66 The (220) ω/2θ rocking curve from a 7μm thick 50% methanol film on a (110) diamond substrate.

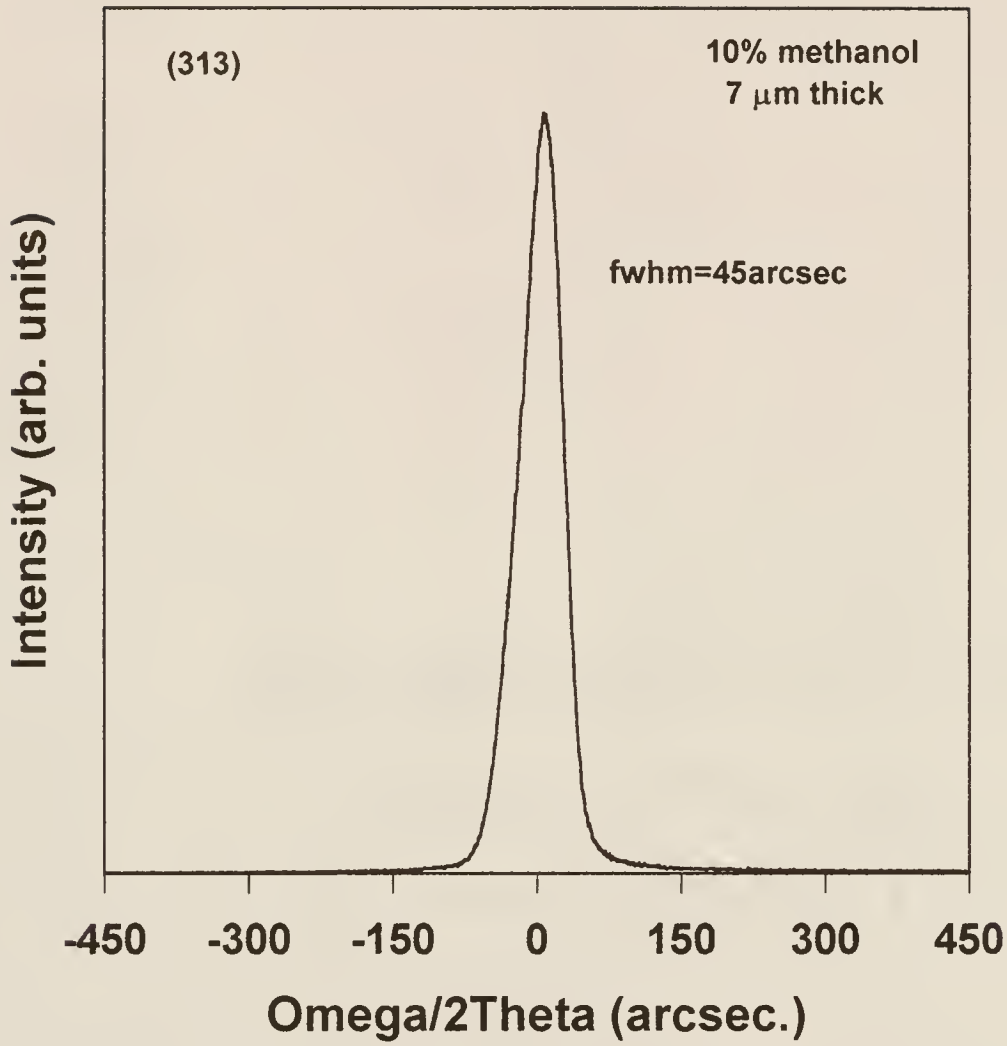

Figure 4.67 The (313) ω/2θ rocking curve from a 7μm thick 10% methanol film on a (110) diamond substrate.

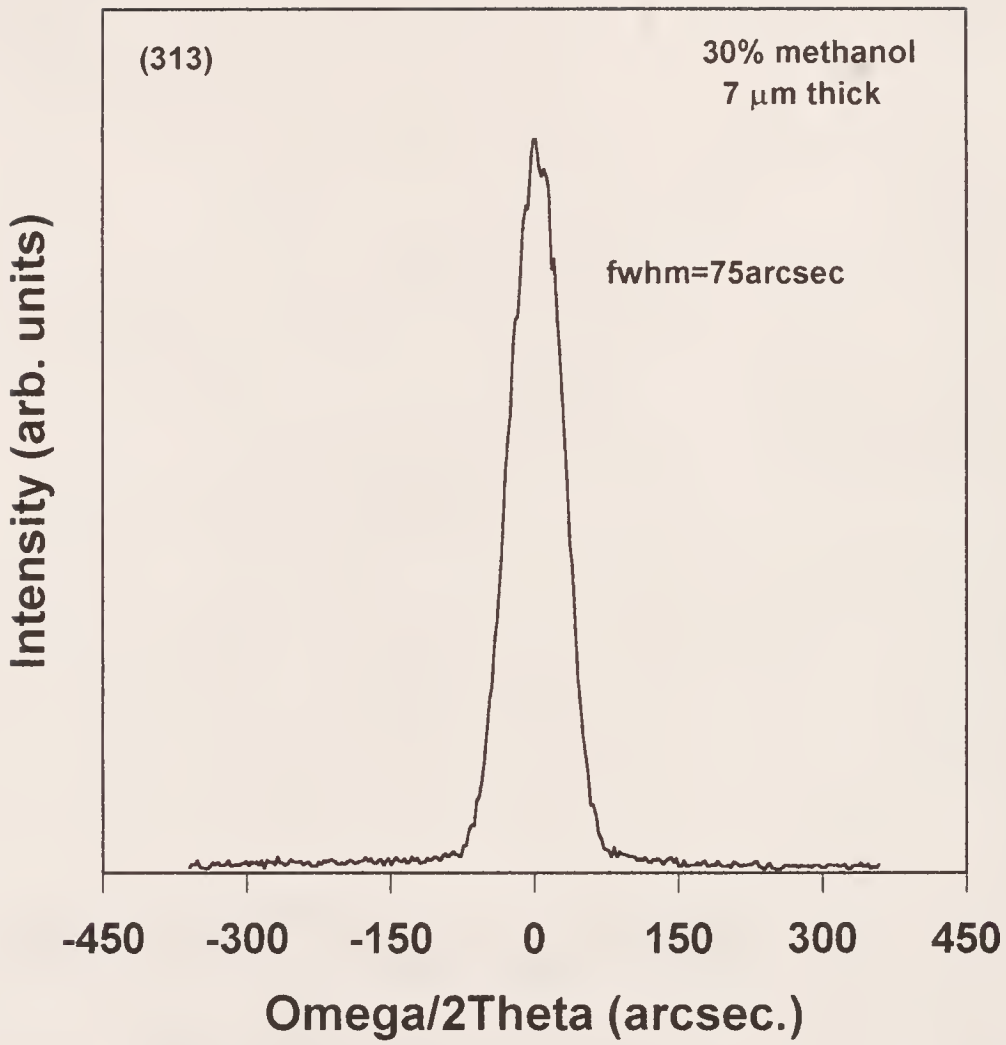

Figure 4.68 The (313) ω/2θ rocking curve from a 7μm thick 30% methanol film on a (110) diamond substrate.

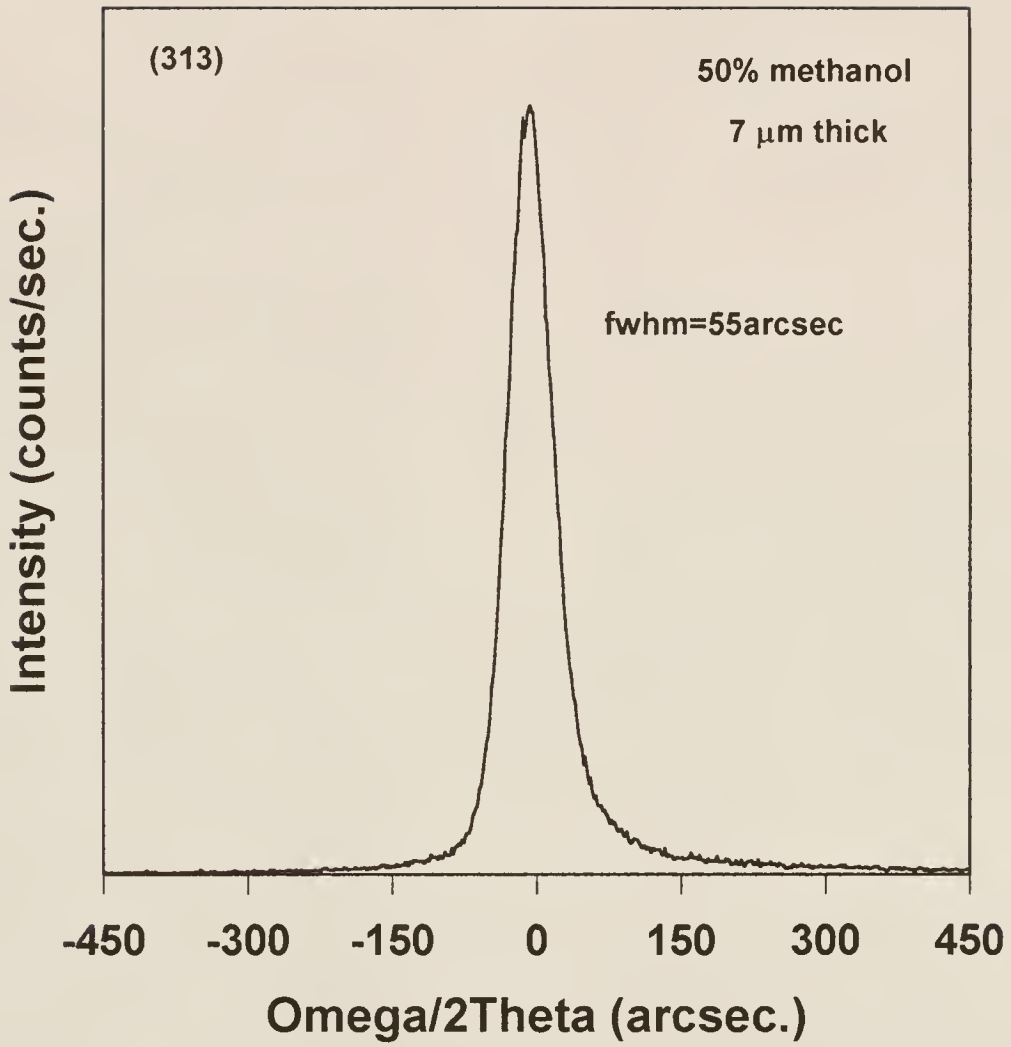

Figure 4.69 The (313) ω/2θ rocking curve from a 7μm thick 50% methanol film on a (110) diamond substrate.

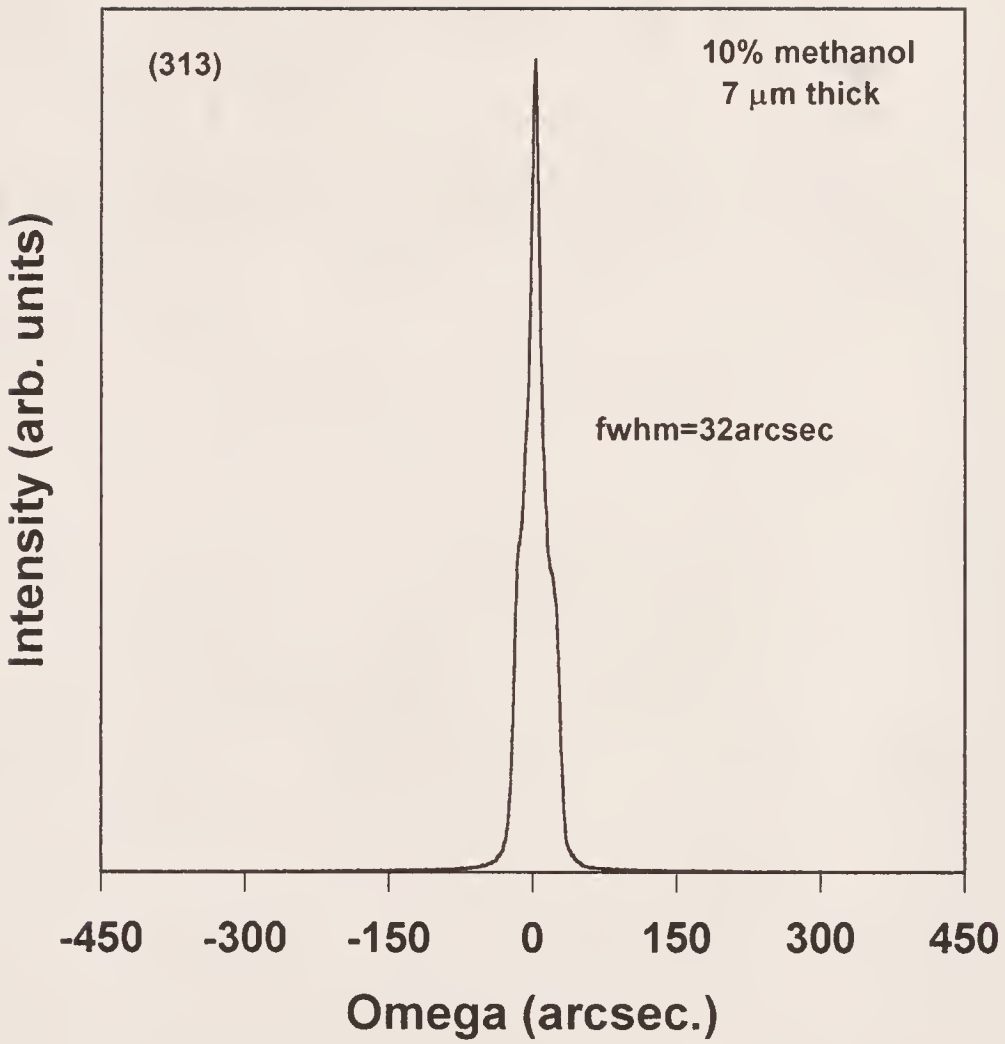

Figure 4.70 The (313) ω rocking curve from a 7μm thick 10% methanol film on a (110) diamond substrate.

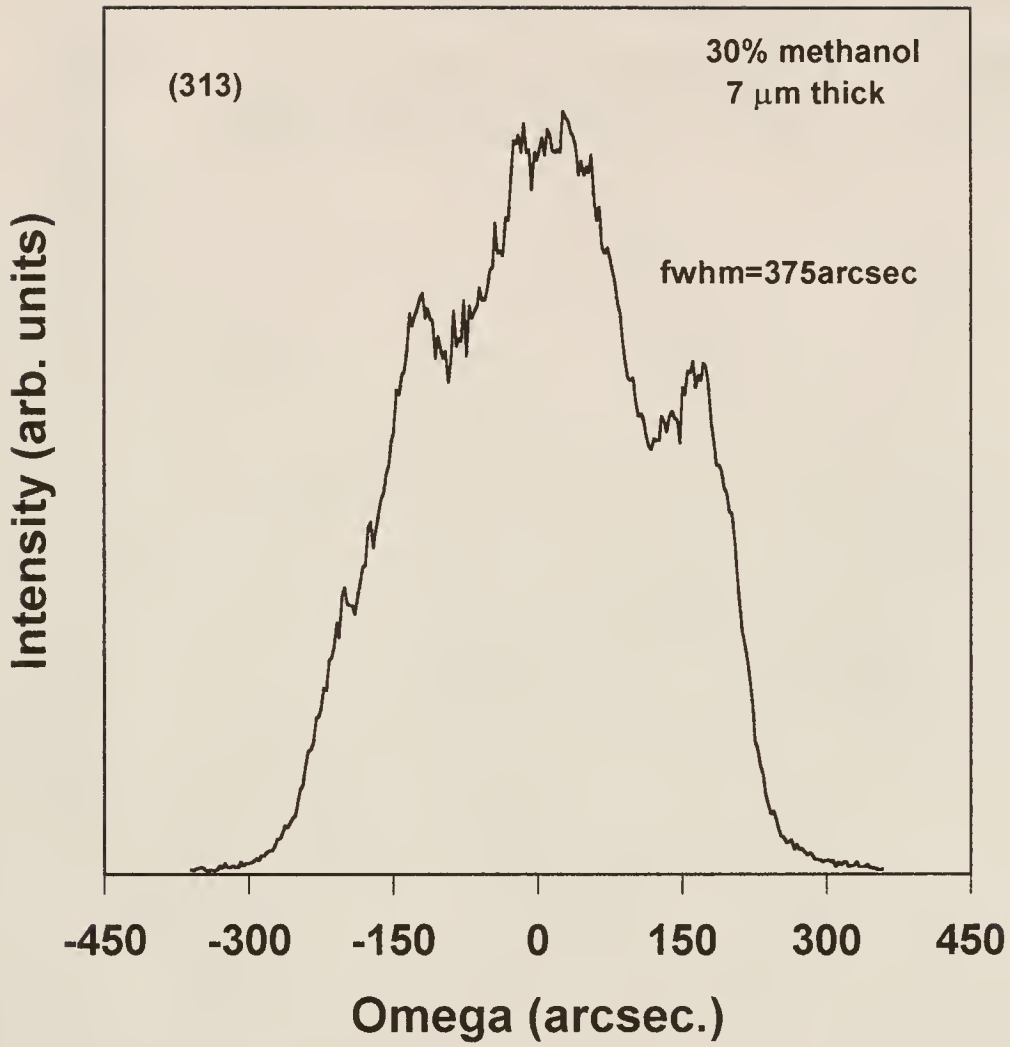

Figure 4.71 The (313) ω rocking curve from a 7μm thick 30% methanol film on a (110) diamond substrate.

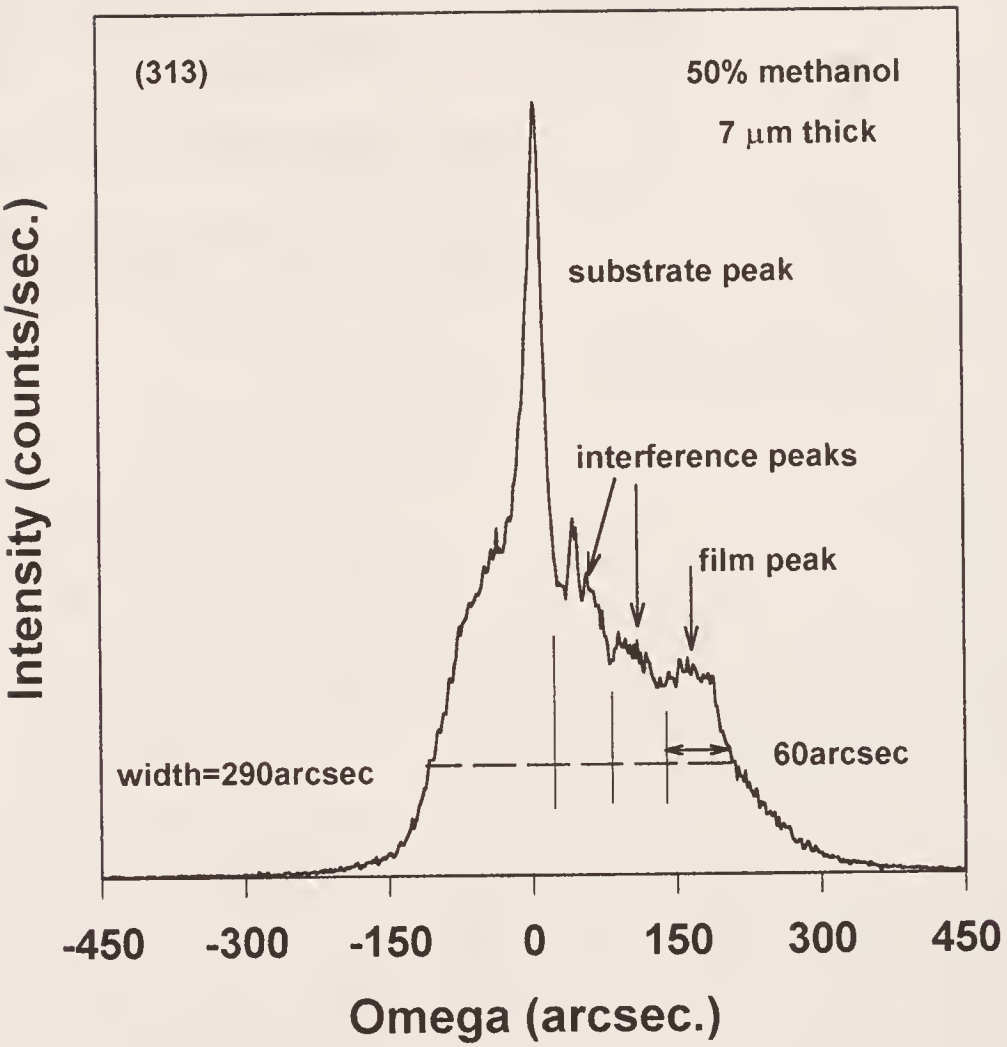

Figure 4.72 The (313) ω rocking curve from a 7μm thick 50% methanol film on a (110) diamond substrate.

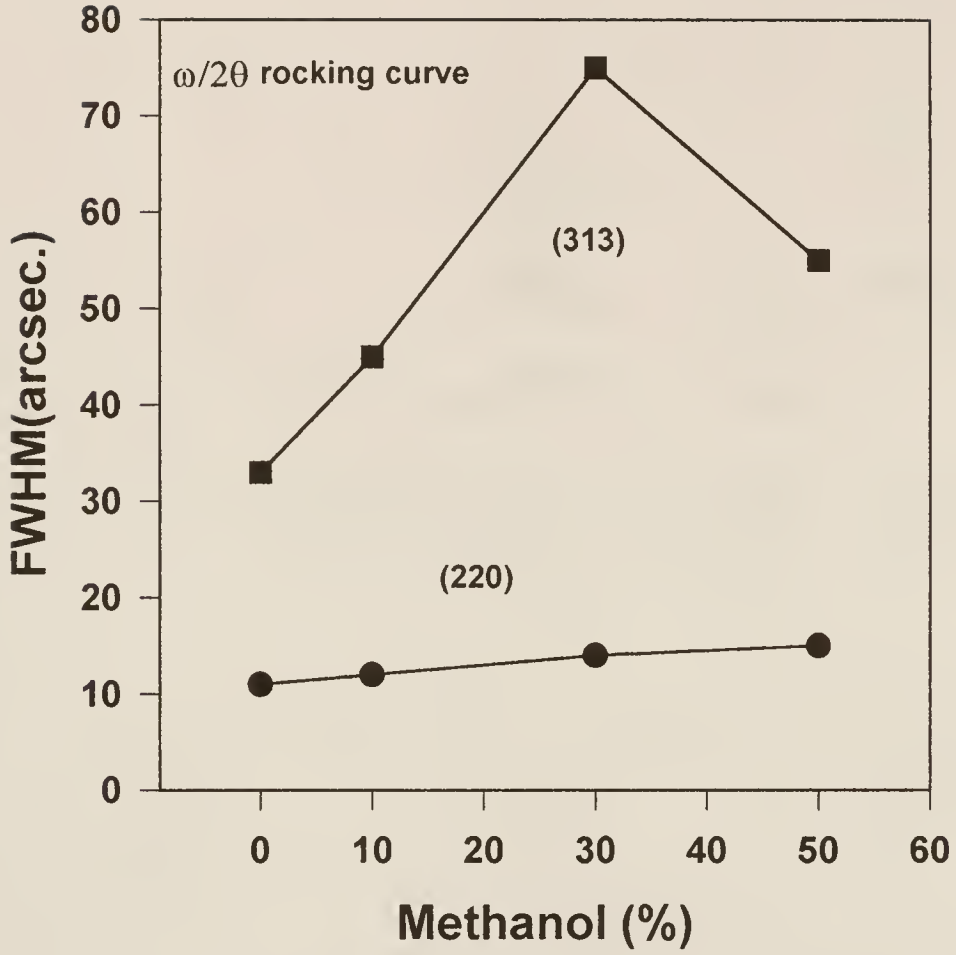

Figure 4.73 FWHM of the (220) and (313) ω/2θ rocking curves versus methanol concentration. The broadening was due to lattice parameter variations or strain.

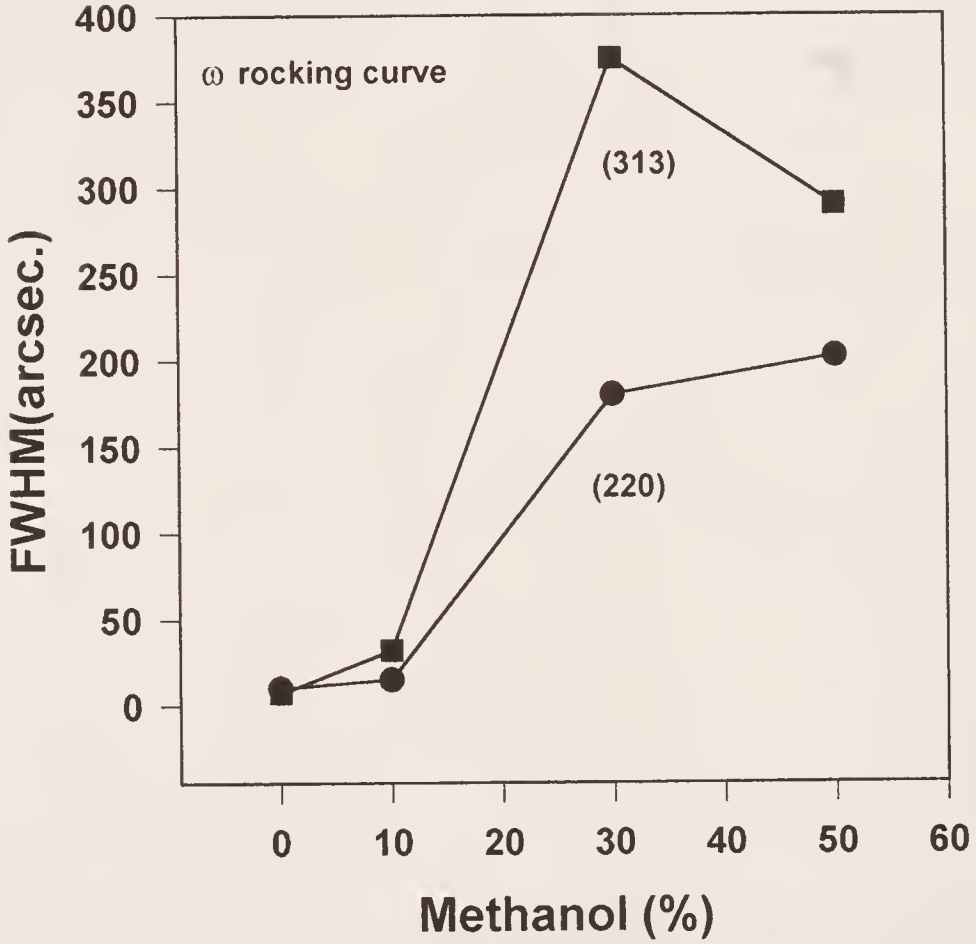

Figure 4.74 FWHM of the (220) and (313) ω rocking curves versus methanol concentration. The broadening was due to mosaic spreading.

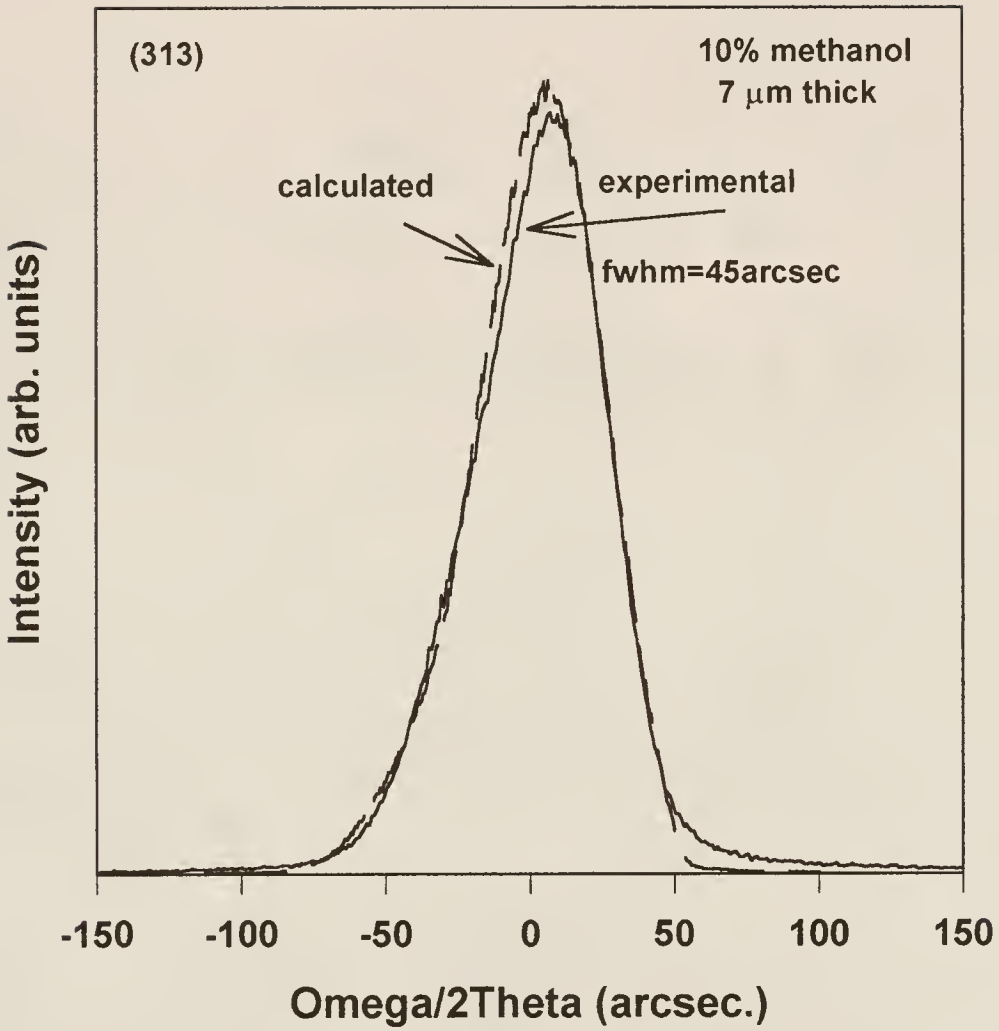

Figure 4.75 The experimental data from Fig. 4.67 was modeled using Philips PC-HRS software. A calculated intensity profile from a 7.5μm thick diamond film on a diamond substrate, where the strain increased exponentially from zero at the interface to +196ppm (tensile strain) at the surface, was constructed. A stress of 224MPa was calculated from the maximum strain value and E=1143GPa.

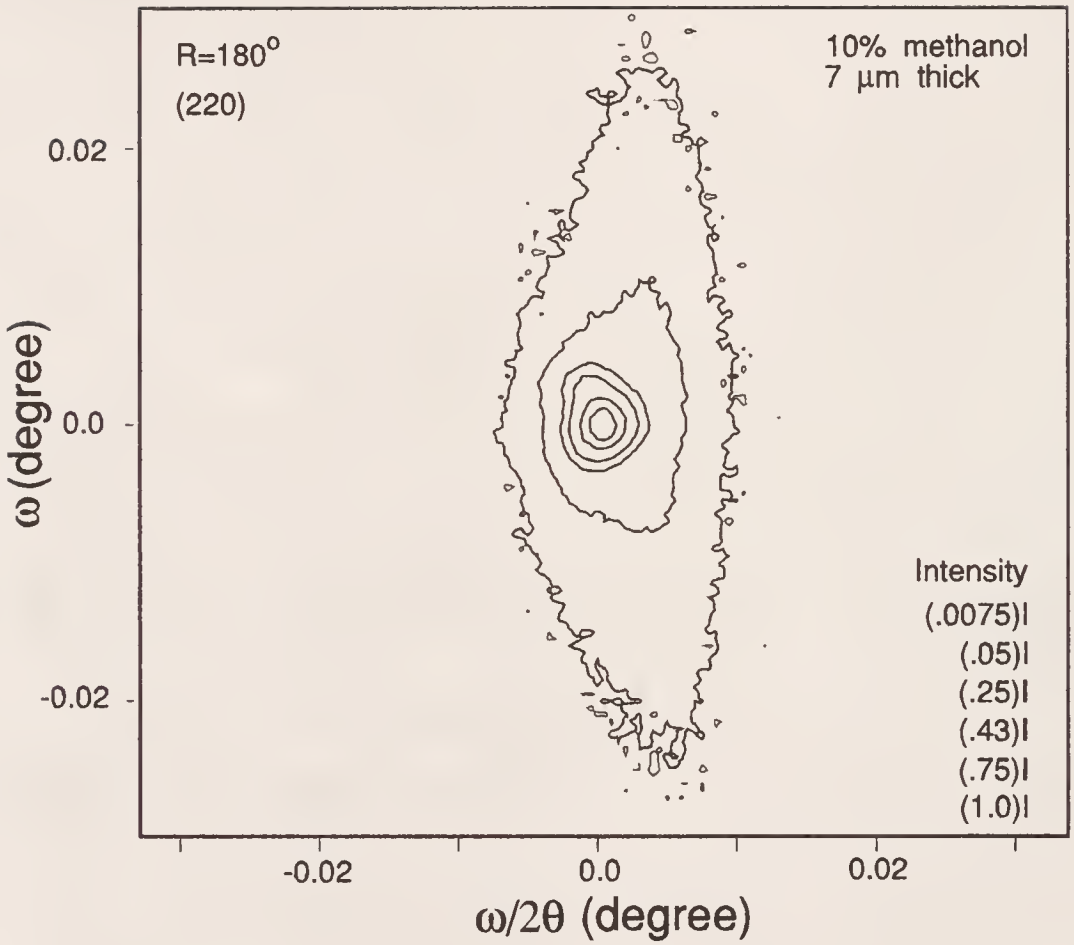

Figure 4.76 The symmetric ω/2θ-ω x-ray map at R=180° from a 7μm thick 10% methanol film on a (110) diamond substrate. The spreading parallel to the ω axis was due to mosaic spreading. The map at R=0° (not shown) also exhibited mosaic spreading.

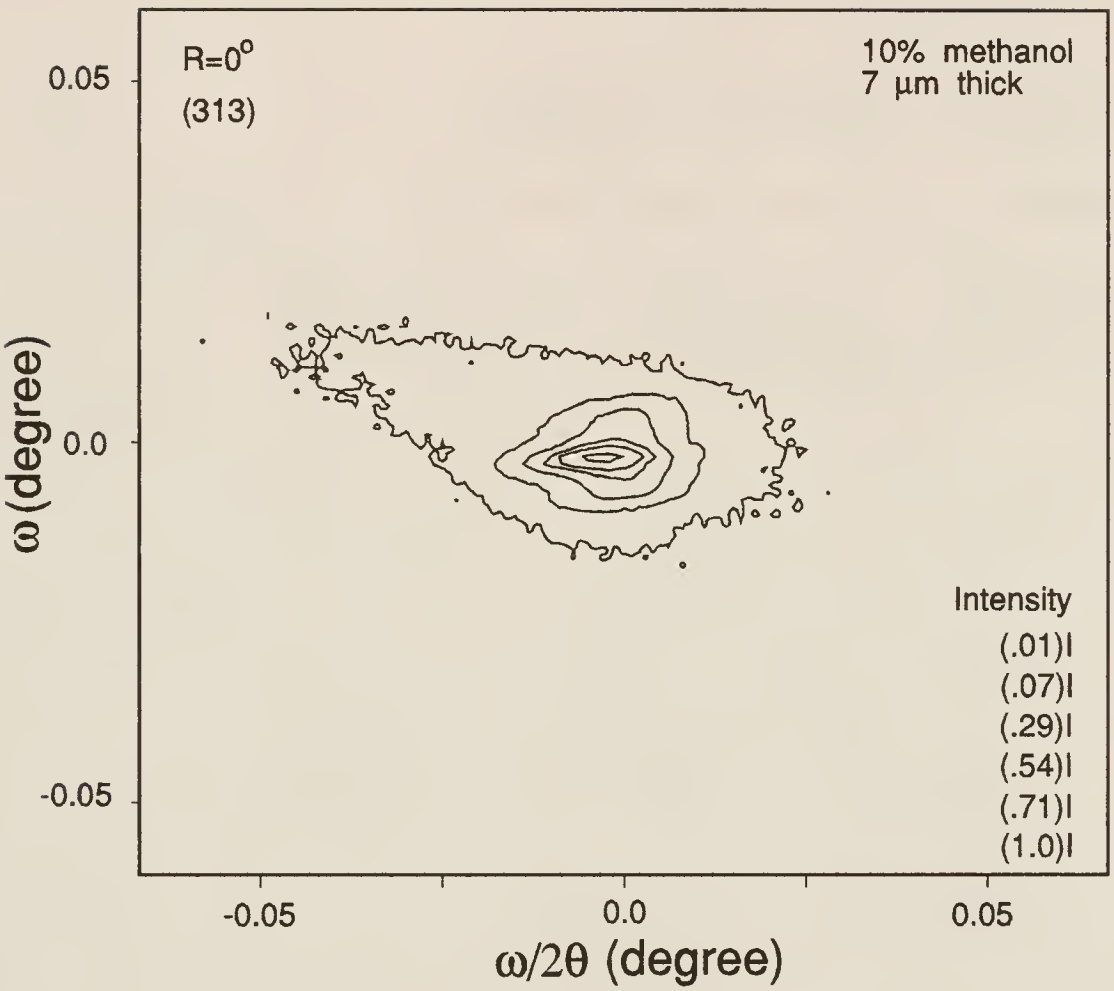

Figure 4.77 The asymmetric ω/2θ-ω x-ray map at R=0° from a 7μm thick 10% methanol film on a (110) diamond substrate. The spreading to lower angles (ω/2θ) was due to tensile strain.

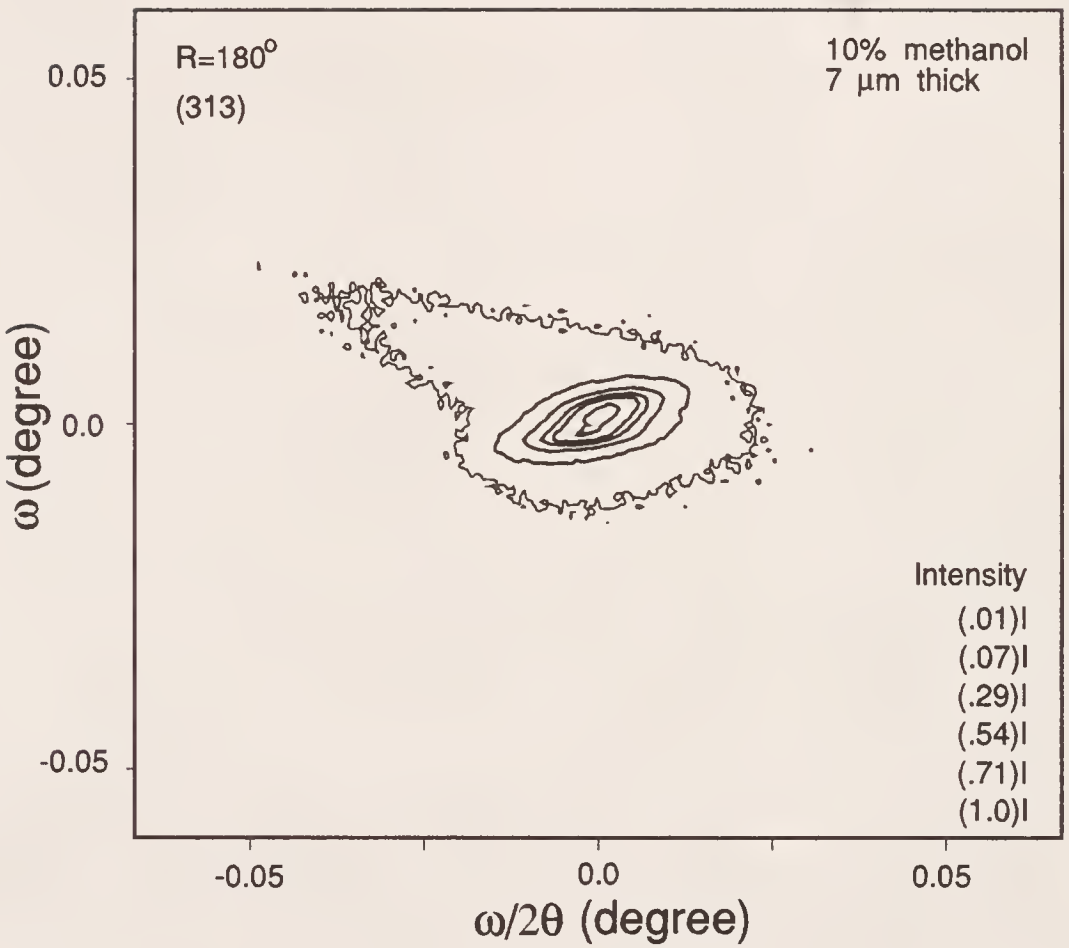

Figure 4.78 The asymmetric ω/2θ-ω x-ray map at R=180° from a 7µm thick 10% methanol film on a (110) diamond substrate. The spreading to lower angles (ω/2θ) was due to tensile strain.

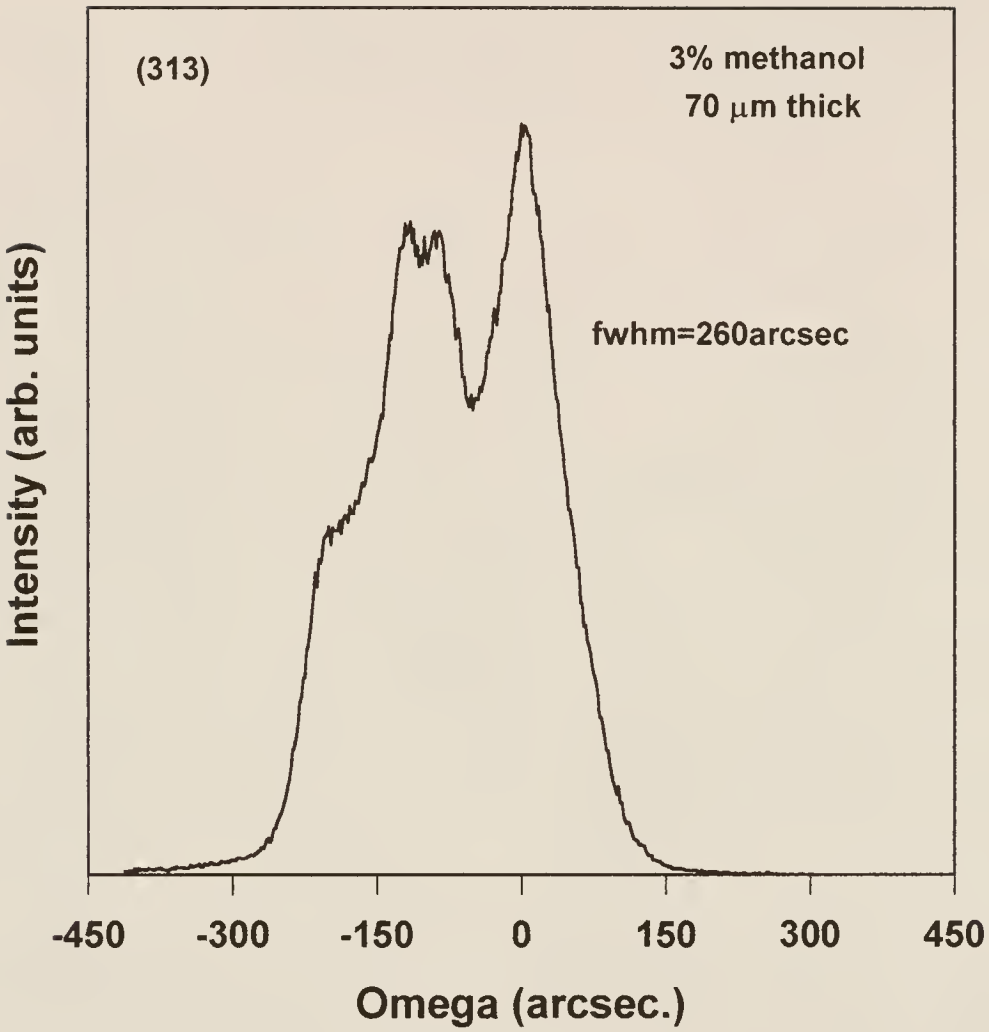

Figure 4.79 Asymmetric ω rocking curve from a 70μm thick 3% methanol film on a (110) diamond substrate. The peaks may be due to layers within the film being misoriented relative to the substrate.

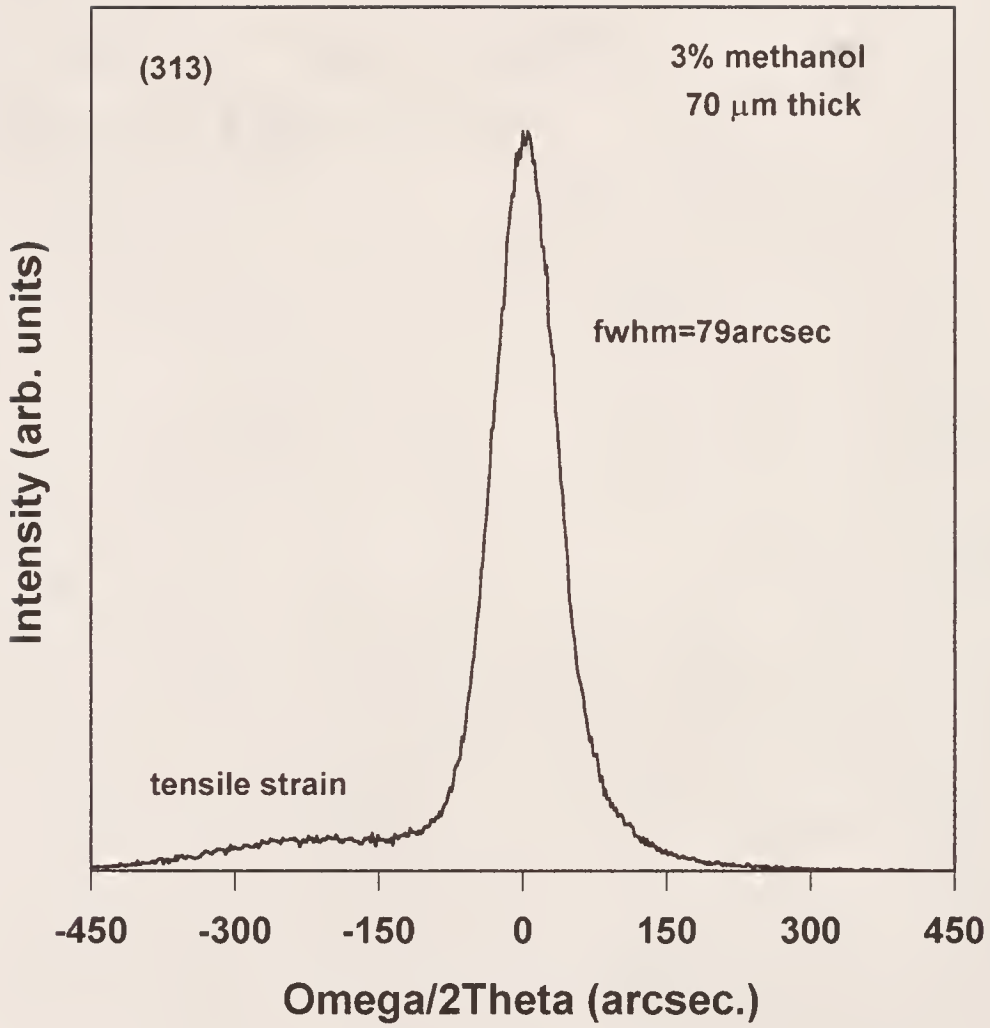

Figure 4.80 Asymmetric $\omega/2\theta$ rocking curve from a 70μm thick 3% methanol film on a (110) diamond substrate. The low intensity to lower angles is due to tensile strain.

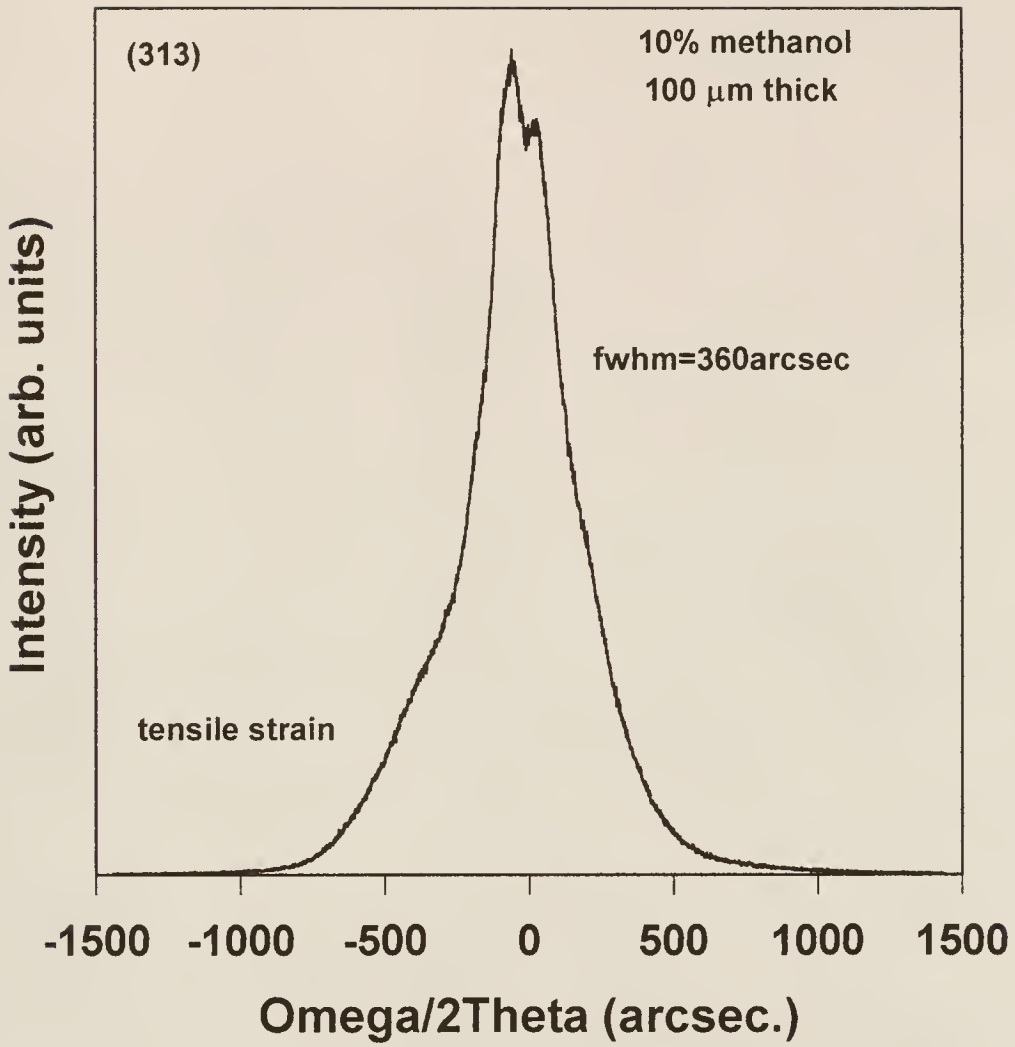

Figure 4.81 Asymmetric ω/2θ rocking curve from a 100μm thick 10% methanol film on a (110) diamond substrate. This film exhibited cracks (below the surface) which were grown over.

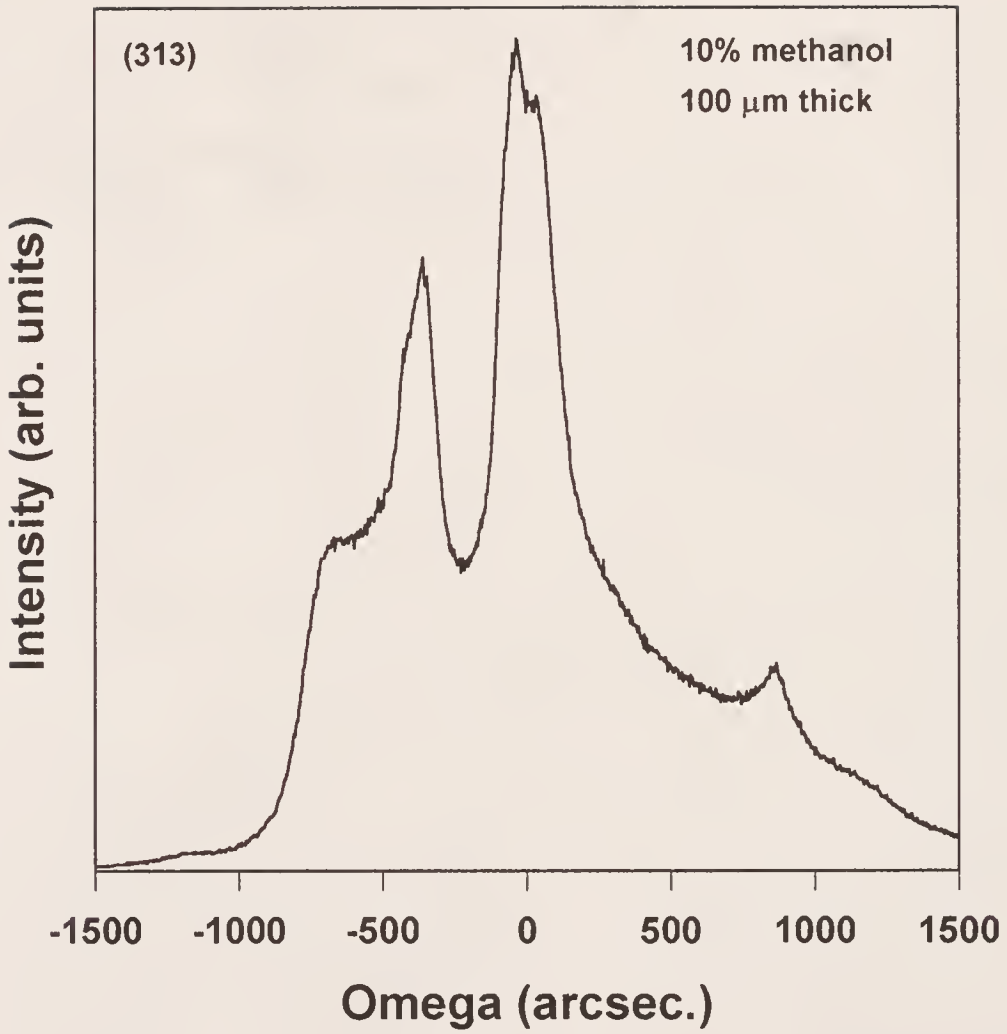

Figure 4.82 Asymmetric ω rocking curve from a 100μm thick 10% methanol film on a (110) diamond substrate. The peaks may be due to layers within the film being misoriented relative to the substrate.

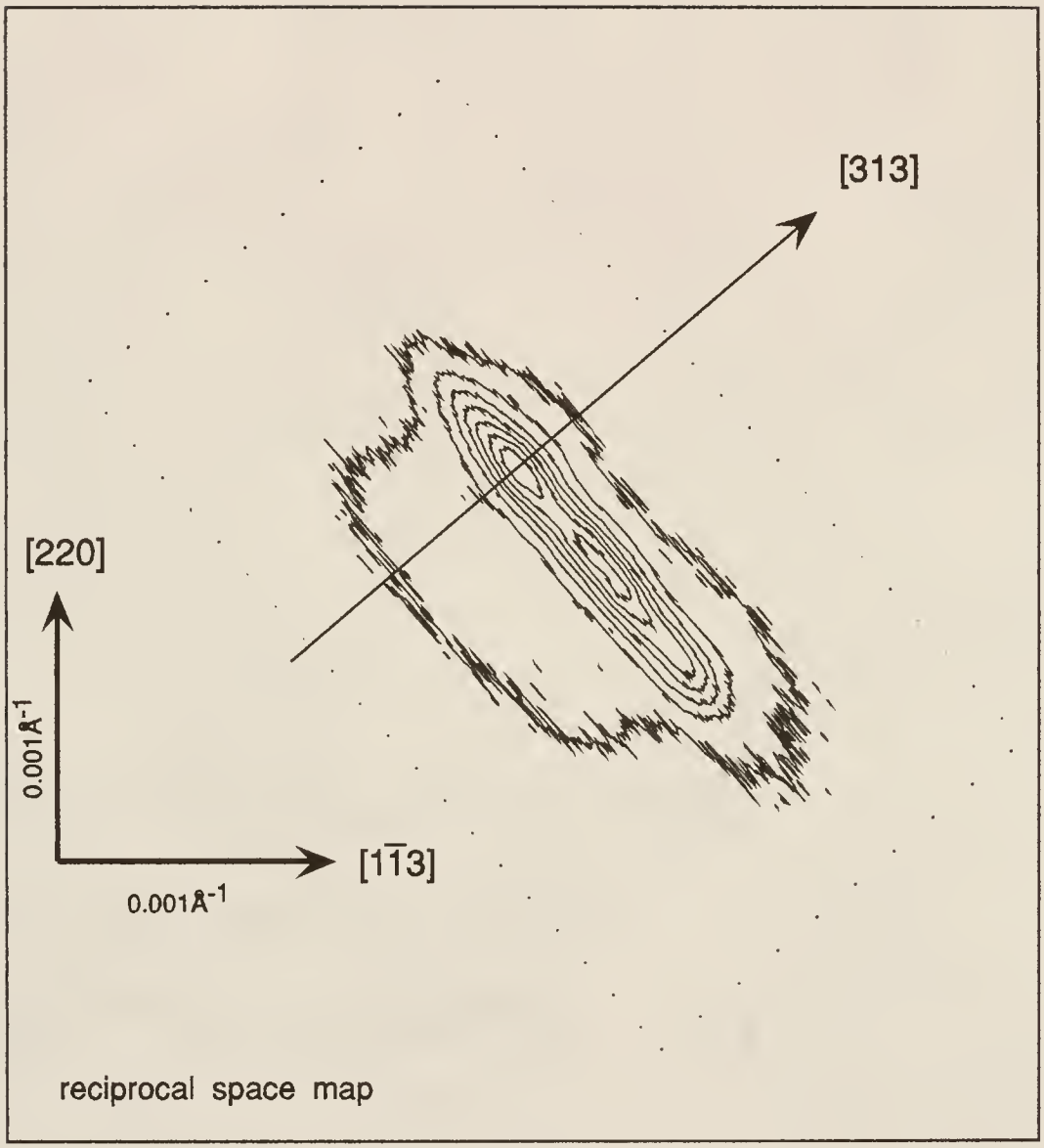

Figure 4.83 Reciprocal lattice space map (converted from an $\omega/2\theta$-ω x-ray map) for a 70μm thick 3% methanol film on a (110) diamond substrate. The spreading perpendicular to the [313] direction is due to mosaicity and the spreading along the [313] direction is due to tensile strain. .

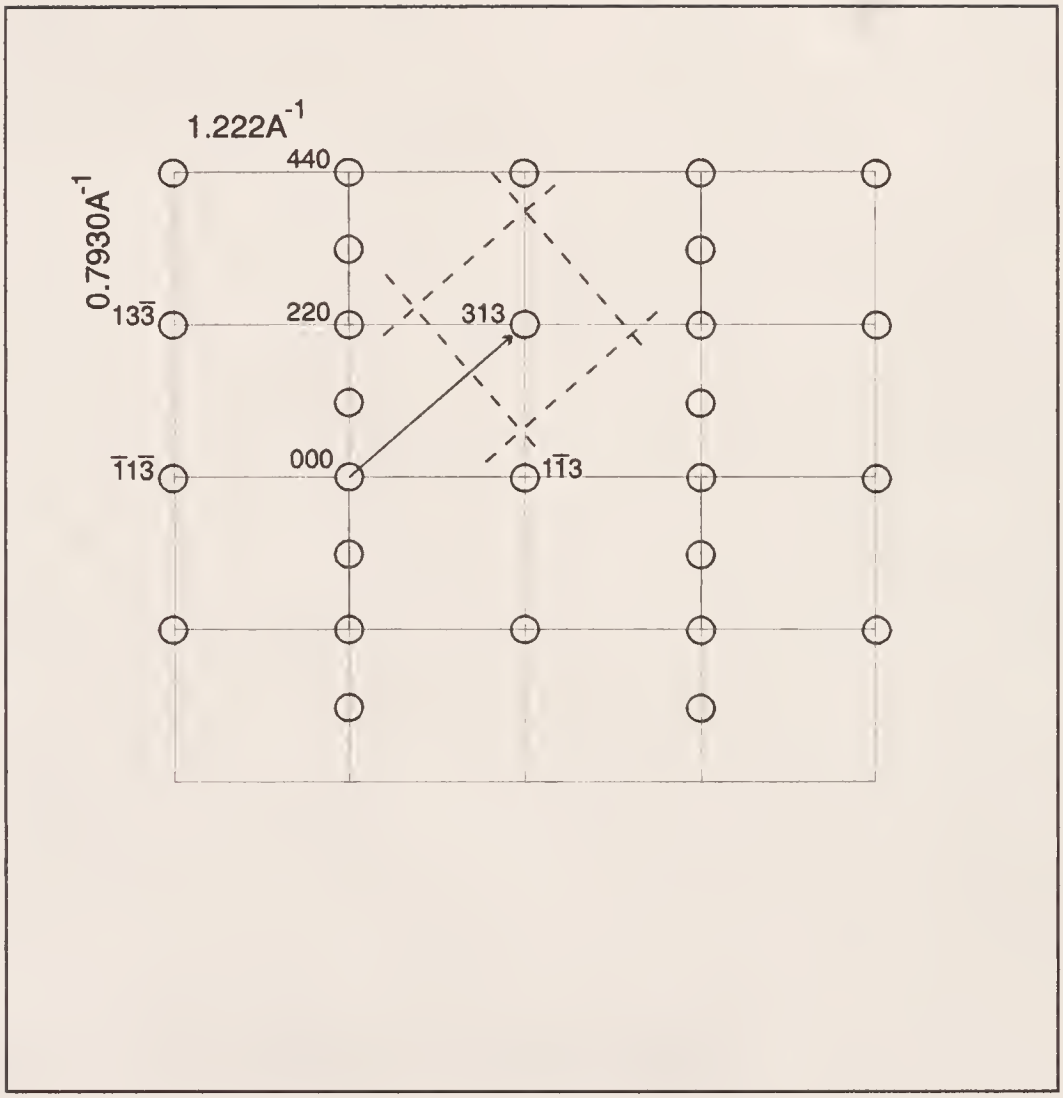

Figure 4.84 Schematic representation of the reciprocal lattice points for [110] oriented diamond and a [1$\bar{1}$3] reference azimuth.

CHAPTER 5
DISCUSSION

Surface Morphology

The surface of the diamond films were characterized with SEM to reveal any surface features or defects. All of the films grown on (111) substrates were polycrystalline. Badzian et al. [Bad93] observed polycrystalline films for growth on the (111) and attributed the loss of epitaxy to defect propagation. Smooth (111) films have been observed [Kon93, Hu92, Chu91], however the thickness of the films were on the order of a few micrometers. The (100) diamond surface exhibited growth steps, penetration twins, and pits defined by {111} surfaces. The surface was smooth around some of the penetration twins and pits. None of the diamond films grown on (100) substrates were smooth without these surface features. Smooth (100) surfaces are commonly observed on diamond crystallites. The features observed on the (100) homoepitaxial films are similar to those observed on the (100)

surface of diamond crystallites. The penetration twins have been modeled (through the α parameter) and explained by the preferred growth on the {111} twin planes. The (110) diamond films did not exhibit the penetration twins, pits, or faceted surface demonstrated by the (100) and (111) films. The (110) surface is the least examined surface of diamond out of the low index faces. Corrugated surfaces have been observed on the (110) surface [Bad93, Sna91], and was related to (111) and $(11\bar{1})$ microfaceting. Cracks were observed in the (110) but not the (100) or (111) films. Other groups have observed cracking in (111) films [Chu91, Hu92]. The films were a few micrometers in thickness and cracked along (111) cleavage planes.

It is note worthy that smooth (110) films were grown and exhibited cracks. Classifying the surface as smooth or rough is rather subjective, and some groups who report the morphology of their homoepitaxial films did not show SEM micrographs of the films [Tsu94, Mag92a, Mag92b, Sut92, Kom93, Chu92, Kon93]. Thus comparisons of our SEM micrographs with the literature was limited, however our results were similar to Kamo et. al. [Kam88], who observed faceting for (111),

smooth and faceted (110), and faceting and smooth surfaces with penetration twins (which they described as pyramidal steps) on (100) films. Films which exhibit polycrystalline facets, pits or penetration twins, were typically referred to as rough and the films without these prominent features are typically referred to as smooth. In addition, the observation of cracks in the (110) films and nor cracks in the (100), is important because below the development of stress, stress relief, and measurement of the stress are discussed below. Further characterization of the diamond film surface was outside the scope of this study. The development of penetration twins have been discussed in depth by Wild et al. [Wil94] and Tamor et al. [Tam94].

Raman Spectroscopy of Deposited Films

Raman spectroscopy is sensitive to the different structures of carbon, and stress in diamond films, as shown in Chapter 2. The results of the Raman analysis pertaining to the different carbon structures in the deposited films is discussed first, followed by discussion of the stress measurements.

The deposition of diamond versus non-diamond carbon was strongly dependent on the precursor and gas chemistry. Films grown with 0.5 and 1% acetone exhibited both diamond and non-diamond carbon, and acetone concentrations of 3% resulted in no detectable diamond deposition [Table 4.2]. In contrast, films grown with 3-100% methanol exhibited diamond Raman peaks. Methanol concentrations of 50% or higher resulted in non-diamond carbon in addition to the diamond. Raman spectroscopy results indicated that diamond was deposited preferentially over graphite at higher concentrations of hydrogen.

Most groups who have grown homoepitaxial diamond films used narrower ranges, if any, of gas compositions than we used in our study, e.g. 0.5% acetone [Hu92], 1% methane [Bad93], 0.2 to 0.85% methane [Sut92], 0.3 to 1% methane [Kam88], and 1 to 2% methane [Tsu94]. In addition, Raman spectrums from some these studies were not shown [Bad93, Sut92, Tsu94]. Zu et. al. showed a Raman spectrum from a 2-3μm thick (111) film, which had cracked. The spectrum exhibited a small peak at 1525cm^{-1} which is indicative of amorphous carbon, and a strong diamond peak. The author did not discuss the amorphous carbon peak; in addition, the diamond peak was suspect. As

discussed in Chapter 2, it is difficult to limit the diamond Raman intensity coming from the substrate and thus this diamond peak in this spectrum may have been due mostly to the substrate. More over, since the film had cracked, the diamond peak position should have been shifted, but this was not the case. This level of Raman analysis of homoepitaxial diamond films was typical.

Diamond and non-diamond carbon peaks were measured with Raman spectroscopy. More specifically, the non-diamond carbon peaks are categorized as graphite/amorphous carbon ($1360cm^{-1}$ and $1585cm^{-1}$) and diamond-like carbon ($1525cm^{-1}$). The homoepitaxial diamond films grown with higher concentrations of carbon (3% acetone and 90% methanol) exhibited the graphite and amorphous carbon peaks while the lower concentrations exhibited diamond-like carbon peaks. One of the objectives of this study was to use Raman analysis to characterize the homoepitaxial films and in the process, modify the experimental procedures to improve the results.

As shown in Figures 2.5 and 2.6 [Kaw87], other groups have observed that diamond films grown with higher hydrogen concentrations exhibit less intense non-diamond Raman peaks. Changing the precursor gas from high carbon to low carbon

concentrations results in films of loosely three groups: 1) amorphous or graphitic carbon, 2) diamond-like carbon and diamond, and 3) diamond.

Since the other growth parameters were held constant only the precursor gas bonding and concentrations were causes of the changed structure of the films. Spear et al. [Spe89] and others [Yar90, Cel91] discussed the importance of atomic hydrogen at the surface to minimize non-diamond and maximize diamond deposition. It is reasonable to postulate that atomic hydrogen concentration at the surface of the growing film was lower for the precursor gas chemistries of higher carbon concentration. For our substrate temperature, filament temperature, and other growth parameters, methanol concentrations lower than 50% were necessary to minimize the formation of non-diamond carbon.

Raman Analysis of Stress in (110) Films

The (110) films exhibited diamond Raman peaks which were shifted to lower wavenumbers. Both the film and substrate peaks were observable for most of the films. The method used in this study to distinguish the diamond film peak from the substrate peak was a significant improvement. No other groups

have reported separation of the film and substrate peaks from homoepitaxial diamond films. As mentioned in Chapter 2, Chu et al. [Chu91, Chu90] and others [Kaw93, Sut92] used isotopically labeled methane so that the film peak could be distinguished form the substrate peak. They recognized the difficulty in distinguishing the diamond film from the substrate peak. Using the methods outlined in Chapter 3 allows the observation and measurement of the diamond film peak without using isotopically labeled precursors.

Diamond Raman peak positions ranged from 1331.6cm^{-1} ($\Delta\nu$=-0.9cm^{-1}) to 1326.8cm^{-1} ($\Delta\nu$=-5.7cm^{-1}) resulting in calculated stresses of ~300MPa and ~1.9GPa, respectively. Chu et al. [Chu91] reported no peak shifts for (100), peak shifts of $\Delta\nu$=-1.1cm^{-1} for (110), and $\Delta\nu$=-5.1cm^{-1} for (111) ~3μm thick films grown with isotopically labeled methane. They did not report the FWHM of the diamond peaks, however by inspection of their Raman spectra, they appeared to be ~8cm^{-1} for the (100), ~10cm^{-1} for the (110), and ~20cm^{-1} for the (111). These widths of these peaks were broader than the typical widths measured in this study. The large FWHM are due to a large range of stresses in the films. They did not observe cracking in the

(110) film, but did observe cracking in the above (111) film after growing for an additional hour. This is not unexpected when compared to our results. The stress in their (111) film before cracking was ~1.7GPa using our calculation (Chapter 3), which was near our largest value of ~1.9GPa for a (110) film. Chu et al. [Chu91] indicated the stress may be due to graphitic inclusions. In contrast, the films used in this study were of better quality as indicated by the FWHM of the diamond peaks. No explanation for crack propagation or orientation was discussed. As mentioned above, Hu et al. [Hu91] observed cracking in (111) films but did not observe any peak shifts in the Raman data. The incorporation of stress and stress relief by cracking will be discussed below.

The Raman data for some of the (110) films showed broader substrate peaks when viewed from the film side versus the substrate side. Figures 4.26 to 4.29 show both the film and substrate peaks for a (110) film. Figure 4.30 shows the Raman spectrum of just the substrate as viewed from the substrate side. The FWHM of the substrate peak when viewed from the film side range from 3.8 to 4.6cm^{-1}, while from the substrate view the FWHM was 2.3cm^{-1}. This difference was due to the stress distribution near the interface. The tensile stress in

the film was balanced by a compressive stress in the substrate. The back of the substrate was stress free and the FWHM of the diamond peak was narrower indicating no stress distribution.

It should be noted that microcrystalline geometries influence the Raman peak position and broadening. The loss of long-range crystalline order results in a relaxation of the $q \approx 0$ selection rules and thus all phonons are allowed. The Raman peak then resembles the phonon density of states, exhibiting both a shift and asymmetric broadening to lower frequencies. Several groups have used Raman spectroscopy to characterize microcrystalline Si [Gon85, Cam86a, Fau85] and Ge [Gon85] films and amorphous Si films [Tsu83, Tsu82]. Campbell et al. [Cam86b] modeled the shape and position of the Raman peak for spherical, columnar, and thin slab microcrystals. Richter et al. [Ric81] theorized that a finite microcrystallite size of ~100Å was required to induce asymmetric broadening of the Raman peak, and others have observed peak shape changes at crystallite sizes of 150Å [Gon85] and 300Å [Fau85]. We did not observe asymmetry in our Raman peaks (we also did not expect are films to consists

of 100Å microcrystals) and therefore the peak shifting was due to tensile stress and not to microcrystalline effects.

Intrinsic Stress

It was initially expected that strain would not develop in a homoepitaxy system, since the lattice parameters and thermal expansion of the film and substrate were nominally the same. However this proved to be untrue. Several mechanisms are known to generate intrinsic stress, including, incorporation of impurities or residual gases in the film, differences in the lattice parameter, variation in interatomic spacing within the individual crystals (or mosaic blocks), low density of deposited films, and voids or dislocations [Ohr92].

In this study, SIMS and FTIR were used to determine that Re, Mo, O_2, and H_2 impurities were distributed throughout the film thickness, often with higher concentrations at the interface. Mosaic structures were also detected in the films by HRXRD, and mosaic structures are generally associated with formation and arrays of dislocations and defects. The quantification of SIMS data and mosaic structure observed with HRXRD will be discussed.

Classification of Natural Diamond and SIMS Analysis of Diamond Films

Natural diamond is generally classified into four categories defined by the nitrogen or boron concentration. Most diamonds are type Ia, containing up to ~0.3% nitrogen as aggregates in the lattice [Fie92]. These diamonds are generally colorless or yellow, but may also be brown or grey [Tre91]. Type Ib diamonds are rare and contain less nitrogen (~0.05%). The nitrogen in type Ib diamond is located on isolated substitutional sites, in contrast to the aggregates in type Ia, and they are inherently yellow [Tre91]. Type IIa diamonds are rare and contain nitrogen as the major impurity, although at concentrations less than type Ib, (i.e. ≤10ppm) [Tre91]. Type IIa diamonds, the type specified by the manufacturer to be the substrate for this study, are near colorless. Type IIb diamonds contain boron as the major impurity, contain little nitrogen (<10ppm), and are typically blue or grey in color [Tre91]. Diamonds can also exhibit characteristics from more than one category. Typical hydrogen concentrations in natural diamond are from 0.05-0.4%, but may be as high as 1.0% [Fie92]. Hydrogen concentrations are not

used for classifying diamonds.

The SIMS analysis showed nitrogen concentrations as high as 0.4-1.0at% in the diamond substrates. The diamond substrates were colorless and of type IIa according to the manufacturer, and should have contained much less nitrogen than was measured by SIMS. The estimated nitrogen fraction from SIMS analysis may be in error, since the relative sensitivity factor (RSF) for nitrogen in diamond was not known. For our calculations, the RSF for nitrogen in diamond was calculated from the ionization potential to be $1.3 \times 10^{23}/cm^3$, which may be accurate to within a factor of 3-5 (or 5 to 10, as discussed in Chapter 3, since the SIMS equipment we used in this study was not the same as the equipment used to measure RSF's in Wilson et al. [Wil89]). A nitrogen concentration of 1% as measured by SIMS has a range from 0.2-5% (or 0.1 to 10%). As mentioned above, Type IIa diamonds should contain ~10ppm N which was far below the level we measured. The N RSF value used for calculations was most likely inappropriate, however the change in N concentration at the film/substrate interface was significant and real. Our diamond substrates were colorless suggesting they did not contain these measured levels of N, which may cause the

substrates to be yellow, brown, or grey.

The Re wire filament and Mo substrate heater block were presumably the source of these impurities in the films. This is also reasonable since Re is unstable at high temperatures in oxygen-containing atmospheres because ReO_3 is formed and will sublime at T>720°C. Similarly, MoO_3 sublimes at T>900°C. Kamo et al. [Kam88] who grew films by PACVD also observed film contamination from the substrate holder. The lifetimes of Re filaments were shorter for growth cycles with higher methanol concentrations which correspond to higher O_2 concentrations and therefore more ReO_3 and MoO_3 formation. The increased concentration of Re at the diamond film/substrate interface can be explained by vaporization of ReO_3 during the initial stages of growth. Only hydrogen was flowed into the growth chamber while the substrate and filament temperatures were raised, and until the chamber pressure and temperatures stabilized. The methanol was then flowed and it is believed that the initial interaction of the Re filament with oxygen (from the methanol) was higher than after stabilization of the filament. Results from SIMS analysis on (100) and (110) films grown with 50% methanol are given in Table 5.1. For both orientations, impurity concentrations are higher at the

interface than in the film.

Table 5.1 Rhenium, molybdenum, and hydrogen concentrations in (110) and (100) diamond films grown with 50% methanol as calculated from SIMS data.

50% methanol films	Re(ppm)	Mo(ppm)	H(ppm)
(110) film	7	0.1	110,000
(110) film/substrate interface	39	0.5	128,000
(100) film	3	0.1	7,000
(100) film/substrate interface	18	0.7	11,000

Table 5.2 Cation or defect radius, impurity concentration, and calculated strain and stress.

Element	Cation radius (Å)	Concentration (ppm)	Lattice parameter difference	Stress (MPa) E=1143GPa
Rhenium	1.37	39 18 7 3	0.003% 0.0014% 0.0006% 0.0002%	35 16 6 2
Molybdenum	1.36	0.7 0.5 0.1	0.00005% 0.00004% 0.00001%	<1 <1 <1
Bond-centered H defect	1.1	128,000 110,000 11,000 7,000	5.5% 4.7% 0.47% 0.30%	62,800 53,900 5,390 3,400

Assuming that Re is substitutional (covalent radius=1.37Å), any change in the lattice parameter for a Re concentration of 39ppm, the concentration at the film/substrate interface, would be +0.003%. This would be the change in lattice parameter of the (110) 50% methanol interfacial layer from Re impurities only. The contribution from Mo is negligible since the covalent radius of Mo (1.36Å) is only ~0.7% smaller than the Re and the concentration is much less. Thus the film which contained 7ppm Re would have experienced a lattice parameter change of +0.0006%. The (100) film grown with 50% methanol which exhibited 3ppm Re in the film and 18ppm Re in the interface, would have experienced a lattice parameter change of +0.0014% and +0.0002%, at the interface and the bulk respectively. Thus, based on these estimates, the concentrations of Re and Mo were not sufficient to cause the magnitude of stress observed in the films. Stresses in the films were 1 to 2 orders of magnitude greater than those calculated from this assumption. This conclusion is also consistent with the fact that (100) film had contaminants, but did not exhibit stress.

Hydrogen concentrations were estimated from SIMS analysis to be 11at% in a (110) film and 0.7at% in a (100) film grown

with 50% methanol. An estimation from FTIR analysis resulted in 5.6at% hydrogen in the (110) film. It should be noted that diamond standards with known concentrations of H_2, O_2, Mo, Re, and N_2 were not available to accurately quantify SIMS data. Similarly, films grown with 30% methanol resulted in hydrogen fractions of 1.9 and <0.1at% for the (110) and (100) diamond films, respectively. Difference in H_2 incorporation for the two different film orientations may lend insight to growth mechanism(s) for these surfaces. In addition, the higher concentrations of the gaseous species in the (110) films could cause larger stresses and create stress concentrators. It was noted that their was inherent H_2 background in the SIMS analysis chamber, however since the intensity decreases through the film/substrate interface, the H_2 signal is a real signal. Kamo et. al. [Kam91] also observed higher H_2 concentrations in (110) and (100) films versus the substrates. In addition, the change in H_2 counts across the interface was more significant for the (110) versus the (100) film. No quantification of the SIMS data or discussion of stress was done.

Hydrogen concentrations from 0.1-5.0% have been reported for CVD films measured by nuclear reaction analysis (NRA) and

Rutherford backscattering spectrometry (RBS) [Dav93]. The 11at% measured in this study for (110) films is somewhat higher than other reported values [Dav93]. However (110) films consistently exhibited higher hydrogen fractions than the (100) films [Figure 4.44].

Theoretical calculations and muon spin-rotation experiments have been used to predict the position of hydrogen in the diamond lattice. Estle et al. [Est87] showed theoretically that bond-centered hydrogen is more stable than interstitial hydrogen. Briddon et al. [Bri88] have completed calculations to determine the structure of a hydrogen molecule in diamond. They show that the hydrogen molecule dissociates into a complex of a bond-centered hydrogen and a hydrogen at an anti-bonding site, which would have an H-C-H-C structure.

The bond-centered hydrogen is not infrared active because it does not exhibit a dipole moment. The frequency of vibration of the bond-centered hydrogen is $3132cm^{-1}$ assuming the carbon atoms are fixed [Bri88], and the hydrogen vibration is Raman active. Raman spectra from a homoepitaxial film which was not grown by HFCVD but with dc-plasma is shown in Figure 4.23 and a peak at $3116cm^{-1}$ is easily detected. Therefore we presume that this Raman peak results from bond-

centered hydrogen. Typically, Raman data from diamond rarely is reported above ~2000cm^{-1}. Hydrogen is expected to be distributed inhomogeneously in diamond and to rapidly diffuse in the diamond lattice. In addition, hydrogen may also sit in internal voids, or bond to carbon dangling bonds [Bri93].

The C-C bond length is 43% longer when the hydrogen is bond-centered [Bri88, Meh92]. To calculate the lattice parameter of the film with bond-centered, we assume a defect radius of 1.1Å. The lattice parameter change and the resultant stress calculated is approximately an order of magnitude larger than was measured [Table 5.2]. Based on the calculations thus far, H_2 defects are the most likely candidate in terms of impurities for causing stress. It should be added that only some of the hydrogen should be bond-centered, with other hydrogen atom being at tetrahedral interstitial positions or paired to other impurities or defects [Bri88, Meh92].

The larger concentration of hydrogen in the (110) films versus the (100) films, for the same growth conditions, is believed to be related to the growth mechanism(s). The steps necessary for diamond growth, which were given in Chapter 2, include the adsorption and desorption of hydrocarbons

and hydrogen. The surface energy for the (110) and (100) faces are different and should affect these gas/surface reactions. In addition, the number of carbon bonds associated with a surface carbon are different, presumably the growth mechanism(s) for the two faces would be different.

FTIR Analysis

SIMS analysis was corroborated with FTIR for measuring H_2 and O_2, and the concentrations increased for with increased methanol concentration. We followed an approach used by Couderc et al. [Cou87] to quantify the concentration of H_2. The number of C-H bonds (N_H) per cm^3 is related to the H_2 percentage [H] by:

$$N_H=\rho N_A[H]/\{m_C[C]+m_H[H]\} \qquad (5\text{-}1)$$

where [C] is the percentage of carbon, m_C and m_H are the atomic masses of C and H_2, respectively, N_A is Avogrado's number, and ρ is the film density. The relationship between the H_2 percentage in the film and the area of the total absorption band of the C-H bonds has been shown to be [Cou87]:

$$[H]=A(10^2)/\{(1.68\text{x}10^5)\rho+91.6A\} \qquad (5\text{-}2)$$

where A is the absorption band in cm^{-2}. The area of the absorption bands were determined by fitting with Voight functions and the results were listed in Table 4.5. Assuming the density of the diamond films was $3.52 g/cm^3$ (value for natural diamond) the H_2 concentration for the 10%, 30%, and 50% methanol films was <0.1%, 3.3%, and 5.6%, respectively. These values are probably only accurate to with an order of magnitude, since standards were not available. However, the concentrations were near those calculated from the SIMS data.

X-Ray Diffraction

The diamond films exhibited broadening of both the ω and $\omega/2\theta$ x-ray rocking curves, indicating mosaic spreading and lattice parameter variations. The increase in FWHM of the asymmetric $\omega/2\theta$ rocking curves indicating lattice parameter differences for the 7μm thick (110) films agree well with Raman data. The mosaic structure effected the broadening of the rocking curves more than the lattice parameter variation and was more significant for the asymmetric versus the symmetric reflections.

A mosaic structure will act as discrete diffracting blocks, whose diffraction vectors will give rise to broadening or peaks in the ω rocking curve. The broadening is dependent on the mosaic blocks misorientation with respect to diffracting plane, in addition to mosaic block size. If the misorientations and block sizes are large compared to the instrument resolution, than the ω rocking curve may exhibit discrete peaks as observed for the thicker films [Figures 4.79 and 4.82]. In addition, discrete layers, which are misoriented through the film thickness, may give rise to these discrete peaks.

It is difficult to quantify the mosaic spreading further than reporting the FWHM of the rocking curves without additional corroborative characterization. Fewster [Few91a] used x-ray topography to image the mosaic blocks in a GaAs substrate which resulted in a FWHM of ~200 arcsec for the ω rocking curve. The blocks had an average diameter of ~0.7mm, an angular distribution of ~35 arcsec relative to each other, and a spread of ~160 arcsec relative to the plane of the x-ray diffractometer. Typically, only the FWHM of the rocking curves are reported and quantification of the mosaic block

size and angular distribution is not done [Few92, Few91b, Few89, Hei94, Kop94, Kop93, Pet94]. We were not able to quantify the mosaic structure further than calculating the FWHM of the rocking curves.

Several intricacies should be considered when interpreting x-ray data from homoepitaxial systems. The film and substrate diffracted intensity contributions overlap and thus make it difficult to separate the independent contributions to the rocking curve. In addition, the initial state of stress and mosaicity of the substrate may change during the deposition of the film. Dislocations or other defects which nucleate at the interface during growth may propagate into the substrate. Further, if the deposited film is not free of stress, the film will induce a stress on the substrate.

We did not observe individual peaks for our $\omega/2\theta$ rocking curves which would facilitate the analysis of strain. However, we did observe an intensity distribution to lower angles for a 70μm thick film shown in Figure 4.80 which was indicative of tensile strain, or more precisely a larger lattice parameter. Fitting the rocking curve with two Gaussian peaks resulted in a peak separation of ~250arcsec

between the main peak (at 0arcsec) and the low intensity peak. This 250arcsec shift results in a tensile strain of ~1575ppm through Braggs law and a tensile stress of ~1.8GPa through Youngs modulus. This value is nearly equal to the value measured by Raman spectroscopy for this film.

In future studies, the mosaic structure revealed by x-ray mapping should by corroborated and quantified with either x-ray topography or TEM. Both x-ray topography and TEM can be used to characterize the size and distribution of mosaic blocks. This information combined with the angular spread of the mosaic blocks provided by x-ray will fully reveal the mosaic structure of the film.

Cracking of Films

Diamond, like other ceramics, is a brittle material and normally fractures before significant plastic deformation can occur. Ceramics can support large loads in compression but are susceptible to cleavage crack propagation under tension. Brittle fracture occurs perpendicular to a resolved tensile stress and proceeds along cleavage planes, and are the {111} planes in diamond, which have high atomic densities. The cleavage energy for several diamond planes are given in Table

5.3. Fracture promoted by resolved shear stress greater than a critical value, results in extensive dislocation glide on a slip plane in a slip direction and is referred to as the shear or ductile mode of fracture [Die86].

The slip system for diamond-cubic structures is the {111}/<110> and dislocations move in response to shear stresses resolved along these close-packed planes and close-packed directions. Shear stresses greater than the critical value for slip may be produced on planes which are not perpendicular or parallel to the applied tensile stress. Slip, in a single crystal, proceeds on the slip system with the highest resolved shear stress. If the stress axis is perpendicular to the slip direction or parallel to the slip plane, then the critical resolved shear stress, τ_{crss}, will be zero and the crystal fractures rather than deform plastically. The critical resolved shear stress is the amount of stress required to cause slip and is crudely related to the yield strength (σ_y) and slip system by:

$$\sigma_y = \tau_{crss}/\cos\phi\cos\lambda \qquad (5\text{-}3)$$

where ϕ is the angle between the slip plane normal and the

stress axis and λ is the angle between the slip direction and the stress axis. The minimum stress required to produce yielding occurs when $\phi=\lambda=45°$. The critical resolved shear stress for diamond at 1100°C has been reported to be 0.7-1.5GPa [Field 93], which is significantly lower than would be expected considering the values for the yield strength and the shear modulus for the {111}/<110> slip systems are 35GPa and 507GPa, respectively. However, this may be explained by dislocation climb at elevated temperatures as will be discussed below.

Fractures observed in the (110) films were due to tensile stresses. Two surfaces, each with a surface energy (γ), are created by fracture in a brittle solid. The critical normal stress for brittle fracture is [Die86]:

$$\sigma_c = P/A \cos^2\phi = \sigma\cos^2\phi \qquad (5\text{-}4)$$

where P is force, A is area of the plane, and ϕ is the angle between the plane normal and the stress axis.

Table 5.3 Theoretical cleavage energies for diamond [Fie92].

Miller indices of plane exhibiting cleavage	Angle between cleavage plane and (111) plane (degree)	Cleavage energy (J/m^2)
111	0, 70.5	10.6
332	10.0	11.7
221	15.8	12.2
331	22.0	12.6
110	35.3, 90.0	13.0
322	11.4	13.4
321	22.2	14.3
211	19.5	15.0
320	36.8	15.3
210	39.2	16.4
311	29.5	16.6
100	54.7	18.4

The critical stress (σ_c) required for crack propagation in a brittle material is given by [Cal94]:

$$\sigma_c=(2\gamma E/\pi c)^{1/2} \qquad (5\text{-}5)$$

where E is Young's modulus of the film, 2γ is the energy of the surfaces created by the crack, and c is one half of the

crack length. The crack tip radius is not used here, but it is assumed that the crack tip radius is on the order of the interatomic spacing [Cal94]. Substituting values of E=1143GPa, $\gamma_{(111)}$=5.3J/m^2, and arbitrary length c=1μm results in a fracture stress of 1.96GPa. This value is nearly equal to the largest stresses measured in this study. When the fracture stress is exceeded the crack grows catastrophically. Stress intensity factors amplify the stress acting on cracks. The stress intensity factor, K_{Ic} is [Her89, Fie93]:

$$K_{Ic}=(2\psi E\gamma)^{0.5} \qquad (5\text{-}6)$$

where ψ is a surface roughness factor and ranges from 1 for ideally smooth surfaces to 1.8-4 for practical surfaces. Cracks are formed when the strain energy in the film is greater than the energy required to create the new surfaces. Field [Fie93] reported a diamond fracture toughness (K_{Ic}) of ~3.4-5.0 MNm$^{-3/2}$, depending on surface roughness. The fracture toughness is strongly dependent upon the crack and sample geometry.

The magnitude of stress and observations of cracks was a function of the film thickness and gas chemistry. A film grown with 50% methanol cracked at 7μm thick while a 3% methanol film did not crack at 70μm thickness. Films grown with 10% methanol cracked at thicknesses between 25μm to 100μm. The largest shift of the diamond Raman peak was -5.7cm^{-1} to 1326.8cm^{-1} measured for a 25μm thick film grown with 10% methanol. Using κ=2.94cm^{-1}/GPa and $\Delta\nu$=5.7cm^{-1} results in a stress of 1.93GPa and strain of 0.17% (assuming E=1143GPa). We calculated that the (110) diamond films would crack at tensile stresses of ~2GPa.

Table 5.4 Theoretical tensile and shear strengths of diamond and silicon [Fie92].

Material property	Diamond	Silicon
Fracture strength in tension <111>	190GPa	32GPa
Critical resolved shear strength <110>{111}	121GPa	14GPa

Since the (110) films exhibited cracking and the (100) films did not, we address the orientation of the slip systems

for the two orientations. Four {111} planes intersect the (100) and (110) surfaces. The angle between the (100) surface plane and the four intersecting {111} planes shown in Figure 5.1 is 54.7°. In contrast, two {111} planes are perpendicular and two {111} planes are at an angle of 35.3° to the (110) surface. The difference between the (100) and the (110) orientation is that under biaxial stress, the shear stress resolved on the slip systems ({111}/<110>) are zero for the {111} planes which are perpendicular to the surface, while tensile stresses have a maximum value. As mentioned earlier, shear stresses occur when the stress axis is not parallel to the slip direction or slip plane normal. Since the shear stress is zero on the {111} planes which are perpendicular to the stress axis, and for tensile stresses (versus compressive), especially for brittle ceramics, this may result in cleavage cracking for (110) films. Shear stresses develop on the {111} planes under plane stress for the (100) films which may be sufficient to activate the slip system. In addition, this stress, especially at elevated temperatures (960°C), may lead to dislocation glide and climb on these cleavage planes.

Dislocation glide is a strain relaxation mechanism and for the diamond cubic lattice, this motion is on {111} planes in a <110> direction. Dislocation motion is impeded by defects such as impurities and other defects. However, at elevated temperatures, dislocations may circumvent obstacles by climbing vertically and then continue by climbing vertically and then continue to glide. Since there were more impurities in (110) films, there were more obstacles to dislocation motion. The impediment of dislocation motion in (110) films may have facilitated large tensile stress. In contrast for (100) films, fewer impurities may have allowed relief of the stress by dislocation motion.

Dislocation motion in semiconductors are typically dominated by the Peierls barrier [Hul92]. The glide activation energies for covalently bonded materials, e.g. Ge (1.6eV) and Si (2.2eV), are higher than for partially covalent materials, e.g. GaAs (1.1eV), for stresses in the 100's of MPa. It is expected that diamond would have a higher activation energy since the bonding between carbon atoms is stronger than that between Si atoms. Dislocations which may be nucleated at an interface as a strain relaxation process, propagate, and interact. The orientation of the film or more

specifically, the angle the {111} glide planes intersect the surface, strongly effect the propagation of these dislocations. Hull and Bean [Hull92] have shown that for GeSi layers on Si, movement of dislocations from the interface for (100) films is more energetically favorable versus (110) films. The nucleation and propagation of the dislocations may allow the (100) films to relieve stress during the growth process and thus minimize the development of the large stresses which were observed for the (110) films.

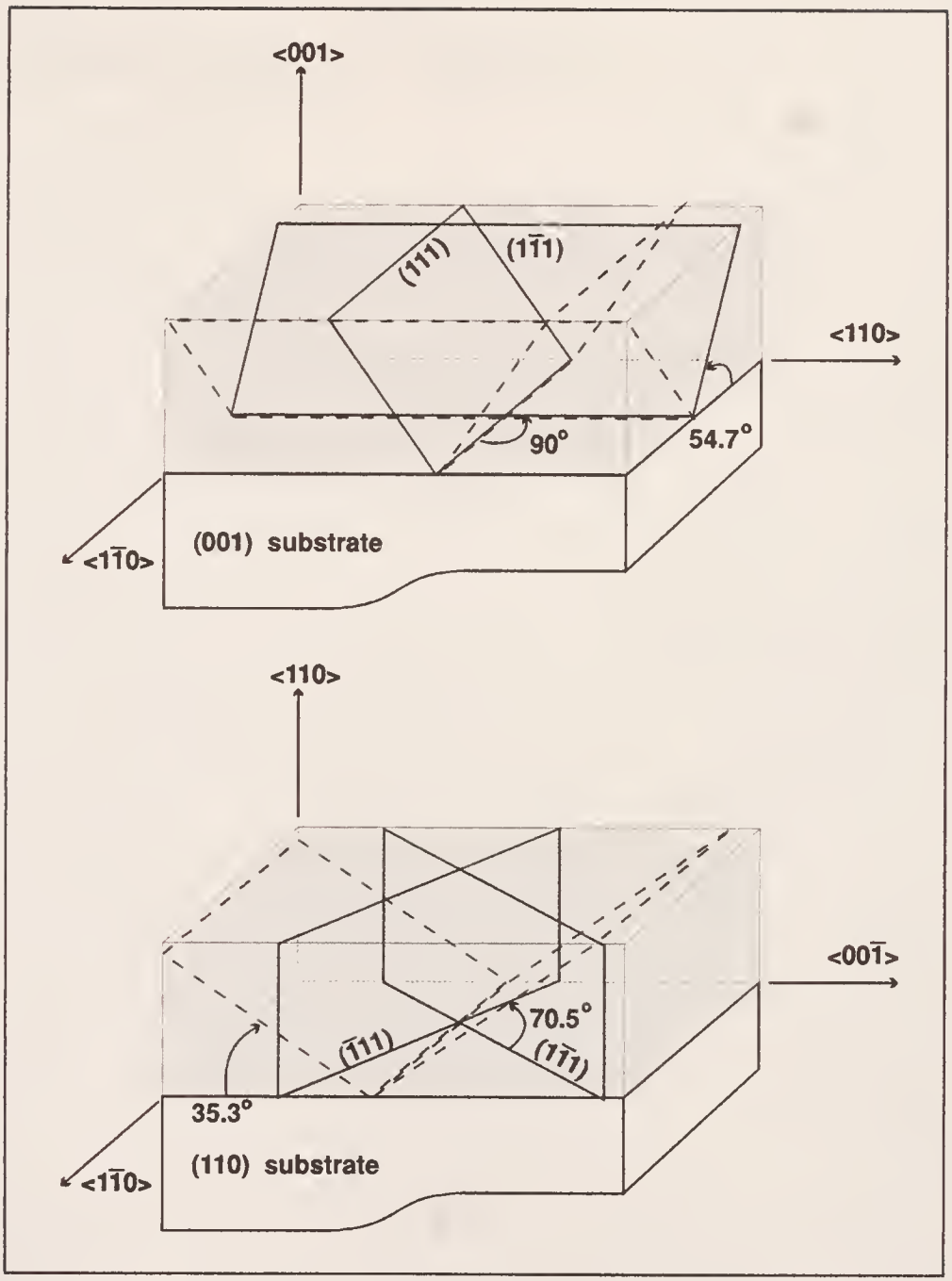

Figure 5.1 Illustration of the orientation of the {111} cleavage planes in a (100) and (110) film.

CHAPTER 6
SUMMARY AND CONCLUSIONS

Diamond films were grown on (100), (110), and (111) oriented natural diamond substrates by hot filament assisted chemical vapor deposition (HFCVD) to thicknesses of 7 to 100μm. The substrate and filament temperatures were 960°C and 2000°C, respectively, and the chamber pressure was 40Torr for all growths. The precursor gas was either 3 to 100% methanol, hydrogen balance, or 0.5 to 3% acetone, hydrogen balance.

Raman spectroscopy was used to measure amorphous or graphitic carbon versus diamond. The Raman spectrum was modeled with Voight functions to determine the FWHM and position of the peaks. Films grown with ~90% methanol exhibited diamond (1332cm^{-1}) and amorphous or graphitic (1360 and 1591cm^{-1}) peaks, while films grown with 3 to 18% methanol exhibited no amorphous or graphitic carbon Raman peaks. Films grown with 0.5, 1, and 3% acetone exhibited amorphous or graphitic carbon peaks while only the 0.5 and 1% acetone

exhibited a diamond peak.

A method for increasing the precision of stress measurement of diamond, via Raman spectroscopy, was developed. A krypton lamp was used to provide and internal calibration line at 1320cm^{-1}. Stress effects the vibrational frequency of the atoms in the lattice and this change in frequency was measured with Raman. Using values from the literature, the diamond Raman mode peak was found to shift as a function of stress by 2.94cm^{-1}/GPa. This approach was used to quantify the magnitude of stress which was as large as 2GPa (tension) and sufficient to cause cracking in some of the (110) films. Films grown on (100) substrates did not exhibit cracking or stress. Further modifications of the Raman spectrometer included a pinhole aperture to reduce the sampling depth of the Raman. Reducing the sampling depth increased the film to substrate intensity ratio measured by the spectrometer. It was difficult to resolve the diamond peak from the film with respect to the substrate peak with out the aperture.

The development of stress was attributed to the incorporation of impurities and the film orientation. Impurities (Re, Mo, O_2, and H_2) were detected and measured with secondary ion mass spectrometry (SIMS). Hydrogen

concentrations as large as ~11% and ~0.7% were measured for (110) and (100) films grown with 50% methanol, respectively. Similarly, Re concentrations were 39ppm versus 18ppm for the (110) and (100) film. respectively. Impurity concentrations were greater at the interface than through the film thickness. Fourier transform infrared spectroscopy (FTIR) was also used to measure H_2 and O_2 impurities in the films and corroborate SIMS data.

The Griffith model of crack propagation versus slip was used to predict the cracking of the (110) films. Two of the {111} cleavage planes are perpendicular to the (110) surface allowing tensile stress to be a maximum. It was speculated that microflaws in the film created stress intensity factors which under tensile stress caused crack propagation. All four of the {111} cleavage planes are orthogonal to the (100) surface resulting in shear stress creating slip on these planes.

Homoepitaxial diamond films were further characterized with seven crystal x-ray diffraction. This is a relatively new characterization tool which allowed the separation of orientation and lattice parameter. This was achieved by combining the monochromated x-ray source provided by a four

crystal monochromator and an analyzer crystal which narrows the acceptance angle of the detector. Broadening of the x-ray rocking curves due to mosaicity ranged from 15 arcsec for a 7μm film to 1000 arcsec for a 100μm thick film, both grown with 10% methanol. The broadening of the x-ray rocking curves due to strain for these same two film was 12 and 360 arcsec, respectively. The mosaic spreading increased with increased film thickness and methanol concentration. Increased mosaicity may be interpreted as increased dislocation density since a dislocation network accommodates the relative tilt of the mosaic blocks.

APPENDIX
CARBON PHASES

Diamond, graphite, and lonsdaleite are crystalline carbon phases and are characterized by the hybridization of the carbon. Both diamond and lonsdaleite consist of sp^3 tetrahedrally bonded carbon and graphite is formed of trigonally hybridized sp^2 carbon. The atomic arrangements of the three carbon phases is shown in Figure A1.

Table A1. Properties of diamond, lonsdaleite, and graphite (from Field [Fie92]).

Property	Diamond	Lonsdaleite	Graphite
Lattice Parameter (Å)	3.57	a=2.52 c=4.12	a=2.47 c=6.71
Bonding	sp^3	sp^3	sp^2
C-C nearest neighbor (Å)	1.54	1.52	1.42
Density (g/cm^3)	3.52	3.52	2.3
Crystal Structure	diamond cubic	hexagonal close packed	hexagonal
Space Group	O_h^7	$D_{6\ h}^4$	$D_{6\ h}^4$

Hybridization is the mixing of atomic orbitals of an atom to give a new set of orbitals, and provides a connection between the observed molecular geometry and electron configuration [Moe84]. In sp^2 bonded carbons, 1 s and 2 p orbitals combine to give 3 sp^2 hybrid orbitals. Similarly, sp^3 bonded carbons 1 s and 3 p orbitals combine to give 4 sp^3 orbitals.

There are various classifications of amorphous and graphitic carbon. The Raman spectra shown in Figures A1 and A2 are from Knight et al. [Kni89] and demonstrate the various peaks exhibited by amorphous and graphitic carbon.

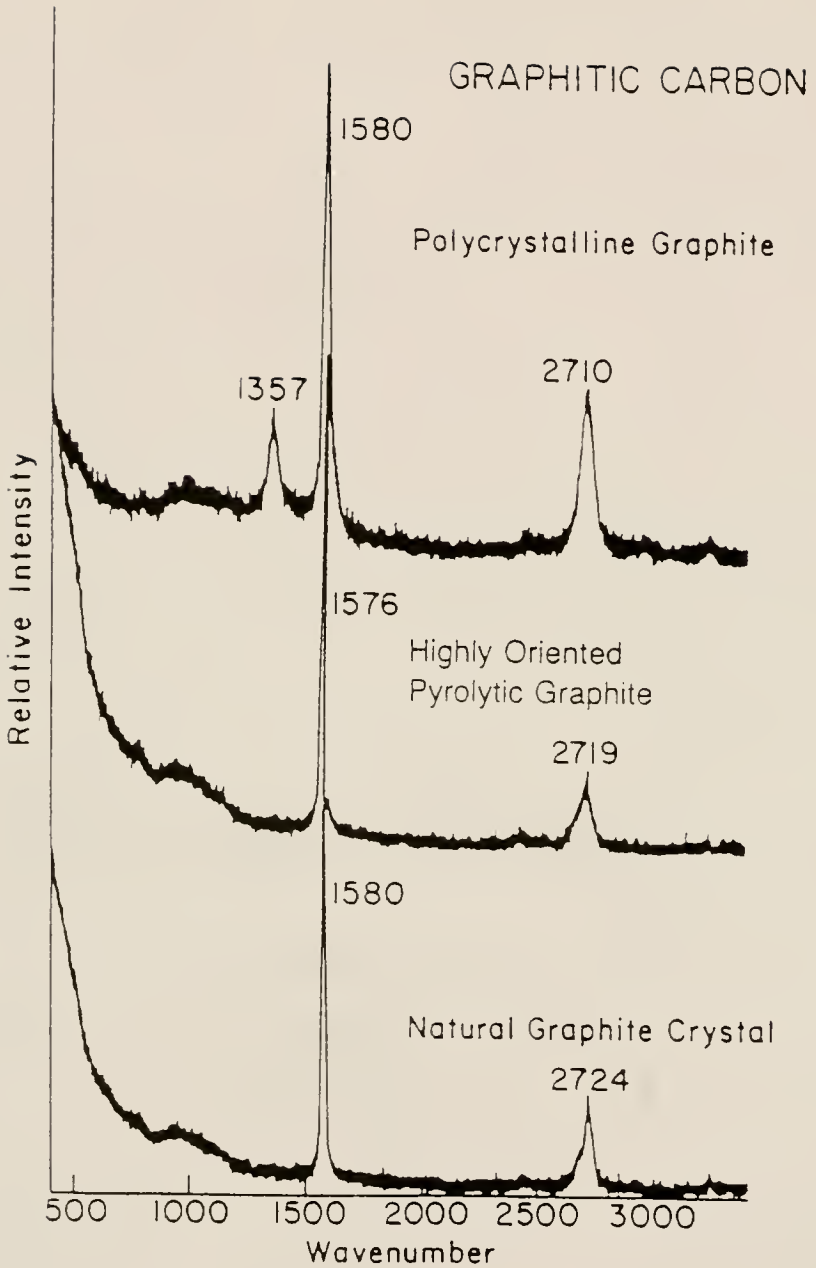

Figure A1 Raman spectra of several graphitic carbons [Kni89].

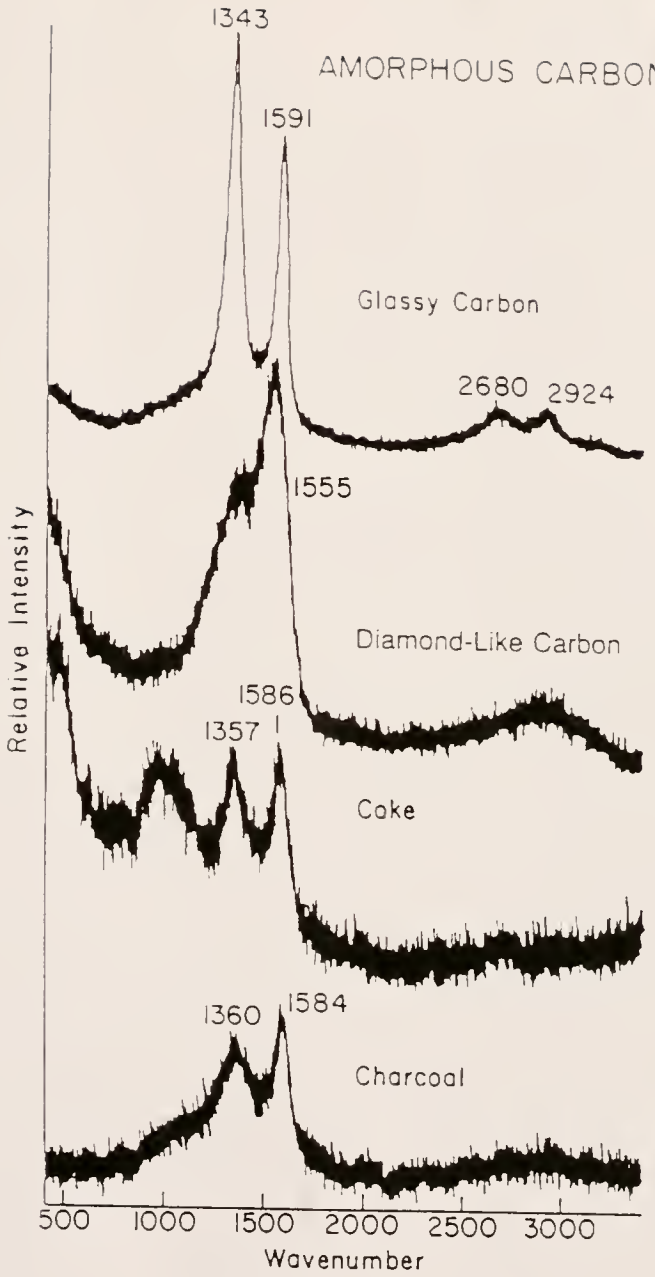

Figure A2 Raman spectra from various amorphous carbons [Kni89].

REFERENCE LIST

Ale92 W.B. Alexander, P.H. Holloway, L. Heatherly and R.E. Clausing, Surf. Coat. Technol. **54/55**, 387 (1992).

Ale94 W.B. Alexander, P.H. Holloway, J. Simmons and R. Ochoa, J. Vac. Sci. Technol. A **12**, 2943 (1994).

Ana70 E. Anastassakis, A. Pinczuk, E. Burstein, F.H. Pollak and M. Cardona, Solid State Comm. **8**, 133 (1970).

Ang68 J.C. Angus, H.A. Will and W.S. Stanko, J. Appl. Phys. **39**, 2915 (1968).

Ang88 J.C. Angus and C.C. Hayman, Science **241**, 913 (1988).

Ang91 J.C. Angus, Y. Wang and M. Sunkara, Annu. Rev. Mater. Sci. **21**, 221 (1991).

Arm67 B.H. Armstrong, J. Quant. Spectrosc. Radiat. Transfer **7**, 61 (1967).

Bac91 P.K. Bachmann, D. Leers and H. Lydtin, Diamond and Related Materials **1**, 1 (1991).

Bad91 A.R. Badzian, T. Badzian, X.H. Wang and T.M. Hartnett, New Diamond Science and Technology; MRS Int. Conf. Proc. **1**, 549 (1991).

Bad93 A. Badzian and T. Badzian, Diamond and Related Materials **1**, 1 (1993).

Bar87 H. Baranska, A. Labudzinska and J. Terpinski, *Laser Raman Spectrometry: Analytical Applications.* J.R.

Majer, Eds., (John Wiley & Sons, New York, 1987).

Bar83 W.J. Bartels, J. Vac. Sci. Technol. B **1**, 338 (1983).

Bon65 U. Bonse and M. Hart, Appl. Phys. Lett. **7**, 238 (1965).

Bop85 H. Boppart, J. van Straaten and Isaac F. Silvera, Phys Review B **32**, 1423-1425 (1985).

Bri88 P. Briddon, R. Jones and G.M.S. Lister, J. Phys. C: Solid State Phys. **21**, L1027 (1988).

Bri93 P.R. Briddon and R. Jones, Physica B **185**, 179 (1993).

Bru92 C.R. Brundle, C.A. Evans and S. Wilson, Eds., *Encyclopedia of Materials Characterization* (Butterworth-Heinemann, Boston, 1992).

Cah95 R.W. Cahn, D. Bloor, M.C. Flemings, R.J. Brook and S. Mahajan, *The Encyclopedia of Advanced Materials* (Elsevier Science Inc., New York, 1994), vol. 3.

Cal94 W. Callister, *Materials Science and Engineering: An Introduction* (John Wiley & Sons, Inc., New York, 1994).

Cam86a I.H. Campbell and P.M. Fauchet, Mater. Res. Symp. Proc. Vol. 53, 311 (1986).

Cam86b I.H. Campbell and P.M. Fauchet, Solid State Comm. **58**, 739 (1986).

Cel90 F.G. Celii, P.E. Pehrsson, H.-t. Wang, H.H. Nelson and J.E. Butler, Proc. 1st Int. Conf. New Diamond Sci. Technol. October 1988 , 17 (1990).

Cel91 F.G. Celii and J.E. Butler, Annual Reviews of Physical Chemistry **42**, 643 (1991).

Cer72 F. Cerdeira, C.J. Buchenauer, F.H. Pollak and M. Cardona, Phys. Rev. B **5**, 580 (1972).

Chu90 C.J. Chu, M.P. D'Evelyn, R.H. Hauge and J.L. Margrave, J. Mater. Res. **5**, 2405 (1990).

Chu91 C.J. Chu, M.P. D'Evelyn, R.H. Hauge and J.L. Margrave, J. Appl. Phys. **70**, 1695 (1991).

Chu92 C.J. Chu, R.H. Hauge, J.L. Margrave and M.P. D'Evelyn, Appl. Phys. Lett. **61**, 1393 (1992).

Cla89 R.E. Clausing, L. Heatherly and K.L. More, Surf. Coat. Technol. **39/40**, 199 (1989).

Cla91 R.E. Clausing, L. Heatherly, E.D. Specht and K.L. More, New Diamond Science and Technology; MRS Int. Conf. Proc. **1**, 575 (1991).

Cou87 P. Couderc and Y. Catherine, Thin Solid Films **146**, 93 (1987).

Cul78 B.D. Cullity, *Elements of X-ray Diffraction* (Addison-Wesley Publishing Co. Inc., Reading, MA, 1978).

Dav93 Robert F. Davis, Eds., *Diamonds Films and Coatings* (Noyes Publications, Park Ridge, N.J., 1993).

Die86 G. E. Dieter, *Mechanical Metallurgy* (McGraw-Hill Book Co., New York, 1986).

Die93 B. Dietrich, E. Bugiel, J. Klatt, G. Lippert, T. Morgenstern, H.J. Osten and P. Zaumseil, J. Appl. Phys. **74**, 3177 (1993).

Est87 T.L. Estle, S. Estreicher and D.S. Marynick, Phys. Rev. Lett. **58**, 1547 (1987).

Eve94 M.P. Everson, M.A. Tamor, D. Scholl, B.R. Stoner, S.R. Sahaida and J.P. Bade, J. Appl. Phys. **1**, 169 (1994).

Fau85 P.M. Fauchet, I.H. Campbell and F. Adar, Appl. Phys. Lett. **47**, 479 (1985).

Few87 P.F. Fewster and C.J. Curling, J. Appl. Phys. **62**, 4154 (1987).

Few89 P.F. Fewster, J. Appl. Cryst. **22**, 64 (1989).

Few91a P.F. Fewster, Appl. Surf. Sci. **50**, 9 (1991).

Few91b P.F. Fewster, J. Appl. Cryst. **24**, 178 (1991).

Few92 P.F. Fewster, J. Appl. Cryst. **25**, 714 (1992).

Few93a P.F. Fewster and N.L. Andrew, J. Appl. Phys. **74**, 3121 (1993).

Few93b P.F. Fewster, Philips J. Res. **47**, 235 (1993).

Fie86 J.E. Field, Inst. Phys. Conf. Ser. **3**, 181 (1986).

Fie92 J.E. Field, Eds., *The Properties of Natural and Synthetic Diamond* (Academic Press, London, 1992).

Fre88 M. Frenklach and K.E. Spear, J. Mater. Res. **3**, 133 (1988).

Fuj90 N. Fujimori, T. Imai, H. Nakahata, H. Shiomi and Y. Nishibayashi, Mat. Res. Soc. Symp. Proc. **162**, 23 (1990).

Gan70 S. Ganesan, A.A. Maradudin and J. Oitmaa, Annals of Physics **56**, 556 (1970).

Gei90 M.W. Geis, Mat. Res. Soc. Symp. Proc. **162**, 15 (1990).

Gil91 G.Sh. Gildenblat, S.A. Grot and A. Badzian, Proceedings of the IEEE **79**, 647 (1991).

Gon85 J. Gonzalez-Hernandez, G.H. azarbayejani, R. Tsu and F.H. Pollack, Appl. Phys. Lett. **47**, 1350 (1985).

Goo90 D.G. Goodwin and G.G. Gavillet, J. Appl. Phys. **65**, (1990).

Gri78 M. H. Grimsditch, E. Anastassakis and M. Cardona, Phys. Rev. B **18**, 901-904 (1978).

Har88 S.J. Harris, A.M. Weiner and T.A. Perry, Appl. Phys. Lett. **53**, 1605 (1988).

Har89 S.J. Harris, J. Appl. Phys. **65**, 3044 (1989).

He93 X. He and M. Razeghi, J. Appl. Phys. **73**, 3284 (1993).

Hei94 H. Heinke, M.O. Moller, D. Hommel and G. Landwehr, J. Cryst. Growth **135**, 41 (1994).

Hir86 Y. Hirose and Y. Terasawa, Jpn. J. Appl. Phys. **25**, L519 (1986).

Hir89 Y. Hirose, S. Amanuma, N. Okada and K. Komaki, Proc. 1st. Int. Symp. Diamond and Diamond-Like Films **12**, 80 (1989).

Hol93 V. Holy, J. Kubena, E. Abramof, K. Lischka, A. Pesek and E. Koppensteiner, J. Appl. Phys. **74**, 1736 (1993).

Hol93 V. Holy, J. Kubena, E. Abramof, A. Pesek and E. Koppensteiner, J. Phys. D: Appl. Phys. **26**, A146 (1993).

Hul92 R. Hull and J. Bean, Critical Reviews in Solid State and Materials Sciences **17**, 507 (1992).

Ito91 H. Itoh, T. Osaki, H. Iwahara and H. Sakamoto, J. Mater. Res. **1**, 3763 (1991).

Kam88 M. Kamo, H. Yurimoto and Y. Sato, Appl. Surf. Sci. **33/34**, 553 (1988).

Kaw87 T. Kawato and K. Kondo, Jpn. J. Appl. Phys. **26**, 1429 (1987).

Kit86 C. Kittel, *Introduction to Solid State Physics* (John Wiley & Sons, Inc., 1986).

Kle86 M.V. Klein and T.E. Furtak, *Optics* (John Wiley & Sons, New York, 1986).

Kni89 D.S. Knight and W.B. White, J. Mater. Res. **4**, 385 (1989).

Kob88 K. Kobashi, K. Nishimura, Y. Kawate and T. Horiuchi, Phys. Rev. B **38**, 4067 (1988).

Koi94 P. Koidl, C. Wild and N. Herres, Proc. NIRIM Intern. Symp. on Advanced Materials , (1994).

Kon93 E. Kondoh, K. Tanaka and T. Ohta, J. Appl. Phys. **74**, 2030 (1993).

Kop94 E. Koppensteiner, P. Hamberger, G. Bauer, V. Holy and E. Kasper, Appl. Phys. Lett. **64**, 172 (1994).

Liu93 Z. Liu, R. Zhang, M. Liu, G. Yang, Q. Liu, R. Wang, W. Wang, W. Ji, X. Ji and D. He, J. Mater. Sci. **28**, 5313 (1993).

Lux91 B. Lux and R. Haubner, Diamond and Diamond-Like Films and Coatings **1**, 579 (1991).

Mar94 M. Marchvwka, S.C. Binari, P.E. Pehrsson and D. Moses, unpublished , (1994).

Mat82 S. Matsumoto, Y. Sato, M. Kamo and M. Setaka, Jpn. J. Appl. Phys. **21**, L183 (1982).

Maz92 A. Mazuelas, J. Melendez, M.L. Dotor, P. Huertas, M. Garriga and D. Golmayo, J. Appl. Phys. **72**, 2528 (1992).

Meh92 S.P. Mehandru and A.B. Anderson, J. Mater. Res. **7**, 689 (1992).

Mel90 Melles Griot, *Optics Guide 5* (Melles Griot, Irvine, 1990).

Mey91 F. Meyer, M. Zafrany, M. Eizenberg, R. Beserman, C. Schwebel and C. Pellet, J. Appl. Phys. **70**, 4268

(1991).

Moe84 T. Moeller, Jr. J.C. Bailar, J. Kleinberg, C.O. Guss, M.E. Castellion and C. Metz, *Chemistry with Inorganic Qualitative Analysis* (Academic Press, Orlando, 1984).

Ohr92 M. Ohring, *The Materials Science of Thin Films* (Academic Press, Boston, 1992).

Ona77 S. Onari, M. Cardona, E. Schonherr and W. Stetter, Phys. Status Solidi B **79**, 269 (1977).

Par77 B.J. Parsons, Proc. R. Soc. Lond. A. **352**, 397 (1977).

Pes91 A. Pesek, K. Hingerl, F. Riesz and K. Lischka, Semicond. Sci. Technol. **6**, 705 (1991).

Pet94 J. Petruzzello, J. Gaines and P. van der Sluis, J. Appl. Phys. **75**, 63 (1994).

Pol91 F. Pollak, *Analytical Raman Spectroscopy*. J.G. Grasselli and B.J. Bulkin, Eds., (John Wiley & Sons, Inc., New York, 1991).

Pue81 J. Puerta and P. Martin, Appl. Opt. **20**, 3923 (1981).

Qua93 L.G. Quagliano and Z. Sobiesierski, Superlatt. Microst. **13**, 105 (1993).

Rav93 K.V. Ravi, Mater. Sci. & Engr. **B19**, 203 (1993).

Rya87 T.W. Ryan, P.D. Hatton, S. Bates, M. Watt, C. Sotomayor-Torres, P.A. Claxton and J.S. Roberts, Semicond. Sci. Technol. **2**, 241 (1987).

Seg89 A. Segmuller, I.C. Noyan and V.S. Speriosu, Prog. Crystal Growth and Charact. **18**, 21 (1989).

Sha85 S.K. Sharma, H.K. Mao, P.M. Bell and J.A. Xu, Journal of Raman Spectroscopy **16**, 350 (1985).

Slu93 P. Van Der Sluis, Philips J. Res. **47**, 203 (1993).

Sna91 K.A. Snail, C.M. Marks, Z.P. Lu, J. Heberlein and E. Pfender, Materials Letters **12**, 301-305 (1991).

Som90 M. Sommer and F.W. Smith, J. Mater. Res. **5**, 2433 (1990).

Som91 M. Sommer and F.W. Smith, New Diamond Science and Technology; MRS Int. Conf. Proc. , 443 (1991).

Som81 G.A. Somorjai, *Chemistry in Two Dimensions: Surfaces* (Cornall University Press, Ithaca, NY, 1981).

Spe89 K.E. Spear, J. Am. Ceram. Soc. **72**, 171 (1989).

Spi81 B.V. Spitsyn, L.L. Bouilov and B.V. Deryagin, J. Cryst. Growth **52**, 219 (1981).

Sri90 G.P. Srivastava, *The Physics of Phonons* (IOP Publishing Ltd, Bristol, 1990).

Sut92a L.F. Sutcu, C.J. Chu, M.S. Thompson, R.H. Hauge, J.L. Margrave and M.P. D'Evelyn, J. Appl. Phys. **71**, 5930 (1992).

Sut92b L.F. Sutcu, M.S. Thompson, C.J. Chu, R.H. Hauge, J.L. Margrave and M.P. D'Evelyn, Appl. Phys. Lett. **60**, 1685 (1992).

Tam94 M.A. Tamor and M.P. Everson, J. Mater. Res. submitted for publication, (1994).

Tar90 A. Tardieu, F. Cansell and J.P. Petitet, J. Appl. Phys. **68**, 3243 (1990).

Tre91 R.J. Trew, J. Yan and P.M. Mock, Proceedings of the IEEE **79**, 598 (1991).

Tsu82 R. Tsu, J. Gonzalez-Hernandez, S.S. Chao, S.C. Lee and K. Tanaka, Appl. Phys. Lett. **40**, 534 (1982).

Tsu83 R. Tsu, J. Gonzalez-Hernandez, J. Doehler and S.R. Ovshinsky, Solid State Comm. **46**, 79 (1983).

Ven73 S. Venugopalan and A.K. Ramdas, Phys. Rev. B **8**, 717 (1973).

Wha76 E. Whalley, A. Lavergne and P.T.T. Wong, Rev. Sci. Instrum. **47**, 845 (1976).

Wil94 C. Wild, R. Kohl, N. Herres, W. Muller-Sebert and P. Koidl, Diamond and Related Materials, submitted for publication, (1994).

Yar90 W.A. Yarbrough and R. Messier, Science **247**, 688 (1990).

Zhu91 W. Zhu, B. Stoner, B. Williams and J. Glass, Proceedings of the IEEE **79**, 621 (1991).

BIOGRAPHICAL SKETCH

William Broxton (Brock) Alexander was born on December 16, 1963, in Columbia, Missouri. He graduated from Susquehannock High School in Glen Rock, Pennsylvania, in 1981. In 1984 he joined the United States Air Force and was stationed at Eglin Air Force Base. He began his college career at night, attending Troy State University, in Ft. Walton, Florida. He left the Air force in 1987 to attend the University of Florida. He graduated in December, 1990 with a Bachelor of Science in Materials Science and Engineering. After receiving a SURA fellowship, he began working at Oak Ridge National Laboratory, and it was here where the interest in research and diamond films began. Consequently, he enrolled in the Department of Materials Science and Engineering at the University of Florida in the fall of 1991 to pursue graduate work in the area of diamond thin films.

I certify that I have read this study and that in my opinion it conforms to acceptable standards of scholarly presentation and is fully adequate, in scope and quality, as a dissertation for the degree of Doctor of Philosophy.

Paul H. Holloway, Chairman
Professor of Materials
Science and Engineering

I certify that I have read this study and that in my opinion it conforms to acceptable standards of scholarly presentation and is fully adequate, in scope and quality, as a dissertation for the degree of Doctor of Philosophy.

Timothy J. Anderson
Professor of Chemical
Engineering

I certify that I have read this study and that in my opinion it conforms to acceptable standards of scholarly presentation and is fully adequate, in scope and quality, as a dissertation for the degree of Doctor of Philosophy.

Robert T. DeHoff
Professor of Materials
Science and Engineering

I certify that I have read this study and that in my opinion it conforms to acceptable standards of scholarly presentation and is fully adequate, in scope and quality, as a dissertation for the degree of Doctor of Philosophy.

Robert M. Park
Professor of Materials
Science and Engineering

I certify that I have read this study and that in my opinion it conforms to acceptable standards of scholarly presentation and is fully adequate, in scope and quality, as a dissertation for the degree of Doctor of Philosophy.

Rajiv K. Singh
Assistant Professor of
Materials Science and
Engineering

This dissertation was submitted to the Graduate Faculty of the College of Engineering and to the Graduate School and was accepted as partial fulfillment of the requirements for the degree of Doctor of Philosophy.

May, 1995

Winfred M. Phillips
Dean, College of Engineering

Karen A. Holbrook
Dean, Graduate School

LD
1780
1995
.A379